Rydberg Atoms in Strong Fields: A Testing Ground for Quantum Chaos

by

Michael Courtney

B.S., summa cum laude, Louisiana State University,
(1989)

Submitted to the Department of Physics
in partial fulfillment of the requirements for the degree of

Doctor of Philosophy

at the

MASSACHUSETTS INSTITUTE OF TECHNOLOGY

February 1995

Signature of Author _____
Department of Physics
November 10, 1994

Certified by _____
Daniel Kleppner
Lester Wolfe Professor of Physics
Thesis Supervisor

Accepted by _____
George F. Koster
Professor of Physics
Chairman, Departmental Committee on Graduate Students

Rydberg Atoms in Strong Fields: A Testing Ground for Quantum Chaos

by

Michael Courtney

Submitted to the Department of Physics
on November 10, 1994, in partial fulfillment of the
requirements for the degree of
Doctor of Philosophy

Abstract

Rydberg atoms in strong static electric and magnetic fields provide experimentally accessible systems for studying the connections between classical chaos and quantum mechanics in the semiclassical limit. This experimental accessibility has motivated the development of reliable quantum mechanical solutions. This thesis uses both experimental and computed quantum spectra to test the central approaches to quantum chaos. These central approaches consist mainly of developing methods to compute the spectra of quantum systems in non-perturbative regimes, correlating statistical descriptions of eigenvalues with the classical behavior of the same Hamiltonian, and the development of semiclassical methods such as periodic-orbit theory. Particular emphasis is given to identifying the spectral signature of *recurrences*—quantum wave packets which follow classical orbits. The new findings include: the breakdown of the connection between energy-level statistics and classical chaos in odd-parity diamagnetic lithium, the discovery of the signature of very long period orbits in atomic spectra, quantitative evidence for the scattering of recurrences by the alkali-metal core, quantitative description of the behavior of recurrences near bifurcations, and a semiclassical interpretation of the evolution of continuum Stark spectra.

Thesis Supervisor: Daniel Kleppner
Lester Wolfe Professor of Physics

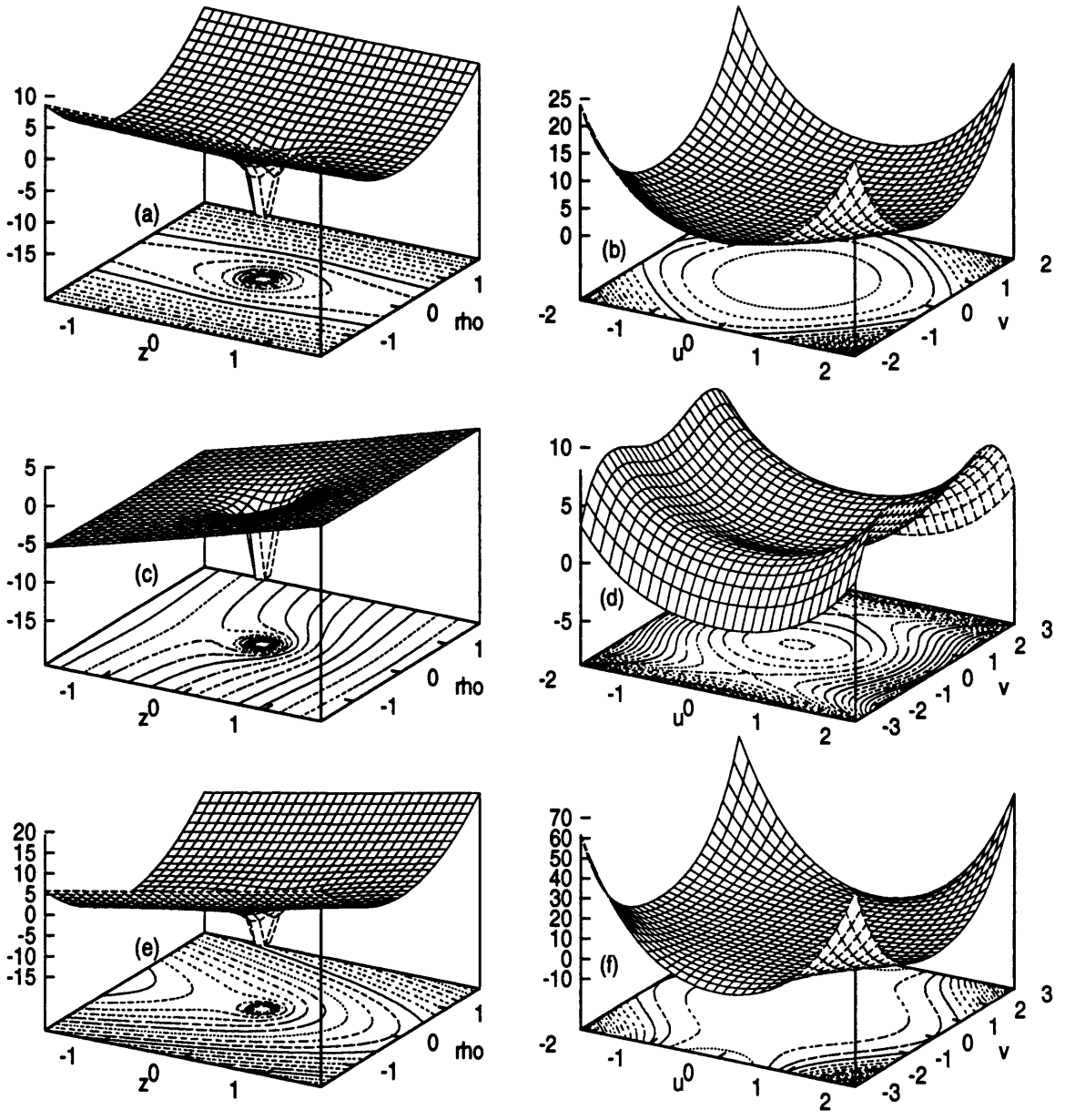

Figure 0-1: Potential surfaces for Rydberg atoms in strong fields. (a), (c), and (e) are in cylindrical coordinates. (b), (d), and (f) are in "regularized" semiparabolic coordinates. (a) and (b) Diamagnetic hydrogen; (c) and (d) Hydrogen in an electric field; (e) and (f) Hydrogen in parallel electric and magnetic fields.

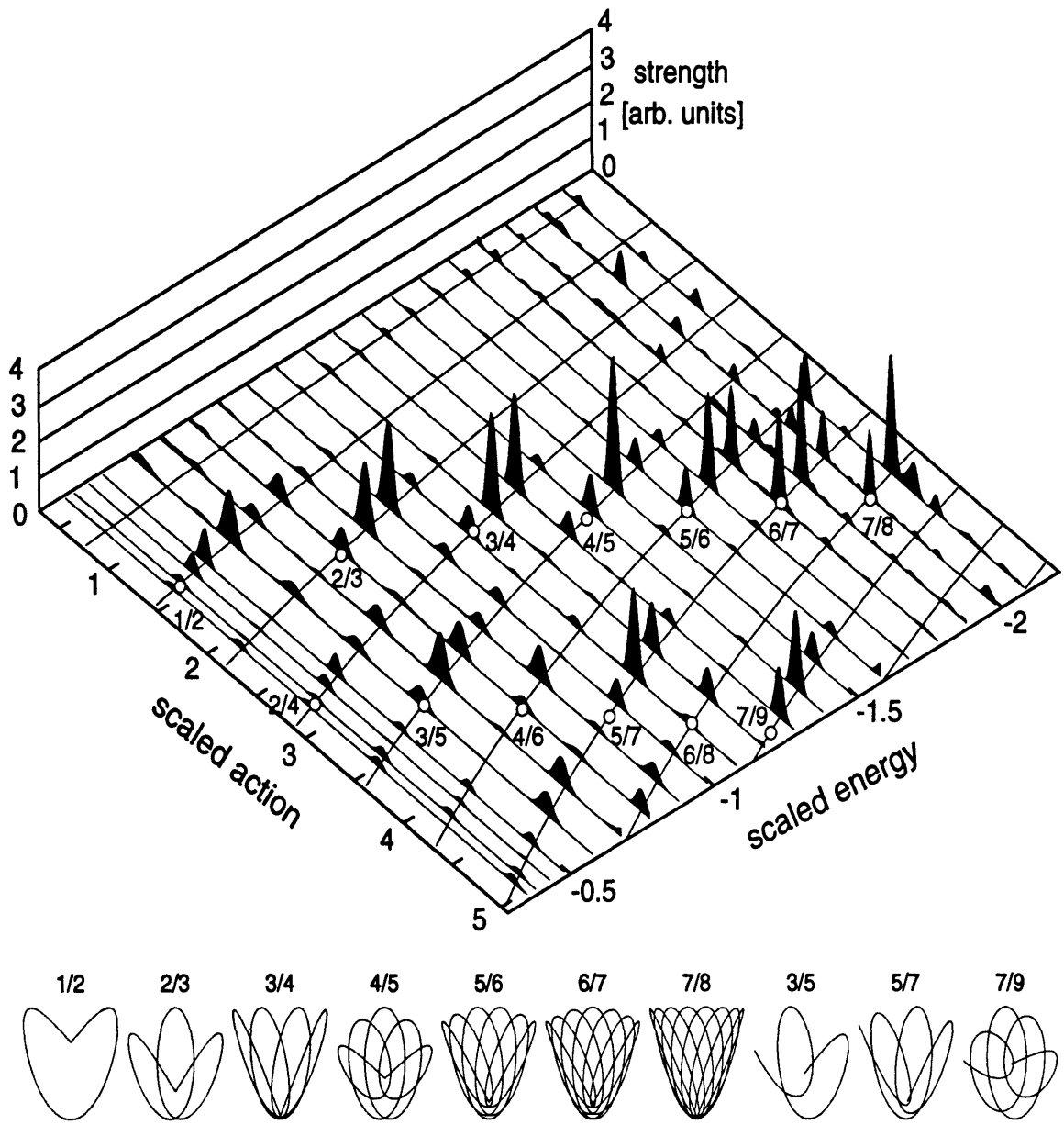

Figure 0-2: Recurrence spectra of lithium in an electric field. Details are described in Chapter 8. The curves in the horizontal plane represent the scaled action of the parallel orbit and its repetitions as a function of scaled energy. Locations of bifurcations are marked with small open circles. New orbits created in bifurcations have almost the same action as the corresponding return of the parallel orbit. Measured recurrence strengths are shown in the z direction. Recurrences are especially strong at scaled energies slightly lower than bifurcations. Orbits created by bifurcation of the parallel orbit are shown along the bottom. The 2/4, 4/6 and 6/8 orbits are repetitions of the 1/2, 2/3, 3/4 orbits respectively, so their shapes are identical.

Contents

List of Tables

List of Figures

Chapter 1

Introduction

Whoever sheds the blood of man, by man shall his blood be shed; for in the image of God has God made man.–Genesis 9:6

In the last twenty years, a great deal of work has been done seeking to understand Rydberg atoms in strong static fields. This work has produced high resolution experimental spectra and accurate calculations in many regions of interest for electric and magnetic field problems either separately or together. Fields are considered strong if their contributions to the Hamiltonian are comparable to or greater than the unperturbed energy. Rydberg atoms are necessary because the field strengths available in the laboratory are small compared with atomic fields of low-lying states.

Two major themes have motivated this work. The first is understanding the detailed quantum mechanical behavior of these novel systems. The second is exploring the connections between quantum mechanics and classical behavior, particularly in regimes of irregular classical motion—a subject that is generally called "quantum chaos."

Hydrogen is the simplest system to study theoretically. Alkali-metal atoms have been used in many experiments despite the fact that they break the zero field degeneracy of hydrogen because alkali atomic beams are easier to make, and the lasers needed to excite alkali atoms to Rydberg states have generally been more available.

However, as we shall see, alkali Rydberg atoms are also of interest for the study of quantum chaos because their core electrons can be a particularly interesting source of chaos.

This thesis presents studies of both the electric and magnetic field problems, including new experimental results for Rydberg atoms in an electric field. The quantum mechanics of alkali Rydberg atoms in strong electric fields is believed to be well understood, and the hydrogen problem is, in principle, exactly solved. A great deal is also understood about hydrogen in a strong magnetic field, but important areas, such as the continuum, remain to be studied. What is known about the diamagnetic hydrogen atom needs to be extended to other atoms. We know relatively little about the Rydberg atoms in parallel electric and magnetic fields and even less about the problem when the fields have perpendicular or arbitrary orientation.

With the notable exception of hydrogen in an electric field, the classical analogues of these systems undergo transitions from order to chaos as the field or energy is increased. In seeking to understand the connection between quantum mechanics and classical chaos, only the problem of hydrogen in a magnetic field has been extensively studied. The more general problem of Rydberg atoms in strong fields provides an even richer testing ground for theories describing quantum chaos.

This thesis deals with systems having rotational symmetry about the field axis. This excludes the case of electric and magnetic fields that are not parallel. As a result, L_z is a constant of motion, simplifying both the classical dynamics and quantum mechanics considerably.

In spite of many advances [GUT90, HAA91], the current state of "quantum chaology" is unsatisfying. There is no theory rigorously derived from first principles which enables us to discern the nature of the classical system from the quantum spectra. There are some semi-empirical theories (mostly dealing with statistical properties of spectra) which appear to work in many situations, but often these test cases are either not real physical systems or have Hamiltonians which are not well understood.

1.1 What is Quantum Chaos?

Quantum chaos needs to be defined before we can use Rydberg atoms in strong fields as a testing ground. Quantum chaos currently is more of a question than a theory. The primary question that quantum chaos seeks to answer is, *What is the relationship between quantum mechanics and classical chaos?* We currently believe that classical mechanics is a special case of quantum mechanics. If this is true, then there must be quantum mechanisms underlying classical chaos. In seeking to answer the basic question of quantum chaos, several approaches have been employed:

- Development of methods for solving quantum problems where the perturbation cannot be considered small.
- Correlating statistical descriptions of eigenvalues with the classical behavior of the same Hamiltonian.
- Semiclassical methods such as periodic-orbit theory.
- Direct application of the correspondence principle.

In this thesis, we will pursue all of these approaches.

1.1.1 Quantum Mechanics in Non-Perturbative Regimes

For conservative systems, the goal of quantum mechanics in non-perturbative regimes is to find the eigenvalues and eigenvectors of a Hamiltonian of the form

$$H = H_s + \epsilon H_{ns}, \tag{1.1}$$

where H_s is separable in some coordinate system, H_{ns} is non-separable in the coordinate system in which H_s is separated, and ϵ is a parameter which cannot be considered small. Physicists have historically approached problems of this nature by trying to find the coordinate system in which the non-separable Hamiltonian is smallest and then treating the non-separable Hamiltonian as a perturbation.

Finding constants of motion so that this separation can be performed can be a difficult (sometimes impossible) analytical task. Solving the classical problem can give valuable insight into solving the quantum problem. If there are regular classical solutions of the same Hamiltonian, then there are (at least) approximate constants of motion, and by solving the classical problem, we gain clues how to find them.

Other approaches have been developed in recent years. One is to express the Hamiltonian in different coordinate systems in different regions of space, minimizing the non-separable part of the Hamiltonian in each region. Wavefunctions are obtained in these regions, and eigenvalues are obtained by matching boundary conditions (for example, [WAG89]).

Another approach is numerical matrix diagonalization. If the Hamiltonian matrix is computed in any complete basis, eigenvalues and eigenvectors are obtained by diagonalizing the matrix. However, all complete basis sets are infinite, and we need to truncate the basis and still obtain accurate results. These techniques boil down to choosing a truncated basis from which accurate wavefunctions can be constructed. The computational time required to diagonalize a matrix scales as N^3, where N is the dimension of the matrix, so it is important to choose the smallest basis possible from which the relevant wavefunctions can be constructed. It is also convenient to choose a basis in which the matrix is sparse and/or the matrix elements are given by simple algebraic expressions because computing matrix elements can also be a computational burden.

A given Hamiltonian shares the same constants of motion for both classical and quantum dynamics.[1] However, if we merely find quantum solutions of a Hamiltonian which is not approachable by perturbation theory, we may learn a great deal about quantum solutions, but we have learned little about quantum chaos. Nevertheless, learning how to solve such quantum problems is an important part of answering the question of quantum chaos.

[1]Quantum systems can also have additional quantum numbers corresponding to discrete symmetries.

1.1.2 Statistical Descriptions of Quantum Chaos

Statistical descriptions of the distribution of energy levels have been found to be useful in studying quantum chaos. These include a simple nearest-neighbor statistic, higher order correlations, and parametric generalizations.

If s is the energy level spacing, and is normalized so that the average spacing is one, then we can define a probability distribution $P(s)$ for the energy level spacings. It has been asserted [BET77, GUT90] that for Hamiltonians with regular classical motion, the quantum solution will yield

$$P(s) = e^{-s}, \tag{1.2}$$

and this has been shown to be true for a number of test cases [HAA91].

In addition, random matrix theory [BOG84] predicts that random matrices which are invariant under time reversal have a distribution well approximated by

$$P(s) = \frac{\pi}{2} s e^{-\pi s^2/4}, \tag{1.3}$$

which is the Wigner distribution. These two distributions are intuitively consistent for small level spacings. An integrable system has degeneracies and is consistent with a finite probability of $s = 0$. A non-integrable system has no degeneracies and is consistent with zero probability of $s = 0$.

A number of classically chaotic quantum systems have been shown to have a Wigner distribution of level spacings, and this is considered to be the signature of quantum chaos by many in the field [DEG86c]. Before testing other statistical descriptions of quantum chaos, a system is usually checked to see whether it has a Wigner distribution. Only systems which do are considered quantum chaotic.

I believe that this is an erroneous criterion for two reasons:

- In Chapter 5 we shall see that there are systems which are chaotic but do not exhibit Wigner statistics. This points to a need for statistical descriptions that are not generalizations of the Wigner distribution.

- The Hamiltonians of chaotic systems are not random matrices. On the contrary, not only can they be computed, but some of them can be expressed as sparse matrices with elements given by simple algebraic expressions. An example is hydrogen in a magnetic field.

However, the successes of these statistical descriptions warrant our attention because they have allowed us to better understand the quantum problems and provide a tool for quantifying certain spectral features in an unambiguous way.

1.1.3 Semiclassical Methods and Periodic-Orbit Theory

Periodic-orbit theory currently provides the most concrete link between classically chaotic systems and their quantum counterparts. Periodic-orbit theory asserts that, in the semiclassical limit, each periodic orbit gives rise to a sinusoidal modulation of the density of states, and there is a recipe for finding the amplitude and phase of the modulation contributed by each periodic orbit. A sum over all of the periodic orbits must be performed to compute a spectrum.

However, their are several unsatisfying issues related to periodic-orbit theory:

- Attempting to find the quantum spectra by a sum over periodic orbits reverses the causal relationship between quantum mechanics and classical dynamics.[2] We believe that classical mechanics is a special case of quantum mechanics. By using orbits to compute the spectrum, we are treating the classical dynamics as the underlying cause of spectral features. It is more satisfying to view periodic-orbit theory as a way of using quantum mechanics to tell us about periodic orbits of the classical system.

- Quantum mechanics can greatly reduce the importance of terms in the Hamiltonian which can cause large effects classically.

- The limits of applicability of periodic-orbit theory are not known.

[2]We tolerate this reversal because periodic-orbit theory only claims to be an approximation.

- In practice, the greatest success of periodic-orbit theory can give a few hundred features which correspond to thousands of eigenvalues. Where did all the lost information go?

- One would expect that a semiclassical method would be formulated in terms of a series expansion in powers of $\hbar$. This would clarify the range of applicability and convergence in the classical limit. However, to date no one has shown periodic-orbit theory to be consistent with a power series in $\hbar$.[3]

In addition to these conceptual difficulties, there are several practical difficulties which need to be addressed:

- The number of periodic orbits proliferates exponentially as a function of action for chaotic systems.

- There are an infinite number of periodic orbits, and the convergence properties of the periodic-orbit expansions are unknown.

- Long-period orbits of chaotic systems are difficult to compute because most trajectories are unstable and sensitive to roundoff errors and details of the numerical integration.

- The amplitude of the sinusoidal modulation predicted by periodic-orbit theory can become infinite for certain orbits. This effect is unphysical and computationally bothersome. More fundamentally, it contributes to the convergence difficulties.

I will discuss these points when I explain periodic-orbit theory and its application to Rydberg atoms in strong fields. In spite of these issues, periodic-orbit theory provides the most tangible link between the quantum and classical dynamics of chaotic systems.

[3]From private communications with Michael Berry, John Delos, and John Shaw, it seems that people have tried to show that periodic-orbit theory is consistent with a power series in $\hbar$. The consensus seems to be that no one has done so yet, and the literature of which I am aware does not directly address this issue.

1.1.4 Direct Application of the Correspondence Principle

Understanding quantum chaos requires understanding the manner in which a quantum system continuously evolves into a classically chaotic system as some parameter is changed so that the system approaches the correspondence principle limit. The real correspondence principle limit, $\hbar \rightarrow 0$, is not physically realizable. Furthermore, we cannot use the limit of large quantum numbers because non-integrable quantum problems do not have good quantum numbers.

Martin Gutzwiller has commented on the problem [GUT90]. He pointed out that the Toda lattice[4] is an integrable system with three variable parameters. A system of units can often be defined in terms of three constants. In such a system of units, $\hbar$ will have a numerical value which depends on the parameters, so it can be made smaller by changing the parameters. The Toda lattice is also interesting because it is integrable but not separable.

Another integrable system which has three variable parameters is the hydrogen atom in an electric field. If we define a system of units where the electronic mass, electronic charge, and external field are all equal to one, then the size of $\hbar$ can be made smaller by changing the parameters. Unfortunately, we do not have a laboratory knob on the charge or mass of the electron. We can still change $\hbar$ by changing the external field, F. The numerical value of $\hbar$ then scales as $\hbar \propto F^{1/4}$.

This same technique is also applicable to non-integrable systems with three parameters. For the case of hydrogen in a magnetic field we would define a system of units where the electronic mass, electronic charge, and external field are all equal to one. The numerical value of $\hbar$ then scales as $\hbar \propto B^{1/3}$.

1.2 Why Rydberg Atoms?

Rydberg atoms provide a testing ground for quantum chaos because they show transitions from order to chaos. Furthermore, Rydberg states of atoms are amenable to

[4]The Toda lattice is a system of particles in one dimension with an exponential potential for interparticle interactions.

semiclassical approximations. Finally, Rydberg atoms are experimentally attractive because they can be studied with the clarity of modern laser spectroscopy.

In classical systems, chaos is described in terms of non-integrability and the destruction of invariant tori. (See Chapter 3.) For the systems under study, chaos only occurs for energies near the ionization limit, hence the need for Rydberg atoms. In quantum systems, irregularity characterizes systems where the perturbation is of the same magnitude as the unperturbed Hamiltonian.

The unperturbed eigenvalues of hydrogen are

$$E_0 = -\frac{1}{2n^2}. \tag{1.4}$$

The perturbation of an applied electric field is $H_F = Fz$, which scales as

$$E_F \propto Fn^2. \tag{1.5}$$

The ratio of the Stark perturbation to the unperturbed Hamiltonian is then

$$\frac{E_F}{E_0} \approx 2Fn^4. \tag{1.6}$$

For an applied field of $1000\,V/cm$, this ratio is 1 for $n \approx 40$. The perturbation of an applied magnetic field is $H_B = B^2\rho^2/8$, which scales as

$$E_B \propto \frac{1}{8}B^2n^4. \tag{1.7}$$

The ratio of the diamagnetic perturbation to the unperturbed Hamiltonian is

$$\frac{E_B}{E_0} \propto \frac{1}{4}B^2n^6. \tag{1.8}$$

For an applied field of $6\,T$, this ratio is 1 for $n \approx 43$. Experimentally the regime of $n > 40$ is readily accessible. Consequently, Rydberg atoms provide systems in which the perturbations can be comparable to the unperturbed energy.

1.3 Outline of Thesis

The quantum mechanics of Rydberg atoms in strong fields is presented in Chapter 2. The various regimes of interest and methods used to compute the spectra are described. The discrete spectra of hydrogen and lithium are presented and discussed for diamagnetism, the Stark effect and the parallel field systems. The role of symmetries in interpreting the spectra is emphasized.

Chapter 3 describes the classical dynamics of atoms in strong fields. Classical chaos is defined for conservative systems, and its basic features are summarized. The onset of chaos in Rydberg atoms in strong fields is described and illustrated using Poincaré surfaces of section. The classical dynamics of alkali atoms is modeled using analytical core potentials which accurately reproduce the measured quantum defects. The dynamics of the alkali-metals is shown to become chaotic in regimes where hydrogen is regular.

The experimental apparatus and techniques used to perform high-resolution spectroscopy of lithium in strong electric and magnetic fields are described in Chapter 4. A number of experimental details are given, and the method of performing precise spectroscopy at constant scaled energy is described. This method allows for accurate measurement of recurrence spectra, the importance of which is described below.

Chapter 5 is devoted to energy-level statistics. The nearest-neighbor distribution of energy levels is compared with the supposed generic behavior. Hydrogen shows the canonical behavior for diamagnetism, the Stark effect, and in parallel fields. Lithium shows the expected behavior for the Stark effect, but can deviate greatly from it in the cases of diamagnetism and parallel fields.

Large scale spectral structures display evidence of recurrences—quantum wave packets which follow classical orbits. Chapter 6 describes the application of periodic-orbit theory and the related closed-orbit theory to Rydberg atoms in strong fields. I summarize the physical picture underlying their principal results which predict that classical orbits produce sinusoidal modulations in quantum spectra and describe difficulties with using these results to compute quantum spectra. I motivate the approach

of using these theories to look for the effect of orbits in quantum spectra and describe methods of computing spectra at constant scaled energy. The Fourier transform of a constant scaled energy spectrum is called a recurrence spectrum because each peak corresponds to a wave packet which follows a classical orbit.

Computed diamagnetic recurrence spectra are presented and discussed in Chapter 7. The evolution of classical orbits during the onset of chaos is described and compared with the evolution of recurrence spectra. The results demonstrate the need for several modifications to closed-orbit theory, including corrections for the alkali-metal core in lithium and corrections for the size of $\hbar$. Chapter 7 presents the most precise confirmation yet achieved of the applicability of closed-orbit theory to include long-period orbits. These results also demonstrate the utility of periodic-orbit theory and closed-orbit theory to glean purely classical information from quantum spectra.

Chapter 8 presents both experimental and computed recurrence spectra of lithium in an electric field. The evolution of the spectra from a single sinusoidal oscillation at large positive energies to a quasidiscrete spectrum below $E = -2F^{1/2}$ is given a natural and intuitive interpretation in terms of the closed-orbits of the system and the large increase of recurrence strength associated with the bifurcation of closed orbits. In addition, the chaotic nature of the quasidiscrete spectrum is described in terms of the scattering of recurrences from one orbit into another by the alkali-metal core.

Computed recurrence spectra of Rydberg atoms in parallel electric and magnetic fields are presented in Chapter 9. The beginning of an interpretation is given in terms of classical orbits. However, these spectra are much more complex than the case of a single field. Consequently, the discussion is primarily qualitative.

Chapter 10 suggests several possible ways of characterizing the amount of chaos in a system from global properties of recurrence spectra. The techniques of counting recurrence peaks, integrating the area under the recurrence spectrum and studying the height distribution of recurrence peaks are tested in diamagnetic hydrogen, diamagnetic lithium, and lithium in an electric field. A summary of the most important features of this work is presented in Chapter 11, where conclusions and unanswered questions are discussed.

Appendix A is a short paper which was published in *Physical Review Letters* [CJS94]. It shows that lithium in an electric field is classically chaotic and identifies the signature of closed orbits in quasidiscrete experimental photoabsorption spectra, including very long period orbits. Appendix B is another short paper which has been submitted to *Physical Review Letters* [CJS95]. It provides experimental evidence for interpreting the evolution of the Stark spectrum from a single sinusoid at large positive energies to a quasidiscrete spectrum at low energies in terms of closed orbits and their bifurcations. Semiclassical formulas for the behavior of the spectrum near classical bifurcations are shown to agree with experiment.

The thesis is long, and I should provide a roadmap of the most interesting points. Chapter 2 is a review of well-known quantum mechanical techniques and results. Chapter 3 will appeal to fans of classical chaos and those who appreciate the beauty of Poincaré surfaces of section. Chapter 4 will interest those who want to know the experimental details. Chapter 5 is brief and to the point that the Wigner and Poisson distributions are not reliable as generic indicators of whether the classical motion is chaotic or regular. Chapters 6, 7, and 8 are the heart of the thesis and present both confirmations and challenges to closed-orbit theory and periodic-orbit theory. Chapters 6, 7, and 8 provide a fair understanding of the most important aspects of this work. Chapters 9 and 10 present preliminary work which contains no profound or important conclusions. They were included (mainly) to interest others in continuing work in these areas.

Chapter 2

Quantum Mechanics of Rydberg Atoms

The LORD *had said to Abram, "Leave your country, your people and your father's household and go to the land I will show you."*–Genesis 12:1

This chapter presents a summary of the quantum mechanics of Rydberg atoms in strong fields. A discussion of field-free one-electron atoms is followed by a description of methods for computing the spectra in applied fields. The basic features of the Stark effect in hydrogen and alkali-metals are reviewed, followed by a discussion of Rydberg atom diamagnetism. Finally, the more complicated problem of Rydberg atoms in parallel electric and magnetic fields is discussed. This chapter emphasizes the role of symmetries in the low-field region.

2.1 One-Electron Atoms

In atomic units ($e = m_e = \hbar = 1$), the Hamiltonian of the hydrogen atom is

$$H = \frac{p^2}{2} - \frac{1}{r}. \tag{2.1}$$

This Hamiltonian is solved in many undergraduate texts by the technique of separation of variables. The spherical symmetry of the problem implies the conservation of angular momentum, L, which is quantized and given by $L^2 = l(l+1)\hbar^2$, where l is an integer. The cylindrical symmetry leads to a conservation of the angular momentum around some quantization axis. This axis is usually taken to be the z axis, and L_z is conserved. L_z is also quantized, and it is given by $L_z = m\hbar$, where $|m| \leq l$.

The boundary condition on the radial wavefunction leads to the well-known expression for the energy eigenvalues in terms of the principal quantum number n,

$$E_{n,l,m} = -\frac{1}{2n^2}. \tag{2.2}$$

The condition that the wavefunction be normalizable leads to the restriction that l be an integer less than n. Each energy level is n^2 degenerate which can be understood in terms of another symmetry, the conservation of the Runge-Lenz vector,

$$\vec{A} = [\vec{p} \times \vec{L}] - \frac{\vec{r}}{r}. \tag{2.3}$$

This symmetry is also the reason why all Kepler orbits are periodic.

Alkali-metal atoms have one valence electron and several core electrons. Since the core electrons make up a filled shell, the charge distribution of the core is spherically symmetric. For energies lower than those needed to excite the core electrons, many features of the system can be understood by modeling the system as a single electron moving in a Coulomb potential plus an average core potential.

The potential experienced by the outer electron is Coulombic for distances much greater than the core radius. It was discovered empirically that the energies of alkalis can be written as

$$E_{n,l} = -\frac{1}{2(n-\delta_l)^2}, \tag{2.4}$$

where the quantum defect δ_l is nearly constant for a given l. The quantum defect is largest for $l = 0$ because only the $l = 0$ wavefunction is non-zero at the origin. The quantum defect decreases with increasing l because the probability of being in the

Table 2.1: Atomic Units

	Hydrogen	Lithium-7
Energy (cm^{-1})	$2.193,551,660(2) \cdot 10^5$	$2.194,574,700(2) \cdot 10^5$
Length (cm)	$5.294,6545(2) \cdot 10^{-9}$	$5.292,1863(2) \cdot 10^{-9}$
Magnetic Field (T)	$2.347,960(3) \cdot 10^5$	$2.350,150(3) \cdot 10^5$
Electric Field (V/cm)	$5.136,611(1) \cdot 10^9$	$5.141,4041(5) \cdot 10^9$

core region decreases with increasing l.

2.2 Atomic Units

This thesis uses atomic units primarily for the theoretical development and spectroscopic units for presentation of spectra. Table 2.1 gives the atomic units of energy, length, magnetic field, and electric field for hydrogen and lithium. The atomic units differ because they are derived using the appropriate reduced mass of the electron.

2.3 Methods of Computation

All computed spectra presented in this thesis are obtained by diagonalization of the Hamiltonian matrix in a suitable basis. The spherical Sturmian basis is used for hydrogen in a magnetic field. Iu [IUC91] used the Λ basis to compute the spectra of diamagnetic hydrogen, and he also adapted the method to compute the diamagnetic spectrum of odd-parity lithium. The basis of zero-field eigenstates is used for both hydrogen and alkali-metal atoms. The Givens-Householder [ORT67, COO61] and Lanczos [LAN50] methods are used for matrix diagonalization.

The goal of numerical diagonalization is to provide accurate eigenvalues and perhaps oscillator strengths or wavefunctions in a particular region of interest. This needs to be accomplished with a minimum of computation time and memory usage. With a given amount of computer speed and memory, we want to compute the spectrum in as many regions of interest as possible.

2.3.1 Spherical Sturmian Basis

Edmonds [EDM73] was the first to compute the spectra of diamagnetic hydrogen in a spherical Sturmian basis. Clark and Taylor [CLT82] recognized the usefulness of being able to change the length scale of the basis depending on the region of energy and field. Delande and co-workers [DBG91] applied a complex rotation to the Sturmian basis to compute the spectrum of diamagnetic hydrogen for positive energy. This technique has recently been extended to other atoms [DTH94].

The spherical Sturmian basis functions are

$$\Psi_{nlm}(r) = S_{nl}^{(\alpha)}(r) Y_{lm}(\theta, \phi), \tag{2.5}$$

where $S_{nl}(r)$ is the radial Sturmian function,

$$S_{nl}^{(\alpha)}(r) = \left(\frac{(n-l-1)!}{2(n+l)!} \right)^{(\frac{1}{2})} \left(\frac{r}{\alpha} \right)^{l+1} e^{-\frac{r}{2\alpha}} L_{n-l-1}^{2l+1} \left(\frac{r}{\alpha} \right). \tag{2.6}$$

$L_i^j(x)$ is the associated Laguerre polynomial (also found in the hydrogen wavefunction).

This basis is useful for computing diamagnetic hydrogen spectra because the Hamiltonian matrix is sparse and can be ordered so that it has a bandwidth of roughly n. In addition, matrix elements are given by simple analytic formulas. Perhaps most importantly, the length scale of the Sturmian basis functions can be varied by varying the parameter α. Choosing α appropriately for a given energy and field region can greatly reduce the number of basis functions needed to accurately compute spectra.

To compute spectra of diamagnetic hydrogen we need to be able to construct eigenfunctions from a linear superposition of the basis set. It is computationally expedient to have as small a basis as possible. It is wise to choose a basis of functions which oscillate in the classically allowed region and which decay exponentially in the classically forbidden region. The length scale of the Sturmian basis functions is $n\alpha$, so the Sturmian functions with $n = \alpha$ have a length scale of α^2.

At a given energy, diamagnetic hydrogen has two relevant length scales, the clas-

sical turning points along the field and perpendicular to the field. The turning point along the field is given by $z = -1/E$ or roughly $2n^2$. The turning point perpendicular to the field is found by solving

$$E = -\frac{1}{\rho} + \frac{1}{8}B^2\rho^2 \tag{2.7}$$

for ρ. The length scale perpendicular to the field is always smaller than the length scale parallel to the field due to the confining effect of the magnetic field. The value of α is chosen to represent a compromise between these two length scales. For energies close to the ionization limit,

$$\sqrt{2}B^{-\frac{1}{3}} < \alpha < \frac{1}{\sqrt{-2E}}. \tag{2.8}$$

The length scale of the Sturmian basis functions varies more slowly than the length scale of the hydrogen basis as a function of n. For this reason, α can be chosen so that more Sturmian basis functions have a length scale closer to the desired energy range than the hydrogen basis with the same number of basis functions.

These functions do not form an orthogonal basis. The elements of the overlap matrix are

$$B_{nl,n'l'} = \int_0^\infty S_{nl}^{(\alpha)}(r) S_{n'l'}^{(\alpha)}(r)\, dr. \tag{2.9}$$

These matrix elements are given by

$$B_{nl,n'l'} = \begin{cases} \alpha n & n' = n \\ -\frac{1}{2}\alpha[(n+l+1)(n-1)]^{\frac{1}{2}} & n' = n+1 \quad l = l'. \end{cases} \tag{2.10}$$

Since the Y_{lm} functions are orthonormal, the overlap matrix elements are all zero if $l \neq l'$. The matrix elements of r^2 are given in [CLT82].

Since the Sturmian functions do not form an orthogonal basis, we must solve the generalized eigenvalue problem,

$$H\Psi = EB\Psi, \tag{2.11}$$

where H is the Hamiltonian matrix, B is the overlap matrix, Ψ is the eigenvector, and E is eigenvalue. The basis is ordered according to l and n, with all the states of maximum $l = l_{max}$ first, followed by the states with $l = l_{max} - 1$, down to $l = l_{min}$. Within each l block, the n's are ordered from $n = n_{max}$ to $n = l + 1$. With this ordering, the overlap matrix is tridiagonal and the Hamiltonian is banded with a bandwidth of about $n_{max} + 3$.

2.3.2 Basis of Zero-Field Eigenstates

If the external fields are a small perturbation to the system, it is natural to use the basis of zero-field eigenstates. For larger fields, a large basis is required to produce convergent eigenvalues, but the zero-field basis still provides a convenient way to compute the spectra of alkali Rydberg atoms in strong fields.

The matrix element of the diamagnetic term in the Hamiltonian is given by

$$< n'l'm|\frac{1}{8}B^2\rho^2|nlm >= \frac{1}{8}B^2 < n'l'|r^2|nl >< l'm|sin^2\theta|lm > . \tag{2.12}$$

The matrix element of the electric field term is

$$< n'l'm|Fz|nlm >= F < n'l'|r|nl >< l'm|cos\theta|lm > . \tag{2.13}$$

Evaluation of the angular matrix elements is trivial. The radial matrix elements are computed numerically.

The unperturbed energy levels $E_{n,l}$ of alkali Rydberg levels can be computed from the known quantum defects. Using these energies the radial equation is integrated inward from infinity. The integration is started at a radius well beyond the classical turning point, where the wavefunction is decaying exponentially. Because we are evaluating the matrix elements between Rydberg states, the integration can be cut off at some radius greater than the core radius. This is because the integrals

$$< n'l'|r^2|nl >= \int_0^\infty R_{n'l'}r^2R_{nl}dr \tag{2.14}$$

and

$$< n'l'|r|nl >= \int_0^\infty R_{n'l'} r R_{nl} dr \tag{2.15}$$

have only a very small contribution inside the core for Rydberg states.

The radial equation is solved for the wavefunctions using the Numerov algorithm [NUM33]. This method is very efficient for ordinary, second order linear differential equations without a first order term. This makes it useful for numerical integration of the Schrödinger equation in many situations. However, since the Numerov algorithm uses a constant step size for the entire integration, it is useful to scale the radial coordinate to give approximately the same number of integration steps between nodes of the radial wavefunction. The scaling and computation of these matrix elements is described in detail in Michael Kash's thesis [KAS88] and Zimmerman's seminal work on Stark spectra of alkali-metals [ZLK79].

2.3.3 Matrix Diagonalization

If we could diagonalize arbitrarily large matrices with little effort, we could solve any quantum system for which we could write the Hamiltonian. We cannot do this, but the increasing speed of computing facilities allows us to diagonalize some large matrices. For this thesis, matrices as large as 10000 × 10000 were diagonalized.

The two techniques used to solve eigenvalue problems in this thesis are the Givens-Householder and Lanczos algorithms. The Lanczos algorithm computes a small number of eigenvalues near a given energy and can be used to compute the overlap of the eigenvectors with an initially fixed vector. This is convenient for computing oscillator strengths because $< \Psi|z|nlm >$ can be computed without computing every eigenvector and then computing the overlaps. In addition, the Lanczos method preserves the banded nature of the matrix during the diagonalization process. As a result, the Hamiltonian matrix requires only *dimension* × *bandwidth* of memory.

The Givens-Householder method computes all of the eigenvalues of the Hamiltonian matrix and can be used to compute eigenvectors also. This is useful if all the eigenvalues are needed, or if the complete eigenvectors are desired. However, most of

Table 2.2: Memory required using different bases and diagonalization techniques. N is largest principal quantum number in the basis.

	Electric	Magnetic	Parallel Fields
dimension	$N^2/2$	$N^2/4$	$N^2/2$
bandwidth (Atomic)	$2N$	$2N$	$3N$
bandwidth (Sturmain)	N	N	$2N$
Givens-Householder memory	$N^4/8$	$N^4/32$	$N^4/8$
Lanczos memory (Atomic)	N^3	$N^3/2$	$3N^3/2$
Lanczos memory (Sturmian)	$N^3/2$	$N^3/4$	N^3

the higher eigenvalues are not converged due to truncation of the basis. For this reason, the Lanczos method is usually preferred. However, the Lanczos method has some trouble with multiply degenerate eigenvalues. It can usually handle a level crossing or small anticrossing with only a small loss of accuracy but fails completely at the multiple degeneracies of zero-field Rydberg atoms. In Table 2.2, memory requirements are compared for the two diagonalization methods for various cases of interest.

2.4 Atoms in an Electric Field

2.4.1 Hydrogen in an Electric Field

The Hamiltonian of hydrogen in an electric field F in the z direction is

$$H = \frac{p^2}{2} - \frac{1}{r} + Fz. \tag{2.16}$$

This Hamiltonian can be separated in the parabolic coordinate system (ξ, η) defined by

$$\begin{aligned} r &= (\xi + \eta)/2 \\ z &= (\xi - \eta)/2. \end{aligned} \tag{2.17}$$

If we define the wavefunction Ψ as

$$\Psi = (\xi\eta)^{-\frac{1}{2}} f(\xi) g(\eta) e^{\pm i m \phi}, \tag{2.18}$$

we can substitute into the Hamiltonian and obtain the equations

$$\frac{d^2 f}{d\xi^2} + \left(\frac{E}{2} + \frac{Z_1}{2} + \frac{1 - m^2}{4\xi^2} - \frac{F}{4}\xi \right) f = 0, \tag{2.19}$$

and

$$\frac{d^2 g}{d\eta^2} + \left(\frac{E}{2} + \frac{Z_2}{2} + \frac{1 - m^2}{4\eta^2} + \frac{F}{4}\eta \right) g = 0, \tag{2.20}$$

where Z_1 and Z_2 are separation parameters related by the constraint

$$Z_1 + Z_2 = 1. \tag{2.21}$$

In zero field, these equations have a simple analytic solution: f and g are Laguerre polynomials of order n_1 and n_2. These parabolic quantum numbers are related to the spherical quantum numbers (n, l, m) by

$$n_1 + n_2 + |m| + 1 = n. \tag{2.22}$$

Solutions to the non-zero field case can be found by applying perturbation theory to arbitrary order in the electric field. The energy through second order is

$$E = -\frac{1}{2n^2} + \frac{3}{2} n (n_1 - n_2) F - \frac{1}{16} n^4 \left[17n^2 - 3(n_1 - n_2)^2 - 9m^2 + 19 \right] F^2. \tag{2.23}$$

This spectrum is shown in Figure 2-1. Unlike the spectra of other Rydberg atoms in strong fields, the energy levels of hydrogen in an electric field actually cross. This is because the problem has an exact constant of motion in addition to the energy which allows the separation of variables [RED64]. This constant of motion is $\vec{F} \cdot \vec{C}$,

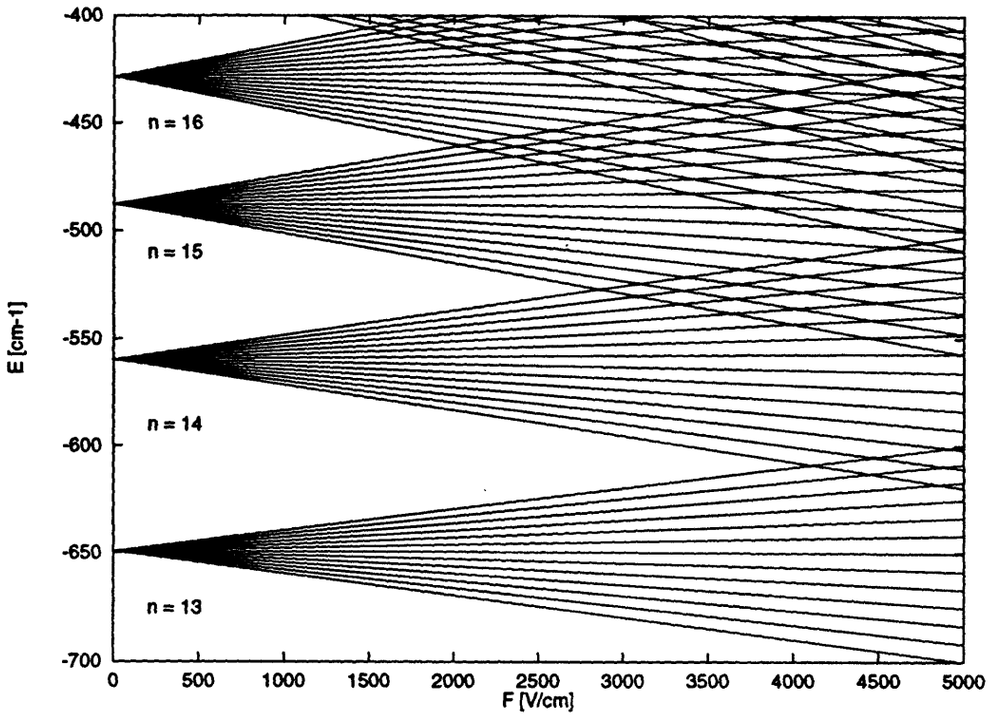

Figure 2-1: Spectrum of Hydrogen in an Electric Field for $m = 0$.

where $\vec{C}$ is a generalization of the Runge-Lenz vector,

$$\vec{C} = \vec{A} - \frac{1}{2}\left[(\vec{r} \times \vec{F}) \times \vec{r}\right]. \tag{2.24}$$

2.4.2 Alkalis in an Electric Field

Alkali-metal atoms have a spherically symmetric core potential which prevents separation of variables and analytical solution. Two common approaches of perturbation theory are:

- Consider the core potential a perturbation to the problem of hydrogen in an electric field and use the known quantum defects to compute the matrix elements of the core potential in the parabolic hydrogenic basis [KGJ80]. This is the Komarov method and it can be used to accurately compute the size of core anticrossings in both the electric and magnetic field problems if the quantum defects are small [IUC91]. Care needs to be taken in applying this method to

compute all the eigenvalues of the problem because the method diverges.

- Consider the electric field to be a perturbation to the field-free alkali and compute the matrix elements of Fz in the basis of the field free eigenstates [LZD76]. This method is useful for computing eigenvalues below the ionization limit and slightly above it.

The spectrum of lithium is shown in Figure 2-2 for $m = 0$. In contrast to hydrogen, the energy levels never cross and often have large anticrossings. The $m = 1$ case of lithium shown in Figure 2-3 is much more hydrogenic. This is because the largest quantum defect mixed in the $m = 1$ basis set is $\delta_p = 0.05$ compared with $\delta_s = 0.4$ for $m = 0$. The $m = 1$ spectrum of lithium is shown in Figure 2-3. The anticrossings are much smaller for $m = 1$.

All alkalis follow this pattern. The spectra become more hydrogenic as m is increased, because the angular momentum barrier keeps the wavefunctions out of the region of the core. For example, sodium has large anticrossings for $m = 0$ and $m = 1$, and becomes hydrogenic for $m = 2$.

2.4.3 Ionization Processes in an Electric Field

Alkali-metal atoms in an electric field ionize by three processes [LKK78]. Photoionization occurs by directly exciting an electron into a continuum resonance. Ionization also occurs by excitation into a quasidiscrete state which then tunnels through the potential barrier along the axis of the applied field. A process called autoionization also occurs whereby the alkali core causes mixing between one quasidiscrete state with little probability of tunneling and either a continuum state or another quasidiscrete state which readily tunnels through the potential barrier.

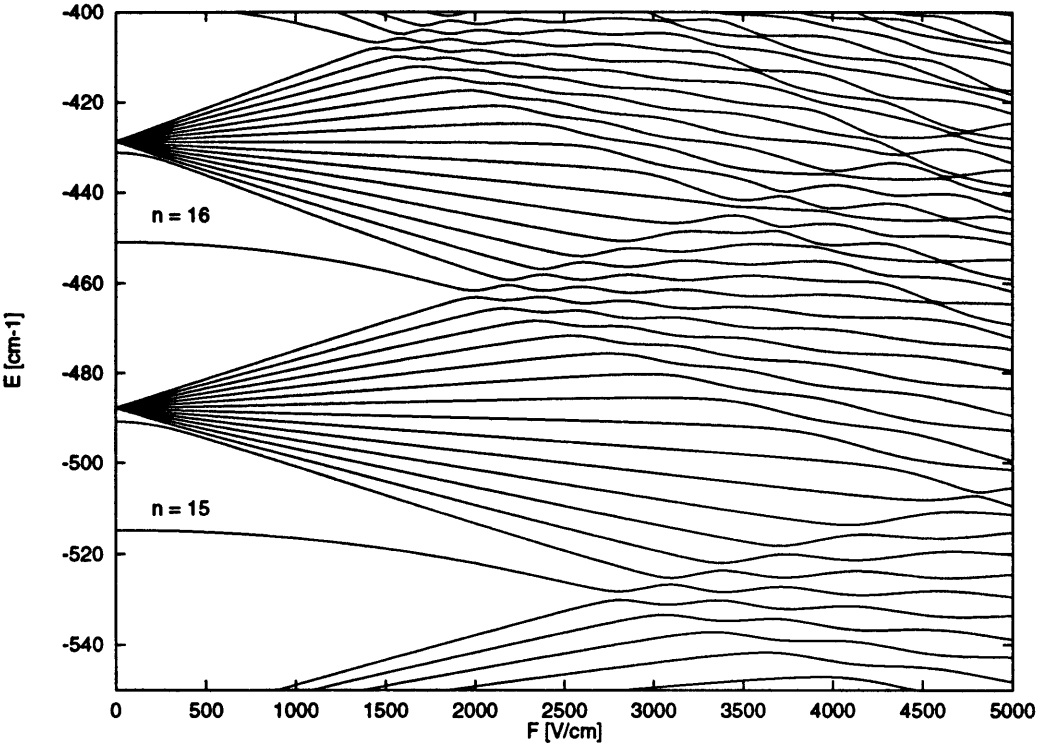

Figure 2-2: Spectrum of Lithium in an Electric Field for $m = 0$.

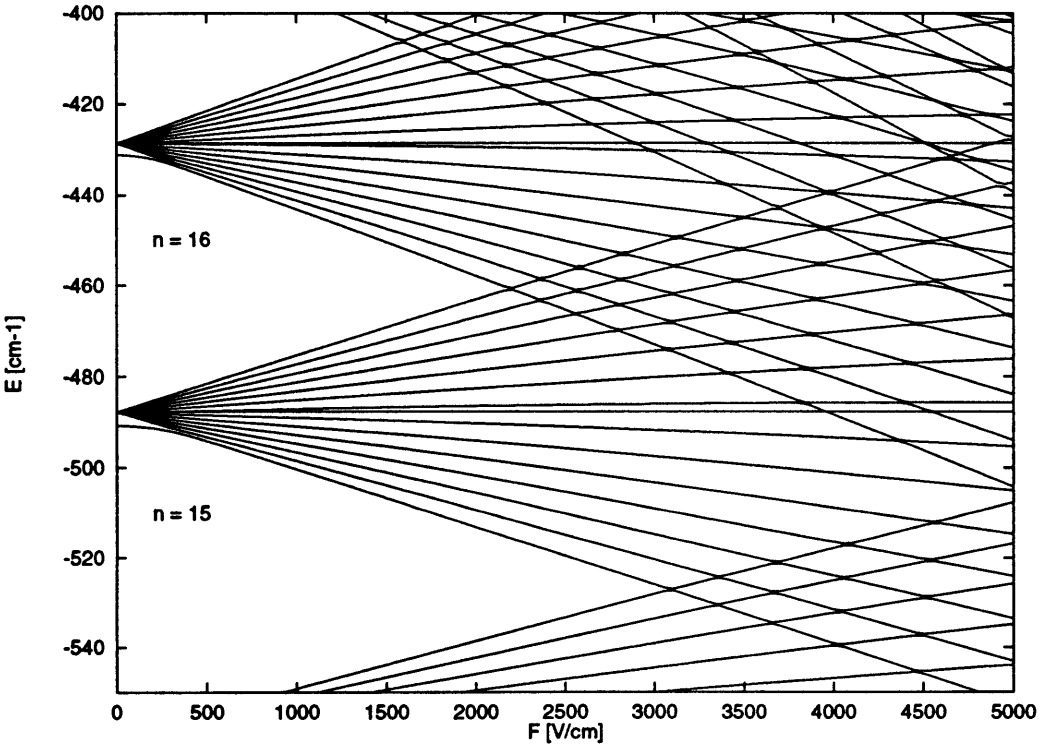

Figure 2-3: Spectrum of Lithium in an Electric Field for $m = 1$.

2.5 Rydberg Atom Diamagnetism

The Hamiltonian for the diamagnetic hydrogen atom, in atomic units, is

$$H = \frac{p^2}{2} - \frac{1}{r} + \frac{1}{2}L_z B + \frac{1}{8}B^2\rho^2. \tag{2.25}$$

This Hamiltonian is not separable in any orthogonal coordinate system [EIS48], and it must be solved by perturbation theory. The paramagnetic term,

$$H_p = \frac{1}{2}L_z B, \tag{2.26}$$

is responsible for the Zeeman effect and is diagonal in the basis of field-free eigenstates. The diamagnetic term,

$$H_d = \frac{1}{8}B^2\rho^2, \tag{2.27}$$

is responsible for the difficult nature of the problem.

2.5.1 Symmetries in Rydberg Atom Diamagnetism

As a result of rotational symmetry about the z axis, the Hamiltonian commutes with L_z, so m is a good quantum number. In other words, we can construct eigenfunctions of the Hamiltonian which are simultaneous eigenfunctions of L_z. The Hamiltonian is also invariant with respect to reflection through the $z = 0$ plane, so the parity π is also a good quantum number. Because $[\pi, L_z] = 0$, we can construct simultaneous eigenfunctions of E, π, and L_z.

There is an approximate symmetry in diamagnetic hydrogen known as the Λ symmetry. Zimmerman *et al.* [ZKK80] observed that anticrossing sizes between levels of different n decreased exponentially with n. Degeneracy at a level crossing implies symmetry, and Zimmerman *et al.* suggested the possibility of an approximate symmetry.

An approximate constant of motion was discovered by Solov'ev [SOL81] in the corresponding classical system. He showed that when B is small the motion can be

represented as a Kepler ellipse plus a slow variation in the ellipse's parameters due to the diamagnetic term in the Hamiltonian. The angular momentum and the Runge-Lenz vector, $\vec{A}$, are chosen to be the parameters which specify the ellipse. Solov'ev pointed out that

$$Q = \frac{L^2}{1 - A^2} \tag{2.28}$$

and

$$\Lambda = 4A^2 - 5A_z^2 \tag{2.29}$$

are approximate constants of motion with errors proportional to B^4. The Runge-Lenz vector is directed along the major axis of the ellipse, and it moves slowly on the surface of constant Λ. Positive Λ corresponds to the Runge-Lenz rotating around the magnetic field axis. Negative Λ corresponds to a vibrational motion of the Runge-Lenz vector along the field axis. In Figure 3-2, the tori which trace out one closed curve are due to orbits with negative Λ. The tori which trace out two closed curves are due to orbits with positive Λ.

This same approximate symmetry was explained quantum mechanically by Herrick [HER82]. Delande and Gay [DEG84] showed that the diamagnetic term in the Hamiltonian can be written

$$H_d = \frac{1}{8}B^2\rho^2 = \frac{1}{16}B^2n^2(n^2 + 3 + L_z^2 + \Lambda). \tag{2.30}$$

The eigenstates of Λ are the eigenstates of diamagnetic hydrogen if no n mixing is considered. In other words, if one uses perturbation theory to compute the eigenvalues and eigenstates of diamagnetic hydrogen but only includes a single n in the computation, one has effectively computed the eigenstates of Λ for that particular n. The eigenvalues of Λ are not generally integers, but they are confined so that $-1 < \Lambda < 4$. The anticrossings in the system are small because the coupling between states of different n is small in the Λ basis. If this coupling were zero, the Λ basis would be the exact eigenstates of the system. As it is, the Λ basis provides a good approximation to eigenstates of the system in the region where only a few n's have

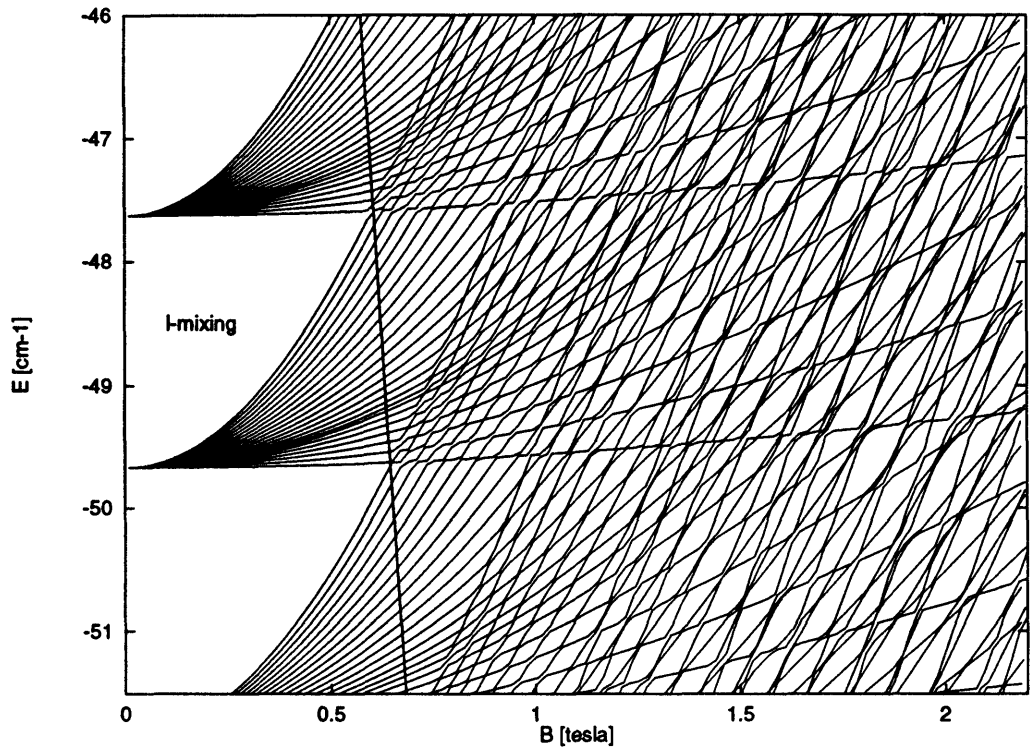

Figure 2-4: Spectrum of hydrogen in a magnetic field, $m = 0$, even-parity. The $l-$mixing regime is labeled. The $n-$mixing is to the high-field side of the thick line.

mixed.

Figure 2-4 shows a computed spectrum of diamagnetic hydrogen. The lowest energy levels ($\Lambda < 0$) in each manifold are nearly degenerate for odd- and even-parity (typical energy difference $< 0.001\, cm^{-1}$). The highest energy levels ($\Lambda > 0$) have the odd- and even-parity states interleaved. This is a manifestation of Λ symmetry which can be understood from a semiclassical picture. Semiclassical wavefunctions can be constructed by quantizing trajectories with $\Lambda < 0$. However, quantizing a single trajectory does not give an eigenstate of parity because the trajectory and resulting wavefunction are both strongly localized on one side of the $z = 0$ plane. Eigenstates of parity are constructed as linear combinations of a semiclassical wavefunction built from a trajectory and its reflection in the $z = 0$ plane. These symmetric and anti-symmetric wavefunctions are exactly degenerate in the semiclassical approximation. In the fully quantum treatment, tunnelling between tori breaks this degeneracy.

2.5.2 Regions of Interest in Rydberg Atom Diamagnetism

Diamagnetism breaks the zero-field l-degeneracy of hydrogen. For a given n and parity, there are roughly $n/2$ degenerate l values which are coupled. For small fields, this degeneracy is broken and a given n produces a fan-like manifold of about $n/2$ levels. This is known as the l-mixing regime. The n-mixing regime begins where the highest level in the $n-1$ manifold crosses the lowest level in the n manifold, and it extends as long as it is possible to determine from which n an energy level originated. The strong mixing regime extends from the point where several n's have mixed out to infinite field and energy. In this region, it is not generally possible to say to which n a particular level belongs. However, some of the eigenvalues in this region have been associated with simple models which have definite quantum numbers. The continuum regime is the region above the quantum mechanical ionization limit, $E_{ionization} = (m + \frac{1}{2})B$.

2.5.3 Diamagnetism in Alkalis

The deviation from a $1/r$ potential near the nucleus of alkali atoms destroys the Λ symmetry in all cases where the basis contains a quantum defect which is significantly different from an integer. In these cases, the spectra will have much larger anticrossings, and as soon as n's are mixed, it becomes difficult to say from which n a particular level originated. Figures 2-5 and 2-6 contrast odd- and even-parity spectra for diamagnetic lithium. Although the Λ symmetry is destroyed by the core for classical mechanics, if the quantum system happens to have near-integer values of quantum defects, the quantum system has smaller anticrossings. For example, odd-parity sodium (largest quantum defect $\delta_1 = 0.856$) has smaller anticrossings than even-parity lithium (largest quantum defect $\delta_0 = 0.400$).

In contrast to hydrogen, where the low-energy states of a given manifold are nearly parity-degenerate and the high-energy states are interleaved, the lithium diamagnetic manifold displays near parity-degeneracies for the high-energy states of a given manifold, while the low-energy states are interleaved. Since odd-parity lithium

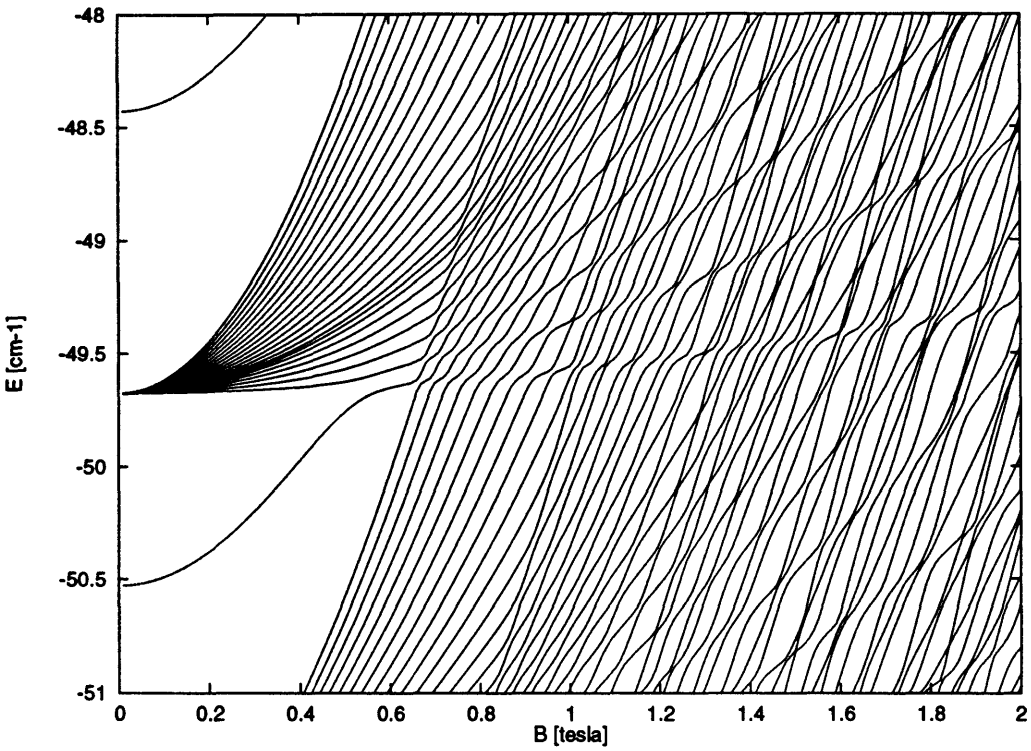

Figure 2-5: Spectrum of lithium in a magnetic field, $m = 0$, even-parity. Note the large anticrossings compared with odd-parity.

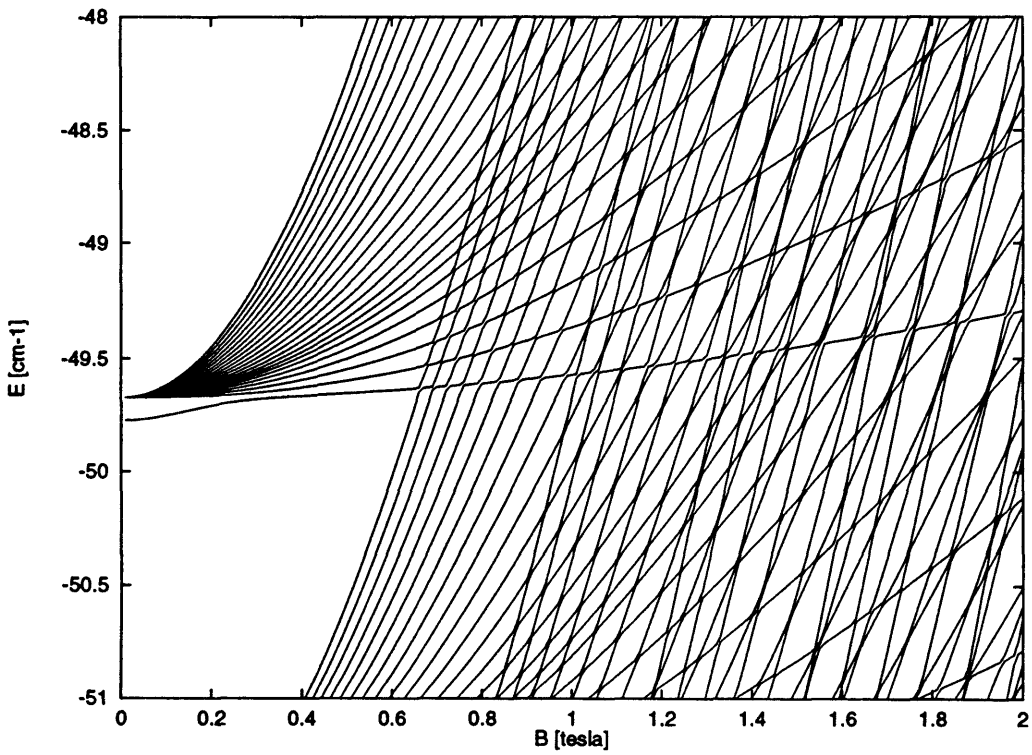

Figure 2-6: Spectrum of lithium in a magnetic field, $m = 0$, odd parity.

and hydrogen spectra are nearly identical, this difference can also be attributed to breaking of the Λ symmetry in even-parity lithium.

2.5.4 Simple Features of Rydberg Atom Diamagnetism

Diamagnetic Rydberg atoms have spectral features which can be connected with simple systems with one degree of freedom.

Rydberg Series

Iu *et al.* [IWK89] discovered orderly structures in the positive-energy spectrum of odd-parity lithium which they explained by a simple one-dimensional model. It is useful to write the Hamiltonian for the diamagnetic hydrogen atom as

$$H = H_\rho + H_z + H', \tag{2.31}$$

where

$$H_\rho = \frac{{p_\rho}^2}{2} + \frac{1}{2}L_z B + \frac{1}{8}B^2\rho^2, \tag{2.32}$$

$$H_z = \frac{{p_z}^2}{2} - \frac{1}{|z|}, \tag{2.33}$$

and

$$H' = \frac{1}{|z|} - \frac{1}{r}. \tag{2.34}$$

H_ρ is the Hamiltonian of an electron in a magnetic field, H_z is the Hamiltonian of one-dimensional hydrogen, and H' is a perturbation to the otherwise trivial Hamiltonian.

The eigenvalues of $H_\rho + H_z$ are

$$E = \frac{1}{2}(2n_\rho + 1 + m + |m|)B - \frac{1}{2n_z^2}. \tag{2.35}$$

Iu *et al.* explained the evenly spaced progressions they observed as Rydberg series of one-dimensional hydrogen converging on different Landau levels. They found that some energy levels can be understood by this simple model even though there is no reason why such a simple model should work at small magnetic fields where there is

strong mixing between different Landau levels.

In his thesis, Iu [IUC91] presented panoramic energy level maps and showed that the lowest energy level in a given n manifold is periodically destroyed and reconstructed. He suggested that the Rydberg series they observed in the positive energy spectrum are continuations of this pattern of reconstruction of these energy levels.

Ng [NGL93] showed that the first region of reconstruction can be connected with the values of $\epsilon_B = EB^{-2/3}$ where the periodic orbit on the z axis is the most stable. She computed regions of stability near the z axis and showed that the larger the region of stability, the smaller the anticrossings of levels passing through the Rydberg level and the better its reconstruction.

Landau Series

The discovery of individual eigenvalues corresponding to the solution of the Hamiltonian with $\rho = 0$ motivated me to look for energy levels corresponding to the solution of the Hamiltonian with $z = 0$. It had been previously discovered that there were periodic modulations in the oscillator strength whose period corresponded with the level spacing found by solving this simple one-dimensional model [GAT69, CZH80], but I set out to find individual energy levels corresponding to solutions of this model.

I compared spectra of even-parity diamagnetic hydrogen with the solution of two-dimensional diamagnetic hydrogen, whose Hamiltonian is

$$H = \frac{{p_\rho}^2}{2} - \frac{1}{\rho} + \frac{1}{2}L_z B + \frac{1}{8}B^2\rho^2. \tag{2.36}$$

H_ρ is obtained simply by setting $z = 0$ in the Hamiltonian for diamagnetic hydrogen.

Since H_ρ has one degree of freedom, the spectrum can be obtained in several ways. One can treat the magnetic field as a perturbation to two-dimensional hydrogen and diagonalize a matrix in the usual way. One can also simply integrate the wavefunction with trial energies and converge to an energy for which the wavefunction has no exponentially increasing component past the classical turning point. Additionally, one can use the WKB method. Eigenvalues obtained with all three methods are in

good agreement. These eigenvalues are plotted as a function of field in Figure 2-7. I call these levels *Landau series.*

When the spectra of diamagnetic hydrogen are directly overlaid with the two-dimensional model, comparison is difficult because there are so many energy levels that the features are muddled. It is useful to compute the anticrossing sizes and positions of diamagnetic hydrogen and compare plots of the anticrossing positions with the simple model.

Figure 2-7 (a) shows the Landau series and the smallest anticrossings of diamagnetic hydrogen. We see that each of the lines in the Landau series can be associated with a line formed by the smallest anticrossings of diamagnetic hydrogen. As mentioned previously, small anticrossings are a hint of an approximate symmetry and all these anticrossings are small compared with the mean level spacing. It is of interest that there is also a line of anticrossings half-way between the Landau series. A quantum explanation might be that these are associated with the two highest energy states in a given n manifold. The highest state becomes a member of the Landau series, and the second highest state becomes the level half-way between.

Figure 2-7, (b), (c), and (d) show the other anticrossings in the system. In (c), one can see that there are also anticrossings making up near-horizontal lines which can be identified with Rydberg series. The fact that the Rydberg series anticrossings are larger than the Landau series anticrossings suggests that any approximate symmetries can be seen better in wavefunctions localized near the $z = 0$ plane. A semiclassical view is that the orbit in the $z = 0$ plane is the last to become unstable as the scaled energy is raised.

2.6 Parallel Electric and Magnetic Fields

Rydberg atoms in parallel electric and magnetic fields have been studied much less extensively than the diamagnetic and Stark problems.[1] The Aimé Cotton group

[1]This section may seem like a bit of a digression because the complexity of the parallel field problem necessitates a longer discussion to summarize its main features. However, in the rest of the

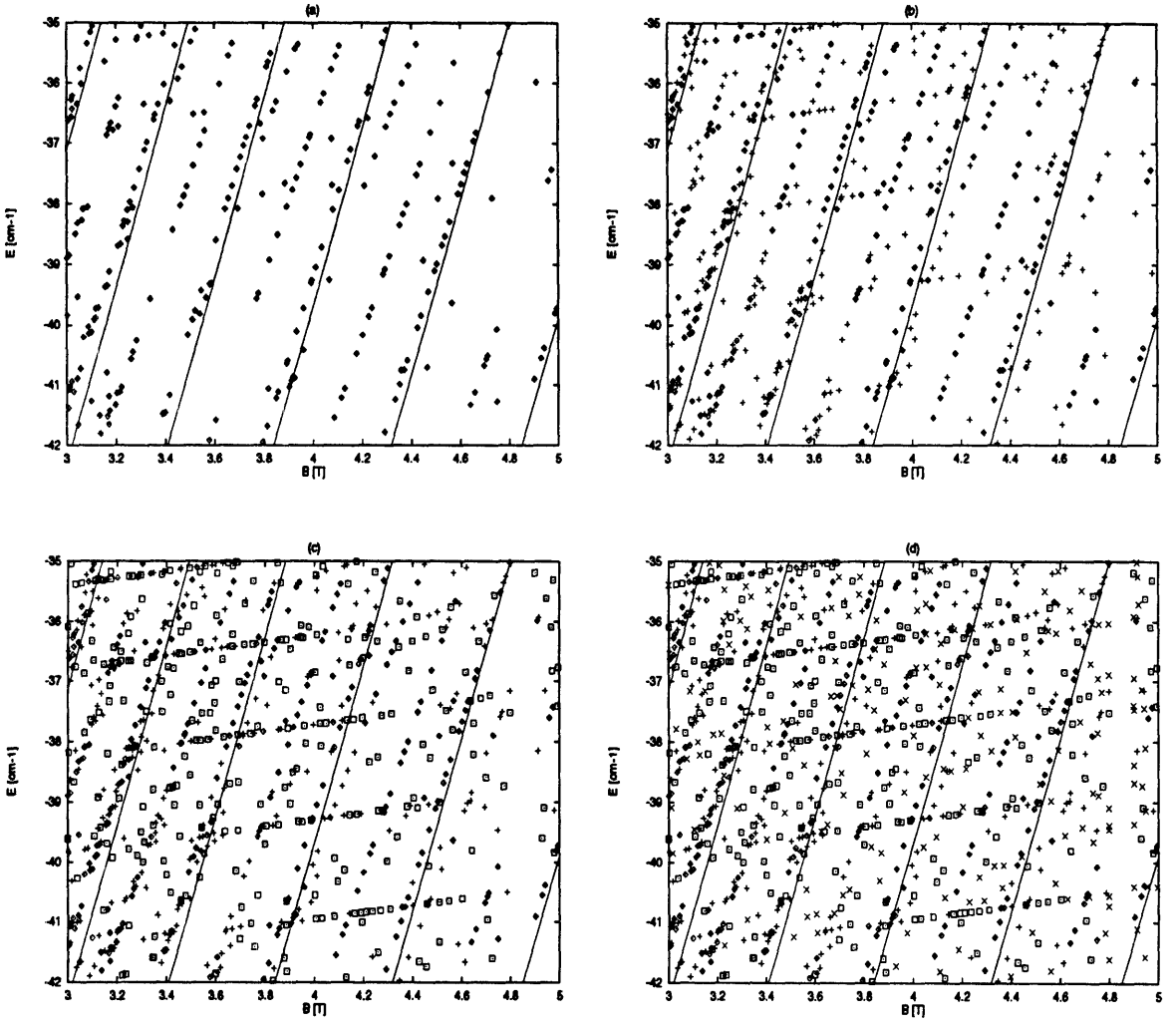

Figure 2-7: Solid lines are eigenvalues of one-dimensional model. Symbols are the position of anticrossings of the full Hamiltonian. (a) Anticrossings less than $0.0037\,cm^{-1}$. (b) Anticrossings less than $0.018\,cm^{-1}$. (c) Anticrossings less than $0.061\,cm^{-1}$. (d) Anticrossings less than $0.24\,cm^{-1}$ (*all anticrossings*).

[CLL88a, CLL88b, CLL88c, CLL89] has done a thorough job of describing the system in the l-mixing regime, but a detailed study of the n-mixing regime is lacking. In addition, low-resolution experiments in the continuum regime have been interpreted semiclassically [MRB93]. This barely scratches the surface compared with the volumes which have been written on the diamagnetic and Stark problems. There are two reasons: physicists are not expecting anything new in the parallel field problem, and a system with two external fields is inherently more complex and difficult to describe.

If all the parallel field problem offers is greater complexity and essentially no new physics, then perhaps it has been justifiably ignored. On the other hand, how can we be sure that there is nothing interesting until we look? Furthermore, when we turn to quantum chaos, there is a great interest in testing the universality of the various approaches. The parallel field problem gives us another parameter to adjust while testing the generality of what has been learned by studying simpler chaotic systems.

There probably *is* new and interesting physics hiding in Rydberg atoms in parallel fields. Perhaps it will be discovered when the approaches of quantum chaos are applied. Perhaps the discovery awaits a detailed study of the continuum, which will not be done in this thesis. In any case, the Aimé Cotton group has laid the foundation for studying the system with their work in the low field regime. Any serious study of the problem should probably begin with understanding that work. The details are too laborious to repeat here, but I hope to convey its relevance to the study of quantum chaos.

2.6.1 Symmetries

The Hamiltonian of Rydberg atoms in parallel fields is rotationally symmetric about the field axis, so m is a good quantum number. The electric field breaks the reflection symmetry through the $z = 0$ plane that characterizes diamagnetism, so parity is not a good quantum number. Of course, the energy is conserved.

Hydrogen in parallel fields has an approximate symmetry which is a generalization

thesis the parallel field problem is given less consideration than the single field problems, and many of the details here are not crucial.

of the Λ symmetry in diamagnetic hydrogen. The constant of motion can be written as

$$\Lambda_\beta = \Lambda + 10\beta A_z, \tag{2.37}$$

where

$$\beta = \frac{12F}{5B^2n^2}. \tag{2.38}$$

Neglecting paramagnetism, the energy can be written as

$$E = E_0 + \frac{1}{16}B^2n^2(n^2 + m^2 + n^2\Lambda_\beta) \tag{2.39}$$

which reduces to diamagnetism for $F = 0$. An equivalent expression is

$$E = E_0 + \frac{3}{20}Fn^2\left(\frac{\Lambda_\beta}{\beta} + \frac{n^2 + m^2}{n^2\beta}\right) \tag{2.40}$$

which reduces to the Stark effect for $B = 0$.

The anticrossings in the low field region of hydrogen in parallel fields are very small as a consequence of the Λ_β symmetry. Furthermore, the symmetry allows the spectrum to be described in terms of three classes of eigenstates which correspond to the semiclassical quantization of three classes of classical trajectories. Classifying these eigenstates and the boundaries dividing the different classes allows for a complete description of the low field spectrum.

In addition to these symmetries, hydrogen in parallel fields possesses a supersymmetry which manifests in striking similarities between the pure diamagnetic manifold for $m_1 \neq 0$, $\beta = 0$ and the parallel field manifold for $m_2 = 0$ and $\beta = |m_1|/\sqrt{5}$. The eigenvalues of Λ_m and Λ_β are equal if $\beta = |m|/\sqrt{5}$. Consequently, except for the paramagnetic shift in energy, the energy levels are identical in the limit of small fields.

2.6.2 Regions of Interest

For low fields[2] three regions of interest can be distinguished, according to which of three classes of motion are supported. The classes are described by the shape of the surface of constant Λ_β on which their Runge-Lenz vectors are confined. Class I motion is confined to a single surface which is formed by the intersection of the $\Lambda < 0$ surfaces caused by the electric field. Class II motion is confined to one of two surfaces which are deformations of the $\Lambda < 0$ surfaces of diamagnetic hydrogen, but which have not yet intersected. Eigenstates corresponding to class I and II motion exhibit a linear Stark effect due to the near degeneracy of $\Lambda < 0$ states in diamagnetic hydrogen. Class III motion is confined to the surface which is a continuous deformation of the $\Lambda > 0$ surface in diamagnetic hydrogen. Eigenstates corresponding to class III motion exhibit a quadratic Stark effect. This is shown in Figure 2-8.

For $\beta < 1/5$, all three classes of motion are present. For $\beta > 1/5$, it is no longer possible to have two separate surfaces for $\Lambda_\beta < 10\beta$, and class II motion no longer exists. As β is increased from 1/5 to 1, states corresponding to class III motion slowly disappear. For $\beta > 1$, only class I states remain, and only a linear Stark effect is apparent in the spectrum. Diamagnetism dominates for $\beta < 1/5$, the magnetic and Stark effects are comparable for $1/5 < \beta < 1$, and the Stark effect dominates for $\beta > 1$.

For alkali-metal atoms, where substantial quantum defects are mixed in, the Λ_β symmetry is broken, and we expect to see strong level repulsions. However, the characterization of the relative strengths of the Stark and diamagnetic interactions by the parameter $\beta = 12F/5B^2n^2$ still seems to hold. Surprisingly, the near degeneracy between states of opposite parity which is present for the higher energy states of a given manifold is still present for $\beta < 1/5$, and these degenerate states of opposite parity are not split by a linear Stark effect.

[2]It is known that fields for which there is no n-mixing are sufficiently low that the Λ_β symmetry holds. However, it is not known for what fields the symmetry breaks down. One issue here is that the scalings for n-mixing do not follow the classical scaling rules discussed in Chapter 3, and n-mixing is an important consideration in the breakdown of the symmetry in the quantum system, but the classical system does not know about n-mixing.

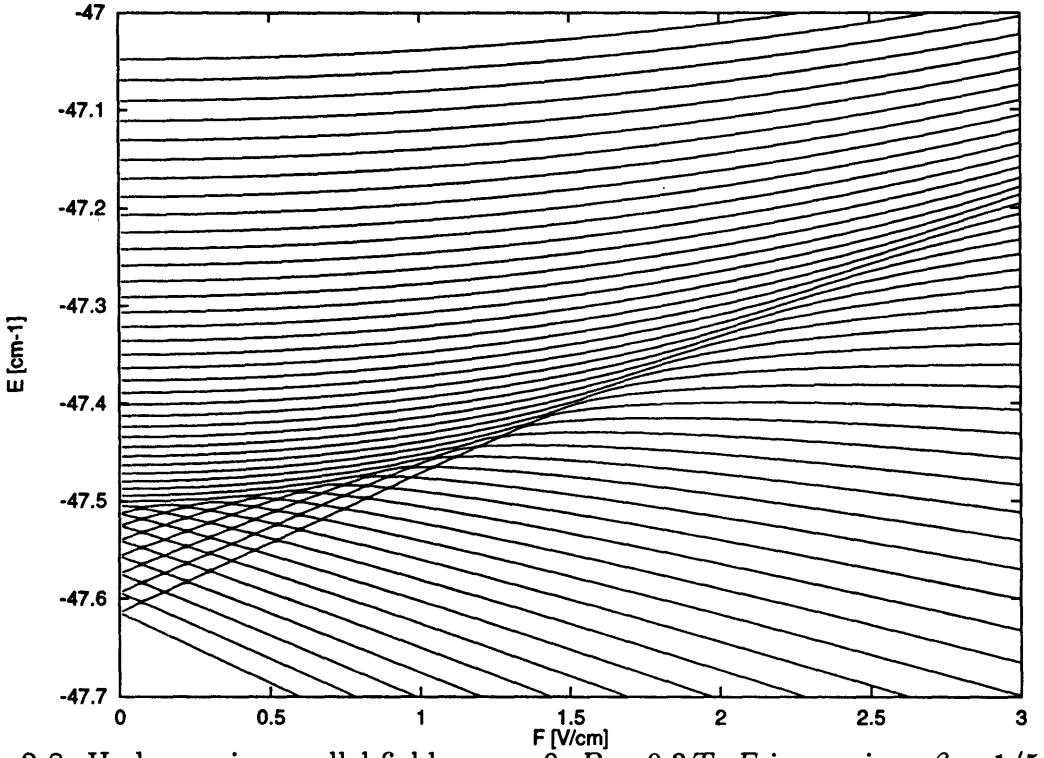

Figure 2-8: Hydrogen in parallel fields. $m = 0$, $B = 0.3\,T$, F increasing. $\beta = 1/5$ at $F = 1.6\,V/cm$, and $\beta = 1$ at $F = 8\,V/cm$. The upper part of the manifold is made up of class III states exhibiting a quadratic shift as F is increased. The lower part of the manifold exhibits linear Stark shifts and is made up of class I and II states for $\beta < 1/5$ and only class I states for $\beta > 1/5$.

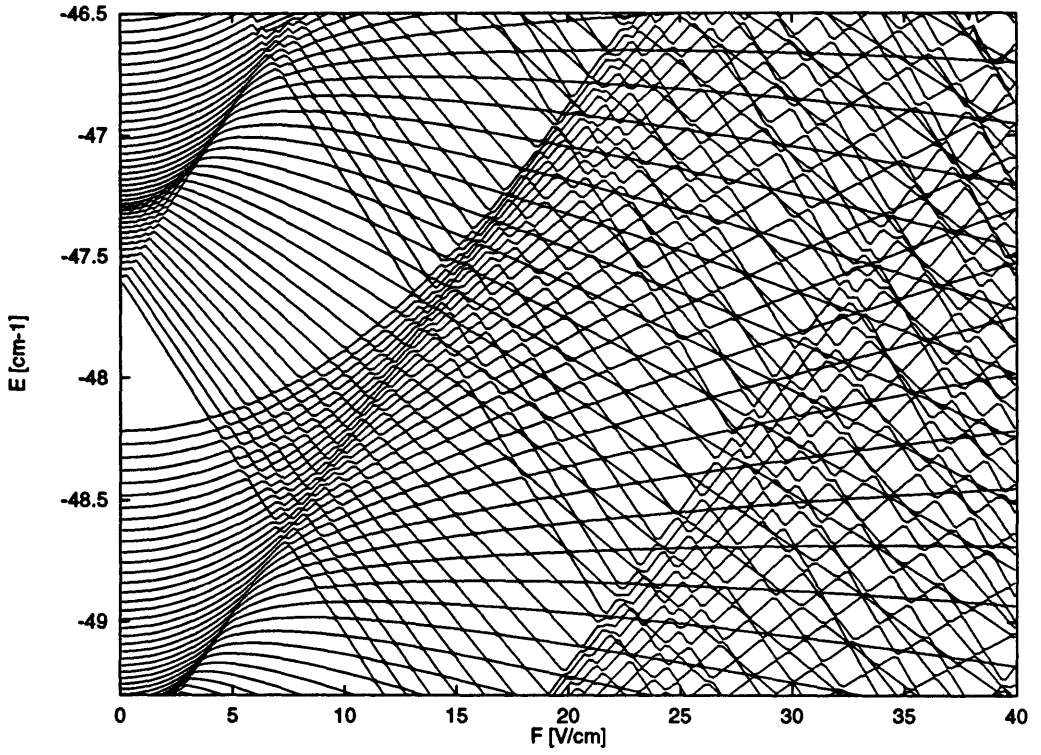

Figure 2-9: Hydrogen in parallel fields. $m = 0$, $B = 0.5T$, F increasing. $\beta = 1/5$ at $F = 4.4\,V/cm$, and $\beta = 1$ at $F = 22\,V/cm$.

2.6.3 Hydrogen in Parallel Fields

Describing general spectral features of Rydberg atoms in parallel fields is difficult because of the multidimensional parameter space (m,F,B,Z). We will restrict ourselves to hydrogen and lithium for $m = 0$ and show various energy level maps by choosing a fixed value for one field while varying the other.

In order to show what happens when different n's are well mixed, Figure 2-9 shows the energy level structure for $B = 0.5\,T$ and increasing F. For $n = 48$ and $B = 0.5\,T$, n-mixing begins near $F = 5\,V/cm$. Class II states disappear at $F = 4.4\,V/cm$. Class III states have all evolved into class I states by $F = 22.2\,V/cm$. In the earlier work on parallel fields, this behavior was only reported for small fields where no n mixing had occurred. Here, we see that this behavior persists even though several n's are mixed. For $F > 22.2\,V/cm$, most of the energy levels have a nearly linear electric field dependence, and most of the anticrossings are much smaller than the average level spacing, although some are not.

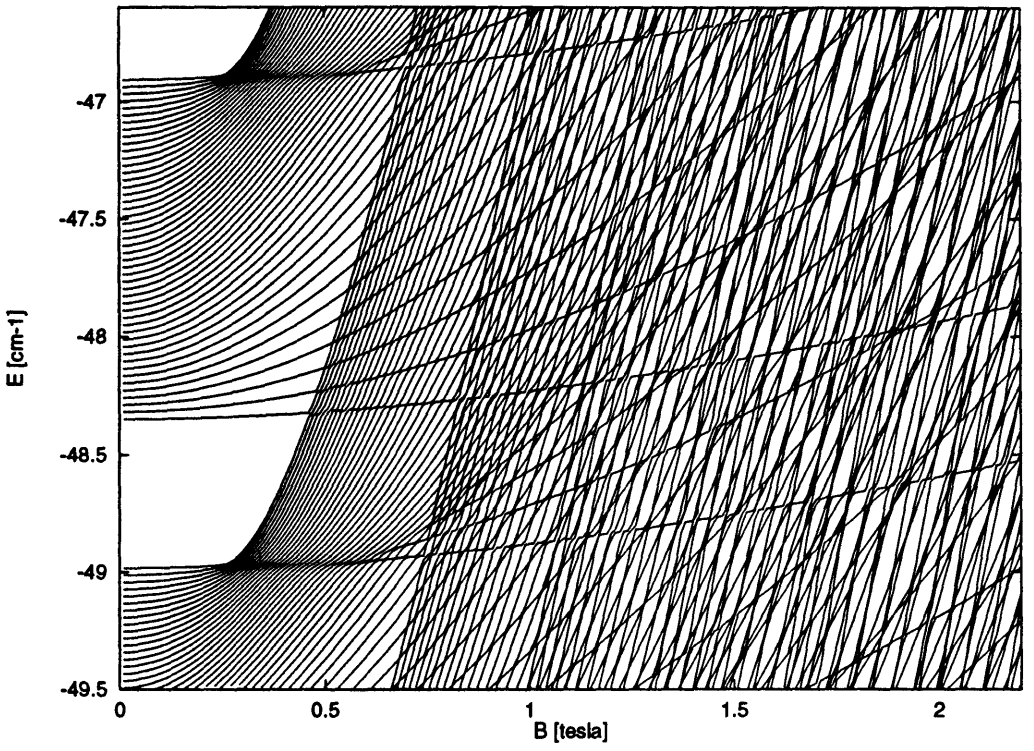

Figure 2-10: Hydrogen in parallel fields. $m = 0$, $F = 5\,V/cm$, B increasing. $\beta = 1/5$ at $B = 0.53\,T$, and $\beta = 1$ at $B = 0.24\,T$.

Beginning with a Stark manifold at a fixed electric field and increasing the magnetic field provides a complementary perspective. Figure 2-10 shows the energy level structure for $F = 5\,V/cm$ and increasing B. For small B, the highest and lowest Stark states of the $n = 48$ manifold show little diamagnetic interaction because they are localized near the z axis. The middle Stark states show strong interactions with the field because they have sizeable extent in ρ. When B is increased so that $\beta = 1$, the middle states begin to interact with the highest Stark state. As B is increased further to $\beta = 1/5$, the manifold evolves to resemble a pure diamagnetic manifold. The small anticrossings and similarity with diamagnetism are the most striking features of the n-mixing regime.

Because of the weak mixing between different n manifolds, this behavior persists even for electric fields strong enough for n-mixing to occur before the magnetic field is applied. Figure 2-11 shows similar behavior for an initial electric field of $10\,V/cm$ which is strong enough to mix the different n manifolds. We find that $\beta = 1$ and

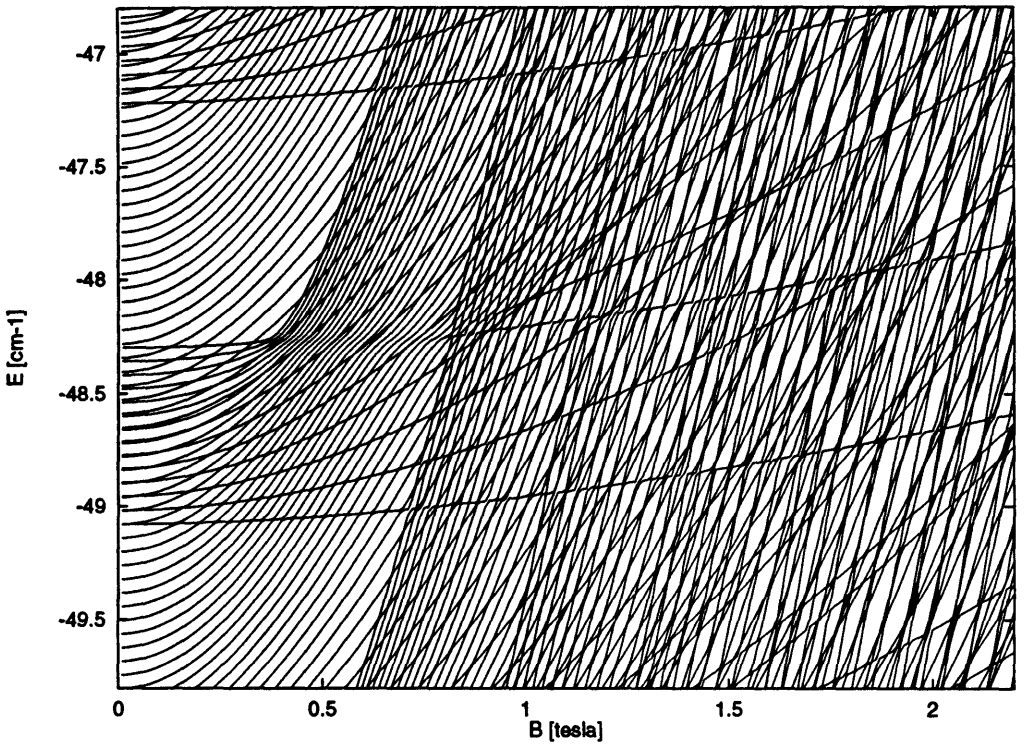

Figure 2-11: Hydrogen in parallel fields. $m = 0$, $F = 10\,V/cm$, B increasing. $\beta = 1/5$ at $B = 0.75\,T$, and $\beta = 1$ at $B = 0.33\,T$. Note very small anticrossings.

$\beta = 1/5$ still represent key points in the spectral evolution and that the system is still characterized by a number of very small anticrossings.

2.6.4 Lithium in Parallel Fields

The differences between hydrogen and lithium are caused by the zero-field nondegeneracy due to the core. Recall that in diamagnetic hydrogen the lowest going states of a given n are parity degenerate and the highest going states are interleaved. The opposite occurs in lithium: the lowest going states are interleaved, and the highest going states are nearly degenerate. Furthermore, recall that even-parity diamagnetic lithium and lithium in an electric field both exhibit sizeable anticrossings due to the large quantum defect of the S state. These considerations and the behavior of hydrogen in parallel fields provide the necessary background for interpreting the spectra of lithium in parallel fields.

The low field behavior of lithium in parallel fields is shown in Figure 2-12. Because

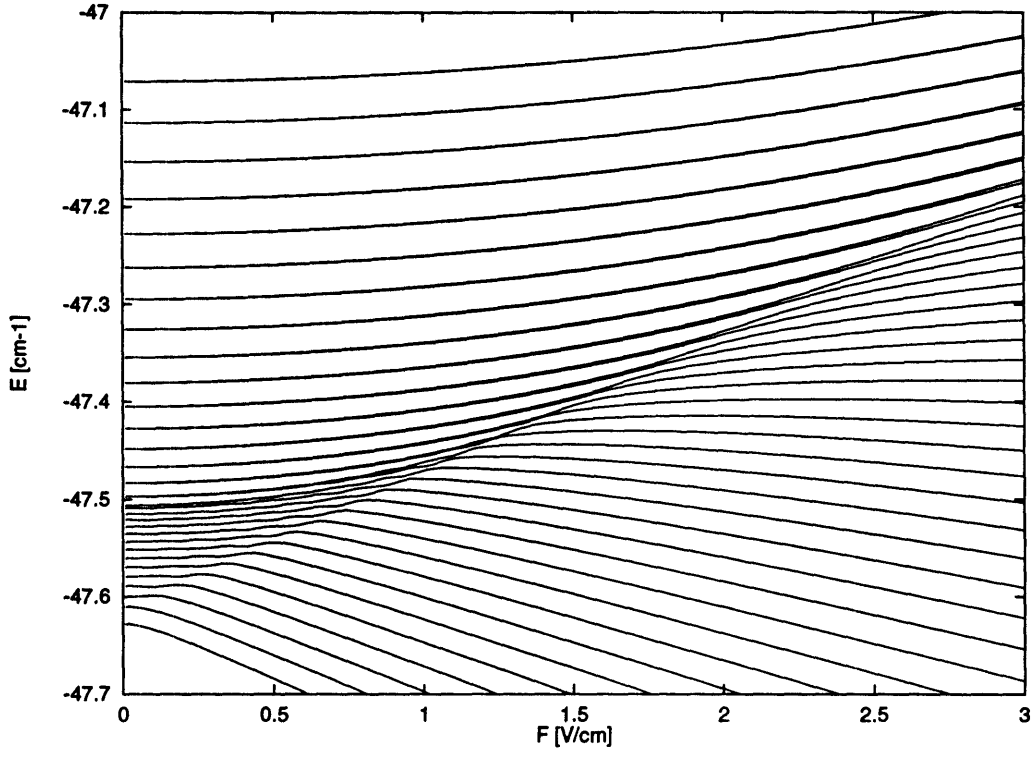

Figure 2-12: Lithium in parallel fields. $m = 0$, $B = 0.3\,T$, F increasing. $\beta = 1/5$ at $F = 1.6\,V/cm$, and $\beta = 1$ at $F = 8\,V/cm$.

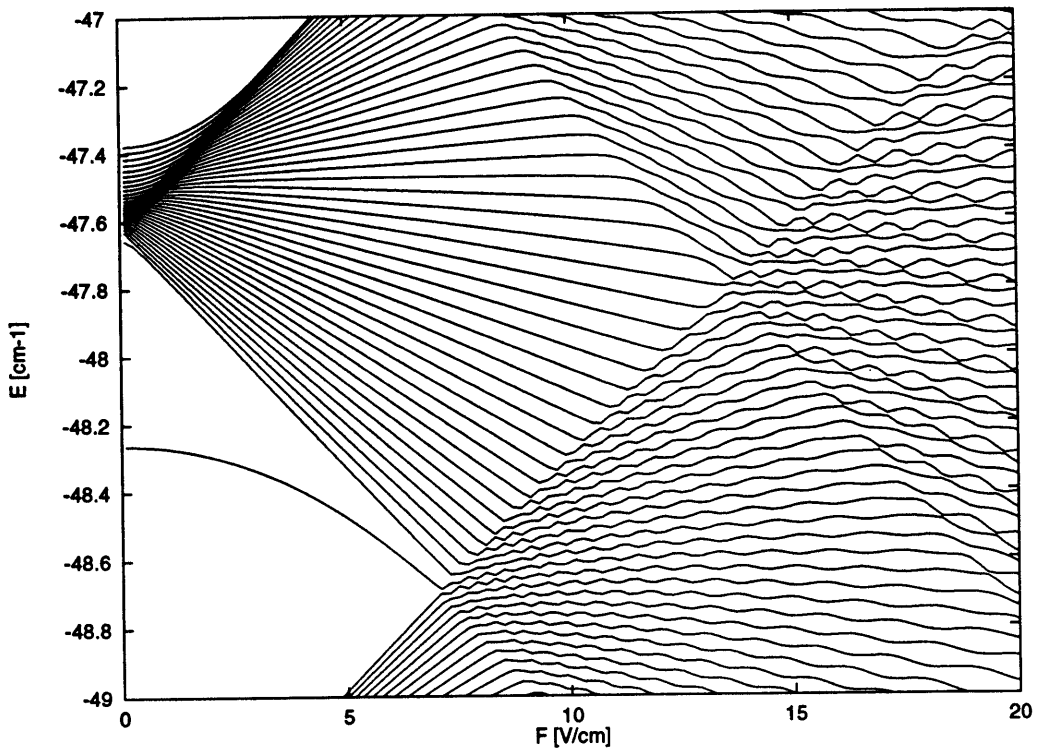

Figure 2-13: Lithium in parallel fields. $m = 0$, $B = 0.2T$, F increasing. $\beta = 1/5$ at $F = 0.71\,V/cm$, and $\beta = 1$ at $F = 3.55\,V/cm$.

the low energy states in diamagnetic lithium are not parity degenerate, they do not experience a linear Stark splitting as does hydrogen. The high going states are parity degenerate, but they do not experience a linear Stark effect for two reasons: (i) They are localized near the $z = 0$ plane. (ii) Unlike the low going states in diamagnetic hydrogen, they cannot be constructed by symmetric and antisymmetric combinations of a wavefunction. Consequently, all of the levels experience a quadratic Stark effect when a small electric field perturbs the diamagnetic manifold. However, in other ways, the manifold is similar to hydrogen in that $\beta = 1/5$ and $\beta = 1$ mark key points in the evolution of the manifold from pure diamagnetism at $\beta = 0$ to a manifold dominated by the linear Stark effect for $\beta > 1$.

In contrast to hydrogen, lithium in parallel fields displays large anticrossings once n-mixing occurs. The spectrum for $B = 0.2T$ and increasing F is shown in Figure 2-13. The anticrossing sizes here are on the order of the mean level spacing, indicating strong level repulsion just as in the case of the Stark effect and even-parity

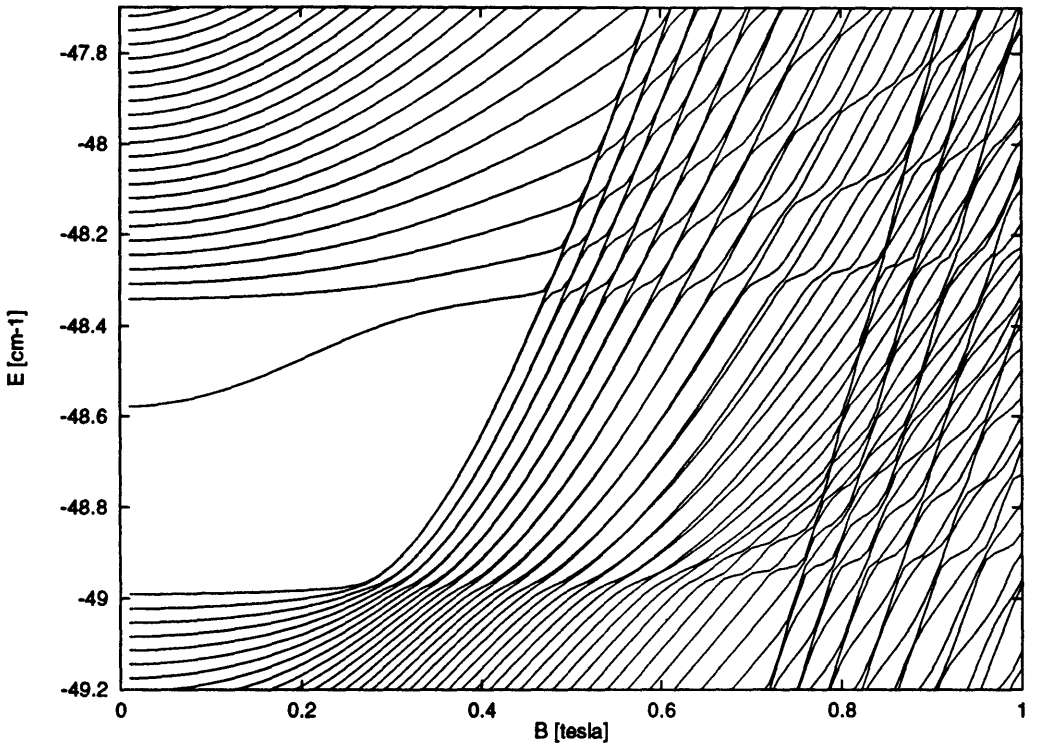

Figure 2-14: Lithium in parallel fields. $m = 0$, $F = 5\,V/cm$, B increasing. $\beta = 1/5$ at $F = 0.5289\,V/cm$, and $\beta = 1$ at $F = 0.2365\,V/cm$.

diamagnetism in the $m = 0$ state of lithium.

The spectral evolution as B is increased at constant F reveals different behavior. The complementary perspective of Figure 2-14 shows the energy level structure for $F = 5\,V/cm$ and increasing B. Just as in hydrogen at low magnetic fields, the highest and lowest Stark states of the $n = 48$ manifold show little diamagnetic interaction because they are localized near the z axis. The middle Stark states show strong interactions with the field because they have sizeable extent in ρ. When B is increased to the value where $\beta = 1$, the middle states begin to interact with the highest Stark state. Unlike hydrogen, these states form nearly degenerate pairs ($\Delta E \approx 0.001\,cm^{-1}$). These nearly degenerate pairs continue to form until $\beta = 1/5$. Beyond $\beta = 1/5$ the spectrum resembles a superposition of odd- and even-parity diamagnetic spectra complete with small anticrossings. The small anticrossings and similarity with diamagnetism are the most striking features of the n-mixing regime.

Blowing up the region of Figure 2-14 where n-mixing begins allows examination of

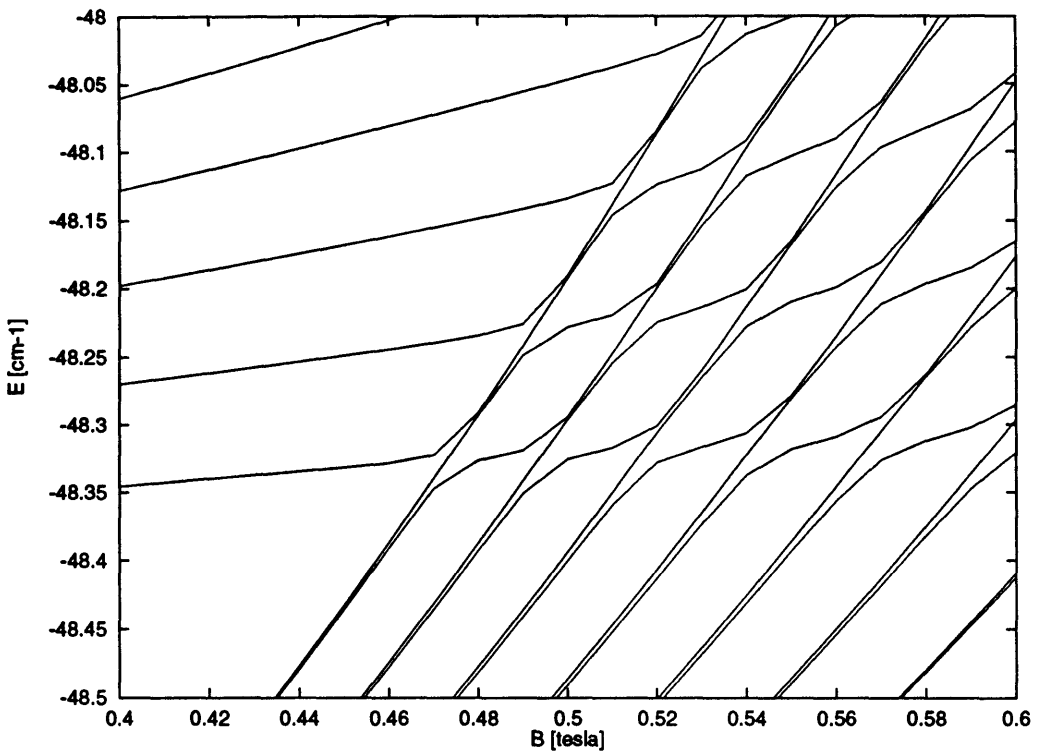

Figure 2-15: Blowup of Figure 2-14 showing degeneracies of high going levels in the diamagnetic manifold.

near degeneracies and small anticrossings. Figure 2-15 shows that the nearly degenerate doublets break up and are reconstructed as the two manifolds interact. Moreover, it appears that the higher level in each doublet hardly interacts at all with the states in the next higher manifold. The explanation is simple: the dominance of diamagnetism over the Stark effect results in eigenfunctions which are nearly eigenfunctions of parity. The upper state in each doublet has nearly an odd-parity wavefunction, and the lower state approximates an even-parity wavefunction. The lowest going states of the upper manifold are nearly even-parity wavefunctions. Consequently, interactions are weak between the upper manifold and higher energy doublet states, and interactions are strong between the upper manifold and lower energy doublet states.

2.6.5 Summary of Parallel Fields

As long as interactions between different n manifolds are small, spectral features of Rydberg atoms in parallel fields depend strongly on the parameter β which is

essentially the ratio of the Stark to the diamagnetic term in the Hamiltonian. Even when hydrogenic manifolds cross, they interact very little and the system can still be characterized by β. In contrast, when manifolds cross for $m = 0$ lithium, the core induces strong interactions between different n manifolds. Consequently, the behavior of lithium in parallel fields can only be characterized by β for fields where there is no n-mixing.

Chapter 3

The Onset of Classical Chaos in Rydberg Atoms

In those days Israel had no king; everyone did as he saw fit.–Judges 21:25

This chapter presents the results of numerical studies of the onset of classical chaos in Rydberg atoms in strong fields. Chaos is defined and described and the Poincaré surface of section is used as a visual indicator of the onset of chaos. Other features of the classical dynamics such as the structure of periodic orbits and orbits which are closed at the nucleus are discussed in the chapters on recurrence spectra.

To address the issue of chaos in a particular quantum system, we need to know the behavior of the corresponding classical system. The issue of choosing the correct classical system requires thought. Strictly speaking, the corresponding classical system has the same Hamiltonian as the quantum system under study. However, many approximations which are easily justified quantum mechanically in arriving at a Hamiltonian are much more difficult to justify classically. For example, the Hamiltonians used to compute spectra in Chapter 2 neglect relativistic effects, spin-orbit coupling, hyperfine structure, and radiative effects. All of these approximations are justified because it is easily shown that the first order perturbations due to these effects are very small for Rydberg atoms. When we turn to the classical system,

neglecting these effects is not easily justified. Accelerating charges radiate, and the energy is not strictly conserved anymore in a classical atom. Furthermore, many classical trajectories pass close enough to the origin that their velocities approach and even exceed the speed of light. And finally, the dipole-dipole interaction between the electron and nucleus will cause a much different trajectory when the electron passes close to the nucleus than the Coulomb potential alone.

In addition, in the quantum mechanics of alkali Rydberg states, the effect of the core electrons can be described by a core potential felt by the electron in the Rydberg state. Which classical problem should we solve, the many-body problem given by Z electrons interacting with a nucleus of charge Z, or the single particle problem of an electron in a hydrogenic potential perturbed by a core potential which gives the same eigenvalues as the many body problem? The many-body problem is completely chaotic and a systematic classical study would be prohibitively difficult. The single particle problem is much more tractable, and since physics usually proceeds with the simplest description which is not yet well understood, I will look at the single particle problem.

However, I should point out that by considering the single particle problem, I am imposing certain quantum features on the classical system. I am demanding that the Rydberg electron not transfer energy to the core electrons. This is a consequence of quantum mechanics, because exciting the core electrons from their ground state requires more energy than the Rydberg electron can have without ionizing. Other effects are neglected in the classical dynamics because I want to understand the dynamics of the simplest Hamiltonian that will give the quantum spectra. However, the fact that different classical systems give the same quantum spectra may prove to be a challenge to those seeking to characterize "quantum chaos."

3.1 What is Chaos?

A conservative classical system with N degrees of freedom is separable if it is possible to write the Hamiltonian in some coordinate system as

$$H = H_1(p_1, q_1) + H_2(p_2, q_2) + \ldots + H_N(p_N, q_N). \tag{3.1}$$

The (p_i, q_i) are generalized momenta and coordinates. Separating the problem is a matter of choosing an appropriate coordinate system. The separable problem has N uncoupled parts, each of which can be solved as a one-dimensional problem. The energy of each one-dimensional Hamiltonian is conserved independently of the energies of the other dimensions. As a result, there are at least N constants of motion.

Classical systems with N degrees of freedom are integrable if they have at least N constants of motion. In separable systems, N of these constants of motion can be expressed as independently conserved energies. In general integrable systems, these constants of motion need not be energies. In other words, all separable systems are integrable, but not all integrable systems are separable.

Systems with N degrees of freedom have a phase space of $2N$ dimensions. A classical trajectory of a system with A constants of motion is confined to a $(2N - A)$-dimensional surface in the $2N$-dimensional phase space. As a result, trajectories of integrable systems are confined to N-dimensional surfaces which have the topology of tori. The motion on these tori can be described by assigning a period or frequency to each dimension of the motion on a torus. If the ratios of these periods can be expressed as rational numbers, a torus is said to be rational and trajectories on this torus are periodic. However, most tori are irrational, and the trajectories on irrational tori are quasiperiodic.

A chaotic system with N degrees of freedom has fewer than N constants of motion, and the motion is not necessarily confined to these tori. If a system can be written as

$$H = H_0 + \epsilon H_1, \tag{3.2}$$

where H_0 is integrable and H_1 is non-integrable, the KAM theorem describes the manner in which tori are destroyed as ϵ is increased. (See [TAB89] for an explanation of the KAM theorem.) It says that all rational tori are destroyed, and that irrational tori in a finite region surrounding rational tori are also destroyed. As a result, periodic orbits no longer lie on tori. The size of this disorderly region grows as ϵ is increased. If ϵ is very small, nearly all of the irrational tori remain. As ϵ grows, nearly all the tori are eventually destroyed.

In a chaotic system, a non-periodic orbit is regular if it is confined to a remaining torus and irregular if it is not. A periodic orbit repeats itself exactly and has a well defined period and action. The regularity of a periodic orbit must be investigated by considering its neighbors. A regular periodic orbit is stable against small perturbations, and its neighbors wind around it. An irregular periodic orbit is unstable against small perturbations and its neighbors diverge from it. The divergence of neighboring trajectories is true of all irregular trajectories. An orbit is unstable if the distance between it and a nearby orbit grows exponentially in time. This enables us to describe chaos as an extreme sensitivity to initial conditions.

Problems which are partially separable generally have the separable part of the Hamiltonian removed before the non-separable part is considered. In our system of an atom in parallel electric and magnetic fields, the angular motion around the z axis has been separated out. It is important to note that the full Hamiltonian must be used in semiclassical quantization schemes to find the Maslov indices.[1] This accounts for the differences in the semiclassical quantization of two systems which are classically identical but quantum mechanically different. For example, three-dimensional hydrogen has the same trajectories as two-dimensional hydrogen, but the two systems have different eigenvalues.

[1]Maslov indices account for the phase change of a semiclassical wavefunction when a trajectory encounters caustics (the multidimensional analog of a turning point) and foci (a point where many neighboring trajectories intersect).

3.2 Symmetries and Constants of Motion

The onset of chaos in Rydberg atoms in strong fields (and many other dynamical systems) is characterized by the breaking of symmetries and destruction of constants of motion. If a system has as many constants of motion as degrees of freedom, one can make a purely analytical case that the motion of the system is regular. The complementary approach has also been used: if one discovers in a numerical study that invariant tori fill most of phase space, then one can make a case that there are constants of motion in the system.

In the case of diamagnetic hydrogen, the system was first investigated numerically, and then the approximate constants of motion were determined analytically [SOL81]. In the case of hydrogen in an electric field, the separability of the problem was well known before using computers to compute surfaces of section became popular. For hydrogen in parallel fields, an approximate constant of motion can be written as a generalization of those in diamagnetic hydrogen [CLL88b]. All of these constants of motion are generalizations of the Runge-Lenz vector, which is only a constant of motion in hydrogen. The core breaks the symmetry in alkali-metals. Consequently, alkali-metals only have two constants of motion (E and L_z) once an external field is applied, and we expect their motion to be chaotic. The total angular momentum of the Rydberg electron is conserved in alkali-metals in the absence of external fields. Turning on an external field breaks the spherical symmetry and induces chaos for all but the smallest fields because there are no longer three constants of motion.

For hydrogen in an electric field, the z component of the generalized Runge-Lenz vector is an exact constant of motion for all field values. As a result, the Hamiltonian is separable and the motion is regular for all field values. The Λ symmetry in diamagnetic hydrogen is approximate with errors proportional to B^4. Consequently, the symmetry is gradually broken as the field is increased. Likewise, in parallel fields, the generalization of the Λ symmetry slowly breaks down as B is increased.

3.3 Scaling Rules

The existence of classical scaling rules greatly simplifies our study. For example, the scaling rule in diamagnetic hydrogen frees us from having to study the system at every possible field and energy and allows us to characterize the system in terms of a single parameter. As we shall see, these classical scaling rules also facilitate connections between the classical dynamics and quantum features.

We have assumed that the classical dynamics of hydrogen in a magnetic field is given by

$$H = \frac{p^2}{2} - \frac{1}{r} + \frac{1}{2}L_z B + \frac{1}{8}B^2\rho^2. \tag{3.3}$$

This Hamiltonian can be rescaled using the relations $r = B^{-2/3}\tilde{r}$, $p = B^{1/3}\tilde{p}$, and $L = B^{-1/3}\tilde{L}$. This gives the scaled Hamiltonian,

$$\tilde{H} = \frac{\tilde{p}^2}{2} - \frac{1}{\tilde{r}} + \frac{1}{2}\tilde{L}_z + \frac{1}{8}\tilde{\rho}^2, \tag{3.4}$$

where $\tilde{H} = B^{-2/3}H$. As a result, the classical dynamics depends only on the parameter $\epsilon_B = B^{-2/3}E$ and not on E and B separately.

The classical dynamics of hydrogen in an electric field is computed using the Hamiltonian,

$$H = \frac{p^2}{2} - \frac{1}{r} + Fz. \tag{3.5}$$

We can look for a scaling of this Hamiltonian similar to the magnetic field case by trying $r = F^a\tilde{r}$, $p = F^b\tilde{p}$. Substituting into the presumed scaled Hamiltonian gives

$$\tilde{H} = F^{2b}\frac{\tilde{p}^2}{2} - F^{-a}\frac{1}{\tilde{r}} + F^{a+1}\tilde{z}. \tag{3.6}$$

If a scaling rule exists, it will satisfy

$$2b = -a = a + 1. \tag{3.7}$$

So we see that $a = -1/2$ and $b = 1/4$. The classical dynamics of hydrogen in an

electric field depends only on the parameter $\epsilon_F = F^{-1/2}E$ and not on E and F separately.

The Hamiltonian used to calculate the quantum spectra of hydrogen Rydberg atoms in parallel electric and magnetic fields is

$$H = \frac{p^2}{2} - \frac{1}{r} + Fz + \frac{1}{2}L_z B + \frac{1}{8}B^2\rho^2. \tag{3.8}$$

This Hamiltonian cannot be scaled to depend on one parameter. It can be scaled to depend on two. This can be seen by applying the magnetic field scaling to the parallel field Hamiltonian. This gives

$$\tilde{H} = B^{-2/3}H = \frac{\tilde{p}^2}{2} - \frac{1}{\tilde{r}} + \frac{1}{2}\tilde{L}_z + \frac{1}{8}\tilde{\rho}^2 + FB^{-4/3}\tilde{z}. \tag{3.9}$$

So the parallel field dynamics only depends on the magnetic scaled energy, $\epsilon_B = EB^{-2/3}$ and the scaled electric field, $\tilde{F} = FB^{-4/3}$. Notice that $\epsilon_F = EF^{-1/2} = \epsilon_B/\sqrt{F}$, so using ϵ_B and ϵ_F is an equivalent way to parameterize the parallel field system.[2]

3.4 Core Potential for Alkalis

3.4.1 A Simple Model

To study the classical dynamics of alkali-metal Rydberg atoms, a spherically symmetric core potential, $V_c(r)$, is added to the hydrogenic Hamiltonian. The core potential is chosen to give the correct quantum defects of the particular alkali under study.

On physical grounds, I have chosen to use core potentials of the form

$$V_c = -\frac{(Z-1)f(r)}{r}, \tag{3.10}$$

[2]It is a generic property of *homogeneous* Hamiltonians that they can be scaled to depend on one less parameter than explicitly contained in the Hamiltonian itself. A homogeneous Hamiltonian is one in which all the terms of the Hamiltonian are proportional to some power of a single momentum or position coordinate, but which contains no terms which are products of different components of momentum and position or which are transcendental functions of momentum or position.

where Z is the nuclear charge and $f(r) = 1$ at $r = 0$, and $f(r) = 0$ at $r \gg a_0$. This gives a potential $-Z/r$ near the nucleus and $-1/r$ at large distances.

If interactions between the valence electron and the core are neglected, one could argue that the best $f(r)$ is given by

$$f(r) = \psi^* \psi, \tag{3.11}$$

where ψ is the Hartree-Fock wavefunction of the core. However, neither the quantum mechanics nor the classical dynamics is strongly dependent on the detailed shape of $f(r)$ but depends instead on its range.

The Hartree-Fock wavefunction of the lithium core has the form

$$\psi = c_1 e^{a_1 r} + c_2 e^{a_2 r} + c_3 r e^{a_3 r} + c_4 r e^{a_4 r}. \tag{3.12}$$

Seven independent parameters and four exponential functions are needed if the Hartree-Fock wavefunctions for lithium are used. Heavier alkalis would require the use of even more parameters and exponential functions. However, to keep things simple and computationally efficient, I have used

$$f(r) = e^{-ar}, \tag{3.13}$$

where the parameter a is chosen to give the best agreement with measured quantum defects. The quantum defects given by this model core potential are compared with the real quantum defects in Table 3.1.

Quantum defects for $l = 0, 1$ and 2 are in reasonably good agreement. The $l = 3$ quantum defect is systematically low for two reasons. One is that the long range probability distribution of the core electrons is proportional to $r^n e^{-r}$ where $n \geq 1$. More importantly, the quantum defects of high l states are due mainly to the polarizabilty of the core and *not* penetration of the wave function into the core. This

Table 3.1: Alkalai Quantum Defects for Model Potential

atom	a	δ_0	δ_1	δ_2	δ_3
Li	2.13	0.400	0.06	0.002	0.00004
	real	0.400	0.05	0.002	0.0003
Na	2.388	1.35	0.868	0.0068	0.00008
	real	1.35	0.856	0.014	0.00156
K	2.08	2.18	1.76	0.14	0.0004
	real	2.18	1.71	0.266	0.0091
Rb	2.47	3.14	2.73	1.07	0.0003
	real	3.14	2.65	1.34	0.0162
Cs	2.46	4.05	3.7	2.14	0.0005
	real	4.05	3.6	2.5	0.033

effect could be taken into account by using the core potential

$$V_{pol} = -\frac{\alpha}{2r^4}, \tag{3.14}$$

where α is the dipole polarizability of the core. The major justification for not doing this is that the quantum defects for higher angular momenta are very small and accounting for them would not affect the classical dynamics significantly. In addition, the $1/r^4$ singularity would be difficult to handle computationally, and we have found that the degree of chaos in these systems depends on the largest quantum defects and not on the detailed shape of the core. Furthermore, the polarization model gives worse values for the first few quantum defects than the model we have used.

Adding the core potential gives a total Hamiltonian

$$H = \frac{p^2}{2} - \frac{1}{r} - \frac{(Z-1)e^{-ar}}{r} + Fz + \frac{1}{2}L_z B + \frac{1}{8}B^2\rho^2. \tag{3.15}$$

We could think of Z, a, F, B, E, and L_z all as variable parameters. However, since we are interested in classical systems with real quantum counterparts, we will mainly consider cases where Z and a correspond to alkali atoms and where L_z is an integer. E, B, and F are treated as continuously varying parameters, subject to the scaling rules described above. The core potential destroys the scaling rules, but they are still

good approximations.

3.4.2 A More Accurate Core Model

As explained above, we are neglecting the fact that our core potential gives wrong values for the quantum defects of the higher angular momentum states. However, we can construct a core potential which will give correct values for all of the quantum defects and only have a $1/r$ singularity at the origin. Letting $q = (Z-1)$, the core potential should look like qe^{-ar}/r for small r and $\alpha/(2r^4)$ at large r. This is accomplished by the use of a weighting function,

$$w(r) = \frac{1}{(1+cr)}, \tag{3.16}$$

where c is chosen to give the correct intermediate quantum defects. The core model reflects penetration into the core at small r and polarizability at large r. The core model becomes

$$V_c(r) = -w(r)\frac{qe^{-ar}}{r} - (1-w(r))\frac{q}{r(1+2qr^3/\alpha)}, \tag{3.17}$$

which gives

$$f(r;a,c,\alpha) = w(r)e^{-ar} + (1-w(r))\frac{1}{(1+2qr^3/\alpha)}. \tag{3.18}$$

This model was not used in computations because it would increase computation time and not change the degree of chaos in a given system, compared with the simpler models actually used.

3.4.3 Estimates of Core Effects

Before presenting computational results, we should consider what the effect of the core potential will be. We expect high L_z states of alkalis to be hydrogenic in their behavior because an angular momentum barrier prevents the electron from going into the region of the core potential. Quantum mechanically, this manifests in small

quantum defects and nearly hydrogenic spectra. In lithium, $\delta_1 = 0.05$, and strong field spectra with no $L = 0$ component are nearly identical to the spectra of hydrogen. Here, we will give simple arguments showing at what value of L_z the classical dynamics of alkali atoms becomes hydrogenic.

Near the origin, the effective potential acting on the valence electron in an alkali is

$$V_{eff} = -\frac{1}{r} - \frac{(Z-1)e^{-ar}}{r} + \frac{L_z^2}{2\rho^2}. \tag{3.19}$$

The largest force due to the core potential that the electron feels is at the point of closest approach to the origin. This point is in the $z = 0$ plane and at ρ given by

$$V_{eff} = -\frac{1}{\rho} - \frac{(Z-1)e^{-a\rho}}{\rho} + \frac{L_z^2}{2\rho^2} = E, \tag{3.20}$$

where E is the energy of the valence electron. The energy of a Rydberg electron is close to zero, and the distance of closest approach ρ_{min} is not strongly dependent on energy. The equation for ρ_{min},

$$-\frac{1}{\rho_{min}} - \frac{(Z-1)e^{-a\rho_{min}}}{\rho_{min}} + \frac{L_z^2}{2\rho_{min}^2} = 0, \tag{3.21}$$

must be solved numerically, but from inspection, we can see that $L_z^2/(2Z) < \rho_{min} < L_z^2/2$.

When this equation is solved numerically, the core potential and force can be compared with the Coulomb potential and force at the point of closest approach. This is done in Table 3.2. For example, the distance of closest approach for potassium is about $L_z^2/(2Z)$ for $L_z = 1$ and $L_z^2/2$ for $L_z = 4$. When the distance of closest approach is small, the core dominates and the force due to the core is at most $(Z-1)$ times the Coulomb force. When ρ_{min} is large, the force due to the core is nearly zero.

This analysis predicts how closely, and for what L_z, the classical dynamics of these alkalis resembles the dynamics of hydrogen. The essential point is that the force is the relevant quantity in classical dynamics; whereas, the potential is the relevant quantity

Table 3.2: Core Potentials and Forces for Alkali Atoms

atom	a	L_z	ρ_{min}	F_c/F	V_c/V
Li	2.13	1	0.223	1.835	1.245
		2	1.938	0.165	0.032
		3	4.499	0.00146	0.000014
Na	2.388	1	0.051	9.93	8.86
		2	0.470	6.91	3.26
		3	4.498	0.0025	0.000022
K	2.08	1	0.013	37.99	36.97
		2	0.058	37.75	33.7
		3	0.159	36.3	27.3
		4	8.000	0.00004	0.000006

in quantum mechanics. Lithium is classically hydrogenic for $L_z > 1$ and quantum mechanically hydrogenic for $L > 0$. Sodium is classically hydrogenic for $L_z > 2$ and quantum mechanically hydrogenic for $L > 1$. Potassium is both classically and quantum mechanically hydrogenic for $L_z > 3$.

3.5 Semiparabolic Coordinates

The Hamiltonian described above is not separable (except for the special case of hydrogen in an electric field). Classical solutions must be sought by numerically integrating the equations of motion. Numerical integration of classical trajectories is poorly behaved near an attractive singular potential. It is convenient to introduce a coordinate system in which the Hamiltonian can be regularized to remove the singularity. The new coordinates (u, v) are defined by

$$\begin{aligned} \rho &= uv \\ z &= (u^2 - v^2)/2. \end{aligned} \tag{3.22}$$

The momenta transform as

$$p_\rho = \frac{1}{u^2 + v^2}(vp_u + up_v)$$

$$p_z = \frac{1}{u^2+v^2}(up_u - vp_v). \tag{3.23}$$

The Hamiltonian is then

$$\begin{aligned} H &= \frac{1}{2(u^2+v^2)}({p_u}^2 + {p_v}^2 + \frac{{L_z}^2}{u^2} + \frac{{L_z}^2}{v^2} - 4) + \frac{1}{8}B^2u^2v^2 + \\ &\quad \frac{1}{2}F(u^2-v^2) - \frac{2(Z-1)e^{-a(u^2+v^2)/2}}{u^2+v^2}. \end{aligned} \tag{3.24}$$

Introducing a regularized Hamiltonian,

$$h = (u^2+v^2)(H-E) + 2, \tag{3.25}$$

gives

$$\begin{aligned} h &= \frac{{p_u}^2}{2} + \frac{{p_v}^2}{2} + \frac{{L_z}^2}{2u^2} + \frac{{L_z}^2}{2v^2} + \frac{1}{8}B^2u^2v^2(u^2+v^2) + \frac{1}{2}F(u^4-v^4) - \\ &\quad 2(Z-1)e^{-a(u^2+v^2)/2} - E(u^2+v^2) = 2. \end{aligned} \tag{3.26}$$

The field-free case with no core potential corresponds to uncoupled harmonic oscillators both having frequency, $\omega = (-2E)^{1/2}$. The electric field introduces anharmonic terms but does not couple the oscillators. The magnetic field and core potentials couple the oscillators. Note that the regularized energy is always equal to two, and the real energy, E, enters the regularized Hamiltonian as a parameter.

3.6 Computational Results

Hamiltonian equations of motion can be written in terms of the regularized Hamiltonian h. This gives four coupled first order differential equations for the variables (u, v, p_u, p_v) and their first derivatives with respect to time. These equations are solved by numerical integration using the fourth order Runge-Kutta technique with a variable step size in time [PFT88].

Our general Hamiltonian gives a four-dimensional phase space. It is most con-

venient to look at the results of orbit calculations in two dimensions. Simple plots of the orbits in (u, v) or (ρ, z) can be revealing. Two-dimensional cuts out of the four-dimensional phase space can also tell us a lot about the dynamics. This kind of plot is called a Poincaré surface of section and is generated by putting a point on a specified plane in phase space every time an orbit passes through the plane. It is useful for our system to put a point on the (v, p_v) plane every time an orbit passes through the surface defined by $u = 0$. If $L_z > 0$, the angular momentum barrier prevents this from ever occurring, so we put a point on the (ρ, p_ρ) plane every time the orbit passes through $z = 0$. Most surfaces of section presented here are generated for about twenty separate trajectories. Trajectories are generally started near the origin and integrated for about 1000 traversals of the Poincaré plane. The initial conditions are changed by stepping the direction of the initial momentum through the possible range of values.

Regular orbits are confined to two dimensional surfaces in phase space called tori. The intersection of a torus with a surface of section is a closed curve. On a Poincaré surface of section, regular orbits trace out the tori on which they are confined. Each pass through the surface of section gives one point on the curve which is the intersection of the plane and the torus on which the regular orbit is confined. Periodic orbits do not trace out the entire curve but only pass through a small number of points on the curve.

Chaotic orbits are not confined to tori. These orbits eventually travel through all of the phase space that is available to them. Their only restriction is that they cannot pass through any remaining tori on which regular orbits are confined. If they passed through, then they would be confined to the tori and be regular orbits themselves. As a result, the remaining tori provide boundaries for the chaotic orbits.

As the parameters of a Hamiltonian are changed so that it makes a transition from regular to completely chaotic, the tori are gradually destroyed. As more tori are destroyed, a greater portion of phase space is available to the chaotic orbits. In a completely chaotic system all of the tori have been destroyed, the classical motion is ergodic, and any orbit travels through all of the phase space that is energetically

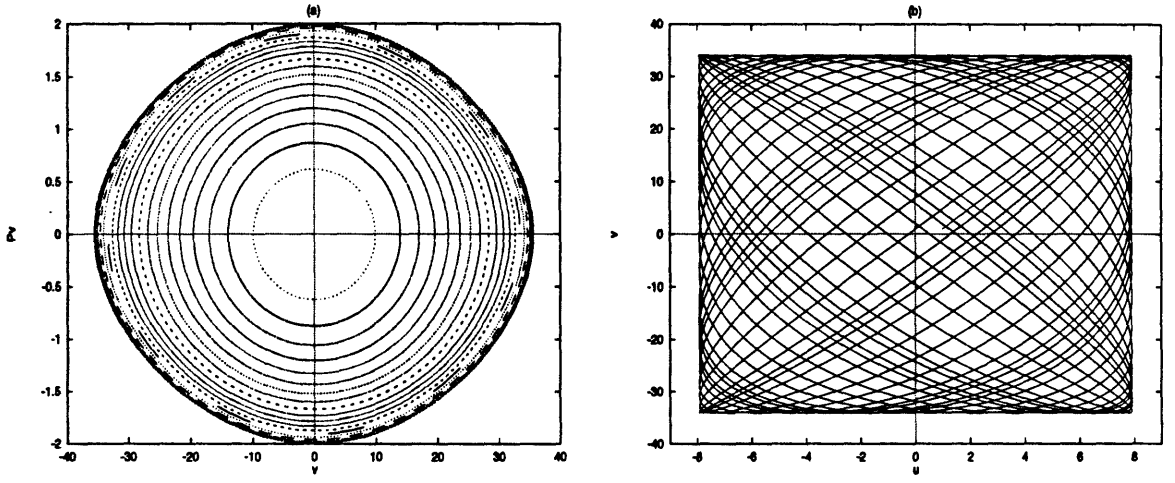

Figure 3-1: Hydrogen for $L_z = 0$, $B = 0T$, $E = -440cm^{-1}$, and $F = 3500V/cm$ ($\epsilon_F = -2.93$). (a) Poincaré plot. No tori are destroyed. Motion is completely integrable. (b) One of the orbits shown in the Poincaré plot.

available to it.

3.6.1 Hydrogen

Hydrogen without external fields is a trivial problem. It exhibits Kepler orbits which are all periodic. An electric field causes the Kepler orbits to precess and trace out a closed curve on a Poincaré plot. As we have seen, hydrogen in an electric field is separable. As a result, the system is regular for all values of ϵ_F. (See Figure 3-1.)

A small magnetic field also causes the Kepler orbits to precess and trace out closed curves on the Poincaré plot. As the magnetic field scaled energy, $\epsilon_B = EB^{-2/3}$, is raised, these tori are gradually destroyed. At $\epsilon_B = -0.54$ the first tori are destroyed, marking the onset of chaos. At $\epsilon_B = -0.127$ all the tori have been destroyed. Figure 3-2 shows some Poincaré plots. Figure 3-3 shows some of the orbits.

If we fix $L_z = 1$, the Hamiltonian for hydrogen in a magnetic field no longer exactly obeys the scaling rule. However, we find that the first tori are still destroyed at $\epsilon_B = -0.54$, and at $\epsilon_B = -0.127$ all the tori have been destroyed. This is shown in Figure 3-4. We can understand this simply. L_z creates an angular momentum barrier along the z axis, but does not change the potential at large values of ρ. The non-integrability is caused by the diamagnetic force, which is greatest at large

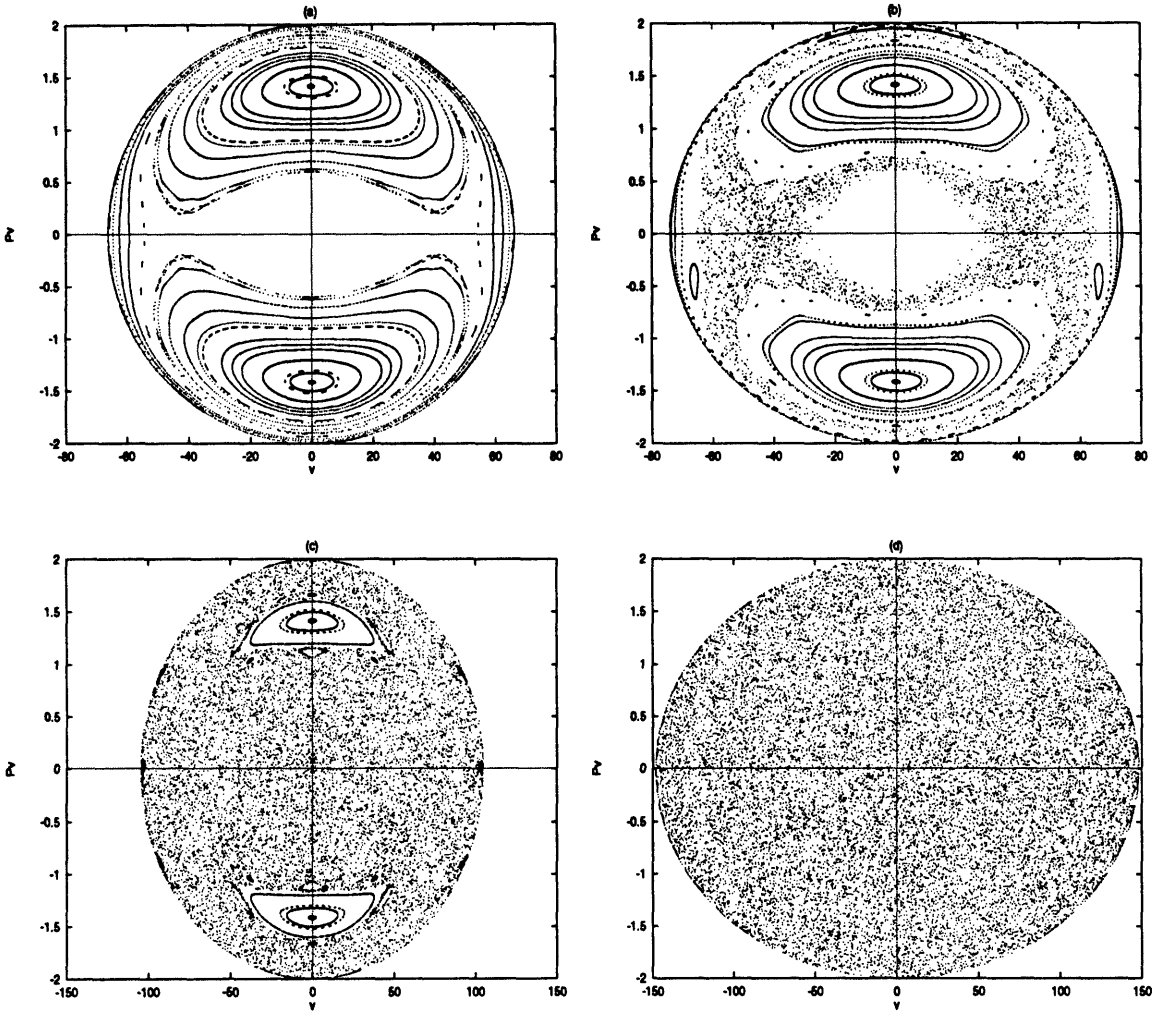

Figure 3-2: Hydrogen Poincaré plots for $L_z = 0$, $B = 6T$, $F = 0V/cm$, and (a) $E = -100cm^{-1}$ ($\epsilon_B = -0.52$). One of the twenty tori shown is beginning to break up. (b) $E = -80cm^{-1}$ ($\epsilon_B = -0.42$). Several of the tori have been destroyed. (c) $E = -40cm^{-1}$ ($\epsilon_B = -0.26$). Only a few tori remain. (d) $E = -20cm^{-1}$ ($\epsilon_B = -0.10$). No tori remain; the classical motion is completely chaotic.

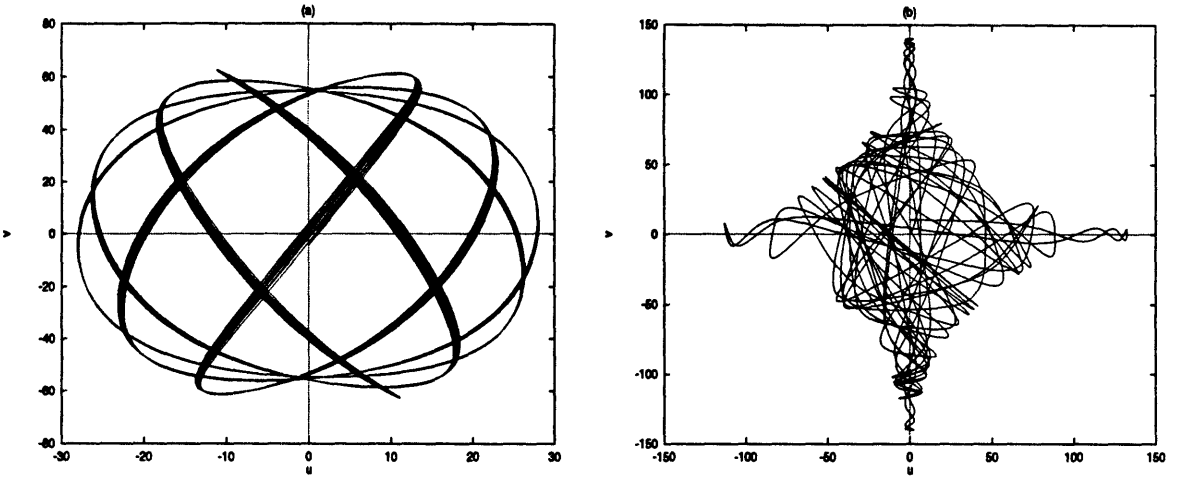

Figure 3-3: Hydrogen orbits for $L_z = 0$, $B = 6T$, $F = 0V/cm$, and (a) $E = -100cm^{-1}$ ($\epsilon_B = -0.52$). A regular orbit. (b) $E = -20cm^{-1}$ ($\epsilon_B = -0.10$). A chaotic orbit.

ρ. Therefore, unless the angular momentum or magnetic field is large enough to appreciably push the angular momentum barrier and the $\frac{1}{8}B^2\rho^2$ potential together, the scaling rule remains good.

As mentioned above, most Poincaré plots presented here are generated with about twenty different trajectories. If a trajectory is regular, it remains on a single torus. An interesting Poincaré plot was generated by a single trajectory for $\epsilon_B = 0$, which corresponds to infinite magnetic field or zero energy, as shown in Figure 3-5. The orbit traces out curves with successive traversals of the Poincaré plane. These curves occur for $v > 5$ and break up for $v < 5$. The motion should be considered chaotic because these curves are not confined to one torus. The explanation is simple. The trajectory spends a great deal of its time far from the origin. In this region, the magnetic field dominates the motion, and the motion stays on a torus until it comes back near the origin where its motion appears chaotic again. At some point, the trajectory again travels far from the origin where its motion is confined to a *different* torus, until it returns to the origin.

Hydrogen in Parallel Electric and Magnetic Fields

One might expect hydrogen with parallel fields to be a great deal more chaotic than hydrogen in only a magnetic field. This is not the case. The introduction of a small

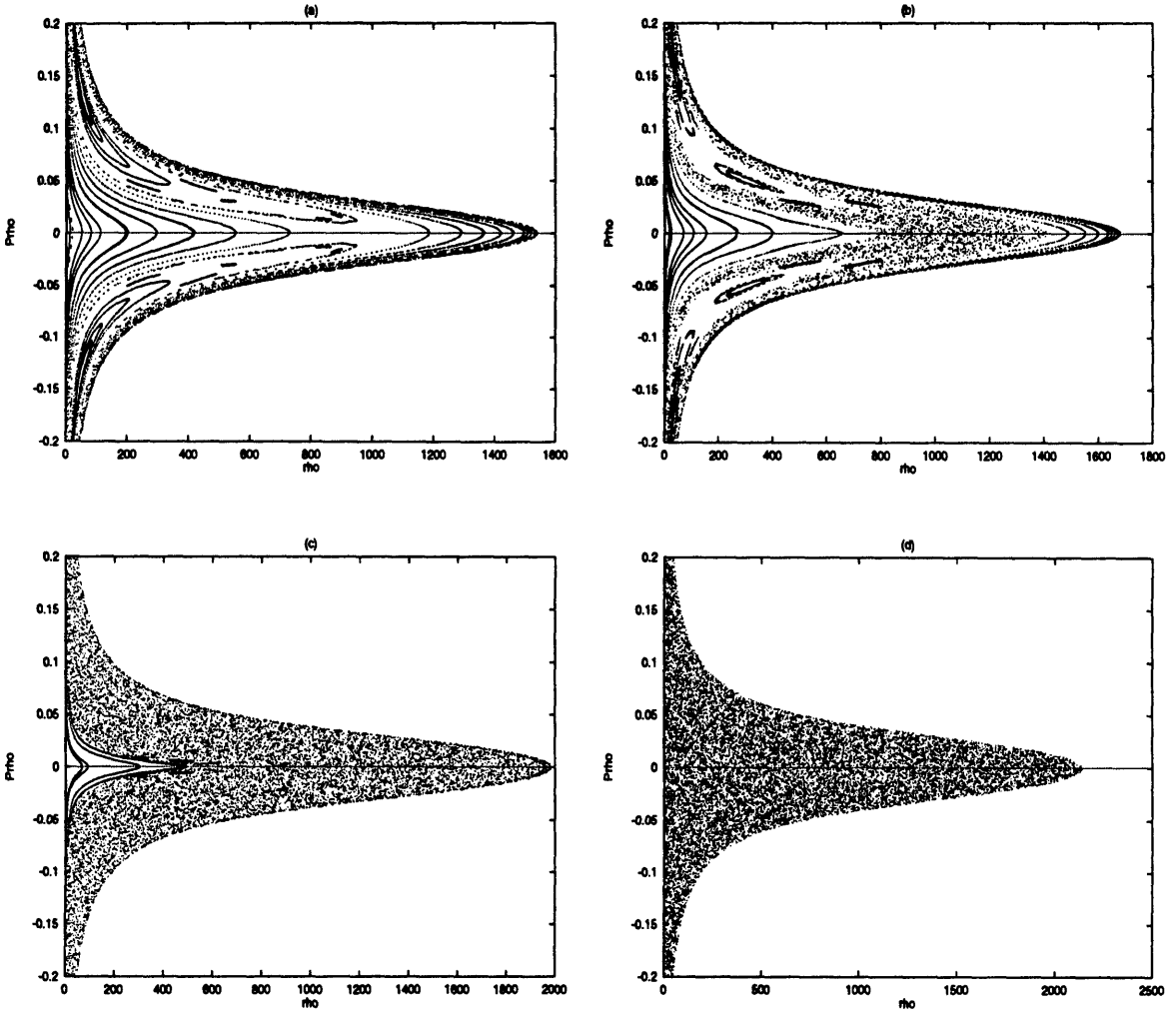

Figure 3-4: Hydrogen Poincaré plots for $L_z = 1$, $B = 6T$, $F = 0V/cm$, and (a) $E = -100cm^{-1}$ ($\epsilon_B = -0.52$). One of the twenty tori shown is beginning to break up. (b) $E = -80cm^{-1}$ ($\epsilon_B = -0.42$). Several of the tori have been destroyed. (c) $E = -40cm^{-1}$ ($\epsilon_B = -0.26$). Only a few tori remain. (d) $E = -20cm^{-1}$ ($\epsilon_B = -0.10$). No tori remain; the classical motion is completely chaotic.

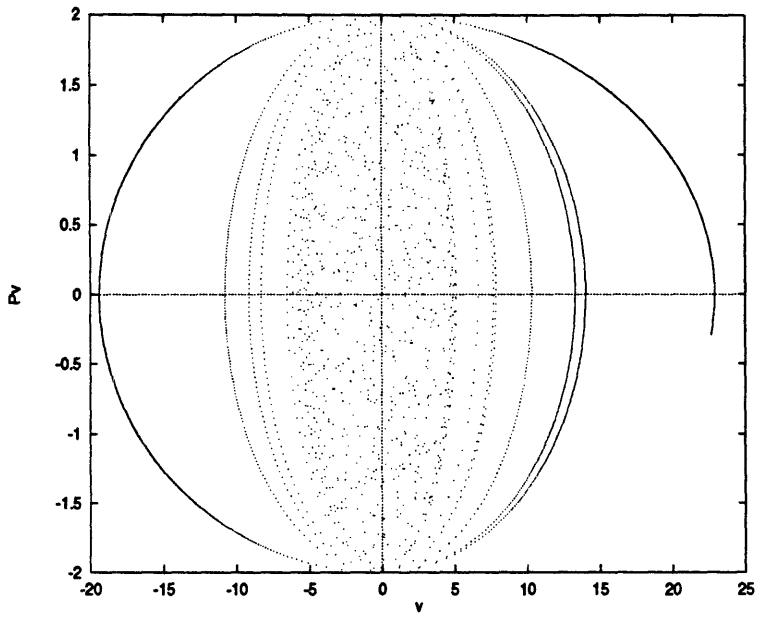

Figure 3-5: Hydrogen Poincaré plot for $L_z = 0$, $\epsilon_B = 0$.

electric field into the diamagnetic hydrogen problem makes the system a little more chaotic (at a given energy and magnetic field strength), but the electric field only causes a few tori to be destroyed. This is true all the way up to the electric field strength required for ionization, where only about half of the phase space is chaotic. This is shown in Figure 3-6. Just as the slow onset of chaos in diamagnetic hydrogen is due to the slow breakdown of the Λ symmetry, the slow onset of chaos in parallel fields is due to the preservation of the Λ_β symmetry.

3.6.2 Lithium

The field-free lithium Hamiltonian is separable in spherical coordinates. The orbits are elliptical in regions far from the origin. An orbit with angular momentum $L+1/2$ precesses through an angle $2\pi\delta_L$ (in cylindrical coordinates) each time it comes near the origin. Figure 3-7 shows an orbit and a Poincaré plot.

Lithium in an Electric Field

The core potential makes the Hamiltonian of lithium in an electric field non-separable. If $L_z > 0$, an angular momentum barrier keeps the particle from seeing much of the core potential.

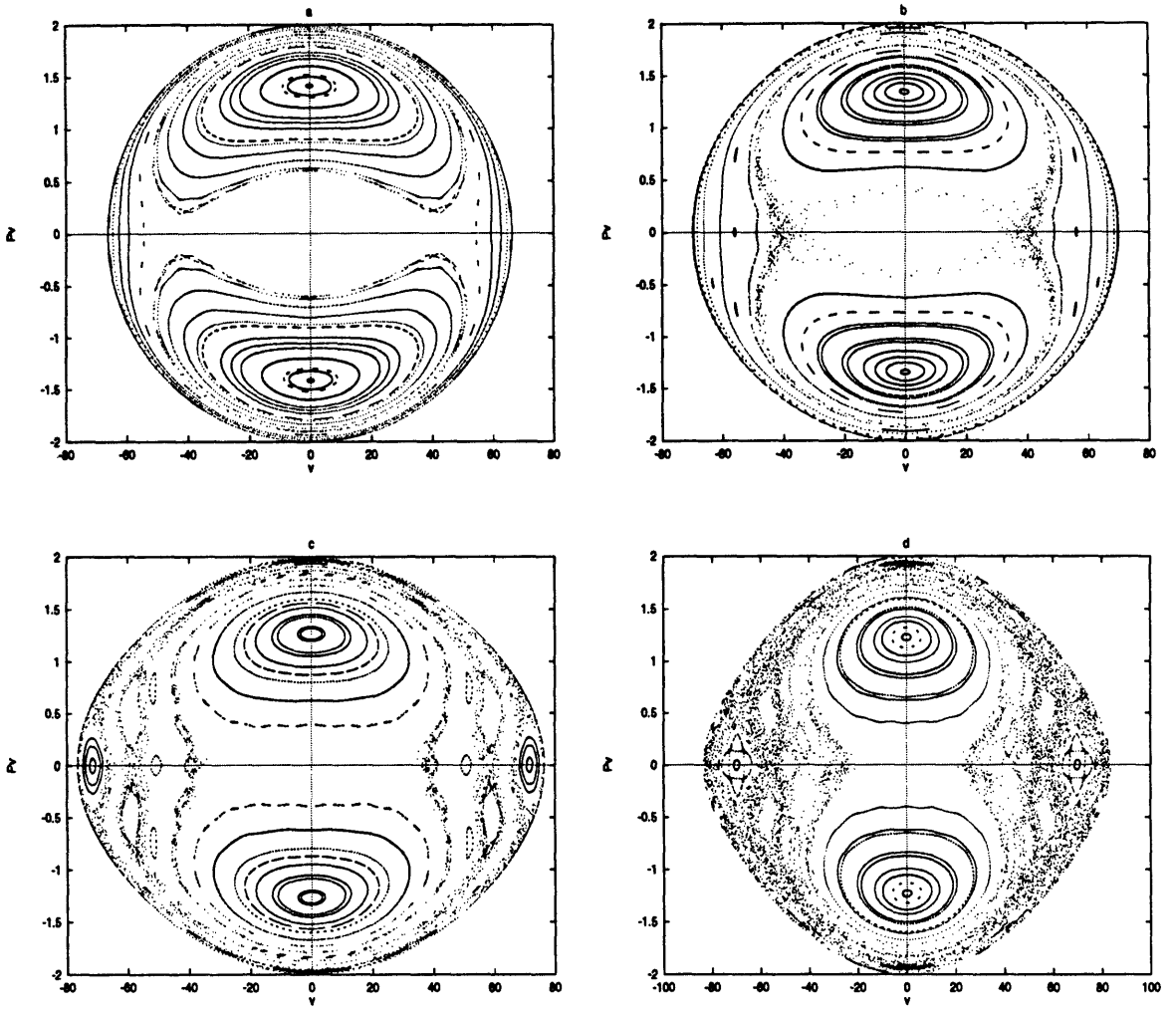

Figure 3-6: Hydrogen Poincaré plots for $L_z = 0$, $E = -100cm^{-1}$, $B = 6T$ ($\epsilon_B = -0.52$) and (a) $F = 0V/cm$ ($\epsilon_F = -\infty$). (b) $F = 100V/cm$ ($\epsilon_F = -3.25$). (c) $F = 200V/cm$ ($\epsilon_F = -2.30$). (d) $F = 250V/cm$ ($\epsilon_F = -2.06$). The ionization limit at this energy is 267 V/cm.

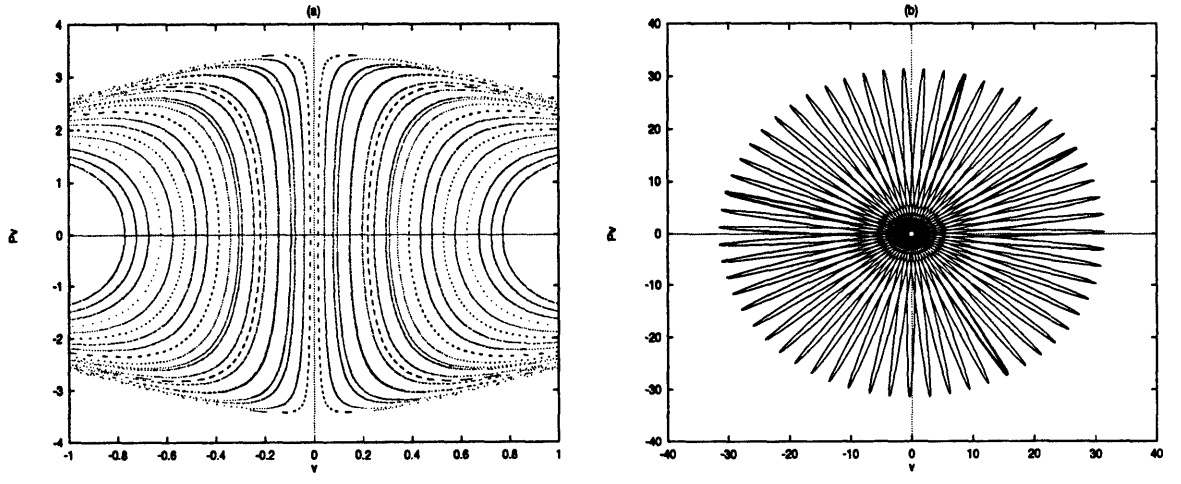

Figure 3-7: (a) Poincaré plot for lithium. $E = -440cm^{-1}$. (b) Orbit in lithium.

Two different core potentials were used to calculate the motion of lithium in an electric field for $L_z = 0$. Both have the form,

$$V_c = -\frac{(Z-1)f(r)}{r}, \tag{3.27}$$

where,

$$f(r) = e^{-ar-br^2}. \tag{3.28}$$

One core potential used $a = 2.13$ and $b = 0$. The other core potential used $a = 1.865$ and $b = 0.42$. The quantum defects of the first core potential are shown in Table 3.1. The second core potential gives $\delta_0 = 0.400$, $\delta_1 = 0.05$, and $\delta_n = 0$ for $n \geq 2$. The amount of chaotic phase space was not strongly dependent on which core potential was used.

The interesting features occur near the core potential, as shown in Figure 3-8. The breakup of tori indicating the onset of chaos is clear in this region. Calculations for $L_z = 0$ show that the onset of chaos approximately obeys the scaling rule. The first tori are destroyed at about $\epsilon_F = -11$. Most of phase space is chaotic for $\epsilon_F = -2.9$. At about $\epsilon_F = -2.9$, the trend toward chaos reverses and more tori appear until the ionization limit $\epsilon_F = -2$. Figure 3-9 shows the re-emergence of tori.

The phenomenon of the system becoming almost completely chaotic as ϵ_F is increased, then becoming regular again was unexpected. The explanation is found by looking at one of the orbits on a torus at $\epsilon_F = -2.1$. Figure 3-10 shows that the orbits on these tori stay so far from the origin that the core potential has no appreciable effect.

For $L_z = 1$ and $E = -440cm^{-1}$, the first tori are destroyed at $F = 200V/cm$. This corresponds to $\epsilon_F = -10$ and is a little higher than where the first tori are destroyed for $L_z = 0$. The system becomes gradually more chaotic until the ionization limit, where most of the tori have been destroyed, but a few tori remain.

The behavior of lithium in an electric field is almost completely regular for $L_z = 2$. Although the tori are shaped differently than the tori for hydrogen with $L_z = 2$, as ϵ_F is increased, few tori have been destroyed by $\epsilon_F = -2$. These results agree

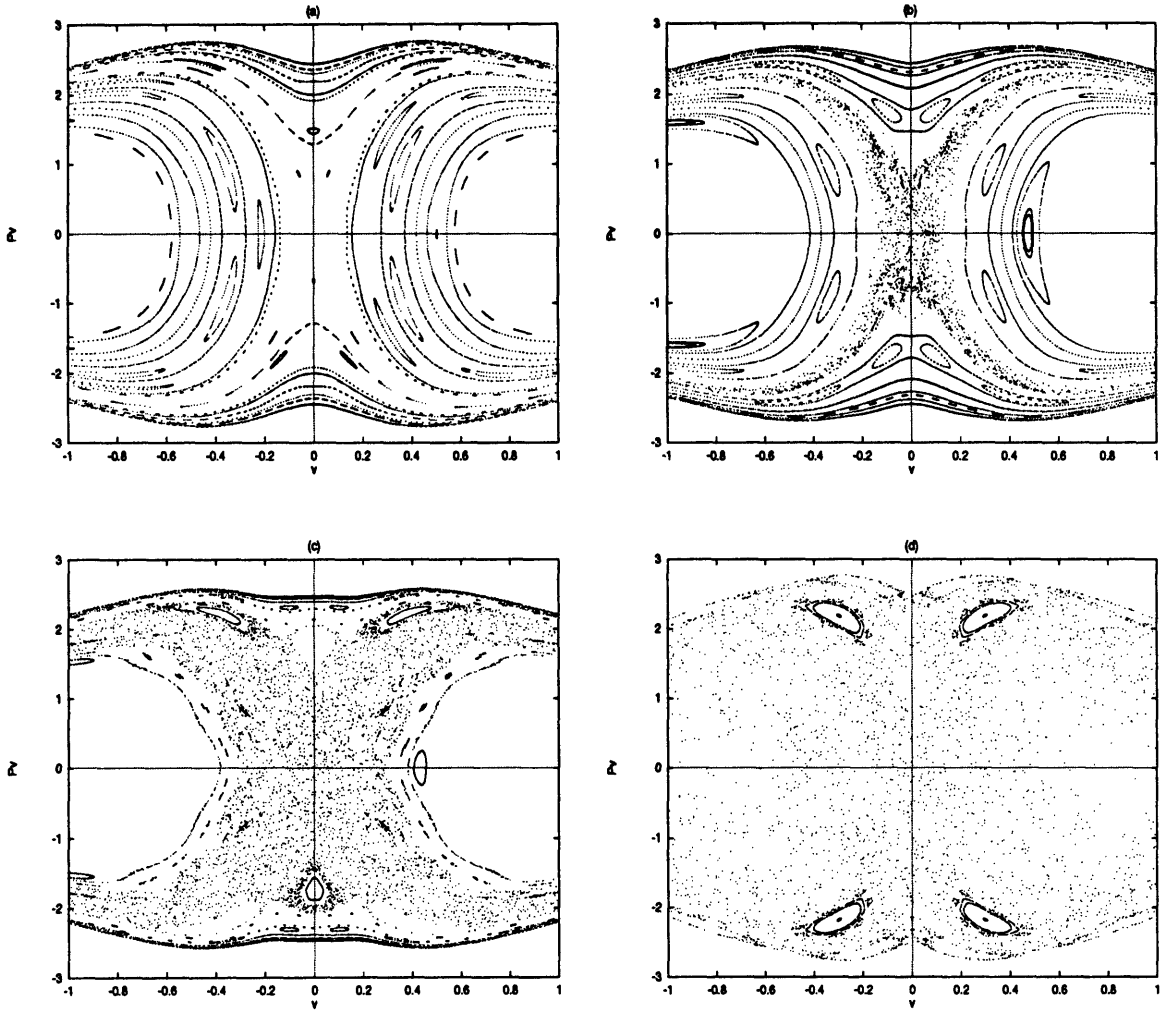

Figure 3-8: Lithium Poincaré plots for $L_z = 0$, $E = -440cm^{-1}$, $B = 0T$ and (a) $F = 150V/cm$ ($\epsilon_F = -11.7$). No tori are destroyed. (b) $F = 200V/cm$ ($\epsilon_F = -10.1$). A few tori are destroyed. (c) $F = 300V/cm$ ($\epsilon_F = -8.3$). More tori are destroyed. (d) $F = 500V/cm$ ($\epsilon_F = -6.4$). Few tori remain.

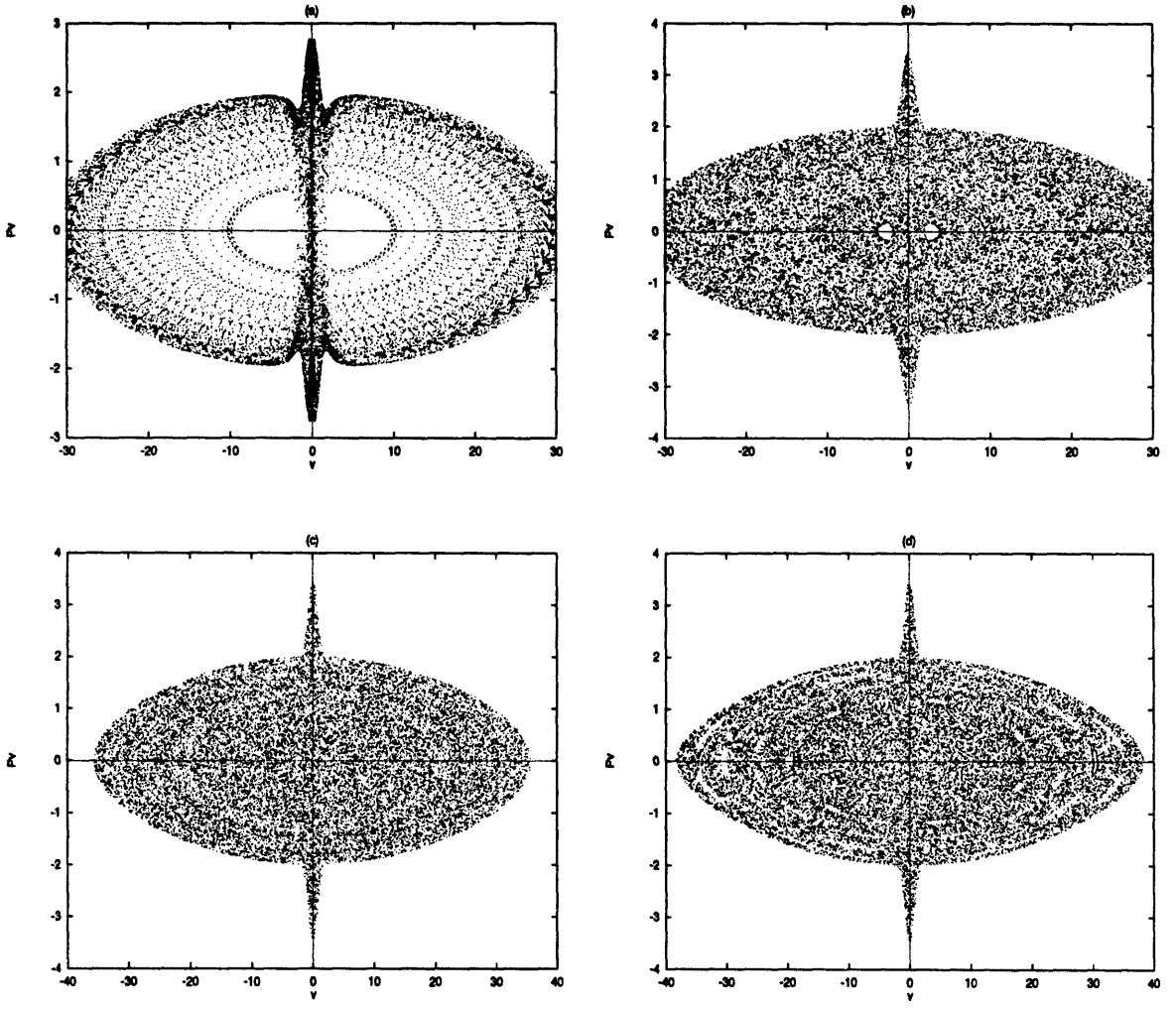

Figure 3-9: Lithium Poincaré plots for $L_z = 0$, $E = -440cm^{-1}$, $B = 0T$ and (a) $F = 500V/cm$ ($\epsilon_F = -6.4$). Few tori remain. Orbits appear to be on tori but the tori break up near the origin. The lobes on the otherwise elliptical plot are due to the core potential expanding the energetically allowed phase space. (b) $F = 1500V/cm$ ($\epsilon_F = -3.7$). No tori are easily visible. Some tori are known to be present because nearly ergodic orbits are excluded from small regions of phase space. (c) $F = 3500V/cm$ ($\epsilon_F = -2.4$). Nearly ergodic orbits are excluded from larger regions of phase space. (d) $F = 4500V/cm$ ($\epsilon_F = -2.1$). Regions of phase space supporting tori are even larger.

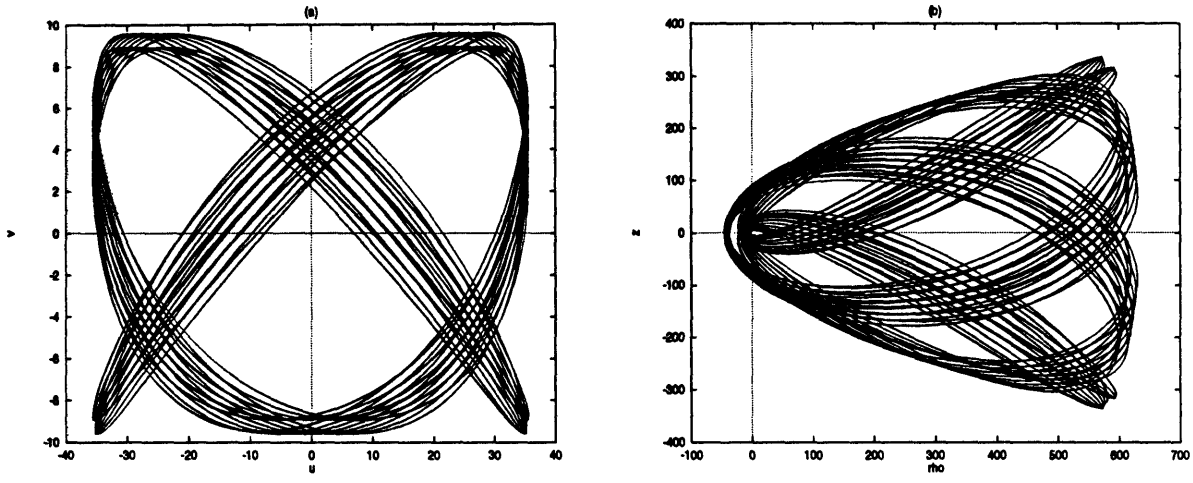

Figure 3-10: Regular orbit for lithium, $L_z = 0$, $B = 0T$, $E = -440cm^{-1}$, and $F = 4500V/cm$. (a) Semi-Parabolic Coordinates. (b) Cylindrical Coordinates.

qualitatively with the analysis given above comparing the force due to the core with the Coulomb force for different L_z.

Lithium in a Magnetic Field

We can understand the dynamics of diamagnetic lithium by viewing the field as a perturbation to lithium. The classical trajectories of hydrogen are Kepler ellipses. The core causes a precession of the semi-major axis of each Kepler ellipse through an angle which is a function of the angular momentum. As a result, incoming trajectories with different angular momenta are scattered differently from each other. In the absence of external fields, angular momentum is conserved. Consequently, each Kepler ellipse precesses the same amount on each pass near the nucleus. When the magnetic field is turned on, angular momentum is no longer conserved, and the trajectory is scattered through a different angle each time it passes through the core.

We can also understand core-induced chaos by viewing the core as a perturbation to diamagnetic hydrogen. Below $\epsilon_B = -0.54$, nearly all trajectories of diamagnetic hydrogen are regular and can be described by an ellipse whose parameters vary slowly

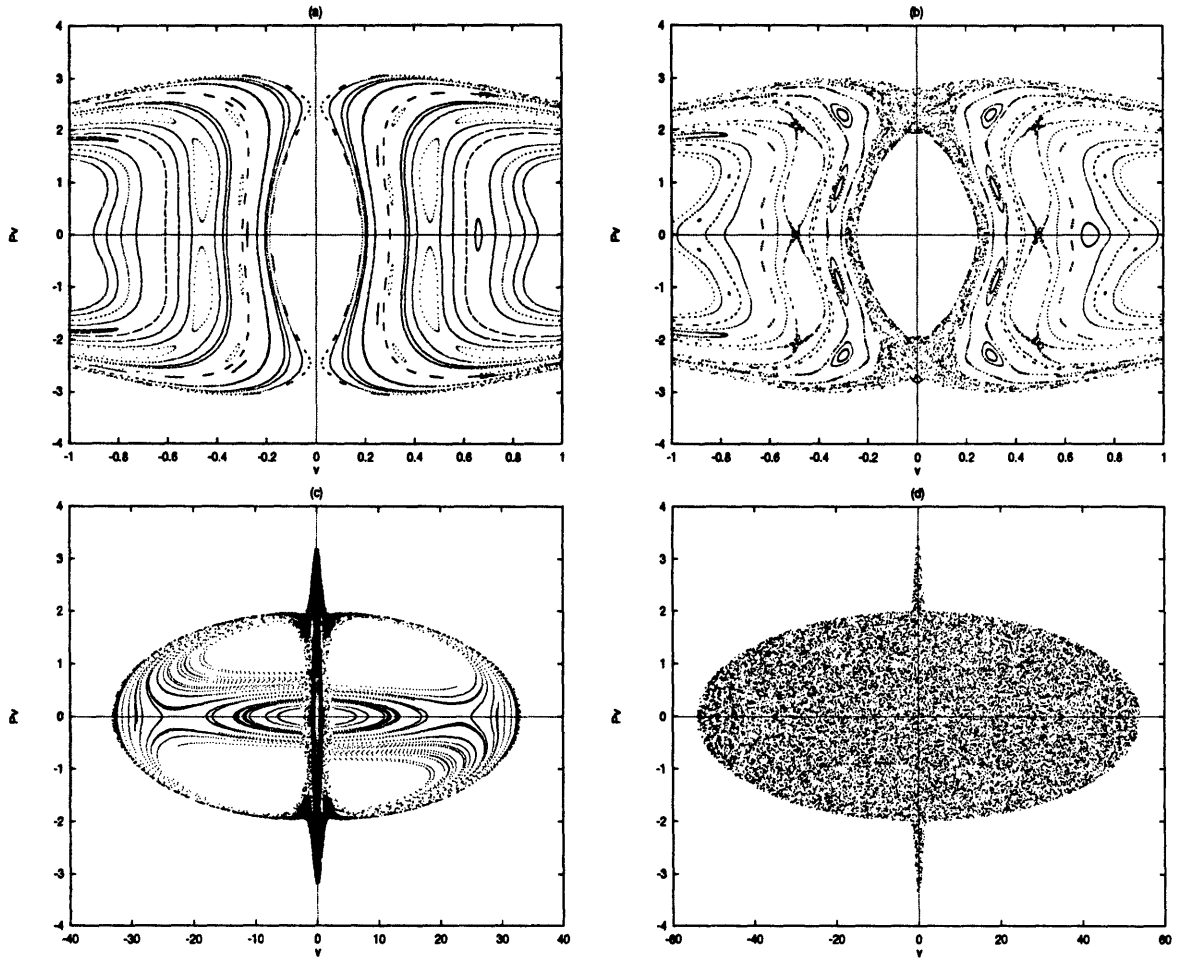

Figure 3-11: Lithium Poincaré plots for $L_z = 0$, $B = 6T$, $F = 0V/cm$, and (a) $E = -600cm^{-1}$ ($\epsilon_B = -3.14$). All tori are intact. (b) $E = -500cm^{-1}$ ($\epsilon_B = -2.60$). Several of the tori have been destroyed. (c) $E = -400cm^{-1}$ ($\epsilon_B = -2.01$). Only a few tori remain. (d) $E = -150cm^{-1}$ ($\epsilon_B = -0.79$). No tori remain; the classical motion is completely chaotic.

due to the magnetic field. These trajectories form regular patterns which resemble woven baskets in cylindrical coordinates. Because angular momentum is not conserved, each of these trajectories eventually has a small angular momentum and passes close to the origin. Outside of the core region, trajectories of diamagnetic lithium follow those of diamagnetic hydrogen. When a trajectory passes through the core, it is scattered into some other hydrogenic trajectory. This scattering from one hydrogenic trajectory to another can lead to ergodic (or nearly ergodic) motion, because through this process a trajectory can explore all of the phase space that is energetically available to it.

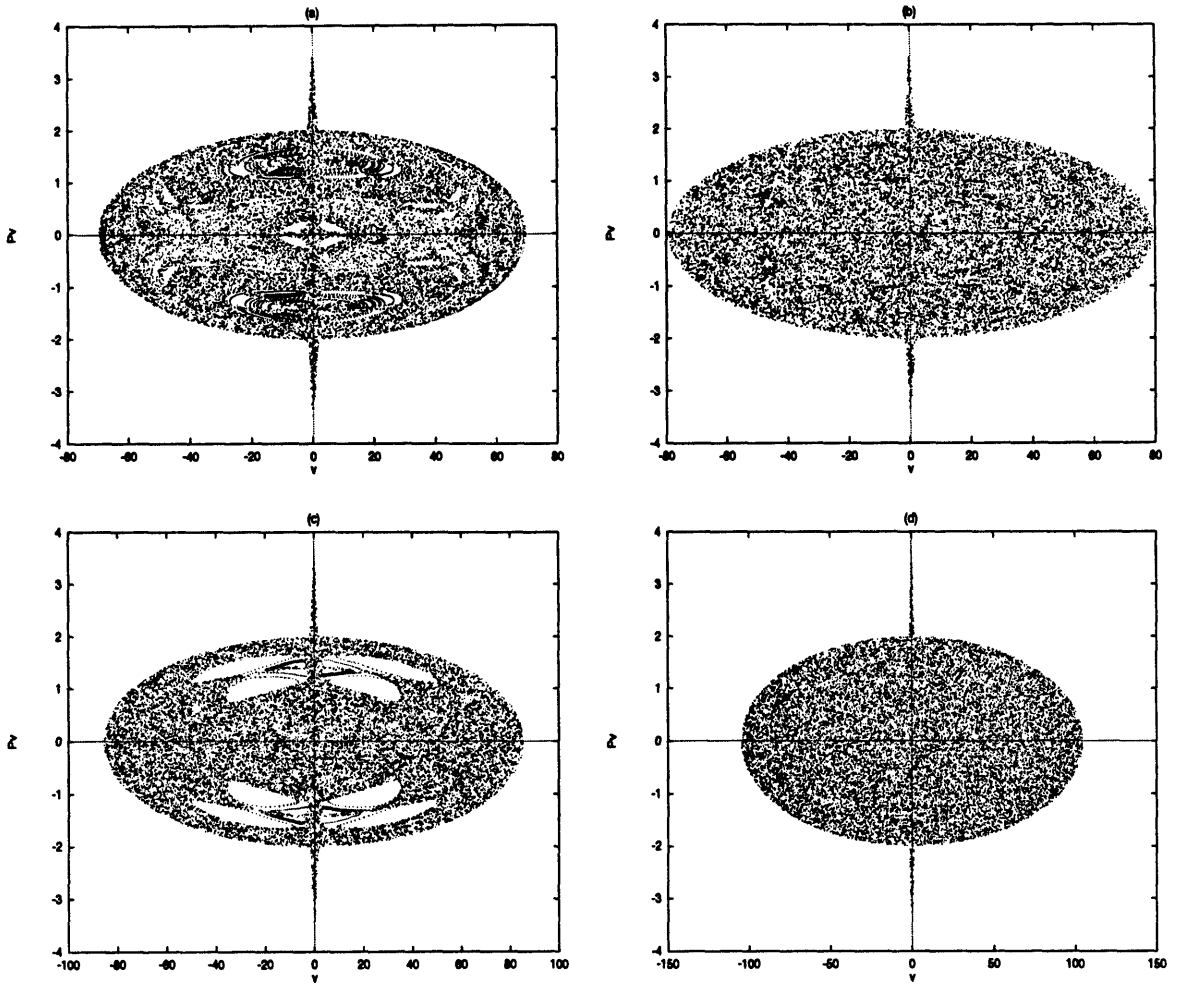

Figure 3-12: Lithium Poincaré plots for $L_z = 0$, $B = 6T$, $F = 0V/cm$, and (a) $E = -90cm^{-1}$ ($\epsilon_B = -0.47$). Several tori have reappeared. (b) $E = -70cm^{-1}$ ($\epsilon_B = -0.37$). Most tori have been destroyed. (c) $E = -60cm^{-1}$ ($\epsilon_B = -0.31$). Tori reappear and exclude orbits from certain regions of phase space. (d) $E = -40cm^{-1}$ ($\epsilon_B = -0.21$). No tori remain; the classical motion is completely chaotic.

Lithium in a magnetic field displays an interesting transition to chaos. For fields between $1T$ and $6T$, the classical scaling rule is good within roughly 10% for predicting the onset of chaos as well as other features. The first tori are destroyed at $\epsilon_B = -3$. This compares with $\epsilon_B = -0.54$ for the onset of chaos in hydrogen. The core potential destroys the approximate symmetry which preserved regularity to higher ϵ_B in the case of hydrogen. This is shown in Figure 3-11.

At $6T$, most of the tori are destroyed at $E = -150cm^{-1}$ ($\epsilon_B = -0.79$). As the energy is raised, regular tori reappear. Raising the energy from this point destroys the tori again. However, at $E = -60cm^{-1}$ regular tori reappear. The system is

completely chaotic for $E = -40cm^{-1}$ ($\epsilon_B = -0.21$) and higher. Figure 3-12 shows this behavior.

Below $\epsilon_B = -0.54$ we can attribute the chaos in the $L_z = 0$ lithium system to the non-integrability of the core potential combined with the magnetic field. In this regime, the A symmetry makes hydrogen completely regular, but lithium does not share this approximate symmetry because of the core. As a result, lithium becomes chaotic at much lower scaled energies. Tori that reappear as the scaled energy is raised always reappear in a region in which the hydrogenic system continues to support tori. These tori do not go near the origin, implying that they do not "see" the core potential.

Comparing surfaces of section of diamagnetic hydrogen and lithium provides an explanation for the reappearance of tori in lithium. For hydrogen at $\epsilon_B = -0.55$, most tori pass near enough to the origin to be destroyed by the core in lithium. As the scaled energy is raised to $\epsilon_B = -0.47$, some hydrogenic tori have broken up into island chains, and there are new tori which do not go near the origin. The essential point is that any torus of diamagnetic hydrogen which does not see the core potential is also a torus of diamagnetic lithium. As a result, lithium regains tori when there are hydrogenic tori which do not go near the origin, and lithium loses these tori when the remaining hydrogenic tori go near the origin.

Lithium for $L_z = 1$ has the first tori destroyed at about $\epsilon_B = -2.23$, compared with $\epsilon_B = -0.54$ for hydrogen. The system becomes completely chaotic at $\epsilon_B = -0.262$, compared with $\epsilon_B = -0.127$ for hydrogen. Poincaré plots are shown in Figure 3-13. The lithium $L_z = 2$ system begins to become chaotic at about $\epsilon_B = -1.05$. However, the onset is very slow and less than 10% of the tori have been destroyed at $\epsilon_B = -0.54$, the point where hydrogen begins to become chaotic. The system becomes completely chaotic at $\epsilon_B = -0.157$, compared with $\epsilon_B = -0.127$ for hydrogen. For $L_z = 3$, the classical dynamics of lithium in a magnetic field is very similar to hydrogen. The first tori are destroyed near $\epsilon_B = -0.54$, and by $\epsilon_B = -0.127$, all the tori have been destroyed.

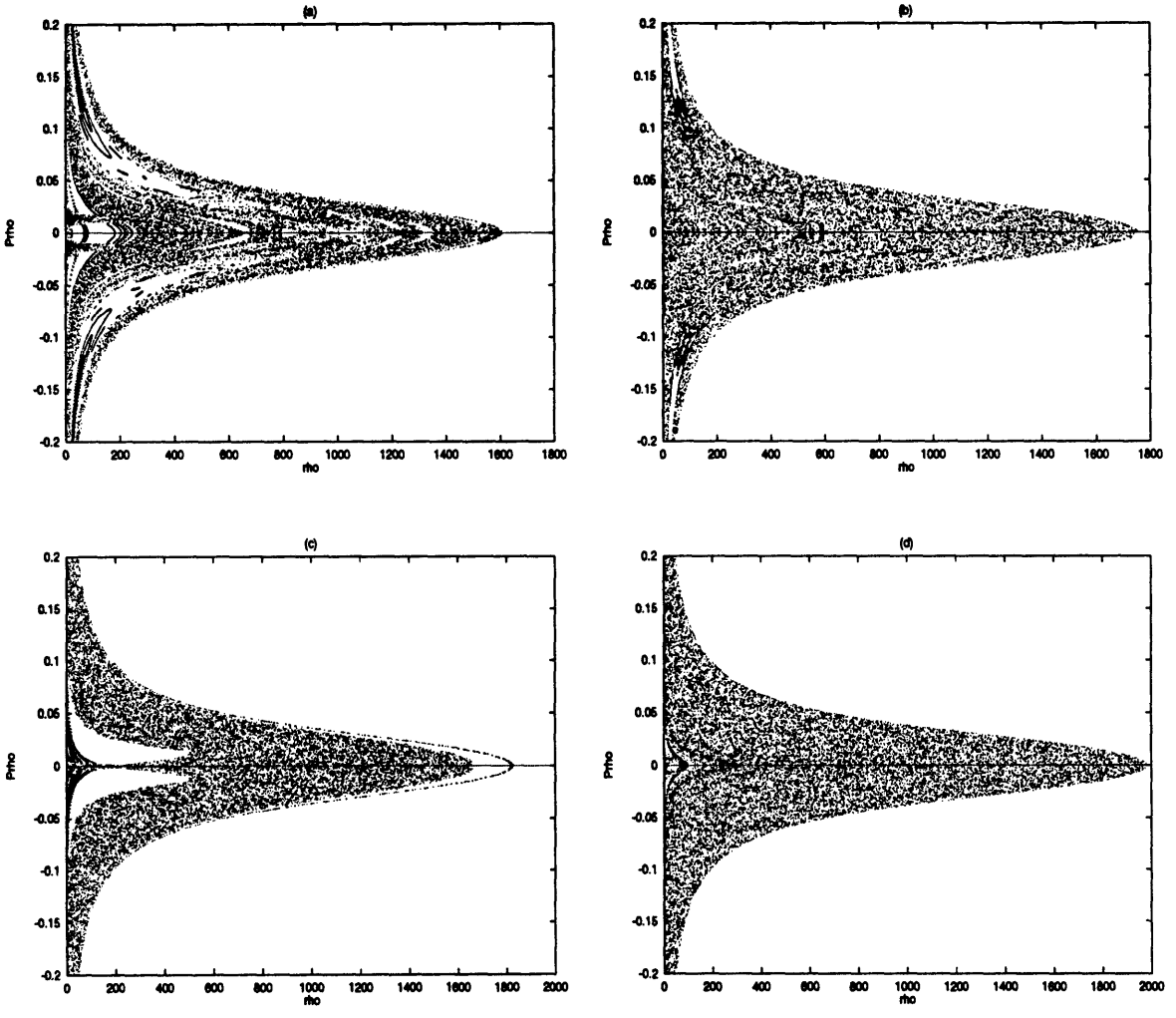

Figure 3-13: Lithium Poincaré plots for $L_z = 1$, $B = 6T$, $F = 0V/cm$, and (a) $E = -90cm^{-1}$ ($\epsilon_B = -0.47$); (b) $E = -70cm^{-1}$ ($\epsilon_B = -0.37$); (c) $E = -60cm^{-1}$ ($\epsilon_B = -0.31$); (d) $E = -40cm^{-1}$ ($\epsilon_B = -0.21$).

Lithium in Parallel Fields

For $L_z = 0$ diamagnetic lithium is chaotic in all but the smallest of magnetic fields, and the amount of chaos in the system is not changed a great deal by the addition of a parallel electric field. Figure 3-14 shows surfaces of section for various scaled energies. The essential point here is that the alkali-metal core destroys the Λ_β symmetry which exists in hydrogen and causes the system to be chaotic at much smaller energies than hydrogen. However, just as in diamagnetic lithium, tori which exist in hydrogen and do not go near the origin are preserved in lithium in parallel fields. The addition of an electric field to diamagnetic hydrogen causes the breakup of tori into island chains, many of which do not go near the origin.

For $\epsilon_B = -0.6, \epsilon_F = -6$, some tori have appeared (Figure 3-14(a)), whereas none were present in pure diamagnetic lithium at $\epsilon_B = -0.6$. When ϵ_F is raised to $\epsilon_F = -2$, only the slightest traces of tori are visible in the surface of section (Figure 3-14(b)). For $\epsilon_B = -0.4, \epsilon_F = -8$ tori are present in a significant amount of phase space (Figure 3-14(c)). When ϵ_F is raised to $\epsilon_F = -3$, the remaining tori are very small (Figure 3-14(d)), and none are visible for $\epsilon_B = -0.4, \epsilon_F = -2$ (Figure 3-14(e)). The surfaces of section for $\epsilon_B = -0.3$; $\epsilon_F = -6$, $\epsilon_F = -3$, and $\epsilon_F = -2$ are similar to each other in that some small tori are preserved while most of phase space is chaotic.

3.6.3 Heavier Alkalis

Rather than present detailed analysis and many more Poincaré surfaces of section, it is sufficient to say that the heavier alkalis are hydrogenic for sufficiently high L_z, and that the force due to the core is a more significant consideration than the potential due to the core. We have an algorithm to investigate the dynamics of any given alkali and combination of field strengths and energy. The dipole polarizability of the core can also be included if desired. We understand the basic mechanisms of the onset of classical chaos in alkali Rydberg atoms. Detailing the precise parameter values where a transition to chaos takes place is only needed for comparison with quantum spectra, and this can be done if required for later work.

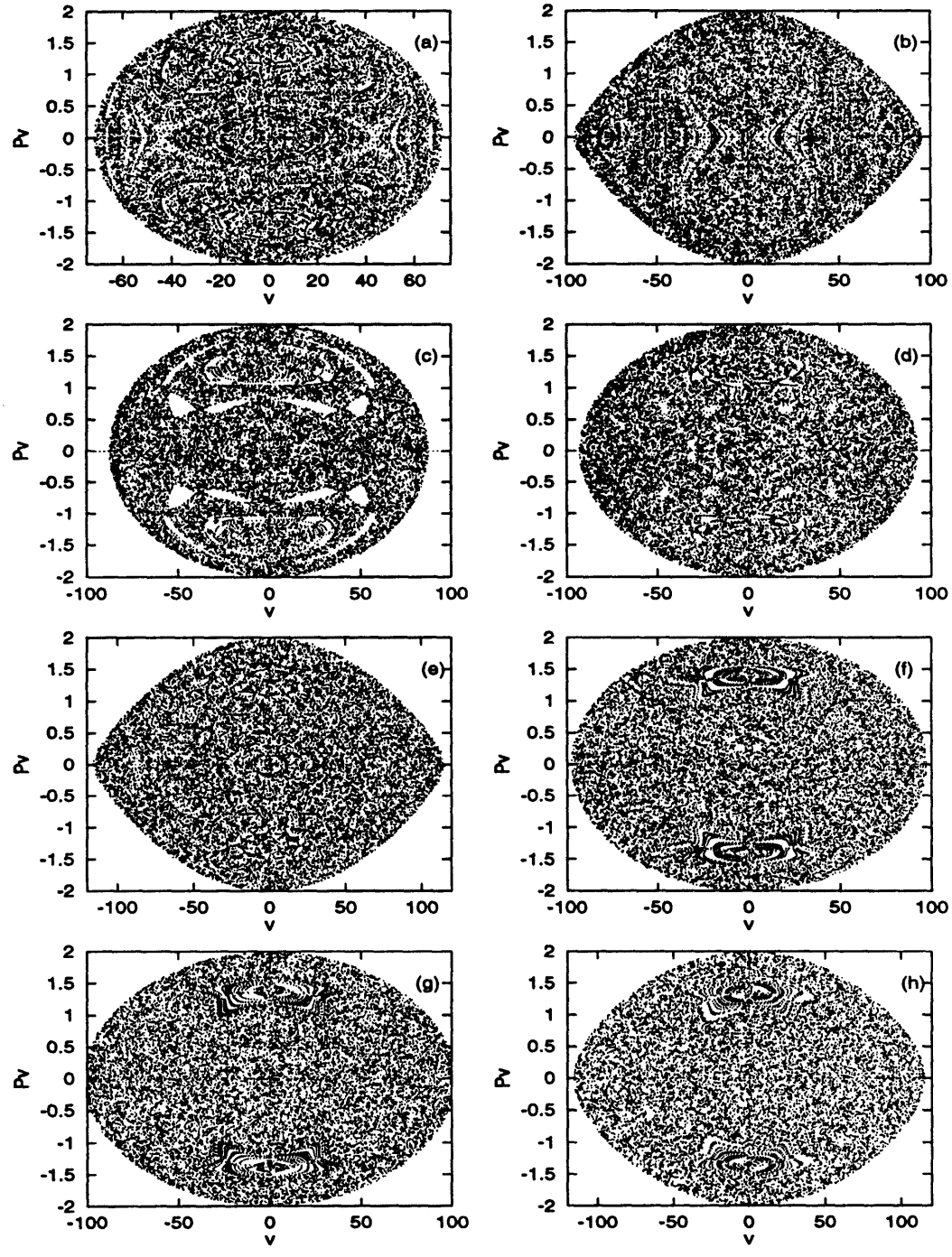

Figure 3-14: Poincaré Surfaces of Section for Lithium in Parallel Fields. (a) $\epsilon_B = -0.6$, $\epsilon_F = -6$; (b) $\epsilon_B = -0.6$, $\epsilon_F = -2$; (c) $\epsilon_B = -0.4$, $\epsilon_F = -8$; (d) $\epsilon_B = -0.4$, $\epsilon_F = -3$; (e) $\epsilon_B = -0.4$, $\epsilon_F = -2$; (f) $\epsilon_B = -0.3$, $\epsilon_F = -6$; (g) $\epsilon_B = -0.3$, $\epsilon_F = -3$; (h) $\epsilon_B = -0.3$, $\epsilon_F = -2$.

3.7 Summary

In summary, we have shown that Rydberg atoms in strong fields generally display a transition from orderly to chaotic classical motion as the energy and fields are increased, and we have found the values of scaled energy where these transitions occur. Hydrogen in an electric field is an exception and remains orderly for all energy and field values. In alkali-metal atoms, the core potential plays a significant role by inducing chaos for scaled energies where the equivalent hydrogenic system is often regular.

Chapter 4

Experimental Method

Do not pollute the land where you are. Bloodshed pollutes the land, and atonement cannot be made for the land on which blood has been shed, except by the blood of the one who shed it.–Numbers 35:33

The goal of the experiment is to obtain high-resolution spectra of lithium Rydberg states at a variety of energies and fields. Laser spectroscopy is performed on an atomic beam of lithium. For magnetic field experiments, the atomic beam travels along the axis of a superconducting magnet. Electrodes apply a parallel electric field if desired. The basic experimental setup is shown in Figure 4-1. Many of the experimental details are described in Michael Kash's thesis [KAS88]. It is not my intent to repeat that material here. I will give a general overview of the experimental methods and describe in detail the features which have been added or changed substantially since Mike Kash wrote his thesis. I will describe the atomic beam source, the superconducting magnet and electric field plates, the excitation scheme and metrology, detection techniques, the interaction regions, data acquisition and constant scaled energy spectroscopy. The experimental results presented in this thesis only involve electric field spectra.

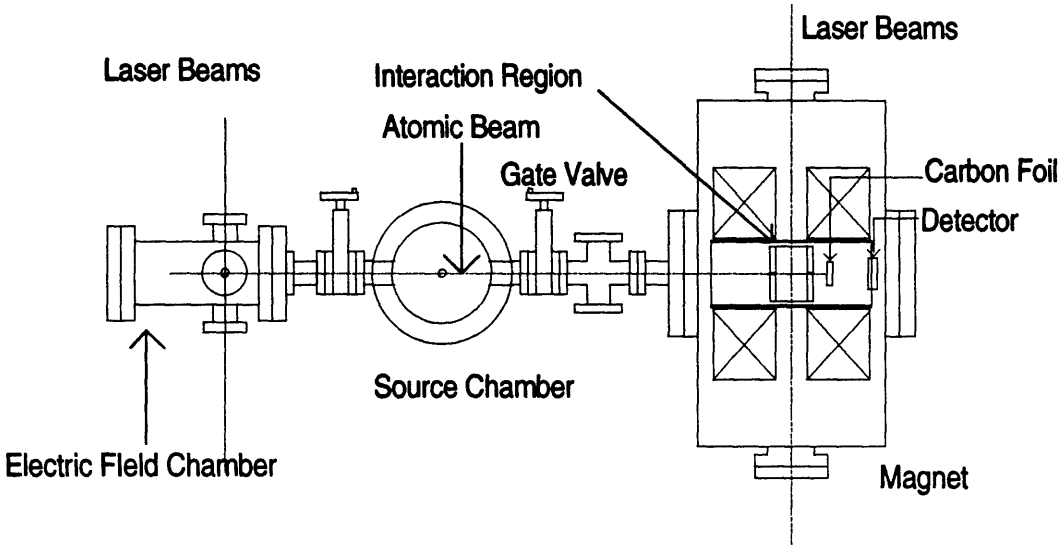

Figure 4-1: Experimental setup for electric and magnetic field studies. The atomic beam can be directed either to the left or to the right.

4.1 Atomic Beam Source

The lithium atomic beam is provided by an effusive lithium source heated to $600 - 700° C$ inside of a stainless steel oven. The oven is constructed out of a 2″ long 0.75″ diameter stainless steel rod which is bored out to hold the lithium. There is a 0.040″ diameter hole in the side to provide for the atomic beam. A 1.33″ conflat flange is welded to the top to provide an opening for loading the lithium and a good seal so that the lithium only escapes through the 0.040″ hole. We use nickel gaskets rather than copper for the conflat flange because lithium reacts with copper at the temperatures used. Several grams of lithium provides for a beam life of several hundred hours.[1]

The stainless steel oven sits inside of a metal block with four 2″ long 0.375″ diameter Watlow Firerod heaters with 2″ no-heat extensions. The first block was made out of copper, but it reacted with the lithium, so we had a block made out of

[1]This atomic beam oven design was provided by Chun-Ho Iu of SUNY-Stonybrook.

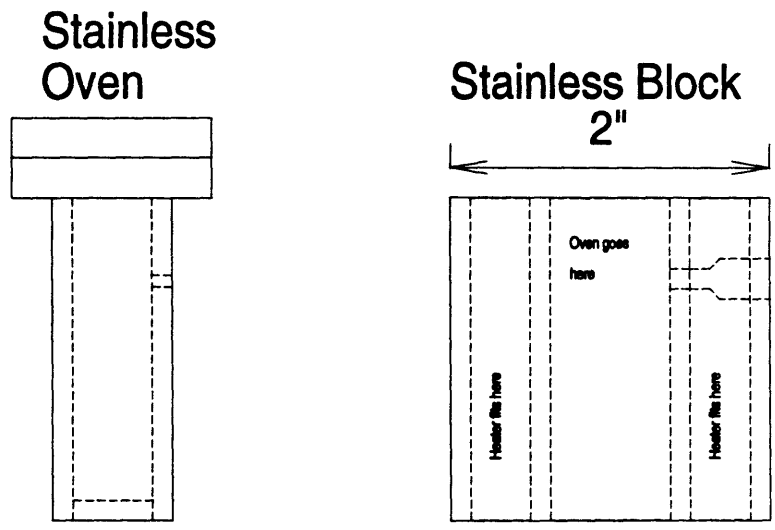

Figure 4-2: Atomic Beam Oven

stainless steel. There is a copper cover over the conflat flanges so they get as hot as the rest of the oven which prevents lithium from condensing on the lid. Each heater has a resistance of about 20Ω. The heaters are connected in parallel and the current is controlled with a variable transformer. The heaters are rated up to $120\,V$ and $1500°\,C$, but the oven assembly reaches $600°C$ at about $40\,V$ which corresponds to $2\,A$ of current through each oven and a total power of $240\,W$. When new heaters are installed, they outgas for several days at about $400°\,C$. The oven and the metal block it sits in are shown in Figure 4-2.

The no-heat extensions provide structural support for the oven and are connected to a water-cooled cold shield which carries away the heat radiated from the oven. The cold shield is attached to the top flange of the oven vacuum chamber. There is a large diameter bellows between this flange and rest of the oven chamber which provides for vertical and horizontal adjustment of the oven position. This is important for aligning the oven to maximize flux through the interaction region. The oven vacuum chamber is shown in Figure 4-3. The oven chamber is equipped with two $2.75''$ conflat flanges so that it can simultaneously be connected to both the electric field chamber and the superconducting magnet. To go from one experiment to the other we need only to rotate the top flange and point the beam the other way.

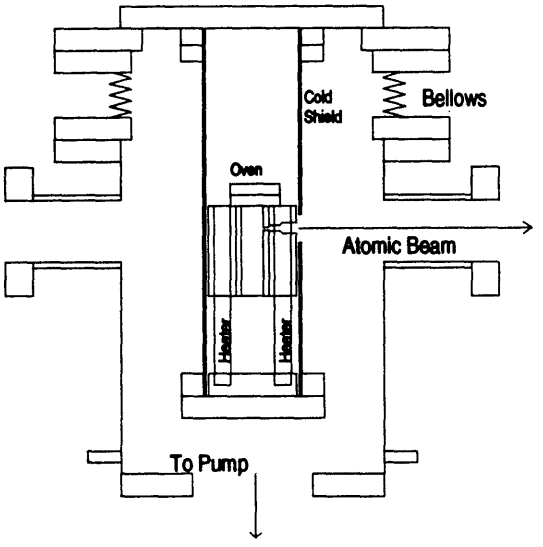

Figure 4-3: Atomic beam oven chamber showing oven, heaters, cold shield, bellows and vacuum chamber.

The oven chamber is evacuated by a Varian V-60 turbomolecular pump. When the oven is hot, the oven chamber has a pressure of about $10^{-6}\,torr$. When the oven is at room temperature, the pressure is less than $10^{-7}\,torr$, which is the lower limit on the Penning gauge measuring the pressure.

Collimation of the atomic beam is obtained by placing apertures between the oven and interaction region. These apertures vary in size and placement. The Doppler broadening varies a bit, but the total experimental resolution is not greatly affected by the particular collimation scheme used.

4.2 Magnetic Field

The magnetic field is provided by a split-coil 5″ diameter bore superconducting magnet which was purchased from American Magnetics. The magnet can reach a field of $7T$ and is positioned at the bottom of a liquid helium dewar inside of a liquid nitrogen dewar inside of a vacuum system. The thermal isolation of the magnet is good; the vacuum design is not.

The magnet chamber is evacuated by a Varian V-60 turbomolecular pump. When pumping down from atmospheric pressure, it takes several days to reach $10^{-6}\,torr$.

Once this pressure is reached, the magnet can be cooled to liquid nitrogen temperature by flowing liquid nitrogen into the helium dewar. Care needs to be taken not to allow liquid nitrogen to collect in the helium dewar because liquid nitrogen is difficult to remove, and helium cannot be added until the liquid nitrogen boils off. The liquid nitrogen dewar is filled at this time. Cryogenic pumping quickly lowers the pressure into the $10^{-7} torr$ range and after 12 hours, the pressure drops to near $10^{-8} torr$. Cooling the magnet from room temperature to $77° K$ causes the magnet to rise a millimeter or two relative to the dewar.

Cooling the magnet to $4° K$ and filling the dewar requires about $100 liters$ of liquid helium. This causes the magnet to rise another millimeter or two relative to the dewar. This is important to remember when positioning the lasers and atomic beam through the interaction region. The magnet is covered with helium when the gauge reads 45% full or more. The magnet must be covered with liquid helium when it is operated. The helium boils off at a rate of $10 - 20\%$ per day, depending on the magnitude and duration of current through the leads. The current is supplied by a $100 A$ supply made by Cryomagnetics. Operation of the magnet and supply are described in detail in the appropriate manuals, which should be read and understood by anyone operating them.

4.3 Electric Field

Electric fields are applied using disk-shaped field plates placed on the atomic beam axis. The plates have holes in the middle for the atomic beam to pass through. This geometry is required to allow spectroscopy both above and below the classical ionization limit. The plate voltages are arranged so that if ionization occurs in the interaction region, the ions are accelerated toward the detector. If ionization does not occur in the interaction region, the atoms drift out of the interaction region into the high-field region and are ionized.

Electric field uniformity over the interaction volume depends on three factors: the holes in the field plates, the separation between the plates, and biasing the plates

symmetrically. The interaction volume consists of the intersection of the laser and atomic beams, and so it is a cylinder of about $50\,\mu m$ in diameter, coaxial with the laser beam and about $3\,mm$ long across the width of the atomic beam. Both the field uniformity and field to voltage ratio obtained from computer modeling of the interaction region are consistent with experimental data. The effect of the holes in the field plates decreases with increasing separation. The effect of finite diameter plates increases with separation. There is a tradeoff between the two effects, and as expected, there is an optimum separation with $hole\,diameter < separation < plate\,diameter$. For 2.5″ plates with 0.125″ holes in the middle, the optimum separation is near 0.75″, which yields a non-uniformity of 0.1% over the interaction volume. A separation of 0.5″ gives a non-uniformity of about 0.3% over the volume. Biasing the plates asymmetrically raises the non-uniformity to roughly 1% over the interaction volume.

4.4 Excitation Scheme and Metrology

Atomic Rydberg states of lithium are excited with a stepwise process. Atoms are excited from the $2S$ to the $3S$ state by a two-photon transition at $735.130\,nm$. Light for this transition is produced by a Coherent 699 ring dye laser with LD700 dye. The dye laser is pumped with about $6\,W$ of multifrequency red light from a Krypton ion laser. The two-photon transition requires high power and a tight laser focus. The beam from the red dye laser is expanded to a diameter of about a centimeter to produce a tighter focus. The expanded laser beam is focused onto the atomic beam with a $40\,cm$ focal length lens.

The red laser at $735.130\,nm$ is locked on the two-photon transition, while another Coherent 699 ring dye laser provides light in the range $610 - 630\,nm$ for exciting Rydberg states. This laser uses Sulphorhodomine B (also called Kiton Red) dye and is pumped with about $7\,W$ of light from an Argon ion laser at $514\,nm$. Both ring lasers have linewidths in the kilohertz range, but their jitter is about $1\,MHz$. The yellow laser beam is also expanded by a telescope and overlapped with the red laser using a dichroic mirror. The overlap of the two beams at their foci is set by intercepting

the beams right after the focusing lens and adjusting the mirrors so that both lasers pass through a $50\,\mu m$ pinhole placed at the focus. After this is done, the overlap can be tweaked using the Rydberg signal directly.

Each laser is set to a desired frequency range by adjusting its birefringent filter and thick etalon while measuring its wavelength with a wavemeter. The wavemeter is a dual laser Michelson-Morley interferometer with a moving arm. The laser beam of unknown wavelength and a known frequency helium-neon laser are propagated together in the wavemeter and the interference fringes of each beam are measured with a photodiode. By measuring the ratio of the number of fringes, we obtain the ratio of the unknown wavelength to the known wavelength. A travel length of about $12''$ yields a frequency measurement of about 1 part in 10^6. This is accurate enough to find the $2S \rightarrow 3S$ transition by scanning the red laser over several GHz and to locate a desired range for the yellow laser within a few GHz.

The wavemeter is used to set the lasers to a desired frequency range. Precision measurement of the yellow laser frequency while measuring Rydberg spectra is accomplished using an iodine cell and spectrum analyzer. Using beam splitters, secondary beams are taken from the main yellow beam. One of these beams is used to record an iodine absorption spectrum simultaneously with the Rydberg spectrum. The frequencies of all the iodine absorption lines in the regions of interest to us are well known and tabulated to an accuracy of $0.0005\,cm^{-1}$ [GVC82, IUC91]. This calibration has been checked and some slight adjustments to the table have been made by comparison with zero-field Rydberg spectra. The transmission fringes of an etalon with a free spectral range of about $300\,MHz$ are also recorded and used to determine how far in frequency each point in a scan is from a given iodine line. In this way, each point in the scan is assigned a frequency relative to the $3S$ state. By knowing the frequency of the $3S$ state relative to the ionization limit, we can assign each point in the scan an energy relative to the ionization limit. A laser scan is shown in Figure 4-4.

The accuracy of this assignment is limited mainly by the uncertainty in the calibration of the iodine reference lines and in the uncertainty in the position of the minimum of the absorption line. Energies are typically determined within $0.001\,cm^{-1}$

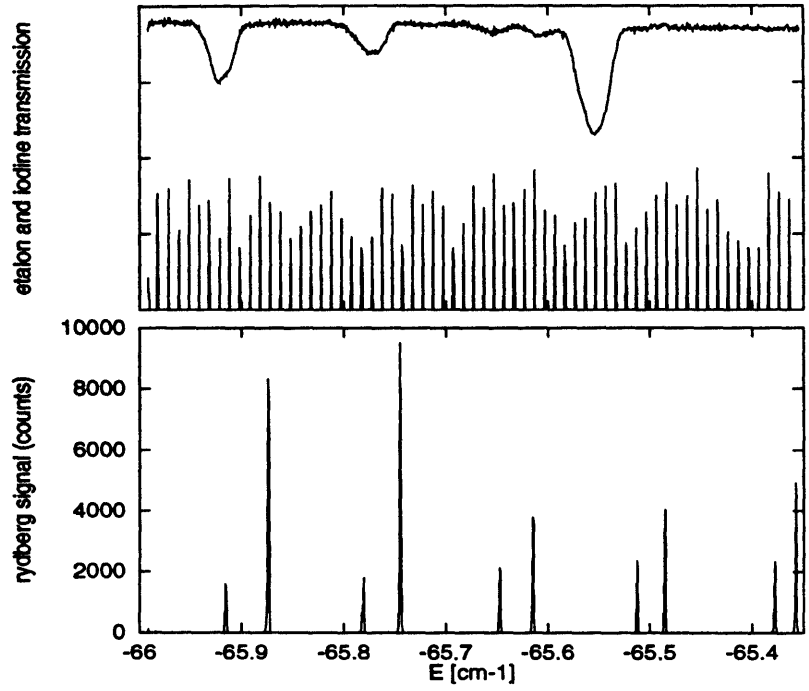

Figure 4-4: Typical laser scan showing iodine and etalon absorption and Rydberg atom signal. Energies are assigned by using the etalon to extrapolate from an iodine line. The Rydberg signal is an $m = 0$ Stark spectrum near $F = 25\,V/cm$.

which is close to the resolution of the experiment. The experimental resolution is limited by several effects of similar magnitude. Doppler broadening contributes up to $12\,MHz$ to the experimental linewidth. The width of the $3S$ level contributes $8\,MHz$. Laser jitter contributes $1\,MHz$. The natural linewidth of Rydberg levels can be neglected. The finite time the atom spends in the laser path also contributes roughly $10\,MHz$ to the linewidth. The convolution of these broadenings yields an experimental linewidth of roughly $25\,MHz$.

4.5 Excitation and Detection

Atoms in the $3S$ state are detected by cascade fluorescence. Fluorescence is collected in a plexiglass light pipe which exits the vacuum through an o-ring seal provided by an ultra-torr connector. The light pipe is then coupled into a $10'$ fiber bundle which

is coupled into a photomultiplier tube (PMT) for photon counting.[2] The photons are passed through a narrow bandpass filter centered at $670\,nm$ (the wavelength of the $2P \rightarrow 2S$ transition.) and focused on the photocathode. This filters out over 99.9% of the light noise from the room and scattered laser light, and passes about 25% of the fluorescence. The PMT has a red sensitive, low dark noise photocathode and has a gain in the $10^6 - 10^7$ range. When cooled, it gives about $5\,counts/s$ dark current. We operate the PMT in counting mode. A Modern Instruments Technology model FT-100 pre-amplifier/discriminator is used to convert pulses from the anode to TTL pulses for counting by our data acquisition system.

We can estimate the $3S$ detection efficiency by multiplying the percent of solid angle used in collection by the transmission from the light pipe to the PMT. Without the aid of collection mirrors (in the electric field interaction region) a $0.5''$ diameter light pipe located $1''$ from the interaction volume subtends about 6% of the solid angle. There is a 50% transmission into the fiber bundle, a 25% transmission over the length of the fiber bundle, a 25% transmission through filters, and a 15% quantum efficiency. Multiplying these gives an estimated efficiency of $3 \cdot 10^{-4}$.

We can also estimate the $3S$ detection efficiency by comparing the number of detected $2P \rightarrow 2S$ photons with the number of detected Rydberg atoms when enough Rydberg atoms are produced to decrease the $3S$ fluorescence. Using the field-free $31P$ state and with a good overlap of the lasers, we observe a 30% depletion of the detected $3S$ signal, indicating an excitation rate of 30% at the $3S \rightarrow 31P$ transition. Typical numbers are $10^4\,counts/s$ of fluorescence photons detected and $3 \cdot 10^6\,counts/s$ of $31P$ atoms detected. The quantum efficiency of the channeltron is about 30%, so about $10^7\,counts/s$ are being made. This implies $3 \cdot 10^7\,s^{-1}$ $3S$ atoms. Making $3 \cdot 10^7\,s^{-1}$ $3S$ atoms and detecting $10^4\,s^{-1}$ implies a detection efficiency of about $3 \cdot 10^{-4}$, which is in agreement with our other estimate. It is probably accidental that we obtain good agreement here. I expected an error of a factor of about four due to uncertainties in quantum efficiencies and transmission coefficients.

[2]The PMT is located $10'$ away from the magnet because it cannot be operated in a magnetic field.

Various interaction regions are employed, depending on the experiment being performed. There is a consistent design philosophy which has been developed through the trials and errors of my predecessors and myself. The goals of the interaction region are:

- Allow the atomic beam to pass through while shielding the atoms from the ionizing electric field.
- Provide for collection of cascade fluorescence for detecting $3S$ atoms.
- Minimize light noise also collected.
- Minimize stray electric field.
- Provide for applying an optional electric field.

For shielding the atoms from the ionizing field, it is sufficient to have the atoms pass through a $3\,mm$ hole in $3/8''$ aluminum when leaving the interaction region. Cascade fluorescence is collected in a light pipe. All of the surfaces are covered with aerodag (graphite) which reduces scattered light and provides a uniform conducting surface which reduces the stray electric field.

The magnetic field interaction region is shown in Figure 4-5. The mirrors increase the solid angle of light collection. The bottom mirror focuses light back on the interaction volume. The top mirror focuses light into the light pipe. The first $2''$ of the light pipe is a polished aluminum tube. The plexiglass light pipe fits into the aluminum tube. This peculiar construction was the last step in a long effort to reduce the stray electric field. Having the plexiglass rod at the bottom mirror was adding about $30\,mV/cm$ to the stray electric field. Another important consideration for attaining low stray fields was adding a heater to the interaction region for baking water and hydrocarbons off of the surfaces. A final factor is the distance of the closest surface to the interaction volume. When the electric field plates are installed, this distance is about $0.5''$, and the stray field is about $20\,mV/cm$. Without the field plates, we have measured stray fields as low as $1\,mV/cm$.

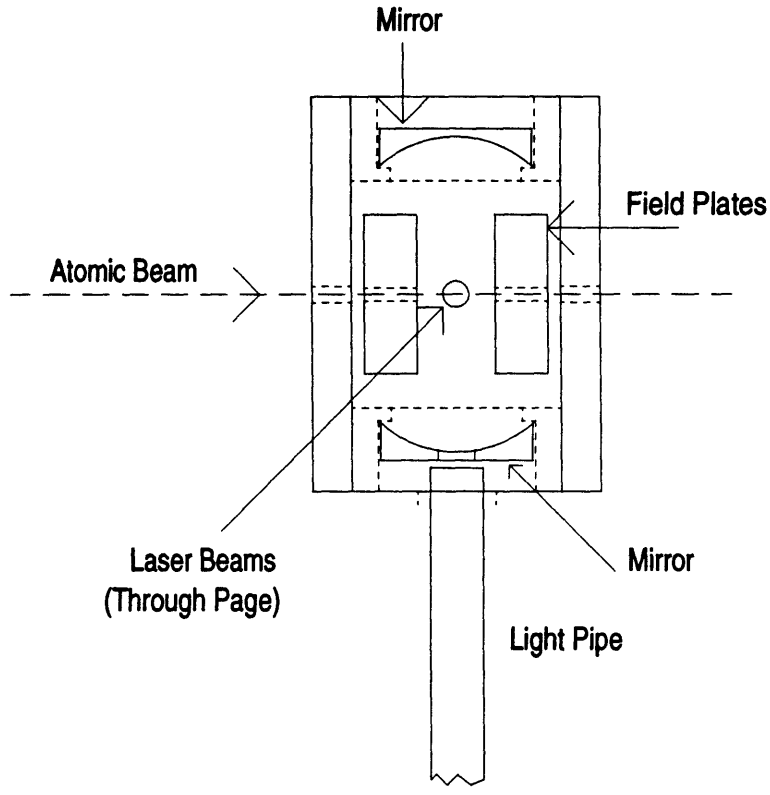

Figure 4-5: Magnetic field interaction region. The atomic beam intersects the lasers at the center of the interaction region. Cascade fluorescence is collected by two mirrors and focused into a light pipe. The atoms drift out of the interaction region and Rydberg atoms are detected by electric field ionization. Optional field plates can be installed if an electric field is also desired.

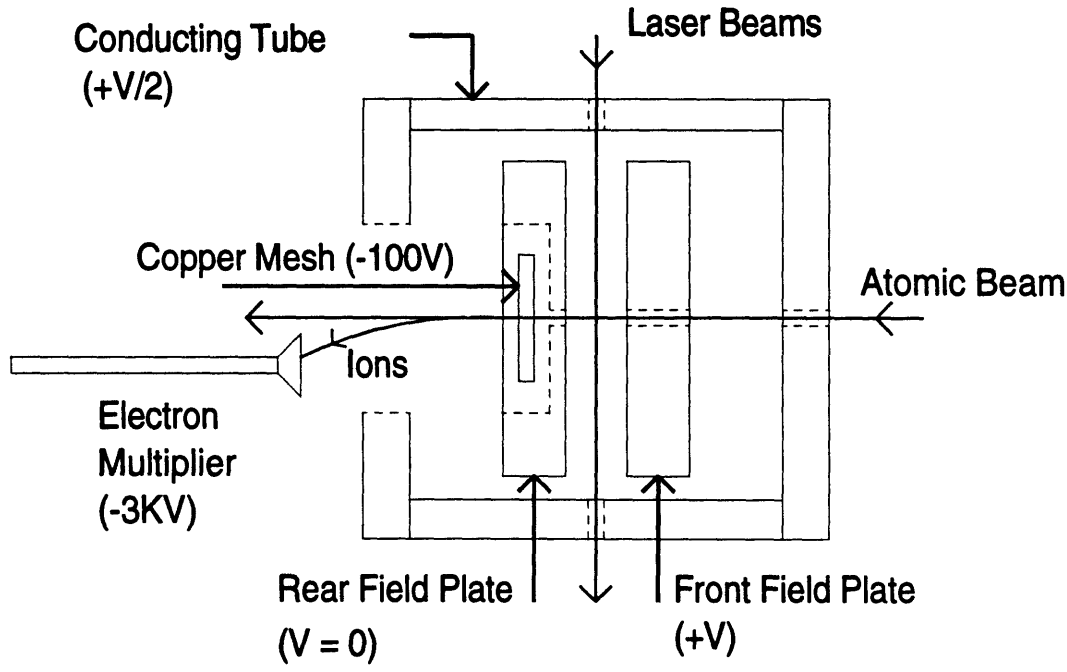

Figure 4-6: Electric field interaction region. The atomic beam enters the interaction region and passes through a 0.125″ hole in the front field plate. The atomic beam intersects the lasers between the field plates and exits through a hole in the rear field plate. The interaction region is electrically isolated from the vacuum chamber so that a symmetric biasing scheme can be employed with a single high voltage supply. The front field plate is biased at $+V$, the interaction region walls at $+V/2$, and the rear field plate is at ground. There is an ionizing grid inside the rear field plate, so that the atoms are ionized after traveling only 0.125″ into the rear field plate. The channeltron is biased at $2-3.5\,KV$ and is located off-axis to avoid the atomic beam.

The electric field interaction region is shown in Figure 4-6. The main design goal was to be able to detect Rydberg states both below the saddle point ionization limit ($\epsilon_F = -2.0$), and states which ionize before drifting out of the interaction region. The biasing scheme is designed to accelerate ions out of the interaction region should ionization occur.

After the atoms are excited by the yellow laser, they drift into a high field region where they are ionized by a strong static electric field. In principle, either ions or electrons can be detected with a suitable charged particle detector. In practice, we detect ions because we see several hundred counts per second of background when detecting electrons.

A channel electron multiplier (channeltron) was used for the electric field experiments. A young channeltron in good condition has a gain of $10^6 - 10^7$ when biased at $-2\,KV$. An older channeltron requires a larger bias to achieve the same gain, but otherwise operates just as well. For detecting ions, the channeltron is biased at -2 to $-3.5\,KV$ (depending on age) in front, and grounded in the rear. The anode is connected to a Modern Instruments Technology model FT-100 preamplifier/discriminator which converts pulses from the anode to TTL pulses for counting by our data acquisition system.

Because the gain of a channeltron drops to zero in a magnetic field of several hundred gauss, a microchannel plate assembly (MCP) is used to detect ions in the magnetic field experiments. The MCP consists of three microchannel plates stacked together and gives a gain of 10^8 when biased at $-3\,KV$ in zero field. The gain drops rapidly as the magnetic field is increased and is 10^5 when the field at the center of the magnet is $1\,T$. The MCP is located on the atomic beam axis and is $6''$ from the center of the magnet. The field at this point is 1/3 of its central value. The gain drops slowly from 10^5 to 10^4 as the central field is raised from 1 to $4.5\,T$. Above $4.5\,T$, the MCP becomes very noisy, and remains noisy for about a day afterward.

The number of Rydberg atoms detected is normalized to remove variations in the laser power and the number of $3S$ atoms produced. A signal proportional to the laser power is obtained by splitting a portion of the yellow laser into a photodiode.

The number of Rydberg atoms detected is divided by the laser power and by the fluorescence signal to obtain a normalized Rydberg signal.

4.6 Data Acquisition and Computer Control

In order to facilitate data acquisition, I have put together a system using a 386 personal computer and several data acquisition boards. Several digital to analog converters provide control of the laser frequencies, field plate voltages, magnet current, and other things which can be controlled with a small voltage. Counters record TTL pulses corresponding to Rydberg atoms and $3S$ atoms. Two analog to digital converters are used to measure voltages corresponding to iodine cell transmission, etalon transmission, laser power references, magnet current, field plate voltages, and other small analog signals. The data taking software graphically displays selected measurements while scanning the yellow laser. In this way, the user can immediately view the data being collected. Full documentation of the data acquisition system is provided in the user's and programmer's guides [COU94a, COU94b].

4.7 Spectroscopy at Constant Scaled Energy

The advantages of obtaining spectra at constant scaled energy are described in Chapter 6. Here, I will describe the details of how it is done.

The electric field case is simplest. It requires constant $\epsilon_F = EF^{-1/2}$. This is accomplished by scanning the yellow laser over the desired energy interval while applying the appropriate voltage to the field plates so that $\epsilon_F = EF^{-1/2}$ is constant. A typical scan is $0.7\,cm^{-1}$ long. Typically, about 20 single scans over adjacent energy ranges are concatenated to give a constant scaled energy spectrum which covers roughly $15\,cm^{-1}$. This energy range is typically somewhere in the $-65\,cm^{-1} < E < -30\,cm^{-1}$ range which corresponds to $40 < n < 60$. The applied electric fields vary from $2\,V/cm$ to $1000\,V/cm$, depending on the scaled energy under study.

Maintaining constant ϵ_F requires knowing the energy at every point in the scan

during the scan. This is accomplished by using the computer to first scan the yellow laser quickly over the desired energy interval while recording the iodine absorption and etalon transmission. This information is used to compute the energy of every point in the scan. The laser is then scanned again while a control voltage is used to apply voltage to the field plates so that a constant scaled energy is maintained.

The applied electric field the atoms feel is a linear function of the control voltage. The ratio of field plate voltage to electric field is measured by looking at the Stark splitting of the $n = 31$ manifold at a field near $50\,V/cm$. By using several of these measurements, we can obtain the field to voltage ratio to better than 0.1%. The linear relationship between the control data and the field plate voltage is obtained at the beginning of the day by stepping through the range of control data and measuring the voltage on the field plates with a Keithley digital multimeter. A least-squares fit of this data yields the slope and offset of this linear relationship. Obtaining the plate voltage as a function of control data in this way avoids the need to tweak offsets and gains of several amplifiers. The field plate voltage as a function of control data is constant over the course of a day to much better that 0.1%, but it can change over the course of a week or two. The 12 bit digital to analog converter has an accuracy and precision of one part in 4096. Low pass filters with a $50\,ms$ time constant smooth out the discrete steps and provide filtering of the $60\,Hz$ noise that is ever present in the lab.

The large inductance of the magnet makes maintaining constant $\epsilon_B = EB^{-2/3}$ more difficult. In contrast to the electric field experiment, where we know the energy and can (nearly) instantaneously set the field by applying a voltage to a pair of field plates, now the magnet runs the show, and we must adjust everything else accordingly. The inductance of the magnet is about $112\,henries$. If a constant voltage is applied across the leads, the current will change according to the inductance equation,

$$\frac{dI}{dt} = \frac{V}{L}. \tag{4.1}$$

The magnetic field is proportional to the current to a very good approximation. We

have not been able to detect a deviation from linearity. By studying the Zeeman splitting of the $n = 21, m = \pm 1$ levels, we have measured the field to current ratio to be $0.115855 \pm 0.0005\, T/A$. As a result, we can quickly measure the field by measuring the current through the magnet. Measuring the field quickly is important for obtaining constant scaled energy spectra because we have to know the field at every data point to be able to set the laser frequency. We typically record a data point every $25 - 100\, ms$.

To quickly measure a current of up to $50\, A$ the current is passed through a shunt resistor which is a thin piece of conducting alloy with small temperature coefficient and a calibrated resistance. Typically one obtains $100\, mV$ across the shunt at full current. We have shunts rated for $5\, A$, $25\, A$, $50\, A$, and $75\, A$. The voltage across the shunt is amplified and read by a 16 bit analog to digital converter. The linear relationship between the current and digital reading is obtained by stepping the current supply through a number of values and reading the current directly with the Keithley digital multimeter and the voltage across the shunt with the a/d. This data is fit to a line and the slope and y-intercept are used to obtain the current from measuring the voltage across the shunt. Here again, doing a least-squares fit avoids the need to tweak offsets and gains of several amplifiers and also avoids the need to measure the shunt resistance accurately.

In practice, it is not sufficient to make a single reading of the a/d and compute an accurate current value. Many a/d readings are averaged together. In addition, we gain additional averaging by fitting to the measured field values of the last 100 data points (as a function of time), and extrapolating the value of the next point to set the laser frequency. Simpler techniques were tried, but this method is the most accurate, and yields an instantaneous field measurement with accuracy better than 0.1%.

Once spectroscopy at constant ϵ_B is achieved, adding a parallel electric field to maintain both ϵ_B and ϵ_F constant is trivial. Once we have set the laser for constant ϵ_B, we simply set the field plate voltage for constant ϵ_F using the same technique as in the electric field experiments.

Chapter 5

Energy Level Statistics and Quantum Chaos

They worshiped their idols, which became a snare to them. They sacrificed their sons and their daughters to demons. They shed innocent blood, the blood of their sons and daughters, whom they sacrificed to the idols of Canaan, and the land was desecrated by their blood. They defiled themselves by what they did; by their deeds they prostituted themselves.–Psalm 106:36-39

Statistical measures of quantum chaos were born out of a desire to quantify spectral features of complex systems. Random-matrix theory [MEH67] was developed in an attempt to characterize spectra of complex nuclei. The remarkable result is that the statistical properties of many systems with unknown Hamiltonians can be predicted using random matrices of the proper symmetry class. Furthermore, random matrix theory also correctly predicts statistical properties of the eigenvalues of many chaotic systems with known Hamiltonians. This makes it useful as a tool for characterizing spectra which require large numerical efforts to compute.

This chapter compares spectra of Rydberg atoms in strong fields with some predictions of random matrix theory. The claims concerning the usefulness of the nearest-neighbor distribution are discussed, along with its practical application to Rydberg

spectra. Diamagnetic hydrogen is then used as a test case which shows the expected behavior, followed by diamagnetic lithium which can deviate from the expected behavior. Comparisons using lithium in an electric field and Rydberg atoms in parallel fields are also presented.

5.1 Claims and Application of Nearest-Neighbor Distribution

A number of statistical measures are available for quantifying spectral features in a simple way. It is of great interest whether or not there are universal statistical behaviors of classically chaotic systems. The statistical tests mentioned here are empirical in that no one has shown from first principles that they should be universal.[1] I will concentrate on the nearest-neighbor distribution (NND) of energy levels because it is the simplest to apply and interpret, and it has been widely used. Furthermore, many other statistical tests of quantum chaos depend on the proper behavior of the nearest-neighbor distribution.

The qualitative observations of level repulsions made in Chapter 2 can be quantified and related to the classical dynamics using energy-level statistics. Energy-level statistics is believed to be an important signature of classical dynamics in quantum systems [BET77, BOG84]. It is thought that regular classical dynamics is manifested by a Poisson distribution of energy levels. In addition, systems which display chaotic classical motion are expected to be characterized by the statistics of random matrix eigenvalue ensembles.

For systems invariant under time reversal, the energy-level statistics of a number of chaotic systems have been shown to be in good agreement with the predictions of the Gaussian orthogonal ensemble (GOE) of random matrices [BOG84, DEG86a, WIF86b], and it has been suggested that this phenomenon is generic for all chaotic

[1] Berry and Tabor [BET77] have put forward strong arguments for a Poisson distribution in the case of regular motion. However, there have been no rigorous results for connecting chaotic classical motion with the statistics of random matrix ensembles.

systems with this symmetry [BGS84]. If the normalized spacing between two energy levels is s, the normalized distribution of spacings is well approximated by

$$P(s) = \frac{\pi}{2} s e^{-\pi s^2/4}, \tag{5.1}$$

which is the Wigner distribution. Other statistical measures such as the $\overline{\Delta}_3$ statistic of Dyson and Mehta [MEH67], curvature statistics [ZAD93], anticrossing statistics [ZDK93], and a parametric generalization [SHC93] have also been used.

Several methods have been proposed to quantify the amount of chaos in a system from the nearest-neighbor distributions [HRW89]. These are continuous deformations of a Poisson distribution (for regular motion) into the Wigner distribution as a parameter is varied from 0 to 1. One method is fitting the nearest-neighbor distribution to a function of the form [BRO73]

$$P(s, Q) = (Q+1)\alpha s^Q e^{-\alpha s^{Q+1}}, \tag{5.2}$$

where

$$\alpha = \left[\Gamma\left((Q+2)/(Q+1)\right)\right]^{Q+1}. \tag{5.3}$$

This distribution, called the Brody distribution, tends to the Poisson distribution for $Q = 0$ and to the Wigner distribution for $Q = 1$. Q is supposed to indicate the amount of chaos in the classical system. This distribution has been successful in showing that some systems which display a transition from regular motion to hard chaos have a nearest-neighbor distribution which displays a transition from Poisson to Wigner, but Q has not been quantitatively correlated to some measure of chaos in the classical system in a satisfying manner. Consequently, I will only use it when it is necessary to quantify deviations from the Wigner distribution.

The NND is simple to compute once one has a spectrum of eigenvalues at a given field. The average level spacing, $< \Delta E >$ is computed by explicitly averaging the spacings in a given energy interval. A given spacing s_i is $(E_i - E_{i-1})/ < \Delta E >$. Then the number of level spacings in each bin is computed. This process may be

repeated at a number of fields to reduce the statistical errors in the distribution. The probability distribution is then normalized by dividing by the total area.

Several things need to be kept in mind: (i) Either the average level spacing should be constant over the interval used, or a floating average should be used. (ii) One needs to be in a region where levels from at least three different n manifolds are mixed because the NND is a measure of level repulsion and levels cannot repel until they come near each other. (iii) To compare with the classical dynamics, all averaging should be done in a region where the degree of classical chaos is nearly constant.

5.2 Diamagnetism

5.2.1 Hydrogen in a Magnetic Field

The energy-level statistics of hydrogen in a magnetic field have been extensively studied by a number of authors [HRW89]. In the regular regime, the NND shows a nearly Poisson distribution. As the scaled energy is raised so that tori are gradually destroyed and the system becomes chaotic, the NND slowly evolves into a Wigner distribution. This behavior is shown in Figure 5-1. The spectra used to compute the NND shown in Figure 5-1 were computed for many field values in the range $1\,T < B < 6\,T$ using diagonalization of the Hamiltonian in a spherical Sturmian basis, as described in Chapter 2.

Note that there are significant deviations from a Poisson distribution in the regular region ($\epsilon_B = -0.65$). Delande and Gay [DEG86c] assert that these deviations are due to the degeneracy of the zero-field energy levels and can explained by the semiclassical arguments of Berry [BET77]. This behavior is consistent with the presence of these deviations from a Poisson distribution in the NND of hydrogen in an electric field.

5.2.2 Lithium in a Magnetic Field

Welch, Kash, Iu, Hsu, and Kleppner [WKI89a] reported experimental and computational energy-level statistics of odd-parity lithium in a regime where hydrogen displays

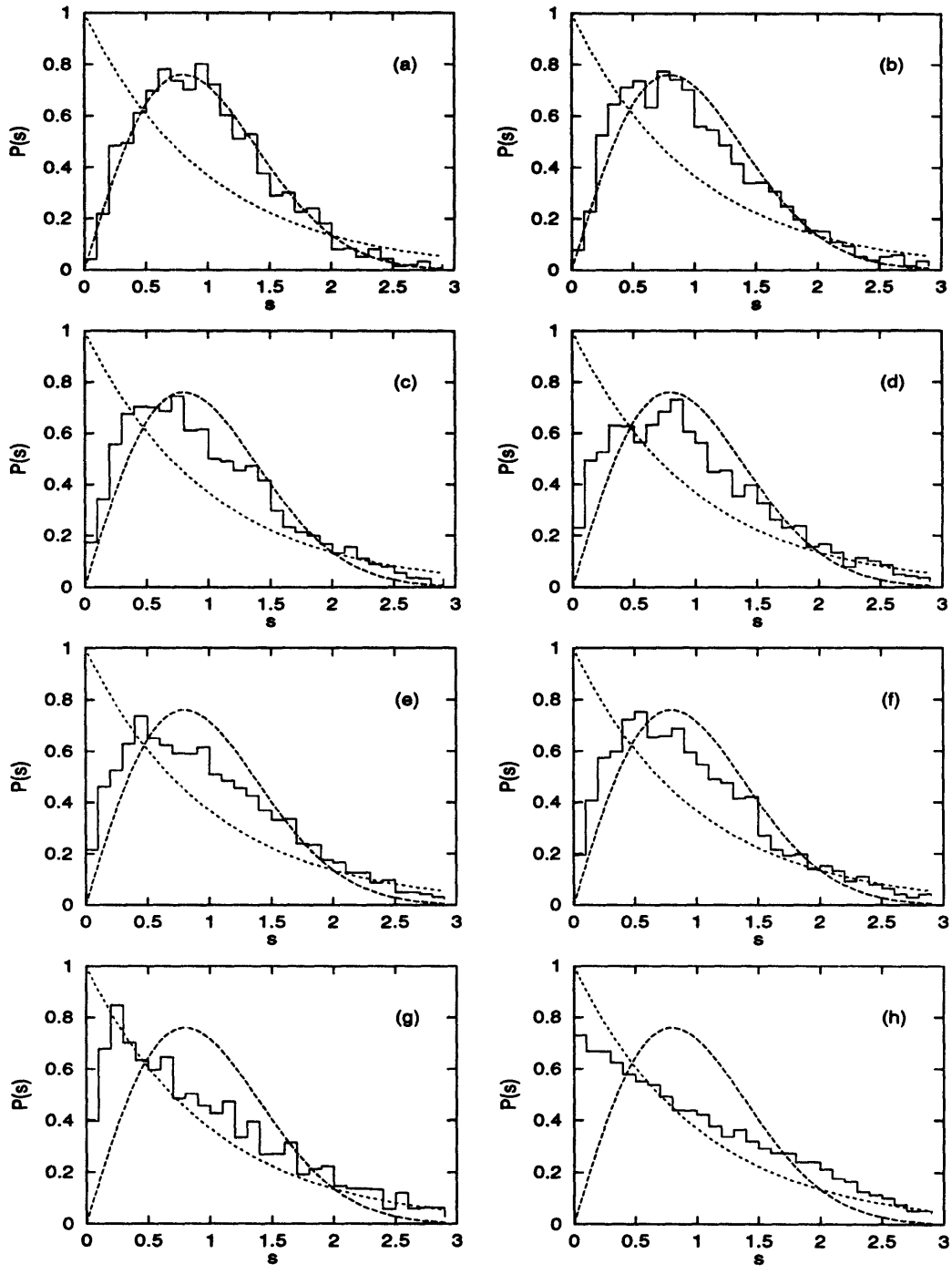

Figure 5-1: Solid lines are NND for diamagnetic hydrogen. Even-parity, $m = 0$. Notice the change in the distribution from the Wigner distribution in the chaotic regime to a nearly Poisson distribution in the regular regime. Distributions computed for scaled energies near (a) $\epsilon_B = -0.11$; (b) $\epsilon_B = -0.14$; (c) $\epsilon_B = -0.20$; (d) $\epsilon_B = -0.23$; (e) $\epsilon_B = -0.26$; (f) $\epsilon_B = -0.29$; (g) $\epsilon_B = -0.32$; (h) $\epsilon_B = -0.65$. Short dashed line is the Poisson distribution, and the long dashed line is the Wigner distribution.

regular classical motion ($-0.8 \leq \epsilon_B \leq -0.54$). They obtained essentially a Poisson distribution for odd-parity lithium in this region. They reasoned that they were probing a system whose classical motion is regular because hydrogen is regular in this region, and the diamagnetic spectrum of odd-parity lithium is nearly identical to hydrogen. We have shown that diamagnetic lithium displays hard chaos in this region. Consequently, what they thought was "the first experimental study of energy-level statistics in a regime of classically regular motion" was actually a study of energy-level statistics in a regime of chaotic classical motion. Rather than providing experimental support for the prevailing notions about energy-level statistics and classical motion, they provided experimental evidence *contradicting* the suggestion that hard chaos in a classical system implies the same nearest-neighbor distribution as the GOE.

Welch *et al.* found little difference between odd-parity lithium and hydrogen. We have used a smaller bin size than Welch *et al.* (0.1 vs. 0.2), and we have found that the odd-parity lithium distribution has a dip at $s = 0.05$ and an enhancement at $s = 0.15$. (See Figure 5-2.) This is due to the core giving a slight repulsion between closely-spaced energy levels.

A simple explanation of nearly Poisson statistics in a region of hard classical chaos is that odd-parity wavefunctions have a node in the $z = 0$ plane and little overlap with the chaos-causing core. Conservation of parity implies that the lowest angular-momentum state mixed into the odd-parity $m = 0$ spectrum is $l = 1$. As a result, the largest quantum defect is $\delta_p = 0.05$ leading to nearly hydrogenic spectra. However, conservation of parity in the quantum system does not keep the classical angular momentum from becoming small, and the classical trajectories experience the core and become chaotic.

One can prevent the classical trajectories from having $L < 1$ by imposing $L_z = 1$. The classical trajectories for $L_z = 1$ barely penetrate the core region, yet roughly 50% of the phase space is chaotic for $\epsilon_B \approx -0.6$, indicating that the core affects the classical dynamics more strongly than the quantum spectrum.

In contrast to the odd-parity spectrum, the even-parity spectrum of diamagnetic lithium has a nearest-neighbor distribution in agreement with the Wigner distribution

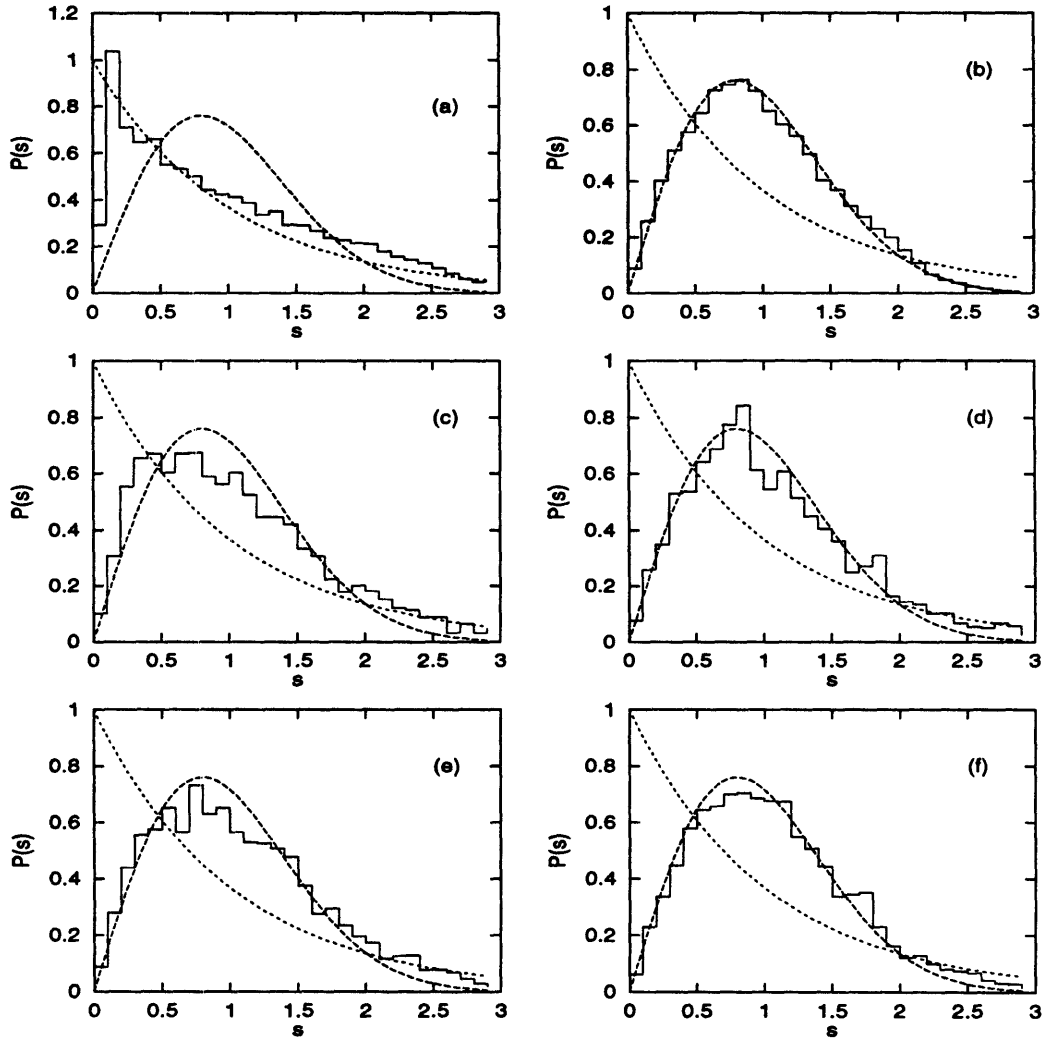

Figure 5-2: Solid lines are NND for diamagnetic lithium $m = 0$. Distributions computed for (a) $-0.75 < \epsilon_B < -0.55$, odd-parity; (b) $-0.75 < \epsilon_B < -0.55$, even-parity; (c) $\epsilon_B \approx -0.47$, even-parity; (d) $\epsilon_B \approx -0.37$, even-parity; (e) $\epsilon_B \approx -0.31$, even-parity; (f) $\epsilon_B \approx -0.21$, even-parity. Short dashed line is the Poisson distribution, and the long dashed line is the Wigner distribution. These NND were computed using many field values for $1\,T < B < 2\,T$.

for $-0.75 \leq \epsilon_B \leq -0.55$, as shown in Figure 5-2(b). This is expected because the Λ symmetry is destroyed by the core, and the even-parity basis includes states with large quantum defects ($\delta_s = 0.4$) resulting in strong level repulsion.

I have studied the nearest-neighbor statistics of even-parity lithium near some of the scaled energies shown in Figure 3-12 in an attempt to relate the NND to the reappearance of tori. At scaled energies where the phase space is completely chaotic, there is a Wigner distribution. At scaled energies where some tori have reappeared, the nearest-neighbor distribution deviates slightly from the Wigner distribution.

At $\epsilon_B = -0.47$ tori have reappeared, indicating soft chaos, as shown in Figure 3-12(a). Figure 5-2(c) shows that the nearest-neighbor distribution near this scaled energy is slightly distorted from Wigner. The distribution rises more quickly, indicating less level repulsion, and it falls off like the Poisson distribution at large level spacings, indicating a degree of randomness. The nearest-neighbor distribution near $\epsilon_B = -0.47$ can be fit by $P(s,Q)$ for $Q = 0.65(3)$, which quantifies our general observations.

At $\epsilon_B = -0.37$ there are no clearly visible tori, suggesting hard chaos, as shown in Figure 3-12(b). The nearest-neighbor distribution shown in Figure 5-2(d) is very nearly Wigner, except that it falls off more slowly at large level spacings. The nearest-neighbor distribution shown in Figure 5-2(d) has $Q = 0.87(5)$ indicating that it is close to the Wigner distribution. The strong level repulsion at small spacings and randomness at large spacings might be explained by remaining tori in the classical system which are too small to see on the scale of Figure 3-12(b). It is known that diamagnetic hydrogen near this scaled energy has many tori which occupy very small regions of phase space, and those tori which do not go near the core survive in diamagnetic lithium.

We expect $P(s)$ to deviate noticeably from the Wigner distribution for $\epsilon_B = -0.31$, because tori have reappeared in a significant fraction of phase space, as shown in Figure 3-12(c). The best-fit $P(s,Q)$ gives $Q = 0.78(4)$, indicating a significant deviation.

By $\epsilon_B = -0.21$, any remaining tori are too small to be visible in Figure 3-12(d),

and the phase space is completely chaotic. As expected, the nearest-neighbor distribution is close to the Wigner distribution (Figure 5-2(f)). The best-fit $P(s,Q)$ gives $Q = 0.97(4)$. (For comparison, the nearest-neighbor distribution of even-parity lithium for $-0.75 \leq \epsilon \leq -0.55$ has $Q = 1.00(2)$.)

To summarize, the nearest-neighbor distribution is a Wigner distribution for even-parity diamagnetic lithium in regions where the classical dynamics shows hard chaos, but there are deviations from the Wigner distribution in regions where tori reappear in the classical system. In contrast, the nearest-neighbor distribution for odd-parity diamagnetic lithium shows no relationship with the classical motion of diamagnetic lithium. Because of the small quantum defect, it is nearly identical to hydrogen.

5.3 Electric Field

5.3.1 Hydrogen in an Electric Field

Hydrogen in an electric field is an integrable system and shows a nearly Poisson NND in all regions where several n's are mixed and below the saddle node ionization limit ($\epsilon_F = -2.0$ for $m = 0$). This behavior is shown in Figures 5-3(a) and (b).

5.3.2 Lithium in an Electric Field

For $m = 0$, lithium exhibits nearly complete classical chaos for all scaled energies where several n's are mixed. Three n's are mixed at roughly $\epsilon_F = -3$ for $n \approx 45$. Nearly all the phase space is chaotic for these scaled energies, and we find that the NND's nearly agree with the Wigner distribution for $\epsilon_F = -3$, $\epsilon_F = -2.5$, and $\epsilon_F = -2$, as shown in Figure 5-3. Figure 5-3(c) shows the NND of lithium for $m = 0$ and $\epsilon_F = -3$. The NND displays a slight enhancement near $s = 0.8$ compared with the Wigner distribution. This is probably because three n's are just beginning to mix in the region where the spectra were computed. For $\epsilon_F = -2.5$, five n's are mixed, and the NND shows better agreement with the Wigner distribution, as shown in Figure 5-3(d). By $\epsilon_F = -2$, roughly seven n's are mixed, and there is good agreement with

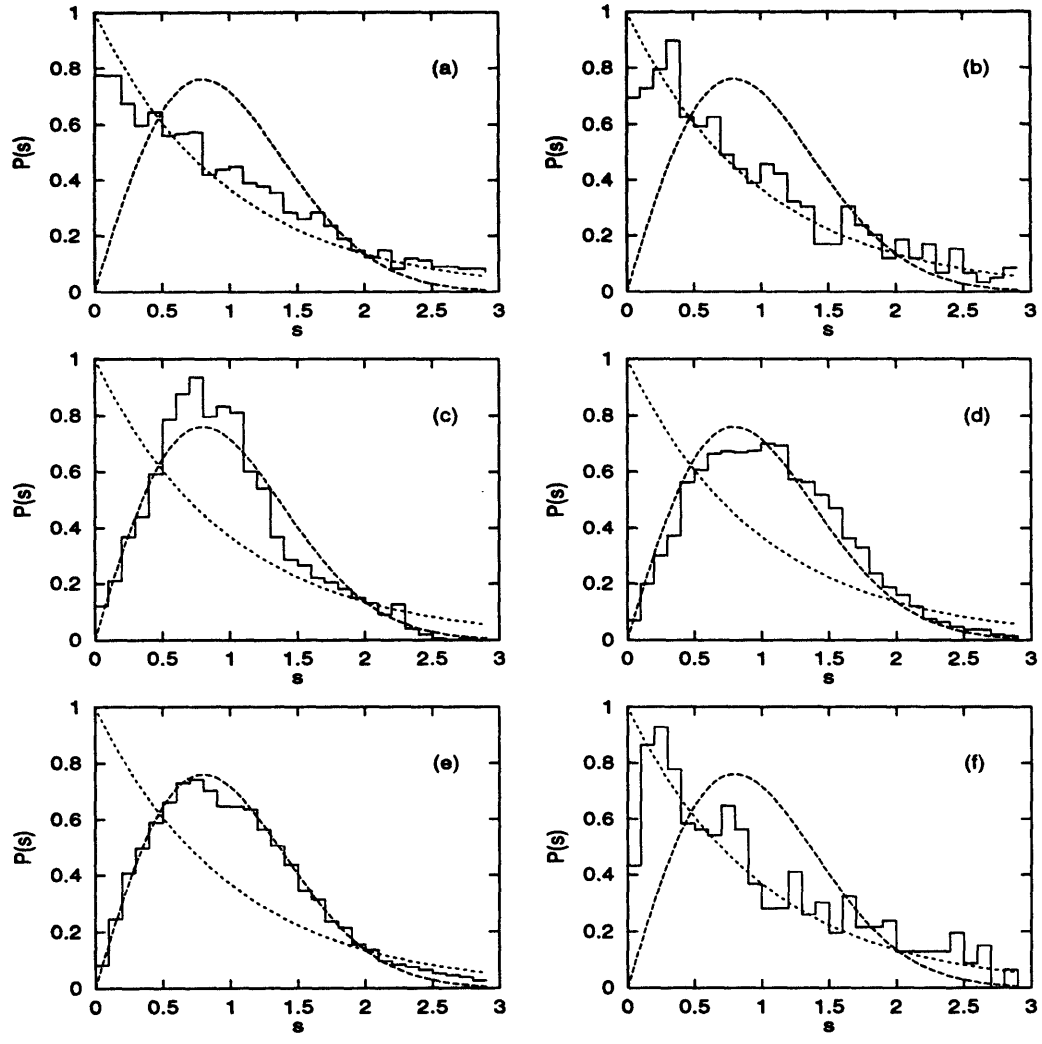

Figure 5-3: Solid lines are NND for Stark energy levels for (a) Hydrogen, $m = 0$, $\epsilon_F = -3$; (b) Hydrogen, $m = 0$, $\epsilon_F = -2$; (c) Lithium, $m = 0$, $\epsilon_F = -3$; (d) Lithium, $m = 0$, $\epsilon_F = -2.5$; (e) Lithium, $m = 0$, $\epsilon_F = -2.0$; (f) Lithium, $m = 1$, $\epsilon_F = -2.5$. Short dashed line is the Poisson distribution, and the long dashed line is the Wigner distribution. These NND were computed using many field values for $25\,V/cm < F < 50\,V/cm$.

the Wigner distribution.

The Stark spectrum of lithium is nearly hydrogenic for $m = 1$ because the angular momentum barrier prevents the wavefunction from having a substantial overlap with the core. The NND shown in Figure 5-3(f) reflects this by being in substantial agreement with the Poisson distribution, except for the dip in the first bin due to level repulsions at very small spacings. However, the classical dynamics is much more sensitive to the core for $m = 1$, and over 50% of the phase space is chaotic. The NND is similar to odd-parity diamagnetic lithium for $\epsilon_B = -0.6, m = 0$, and the NND again fails to discern the chaotic nature of the classical motion. However, in contrast to diamagnetic lithium, this failure is not complete, because the statistical expectations are weaker for systems which demonstrate soft chaos. As Berry has pointed out [BET77], it is possible for a single remaining KAM torus to cause a chaotic system to have a Poisson distribution. This makes correlating the amount of chaotic phase space with the NND effective only in systems which are either completely regular or completely chaotic. Furthermore, none of the means which have been proposed for "interpolating" between a Poisson and Wigner distribution gives peaks in the NND which is higher than 1. This is a feature which we see in many of the nearest-neighbor distributions presented in this chapter. However, it is still satisfying to see the NND evolve from Poisson to Wigner as the KAM tori are destroyed.

We cannot see a gradual onset of chaos in the NND as the scaled energy is raised because lithium is already nearly completely chaotic by the time enough n-mixing has occurred to allow for a valid NND. Although it is somewhat artificial, we can observe the onset of chaos in the NND by looking at defectium (hypothetical atom with variable quantum defect) for δ_s between 0 (hydrogen) to 0.4 (lithium) for $\epsilon_F = -2.5$. The results are shown in Figure 5-4. Notice the gradual change from nearly a Poisson distribution for $\delta_s = 0.04$ to nearly a Wigner distribution for $\delta_s = 0.32$. In contrast to the gradual change in the NND as δ_s is raised, the onset of chaos is abrupt and for $\delta_s = 0.04$ most of the phase space is chaotic in our classical model.[2] The tori which

[2]Here the amount of classical chaos is sensitive to which parameter is varied to give the correct quantum defect. For comparisons with quantum mechanics it seems more reasonable to vary δ_s by

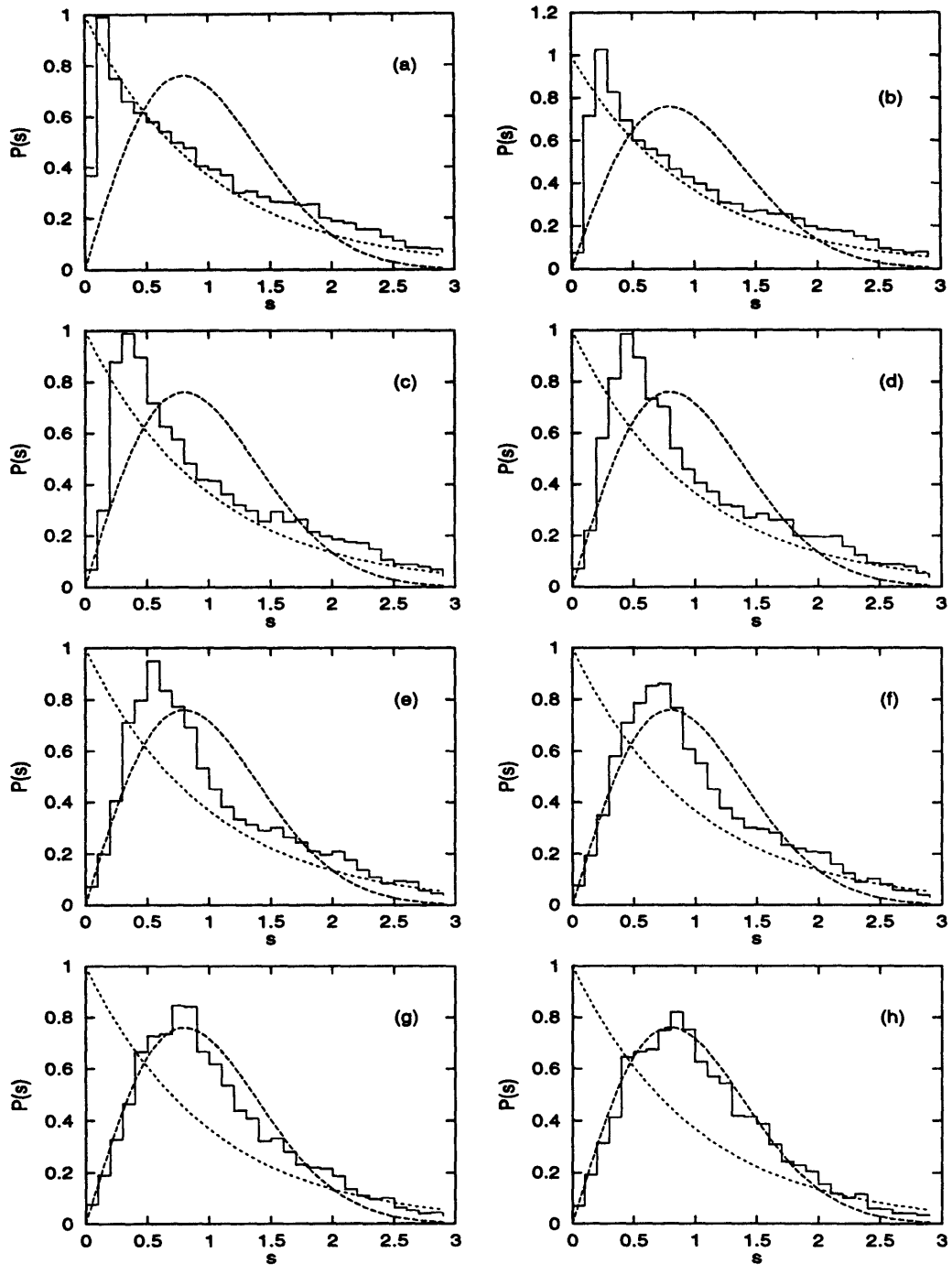

Figure 5-4: Solid lines are computed NND for $m = 0$ states of defectium in an electric field for $\epsilon_F = -2.5$. (a) $\delta_s = 0.04$; (b) $\delta_s = 0.08$; (c) $\delta_s = 0.12$; (d) $\delta_s = 0.16$; (e) $\delta_s = 0.20$; (f) $\delta_s = 0.24$; (g) $\delta_s = 0.28$; (h) $\delta_s = 0.32$. Short dashed line is the Poisson distribution, and the long dashed line is the Wigner distribution. These NND were computed using many field values for $25\,V/cm < F < 50\,V/cm$.

remain for $\delta_s = 0.04$ and $\epsilon_F = -3$ break up very slowly as δ_s is raised to 0.4.

5.4 Parallel Electric and Magnetic Fields

5.4.1 Hydrogen in Parallel Fields

As discussed in Chapter 2, hydrogen in parallel fields has an approximate constant of motion and is not a great deal more chaotic than diamagnetic hydrogen at a given ϵ_B. The system has small anticrossings for low scaled energies, and we expect the NND's to resemble a Poisson distribution. Many of them do, as shown in Figure 5-5.

I have computed parallel field spectra and NND's for a number of scaled energies below $\epsilon_B = -0.3$ and $\epsilon_F = -2$. The classical system does not demonstrate hard chaos in this region, so we do not expect a Wigner distribution. The large basis size required for computations (7200 states for the highest scaled energies reported here) prohibited computations at higher scaled energies on a PC. However, the trend in the evolution of the NND's is clear, and I expect the system to exhibit a Wigner distribution when the classical dynamics exhibits hard chaos.

The parallel field NND is closer to Poisson for $\epsilon_B = -0.6, \epsilon_F = -8$ (Figure 5-5(a)) than the diamagnetic spectrum in the regular regime. This supports Delande and Gay's assertion [DEG86c] that the deviation from a Poisson distribution for diamagnetic hydrogen is due to a zero-field degeneracy. Perturbing hydrogen with two fields is qualitatively different because it can be viewed as perturbing diamagnetic hydrogen with an electric field. Consequently, as far as the electric field perturbation is concerned, the system for $F = 0$ was not degenerate, and better agreement with the Poisson distribution is expected. The degree of chaos in the spectrum for $\epsilon_B = -0.6$ only increases a small amount as ϵ_F is raised to -2 (Figure 5-5(b)). This represents an increase in the electric field strength by a factor of 16.

The NND of hydrogen for $\epsilon_B = -0.4, \epsilon_F = -8$ (Figure 5-5(c)) is also closer to a Poisson distribution than diamagnetic hydrogen in the regular regime. At these

varying Z in the model of the core potential. One can also vary the range of the potential, $1/a$. If one makes the quantum defects small by making a larger, the system is more regular.

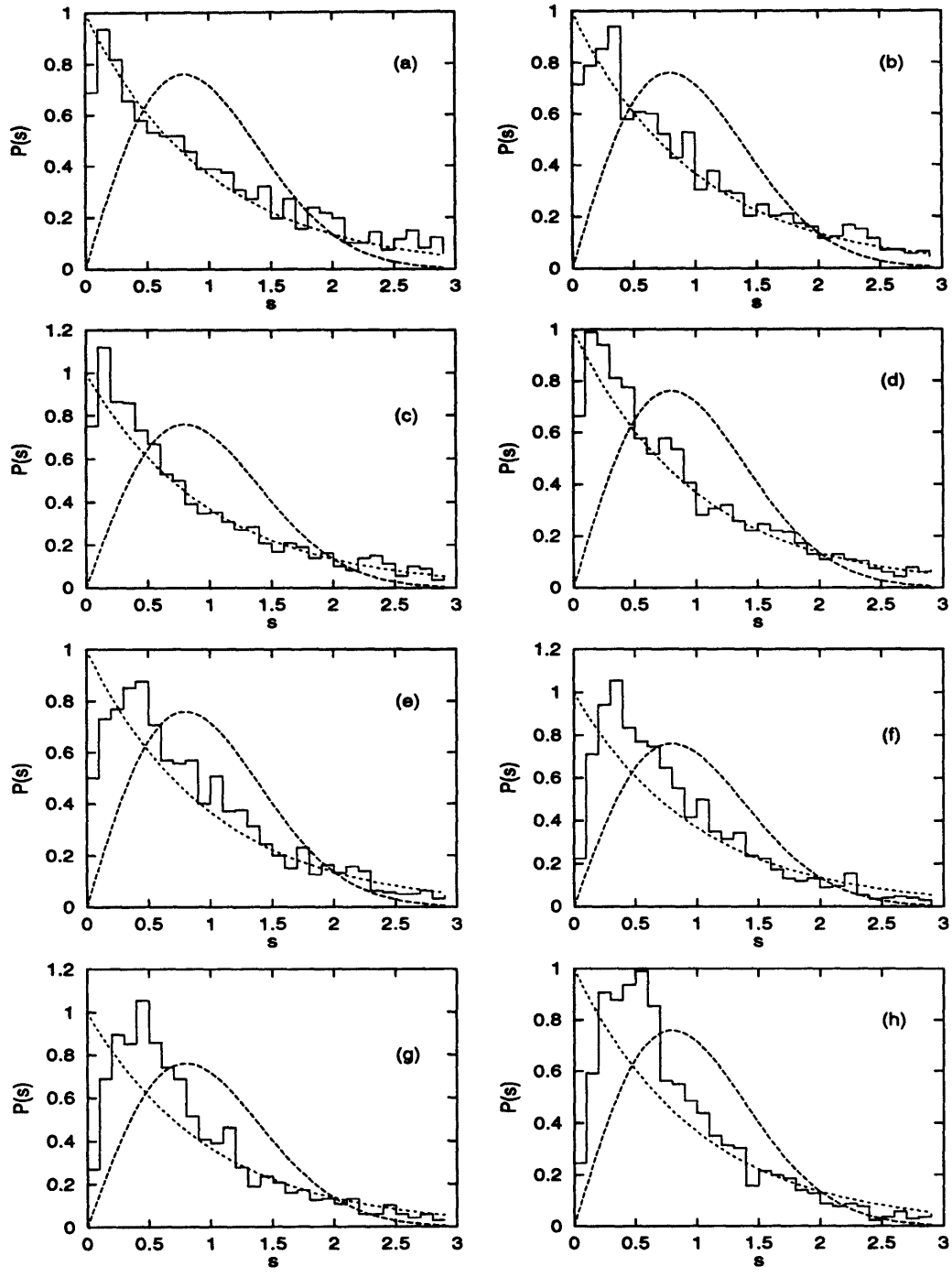

Figure 5-5: Solid lines are computed NND for $m = 0$ states of hydrogen in parallel fields. (a) $\epsilon_B = -0.6$, $\epsilon_F = -8$; (b) $\epsilon_B = -0.6$, $\epsilon_F = -2$; (c) $\epsilon_B = -0.4$, $\epsilon_F = -8$; (d) $\epsilon_B = -0.4$, $\epsilon_F = -3$; (e) $\epsilon_B = -0.4$, $\epsilon_F = -2$; (f) $\epsilon_B = -0.3$, $\epsilon_F = -6$; (g) $\epsilon_B = -0.3$, $\epsilon_F = -3$; (h) $\epsilon_B = -0.3$, $\epsilon_F = -2$. Short dashed line is the Poisson distribution, and the long dashed line is the Wigner distribution. These NND were computed using many field values for $1\,T < B < 2\,T$.

scaled energies, tori have broken up in a significant amount of phase space. As the electric field is raised to $\epsilon_F = -3$ (Figure 5-5(d)) and $\epsilon_F = -2$ (Figure 5-5(e)), the NND begins to deviate from a Poisson distribution in the direction of the Wigner distribution. Notice that the NND falls off like the Wigner distribution at large s for $\epsilon_F = -2$.

For $\epsilon_B = -0.3, \epsilon_F = -6$ (Figure 5-5(f)), there is a significant dip in the NND for the first bin ($s = 0.05$). As ϵ_F is raised to $\epsilon_F = -3$ and $\epsilon_F = -2$, the peak in the NND moves to higher s, indicating a more irregular spectrum. For $\epsilon_B = -0.3, \epsilon_F = -2$, the NND seems to be a roughly even compromise between the Wigner and Poisson distributions.

5.4.2 Lithium in Parallel Fields

Lithium in parallel fields for $m = 0$ presents difficulties in trying to characterize classical systems by their nearest-neighbor distributions. This is not unexpected since we found a large number of near-degeneracies in the quantum spectrum and largely chaotic motion in the classical system.

For $\epsilon_B = -0.6, \epsilon_F = -6$, the surface of section reveals some small tori present in a sea of chaotic motion (Figure 3-14(a)), whereas none were present in pure diamagnetic lithium at $\epsilon_B = -0.6$. However, the NND is not nearly as close to the Wigner distribution as we might have expected from the surface of section. Can such small regions of phase space really support regular eigenstates? When ϵ_F is raised to $\epsilon_F = -2$, only the slightest traces of tori are visible in the surface of section (Figure 3-14(b)). However, the NND is still not as close to the Wigner distribution as we might have expected.

For $\epsilon_B = -0.4, \epsilon_F = -8$ tori are present in a significant amount (but still less than 50%) of phase space (Figure 3-14(c)). The NND is well approximated by the Poisson distribution, except for the first bin at $s = 0.05$. When ϵ_F is raised to $\epsilon_F = -3$, the remaining tori are very small (Figure 3-14(d)). Yet the peak in the NND is much higher than the Wigner distribution, and except for the first bin, the NND is uncomfortably close to the Poisson distribution. No tori are visible for

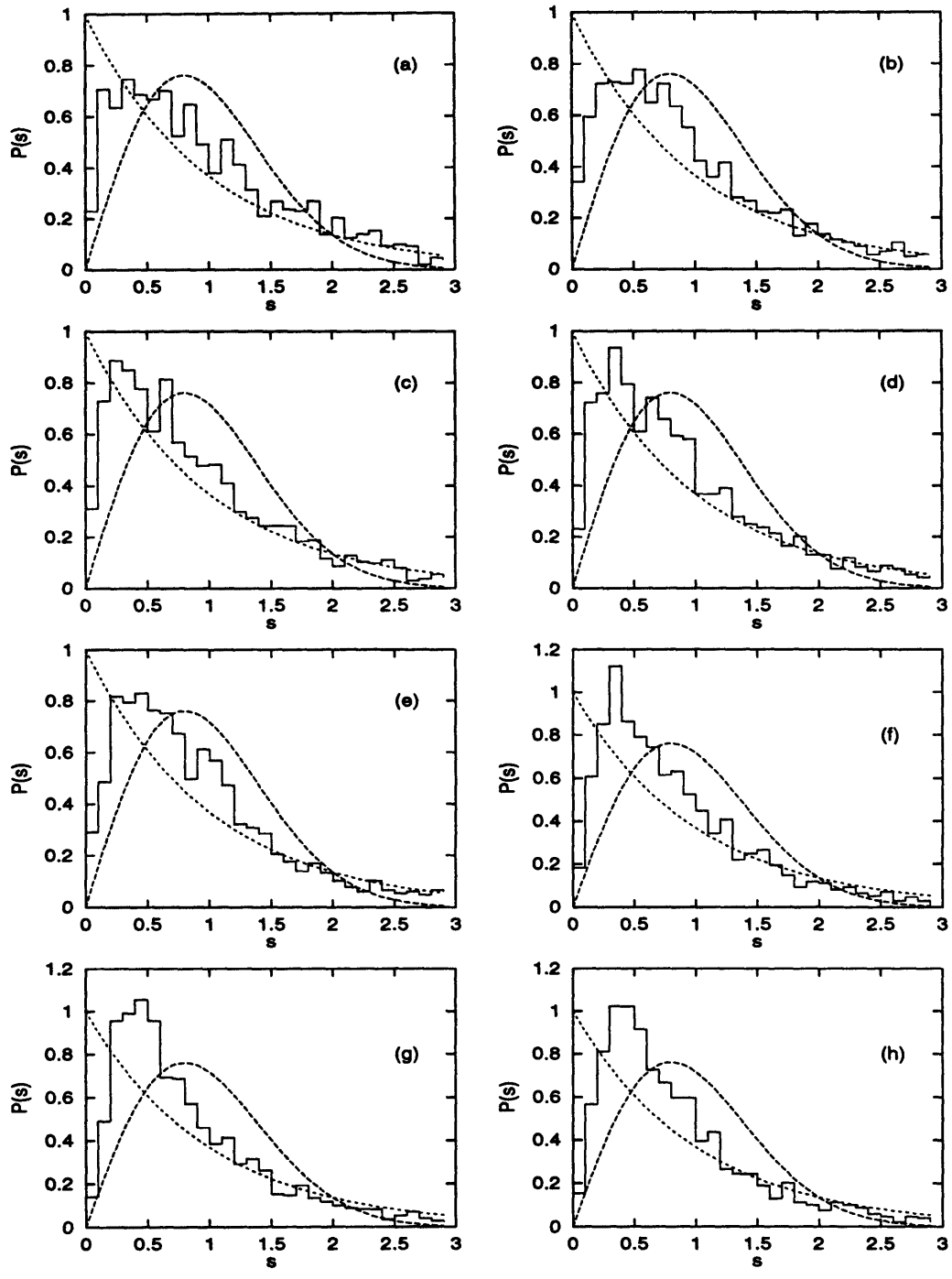

Figure 5-6: Solid lines are computed NND for $m = 0$ states of lithium in parallel fields. (a) $\epsilon_B = -0.6$, $\epsilon_F = -6$; (b) $\epsilon_B = -0.6$, $\epsilon_F = -2$; (c) $\epsilon_B = -0.4$, $\epsilon_F = -8$; (d) $\epsilon_B = -0.4$, $\epsilon_F = -3$; (e) $\epsilon_B = -0.4$, $\epsilon_F = -2$; (f) $\epsilon_B = -0.3$, $\epsilon_F = -6$; (g) $\epsilon_B = -0.3$, $\epsilon_F = -3$; (h) $\epsilon_B = -0.3$, $\epsilon_F = -2$. Short dashed line is the Poisson distribution, and the long dashed line is the Wigner distribution. These NND were computed using many field values for $1T < B < 2T$.

$\epsilon_B = -0.4, \epsilon_F = -2$ (Figure 3-14(e)). However, the NND shows marked differences from the Wigner distribution.

The surfaces of section for $\epsilon_B = -0.3$; $\epsilon_F = -6$, $\epsilon_F = -3$, and $\epsilon_F = -2$ reveal tori in small regions of phase space (Figure 3-14(f-h)). The similarities among the surfaces of section seem to carry over, and the NND's are all similar and seem like a compromise between the Poison and Wigner distributions. This is a bit comforting for proponents of the NND as a revealer of classical chaos, but it is not enough to rescue it from its failure to discern hard chaos for $\epsilon_B = -0.4, \epsilon_F = -2$ and in odd-parity diamagnetic lithium.

5.5 Summary and Discussion

The nearest-neighbor distribution works well as an indicator of the nature of the classical motion for purely hydrogenic Rydberg atoms in strong fields. However, in cases where the chaos is caused by the alkali-metal core,[3] the NND is a much better indicator of level-repulsions induced by the quantum defects than of chaos in the classical system. If energy-level statistics is to be useful in these systems, it needs to be as a measure of interactions between states and not as a means to discern the nature of the classical motion.

Energy-level statistics provide a convenient way to quantify spectral properties of many eigenvalues and correlate them with the classical motion of some systems. However, there is no guarantee that energy-level statistics reveal the nature of the classical motion, and we have found that in some cases the NND fails to discern chaos in the classical system. The NND should either be thrown away, or the claims concerning its relationship to classical chaos should be modified. It is significant that the failures of the NND occurred in systems where the chaos was caused by the alkali-metal core. Introducing the core causes an inherent breakdown of the semiclassical approximation because any trajectory close enough to the nucleus to see the core

[3]By this I mean that hydrogen has regular motion for these scaled energies, but the alkali does not.

has an angular momentum of a few atomic units. Such small angular momenta are quantized in any real physical system, and we will see in the next three chapters that the scattering of an electron from the core of an alkali-metal should be treated with a partial wave expansion.

The failure of energy-level statistics might have been anticipated because there is no complete quantitative understanding of why chaotic classical dynamics gives energy-level statistics which agree with random matrix ensembles. Empirical models which are not followed by more rigorous results often fade in importance. In contrast, periodic-orbit theory provides a well understood foundation for using the Fourier transform to identify spectral correlations which are directly related to classical trajectories.

Chapter 6

Periodic Orbit Spectroscopy

Therefore the LORD *was angry with his people and abhorred his inheritance. He handed them over to the nations, and their foes ruled over them. Their enemies oppressed them and subjected them to their power.* –Psalms 106:40-42

Large scale spectral structures display evidence of recurrences—quantum wave packets which follow closed orbits. The periodic-orbit theory of Gutzwiller [GUT90] and the closed-orbit theory developed by Delos and co-workers [DUD87, DUD88a] provide the theoretical tools for understanding large scale spectral structures in terms of classical trajectories. Periodic-orbit theory asserts that each periodic orbit produces a sinusoidal modulation of the density of states. Closed-orbit theory asserts that each orbit which is closed at the nucleus produces a sinusoidal modulation in the transition probability from a low-lying state to a Rydberg state. Consequently, the Fourier transform relates large scale spectral structures to classical trajectories. This chapter describes the basic physical picture of periodic-orbit theory and closed-orbit theory, presents their principal results, describes how recurrence spectra are computed quantum mechanically, and summarizes the approach taken in this thesis to testing these theories.

6.1 Periodic-Orbit Theory

Periodic-orbit theory gives a recipe for computing spectra from the periodic orbits of a system. In contrast to the Einstein-Brillouin-Keller method of action quantization, which applies only to integrable or near-integrable systems and computes individual eigenvalues from each trajectory, periodic-orbit theory is applicable to both integrable and non-integrable systems and asserts that each periodic orbit produces a sinusoidal fluctuation in the density of states [GUT90]. This section describes periodic-orbit theory by reviewing the basic quantum mechanical results which allow eigenvalues to be computed from the time evolution of a wavefunction and by summarizing the semiclassical approximations which are used to compute the time evolution of a wavefunction.

To understand the connection between the time evolution of the classical system and the energy levels, it is helpful to recall some basic results of quantum mechanics concerning the relationship between the energy and time domains. The time dependent Schrödinger equation is

$$i\frac{\partial \Psi(t)}{\partial t} = H\Psi(t), \tag{6.1}$$

where $\Psi(t)$ is the time dependent wavefunction and H is the Hamiltonian. If an initial wavefunction is $\Psi(0)$, then the time evolution is given by

$$\Psi(t) = e^{iHt}\Psi(0). \tag{6.2}$$

If H is a time independent Hamiltonian with eigenvalues E_n and $\Psi(0)$ is written as a linear superposition of eigenvectors $\Psi(0) = \sum_n a_n\phi_n$, then the time evolution of $\Psi(0)$ is

$$\Psi(t) = \sum_n a_n e^{iE_n t}\phi_n. \tag{6.3}$$

The overlap of the time-evolved wavefunction $\Psi(t)$ with the initial wavefunction $\Psi(0)$ (the autocorrelator) is

$$< \Psi(0)|\Psi(t) >= \sum_n a_n e^{iE_n t}. \tag{6.4}$$

Consequently, the Fourier transform of $< \Psi(0)|\Psi(t) >$ is a series of peaks whose positions give the energy spectrum and whose amplitudes give the projection of the initial state onto the eigenvectors.

This relationship between time and energy domain quantum descriptions enables us to find the energy spectrum of a Hamiltonian by computing the time evolution of an initial wavefunction and taking a Fourier transform of the autocorrelator. There are a couple of additional requirements for this to work. Our initial wavefunction must be a linear combination of all the eigenfunctions of the system. In principle, this could be a problem because we do not know the eigenfunctions beforehand. It is not a problem in practice because (aside from simple symmetry considerations) it would be difficult to choose a $\Psi(0)$ which is not a linear combination of all the eigenfunctions. Furthermore, to compute the energy spectrum, we must compute the autocorrelator to very long times. Resolving eigenvalues separated by ΔE requires computing the autocorrelator to roughly $T = 1/\Delta E$.

In practice, directly integrating the time independent Schrödinger equation to obtain the time evolution of a wavefunction for a chaotic Hamiltonian is usually more difficult than finding the eigenvalues and eigenvectors and computing the time evolution as a series over the eigenfunctions and amplitudes. However, the time domain representation provides a physical picture for connecting the energy spectrum with the time evolution of the classical system because the classical trajectories can be used to approximate the time evolution of the quantum system.

Using this physical picture to derive a formula for the eigenvalues of a system is complicated, and the details will not be repeated here. Several references give a good explanation [GUT70, GUT90, DUD88b, TOH91], but the semiclassical language and approach is initially unfamiliar to most physicists. The basic and beautiful physical picture should not be obscured by the difficult details of the derivation. The exact quantum propagator which takes a state from $\Psi(\vec{q}_1;0)$ to $\Psi(\vec{q}_2;t)$ is replaced by a semiclassical propagator which approximates the evolution of the wavefunction by a sum over all of the classical trajectories from $\vec{q}_1$ to $\vec{q}_2$ in time t. The exact time-

dependent quantum propagator is

$$K(\vec{q}_1, \vec{q}_2; t) = < \vec{q}_2 | e^{-iHt/\hbar} | \vec{q}_1 > . \tag{6.5}$$

The propagation of an initial state $\Psi(\vec{q}_1; t = 0)$ is then

$$\Psi(\vec{q}_2; t) = \int_{-\infty}^{\infty} K(\vec{q}_1, \vec{q}_2; t) \Psi(\vec{q}_1; 0)\, d\vec{q}_1. \tag{6.6}$$

The fundamental approximation is to replace $K(\vec{q}_1, \vec{q}_2; t)$ with a semiclassical approximation [GUT90, TOH91],

$$K_{sc}(\vec{q}_1, \vec{q}_2; t) = \left(\frac{1}{2\pi i\hbar}\right)^{d/2} \sum_j \left| \det \left(\frac{\partial^2 S_j(\vec{q}_1, \vec{q}_2; t)}{\partial \vec{q}_1 \partial \vec{q}_2} \right) \right|^{1/2} \exp \left(\frac{i S_j(\vec{q}_1, \vec{q}_2; t)}{\hbar} - i\pi\alpha_j/2 \right), \tag{6.7}$$

where the sum over j is for all trajectories connecting q_1 and q_2 in time t. The number of degrees of freedom is d. The classical action is $S_j(\vec{q}_1, \vec{q}_2; t)$. The phase accumulated by the wavefunction along each classical path is linear in the classical action (divided by $\hbar$) and has an additional factor—α_j, the Maslov index—to account for caustics and foci along the trajectory.

Each term in the sum over trajectories is multiplied by a semiclassical amplitude which is essentially the square root of the density of neighboring trajectories. This is called the fundamental approximation because it is the starting point for all forms of semiclassical theory for chaotic systems.

When computing an autocorrelator, the initial and final positions of the wavefunction are the same. A crucial point is that (to a good approximation) all the classical trajectories which return with a momentum different from the initial momentum interfere destructively and cancel, leaving only the periodic trajectories. Grinding through a Fourier transform gives the spectrum. The Fourier transform can also be performed at an earlier stage from which the derivation proceeds in the energy domain.

The principal result of this development is an expression for the density of states

which is the trace of the semiclassical Green's function and is given by the Gutzwiller trace formula [GUT90]:

$$g_c(E) = \sum_k T_k \sum_{n=1}^{\infty} \frac{1}{2\sinh(\chi_{nk}/2)} e^{i(nS_k - \alpha_{nk}\pi/2)}. \tag{6.8}$$

The index k distinguishes the primitive periodic orbits: the shortest period orbits of a given set of initial conditions. T_k is the period of the primitive periodic orbit and S_k is its classical action. Each primitive orbit retraces itself, leading to a new orbit with action nS_k and a period which is an integral multiple n of the primitive period. Hence, every repetition of a periodic orbit is another periodic orbit. These repetitions are separately classified in Eqn. 6.8 by the intermediate sum over the indices n. α_{nk} is the orbit's Maslov index. The amplitude factor, $1/\sinh(\chi_{nk}/2)$, represents the square root of the density of neighboring orbits. Neighboring trajectories of an unstable periodic orbit diverge exponentially in time from the periodic orbit. The quantity χ_{nk} characterizes the instability of the orbit. A stable orbit moves on a torus in phase space, and neighboring trajectories wind around it. For stable orbits, $\sinh(\chi_{nk}/2)$ becomes $\sin(\chi_{nk}/2)$, where χ_{nk} is the winding number of the periodic orbit. $\chi_{nk} = 2\pi m$, where m is the number of times that neighboring orbits intersect the periodic orbit in one period. This presents a difficulty because $\sin(\chi_{nk}/2) = 0$ at a classical bifurcation. This causes that orbit's contribution to the energy density to diverge. We shall return to this problem later in the context of photoabsorption spectra.

Using the trace formula to compute a spectrum requires summing over all of the periodic orbits of a system. This presents several difficulties for chaotic systems:

- The number of periodic orbits proliferates exponentially as a function of action.
- There are an infinite number of periodic orbits, and the convergence properties of periodic-orbit theory are unknown.[1]
- Long-period orbits are difficult to compute because most trajectories are unsta-

[1]This difficulty is also present when applying periodic-orbit theory to regular systems.

ble and sensitive to roundoff errors and details of the numerical integration.

Gutzwiller applied the trace formula to approach the anisotropic Kepler problem (a single particle in a $1/r$ potential with an anisotropic mass tensor) semiclassically [GUT70]. He found agreement with quantum computations for low lying (up to $n = 6$) states for small anisotropies by using only a small set of easily computed periodic orbits, but the agreement was poor for large anisotropies.

A key advance in the practical application of the trace formula is so-called "cycle expansions" [CVE89] which allow many long-period orbits to be approximated by a few shorter ones and specified corrections. This technique has been used in the quantization of various billiards and helium [WRT92, ERT91]. However, the general applicability and accuracy of this technique are unknown.

In this thesis, I will take an inverted approach to testing the trace formula. The trace formula asserts that each periodic orbit contributes a sinusoidal term to the spectrum. Rather than dealing with the computational difficulties surrounding long-period orbits to try and find the eigenvalues, I will compute eigenvalues and use the Fourier transform to look for the periodic modulations of the spectrum which are the signature of periodic orbits. Interpreting the spectrum then amounts to finding the orbits which correspond to peaks in the Fourier transform.

6.2 Closed-Orbit Theory

Most spectroscopic experiments measure a transition probability and not a density of states. The closed-orbit theory developed by John Delos and co-workers provides an adaptation of the principles of periodic-orbit theory which is suitable for computing transition strengths from low-lying atomic states to Rydberg states of atoms in strong fields. This approach simplifies periodic-orbit theory because only the periodic orbits which are closed at the origin need to be considered and because the theory models the excitation of a low-lying electron (localized near the origin) as a superposition of orbits beginning and ending at the origin. Furthermore, the difficulties with convergence and long-period orbits of chaotic systems are avoided because closed-orbit theory

computes an oscillator-strength density which is an average over some finite resolution ΔE. As a result, orbits with periods greater than $2\pi\hbar/\Delta E$ do not need to be included in the sum over the closed orbits.

The physical picture of closed-orbit theory is simple [DUD88b]. The atom begins in a well-localized initial state. The oscillating laser field produces zero-energy[2] Coulomb waves which propagate outward in all directions. For distances greater than about 50 atomic units, a semiclassical approximation is appropriate, and the wave can be propagated following classical trajectories. When a trajectory returns to the boundary sphere, it can be described by an incoming zero-energy Coulomb wave which propagates inward until it overlaps with the initial state. Interference between steadily produced outgoing and incoming waves leads to oscillations in the absorption spectrum.

According to closed-orbit theory, the average oscillator strength density is given by a slowly varying background plus an oscillatory sum of the form [DUD88a]

$$Df(E) = \sum_k \sum_{n=1}^{\infty} A_{nk} \sin(nS_k - \alpha_{nk}\pi/2 - \phi_{nk}), \tag{6.9}$$

where E is the energy. A_{nk}—the recurrence amplitude of a closed orbit—contains information about the stability of the orbit, its initial and final directions, and the matrix element of the dipole operator between the initial state and a zero-energy Coulomb wave. α_{nk} is the Maslov index, and ϕ_{nk} is an additional phase which depends on details of the orbit. For low resolution, where only short period orbits need to be considered, the theory has enjoyed considerable success computing spectral features of diamagnetic hydrogen [DUD87, MWW94], and sodium in an electric field [GDB92].

The derivation of Eqn. 6.9 is similar to that of the trace formula, except that the semiclassical approximations compute the oscillator strength spectrum which is the Fourier transform of the autocorrelator of the dipole operator acting on the initial state. For Rydberg atoms excited from a low-lying state, the initial state is localized so

[2]This is a reasonable approximation for Rydberg states, but there are small corrections if the final state is too far from $E = 0$.

close to the nucleus compared with the size of the atom that, to a good approximation, the initial and final positions of the classical trajectories in the sum can be taken to be at the nucleus. Consequently, only orbits which are closed at the nucleus contribute. The addition of the dipole operator into the autocorrelator makes it necessary to consider details of the angular distributions of the initial state and outgoing waves.

The classical scaling rules discussed in Chapter 3 greatly simplify the application of closed-orbit theory to Rydberg atoms in strong fields. At a fixed field, the closed orbits of a system change as the energy changes, and applying Eqn. 6.9 would require computing all of the closed orbits and semiclassical amplitudes at every energy and field independently. The classical scaling rules allow computation of the absorption spectrum at a fixed scaled energy using a single set of closed orbits.

As mentioned previously, I will take an inverted approach to testing these semiclassical theories by using the Fourier transform to look for the predicted periodic modulations of the spectrum which are the signature of classical orbits. The action S of a classical orbit scales as $S = w\tilde{S}$, where $w_B = B^{-1/3}$ and $w_F = F^{-1/4}$. Consequently, sinusoidal modulations will be most pronounced if spectra are obtained as a function of w at constant scaled energy. The Fourier transform of such a spectrum is called a *recurrence spectrum*, and each peak in the recurrence spectrum is located at the scaled action of the corresponding periodic orbit. This technique was originally used by Holle *et al.* in experiments on diamagnetic hydrogen [HMW88]. It has also been applied in studies of diamagnetic helium [VVH93], sodium in an electric field [ERW88], general Rydberg atoms in a magnetic field [MOW90], and lithium in an electric field [CJS94, CJS95].

6.2.1 Bifurcations

For Rydberg atoms in strong fields, the shape and classical properties of a given closed orbit change continuously as the scaled energy changes. In addition, new orbits spring into existence through bifurcations of existing orbits. In the magnetic field case, new orbits can appear as the scaled energy is raised. In the electric field case, new orbits can appear as the scaled energy is either raised or lowered. In general, the exponential

proliferation of periodic orbits in chaotic systems results from orbits splitting off of existing orbits or being created "out of nowhere" by bifurcations as some parameter is changed.

Understanding how orbits are created by bifurcations is key to the application of closed-orbit theory. However, bifurcations present a problem because the semiclassical amplitude diverges at a classical bifurcation. The recurrence strength is proportional to the density of returning neighbors, $1/\sin(\chi_{nk}/2)$, which becomes infinite at a bifurcation because the winding number χ_{nk} passes through a multiple of 2π. Furthermore, new orbits created by bifurcations can be seen in measurements before the bifurcation actually occurs [MWW94, KHD93].

To illustrate the bifurcation process, pictures of outgoing and returning orbits near a bifurcation are shown in Figure 6-1. Orbits which are neighbors of a closed orbit (i.e., having the same scaled energy and beginning at the nucleus, but having slightly different initial directions) form a cusp structure upon returning near the nucleus. As the energy is varied, this cusp moves along the z axis: at the bifurcation, the tip of the cusp touches the nucleus. Therefore, near a bifurcation, there is a family of neighbors which also returns to the nucleus. This focusing effect causes a large increase in the recurrence strength as the scaled energy passes through a bifurcation.

In its original formulation, closed-orbit theory diverges at a bifurcation [GAD94, MWW94]. Such divergences are familiar in geometrical optics which predicts infinite intensity if a plane wave is focused to a point. These theories are corrected by accounting for diffraction. Jing Gao and John Delos have modified closed-orbit theory to include such diffraction effects [CJS95].

For waves in one dimension, the semiclassical formula diverges at an ordinary classical turning point where the behavior of the wavefunction changes from oscillatory to exponential. This divergence is corrected using Airy's diffraction integral. The same also holds at a simple boundary between classically allowed and forbidden regions in more than one dimension. In two dimensions, it is common for such regions to come together and form a cusp, as in Figure 6-1. The associated diffraction integral is known as a Pearcey function. However, the cusp in our problem has a special sym-

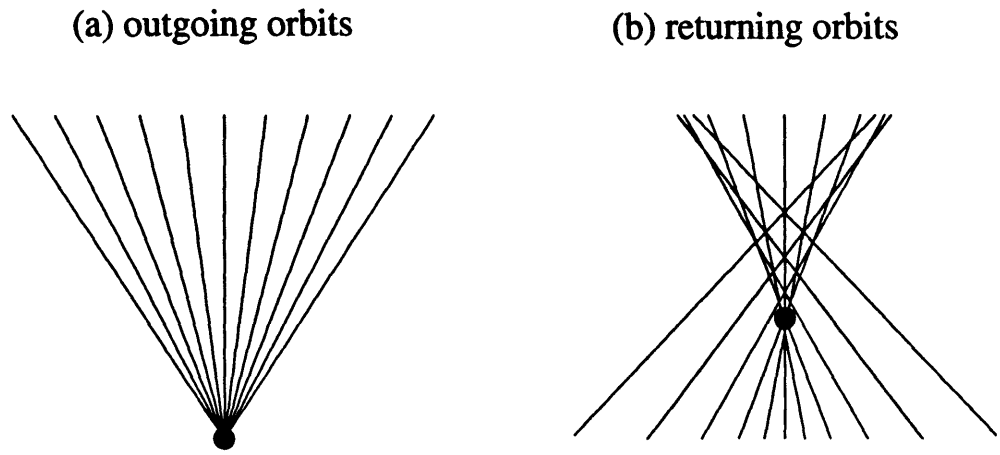

Figure 6-1: Cusp structure associated with a family of (a) outgoing and (b) returning orbits near a bifurcation in semiparabolic coordinates. (Figure courtesy of Jing Gao.)

metry: the axis of the cusp coincides with the direction of the electric field, so the cusp is actually three-dimensional and cylindrically symmetric about the vertical axis in Figure 6-1. Such cusps are produced by an optical lens, and they cause spherical aberration of a point image. The diffraction function that describes them is a Fresnel integral [PAR89].

The cusp in our problem has yet another symmetry. The cusp in Figure 6-1 is cylindrically symmetric not only about the vertical axis through the nucleus, but also about the horizontal axis through the nucleus. The formulas that describe this cusp make use of the close connection between a hydrogen atom and a four-dimensional harmonic oscillator. The cusp shown in 6-1 is a slice through a structure that exists in a four-dimensional extension of the (u, v) space.[3] This peculiar feature is a result of the cylindrical symmetry about the z axis and the fact that the positive and negative z axes are perpendicular to each other in semiparabolic coordinates. As a result, a four-dimensional space is needed to describe the symmetry in semiparabolic coordinates.

In spite of the complexity of the cusp, the behavior of the recurrence strengths

[3]Semiparabolic coordinates, (u, v), are described in Chapter 3.

near a bifurcation is simple. The basic result is that: (i) the recurrence strength is small but non-zero before the classical bifurcation because of wave diffraction effects or tunnelling into the classically forbidden region; (ii) as expected, the recurrence strength is finite at the bifurcation; (iii) the recurrence strength has its maximum after the bifurcation, just as waves are largest slightly inside of a classically-allowed boundary. As described in Chapter 8, our experiments on lithium in an electric field provide the first experimental verification of this behavior and the new formulas describing this process [CJS95].

6.2.2 Core-Scattered Recurrences

The original formulation of closed-orbit theory predicts recurrences at the scaled actions of closed orbits. This general behavior has been confirmed in both hydrogenic and non-hydrogenic systems [MWW94, ERW88]. However, in addition to the expected recurrences, non-hydrogenic systems also display recurrences which are not located at the scaled action of a closed orbit [DTH94, CJS94]. These extra recurrences are located at scaled actions which are the sum of two or more closed orbits.

The scattering of an incoming wave from one closed orbit into another was predicted by Gao and Delos [GAD92]. For a purely $1/r$ potential, the incoming wave following a closed orbit is backscattered, and it propagates away from the nucleus in the same direction from which it came. For potentials which deviate from $1/r$, the incoming wave is not only backscattered, but a component of the wave is scattered in all directions. As a result, it then propagates along all of the closed orbits of the system. Consequently, recurrences occur at the scaled actions of closed orbits and also at the sum of actions of any combination of closed orbits.

This represents an important modification in closed-orbit theory because it introduces many more terms in the sum. All possible permutations and combinations of closed orbits need to be considered, and accurate amplitudes and phases need to be computed for all of the possible permutations and combinations of orbits. The

recurrence produced by scattering orbit i into orbit j should have an amplitude,

$$A_{i+j} \propto A_i A_j P_{\theta_i,\theta_j}, \tag{6.10}$$

where A_i and A_j are the amplitudes of the i and j orbits and P_{θ_i,θ_j} is the scattering probability from the incoming angle of i to the outgoing angle of j. There will also be recurrences generated by multiple scatterings. The basic physical picture is easy to understand, and John Shaw of William and Mary has preliminary results which include this effect into closed-orbit theory (private communication).

Small core-scattered recurrences have been identified in the odd-parity diamagnetic helium spectrum [DTH94]. We will identify large core-scattered recurrences in even-parity diamagnetic lithium and show that all possible combinations of recurrences are present at low action. We will also identify core-scattered recurrences in experimental spectra of lithium in an electric field and describe the role that core scattering plays in the evolution of the recurrence spectrum. And finally, by counting recurrences, we will use core-scattering as the basis for determining whether a system is chaotic.

6.3 Computing Recurrence Spectra

Testing semiclassical methods by quantum computation is generally not as persuasive as direct experimental verification. However, unlike quantum computations on model systems with no experimental counterparts, the quantum mechanical methods used to compute spectra of Rydberg atoms in strong fields have been experimentally verified (See Chapter 2 and references therein.) Reliable quantum computations are now available in many regimes of Rydberg atoms in strong fields, and testing semiclassical methods against quantum computations is cheaper and easier in many cases than performing the experiments. Furthermore, obtaining a spectrum at constant scaled energy can be done much more accurately numerically than experimentally, and computing accurate transition probabilities does not require long integration

times. In short, quantum computations provide for more thorough testing of semiclassical methods and should not be shunned.

As previously discussed, sinusoidal modulations will be most pronounced if spectra are obtained at constant scaled energy. To compute spectra at constant ϵ, the Hamiltonian matrix is diagonalized at closely spaced field values (as explained in Chapter 2), and energy levels and oscillator strengths are obtained in the ranges where the scaled-energy spectra are desired. The energy levels, $E_i(B)$ (or $E_i(F)$), and oscillator strengths, $f_i(B)$, (or $f_i(F)$) are obtained as continuous functions of field by interpolation. The values of $w_B = B^{-1/3}$ (or $w_F = F^{-1/4}$) where a line of constant ϵ intersects the energy levels are found by solving $E_i(B) = \epsilon_B B^{2/3}$ (or $E_i(F) = \epsilon_F F^{1/2}$). The result is a scaled energy spectrum giving the absorption spectrum as a function of w at a given value of scaled energy. Fourier transforming this scaled energy spectrum yields the recurrence spectrum. The accuracy of recurrence spectra at high action is limited by inaccuracies in the interpolation. These inaccuracies can be reduced by reducing the spacing between adjacent field points. The recurrence spectra computed in this way are accurate to at least $\tilde{S}_B = 200$ and $\tilde{S}_F = 50$.

In principle, computing a parallel field spectrum for constant ϵ_F and ϵ_B should be more complicated. In practice, it is only less efficient. The two fields and the energy are chosen to give the desired scaled energies. The technique described above is used, but both fields are varied at the same time as eigenvalues are computed near a given energy. This technique is less efficient because only a single constant scaled-energy spectrum can be extracted from a data set.

The oscillator strength spectrum is a series of impulses at values of w where a line of constant scaled energy intersects energy levels. The density of states is a series of Dirac-delta functions at the same values of w. The Fourier transform of the oscillator strength spectrum gives the amplitudes and frequencies of its sinusoidal modulations.

The recurrence spectrum is explicitly computed as[4]

$$R_{os}(\tilde{S}) = \left| \sum_i f(w_i) e^{i2\pi w_i \tilde{S}} \right|^2, \tag{6.11}$$

where $f(w_i)$ is the oscillator strength at an eigenvalue. Each peak in R_{os} should occur at the action of an orbit of the classical system which is closed at the nucleus.[5]

We will also be interested in the Fourier transform of the density of states:

$$R_{ds}(\tilde{S}) = \left| \sum_i e^{i2\pi w_i \tilde{S}} \right|^2. \tag{6.12}$$

Each peak in R_{ds} should occur at an action of a periodic orbit. R_{os} and R_{ds} are called *recurrence spectra* because each peak corresponds to a recurrence. The recurrence amplitudes are the factors which multiply the oscillatory terms in Eqs. 6.8 and 6.9, and the recurrence strengths are the squares of these terms. The heights of the peaks in the recurrence spectra, R_{os} and R_{ds}, should be the same as these recurrence strengths.

6.4 Classical Scaling Rule and Alkali-Metals

The position of each peak in a fully resolved recurrence spectrum should be located at the scaled action of a closed orbit. We need to know how to compute the scaled action of orbits in alkali metals. The scaling rule holds outside a certain radius (nominally the core radius), but breaks down inside this radius. The total action S of the first repetition of a closed orbit of an alkali-metal Rydberg atom in a strong field can be written

$$S_{alkali} = 2\pi(w\tilde{S}_H + \delta_s), \tag{6.13}$$

[4]In real computations, a $\sin[\pi(w - w_{min})/(w_{max} - w_{min})]$ window function is used to reduce spectral leakage.

[5]Because of the factor of 2π in the exponent, there is a difference of 2π between the action of a classical orbit and the position of the recurrence peaks. This factor is a convention established by early experimental papers and is retained to facilitate comparison.

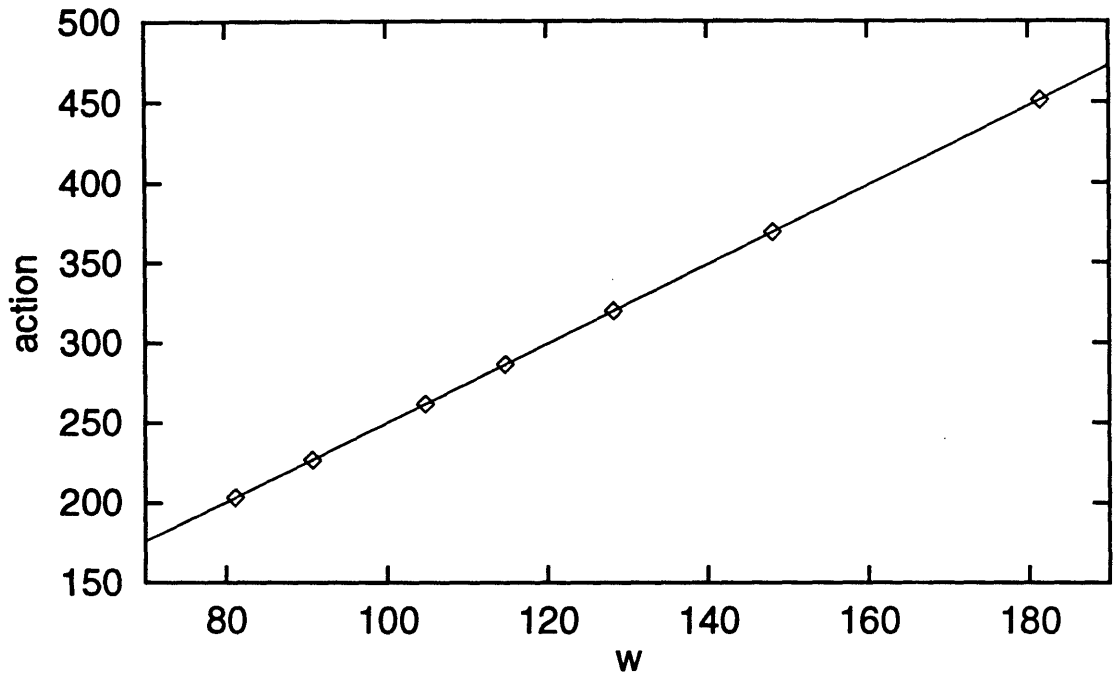

Figure 6-2: S vs. w_F for uphill parallel orbit at $\epsilon_F = -3$. The diamonds are the computed values. The solid line is the least-squares fit.

where δ_s is the s state quantum defect of the alkali-metal, and $\tilde{S}_H$ is the scaled action of a hydrogenic orbit. The action of the hydrogenic orbit is $S_H = 2\pi w \tilde{S}_H$. From a quantum mechanical viewpoint, Eqn. 6.13 is obvious because the phase a wave accumulates is simply the classical action, and the quantum defect is the phase shift of the radial wavefunction. Consequently, the additional classical action due to the core is equal to $2\pi\delta_s$. In the sum over closed orbits, the quantum defect is a constant phase which is multiplied by the number of repetitions the orbit has made, but has no dependence on w, so the core should have no effect on the positions of recurrences.

Eqn. 6.13 can be verified numerically by using a model core potential which gives the desired quantum defects, computing the actions of closed orbits of Hamiltonians which include that core potential for various values of w, and doing a least-squares fit to $S(w)$. The slope of the line $S(w)$ is $2\pi\tilde{S}$, and the y-intercept is $2\pi\delta_s$.

By adding a core potential to the Hamiltonian of hydrogen in an electric field, one can compute the action of closed orbits as a function of $w_F = F^{-1/4}$. Consider the "uphill" parallel orbit (the orbit on the z-axis between the origin and the classical turning point in the direction toward infinite potential). The scaled action of this

orbit is

$$\tilde{S}_H = \frac{1}{2\pi}\oint \tilde{\mathbf{p}}\cdot d\tilde{\mathbf{q}} = \frac{1}{2\pi}\oint \tilde{p}_z\, d\tilde{z}. \tag{6.14}$$

This is easily shown to be

$$\tilde{S}_H = \frac{1}{\pi}\int_0^{\tilde{z}_{max}} \sqrt{2(\epsilon_F + \frac{1}{\tilde{z}} - \tilde{z})}\, dz, \tag{6.15}$$

where $\tilde{z}_{max}$ is the classical turning point. For $\epsilon_F = -3$, $\tilde{S}_H = 0.3935$.

The action of this orbit in lithium is

$$S_{Li} = \oint \mathbf{p}\cdot d\mathbf{q} = \oint p_z\, dz. \tag{6.16}$$

This is easily shown to be

$$S_{Li} = 2\int_0^{z_{max}} \sqrt{2(E + \frac{1}{z} - Fz + (Z-1)\frac{e^{-az}}{z})}\, dz, \tag{6.17}$$

where z_{max} is the classical turning point. The core potential, $V_c = -(Z-1)e^{-az}/z$, corresponds to $\delta_s = 0.400$ and was described in Chapter 3. This action is shown as a function of $w_F = F^{-1/4}$ in Fig. 6-2 along with the best-fit line. The slope yields $\tilde{S}_{Li} = 0.3935(1)$, and the y-intercept yields $\delta_s = 0.426(7)$. (The numbers in parentheses indicate the error in the last digit.) A similar computation for the uphill parallel orbit at $\epsilon_F = -0.4$ gives $\tilde{S}_{Li} = 0.6903(2)$ and $\delta_s = 0.42(1)$. The scaled action for hydrogen is $\tilde{S}_H = 0.6902$. The agreement with Eqn. 6.13 is excellent for the scaled actions and good for the quantum defects.

6.5 Paradox

If closed-orbit theory can be used to compute an oscillator strength density where individual spectral lines are resolved in a discrete spectrum, then the density of states can be obtained by considering only the closed orbits, and one need not consider all the periodic orbits as the Gutzwiller trace formula suggests. For example, for

diamagnetic Rydberg atoms, we will show that a periodic orbit around the nucleus has a signature in the density of states. But if closed-orbit theory can be applied with high enough resolution, we can (hypothetically) compute an oscillator strength spectrum in which every spectral line is resolved. Knowing every spectral line means knowing the density of states. If we then Fourier transformed the density of states, we would see the signature of every periodic orbit, including, for instance, the periodic orbit around the nucleus that was ignored in the original computation!

There are two possible answers to this paradox:

- The applicability of closed-orbit theory to very high resolution is not known. Perhaps closed-orbit theory cannot really be applied to yield such a high-resolution density of states.

- Perhaps the closed orbits carry the complete information about the eigenstates of the system.

At present, the difficulty in finding and computing long-period orbits and their recurrence strengths prevents resolution of this paradox. I lean toward the suggestion that the closed orbits contain complete information about the system, because in a system with hard chaos, the closed orbits are free to explore all of phase space and can spend time as neighbors of periodic orbits which are not closed at the nucleus.

6.6 Effects of Finite $\hbar$

Periodic-orbit theory and closed-orbit theory only claim applicability in the semiclassical limit. Strictly speaking, this means the limit $\hbar \to 0$. However, it has not been shown that either theory can be formulated as an expansion in powers of $\hbar$.

We need to keep this in mind when looking at the recurrence spectra in the next several chapters. What effects would not exist in the limit $\hbar \to 0$? These effects are artifacts which are added to the semiclassical theories to find agreement with the fully quantum results. In particular, diffraction effects, pre-bifurcation recurrences, core-scattering and recurrence broadening all disappear as $\hbar \to 0$. None of these

effects were included in the original theories. Some of them still are not accounted for. Consequently, I think it is fair to consider them the first-order corrections to the original formulation of these theories.

The next three chapters consider these effects in diamagnetic, Stark, and parallel field recurrence spectra. Recurrence spectroscopy is a relatively young field, and there is a lot to do and a lot to learn. By studying the recurrence spectra of Rydberg atoms in strong fields we are simultaneously trying to gain new insights into these atomic systems and trying to illuminate the application of recurrence spectroscopy.

Chapter 7

Recurrence Spectroscopy of Diamagnetic Rydberg Atoms

Surely these things happened to Judah according to the LORD'S *command, in order to remove them from his presence because of the sins of Manasseh and all he had done, including the shedding of innocent blood. For he had filled Jerusalem with innocent blood, and the* LORD *was not willing to forgive.* –2 Kings 24:3-4

Interest in the connections between the spectra of atoms in strong magnetic fields and classical dynamics began when Garton and Tomkins discovered a sinusoidal oscillation near the ionization limit in the low resolution photoabsorption spectrum of barium in laboratory fields of several tesla [GAT69, LTG78]. This sinusoidal modulation became known as the quasi-Landau modulation because its frequency was 3/2 the spacing between Landau levels (energy levels of an electron in a magnetic field). Soon afterwards, Edmonds [EDM70] pointed out that this spacing corresponds to the energy spacing given by quantization of the classical trajectory localized in the $z = 0$ plane.

In the following years, higher resolution spectra were gradually obtained by a number of groups, and steady progress was made in the development of quantum mechanical methods for computing spectra [FRW89]. It was discovered that the classical

dynamics became chaotic near the ionization limit and the system was divided into orderly, mixed, and chaotic regimes. After the discovery of an approximate symmetry, diamagnetic hydrogen was successfully quantized [CLL88a] in the regular regime, but progress making connections between classical motion and the quantum system languished in the chaotic regime.

In the mid-eighties, Karl Welge and co-workers performed a brilliant series of experiments which opened the door to understanding diamagnetic hydrogen in the chaotic regime. Using laser spectroscopy with $0.01\,cm^{-1}$ resolution, they measured a photoabsorption spectrum of hydrogen over the range $-30\,cm^{-1} < E < 30\,cm^{-1}$ at $B \approx 6T$. The spectrum showed no easily identifiable features. In particular, there were no apparent quasi-Landau modulations. However, a Fourier transform of the energy spectrum revealed the underlying periodicities corresponding not only to the quasi-Landau period, but also to other closed orbits in the system [HWM86]. These experiments were followed by the development of closed-orbit theory [DUD87, DUD88a].

A difficulty in interpreting these early experiments was that the classical dynamics of the system changed a great deal over the energy range of the spectrum. Consequently, only the small subset of orbits whose periods were slowly changing could be seen in the experiments. To solve this problem, Welge and co-workers invented scaled-energy spectroscopy. By varying the energy and magnetic field simultaneously as the spectra were recorded, they solved the problem of changing classical dynamics over their scan range [HMW88]. The scaled action $\tilde{S}_B$ and scaled field, $w_B = B^{-1/3}$, are the relevant transform variables. Some time later, Tonny van der Veldt applied this technique to measure recurrence spectra of diamagnetic helium [VVH93].

This chapter presents studies of computed diamagnetic Rydberg spectra. The computational techniques employed have been experimentally verified, as discussed in Chapter 2. Recurrence spectra of diamagnetic hydrogen are presented in the region of the onset of chaos. The need to modify closed-orbit theory to account for the contribution of an orbit's neighbors to its recurrence strength is demonstrated. The recurrence amplitudes of the near-circular orbit in R_{ds} are shown to agree with

periodic-orbit theory. Pre-bifurcation recurrences are studied as a function of $\hbar$. The signature of very long period orbits is shown in recurrence spectra. Core scattering in even-parity lithium is shown to be consistent with a quantitative model. Finally, the proliferation of recurrences is used as a signature of chaos.

To interpret the diamagnetic recurrence spectra, we recall the basic structure of the periodic orbits in diamagnetic hydrogen. At large negative scaled energies, there are four primitive short-period orbits: one moves on the ρ axis, two move on the $\pm z$ axis, and one approaches a circle in the ρ–z plane [DKN84, MWW94]. Most longer-period primitive periodic orbits are created by bifurcations of these orbits and their repetitions. The orbits on the ρ axis and those which bifurcate from them are called *rotators*. Recurrences corresponding to these orbits will be labeled R_n^b, where the subscript n denotes the repetition of the orbit on the ρ axis from which the orbit bifurcated, and the superscript b distinguishes between different orbits which bifurcated from the same parent. The orbits on the z axis and those which bifurcate from them are called *vibrators*. Recurrences corresponding to these orbits are labeled V_n^b, where n and b have the same meaning as for the rotators. The orbit which approaches a circle in the ρ–z plane should be visible only in R_{ds} and not R_{os} because it is not closed at the nucleus. Recurrences corresponding to this orbit and its repetitions are labeled O_n. There are also closed orbits which appear "out of nowhere" and are not created from bifurcations of the rotators or vibrators. These orbits are called exotic orbits and are labeled X_n. Figure 7-1 shows some of the closed orbits in diamagnetic hydrogen.

Computing the scaled action of closed orbits is straightforward. The scaled Hamiltonian was given in Chapter 3. The scaled action of the parallel orbit is

$$\tilde{S}(V_1) = \frac{1}{2\pi}\oint \tilde{\mathbf{p}} \cdot d\tilde{\mathbf{q}} = \frac{1}{2\pi}\oint \tilde{p}_z \, d\tilde{z}. \tag{7.1}$$

This is easily shown to be

$$\tilde{S}(V_1) = \frac{1}{\pi}\int_0^{\tilde{z}_{max}} \sqrt{2(\epsilon_B + \frac{1}{\tilde{z}})}\, d\tilde{z}, \tag{7.2}$$

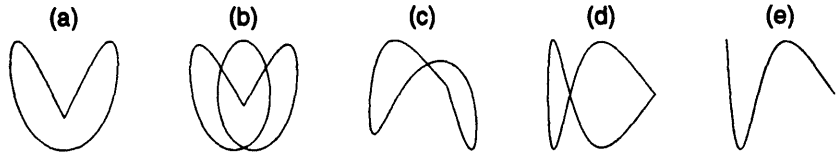

Figure 7-1: A few closed orbits in diamagnetic hydrogen. (a) R_2^1; (b) R_3^1; (c) X_1; (d) V_1^3; (e) V_1^4.

where $\tilde{z}_{max} = -1/\epsilon_B$ is the classical turning point. Evaluating the integral gives $\tilde{S}(V_1) = \sqrt{-8/\epsilon_B}$. The scaled action of the perpendicular orbit is

$$\tilde{S}(R_1) = \frac{1}{2\pi}\oint \tilde{p}_\rho \, d\tilde{\rho} = \frac{1}{\pi}\int_0^{\tilde{\rho}_{max}} \sqrt{2(\epsilon_B + \frac{1}{\tilde{\rho}} - \frac{\tilde{\rho}^2}{8})}\, d\tilde{\rho}, \tag{7.3}$$

where $\tilde{\rho}_{max}$ is the classical turning point and is given by the real root of

$$\epsilon_B + \frac{1}{\tilde{\rho}} - \frac{\tilde{\rho}^2}{8} = 0. \tag{7.4}$$

The actions of these orbits can be computed analytically (with some work). The action of more complicated orbits must be computed by numerically integrating

$$\tilde{S} = \frac{1}{2\pi}\oint \tilde{\mathbf{p}} \cdot d\tilde{\mathbf{q}} \tag{7.5}$$

as the orbits themselves are obtained from numerical integration of Hamilton's equations. As discussed in Chapter 3, semiparabolic coordinates are used for the numerical integrations.

7.1 Hydrogen

Hydrogen is the simplest diamagnetic atom to study. There is no core scattering and all of the recurrences can be interpreted directly in terms of closed or periodic orbits.

7.1.1 Onset of Chaos

Welge and co-workers [HMW88] performed a thorough experimental investigation of recurrence spectra for $-0.3 \leq \epsilon_B \leq 0$ for even-parity diamagnetic hydrogen. They saw repetitions of the basic rotator and vibrator closed orbits and many orbits which bifurcated from them. They also saw recurrences associated with exotic orbits which are created by bifurcations "out of nowhere" typically in the regions of $\tilde{S}_B$ between rotators and vibrators. A detailed interpretation of these results in terms of closed-orbit theory was published several years later [MWW94].

I have computed the recurrence spectra of even-parity hydrogen for most of the same region ($-0.3 \leq \epsilon_B \leq -0.1$). The region for $\epsilon_B > -0.1$ was omitted because the matrices which need to be diagonalized were prohibitively large. For the region below $\epsilon_B = -0.1$, Sturmian basis sets with principal quantum number up to $n_{max} = 200$ (corresponding to 10000 basis functions) were used, and Hamiltonian matrices were diagonalized on a Cray supercomputer. Computing the spectra in this region took roughly 10 hours of Cray time. Convergence was checked for a given energy, field, and α (the length scale of the Sturmian basis, see Chapter 2) by comparing eigenvalues and oscillator strengths for different basis sizes. When the eigenvalues and oscillator strengths were identical for a given n_{max} and $n_{max} + 10$, then the eigenvalues were considered converged for the basis set with n_{max}.

By using a larger field range ($1\,T \leq B \leq 8T$), the recurrence spectra presented here have roughly three times higher resolution than in Welge's experiment (with range $3.0\,T < B < 5.2\,T$). Furthermore, the computed spectra are reliable to higher action ($\tilde{S}_B > 200$) than the experimental recurrence spectra, which are only reliable to $\tilde{S}_B \approx 5$. The experimental limit is set by uncertainties in the magnetic field and the laser resolution. The absence of noise in the computations also provides for more accurate spectra, and the computed spectra are generally easier to normalize.[1] Finally, once the spectrum is computed in a region, scaled-energy spectra can be obtained at any desired step size in ϵ_B with minimal effort.

[1]Except as noted, recurrence spectra presented in this thesis are normalized by making the integral over the oscillator strength equal to 1 before taking the Fourier transform.

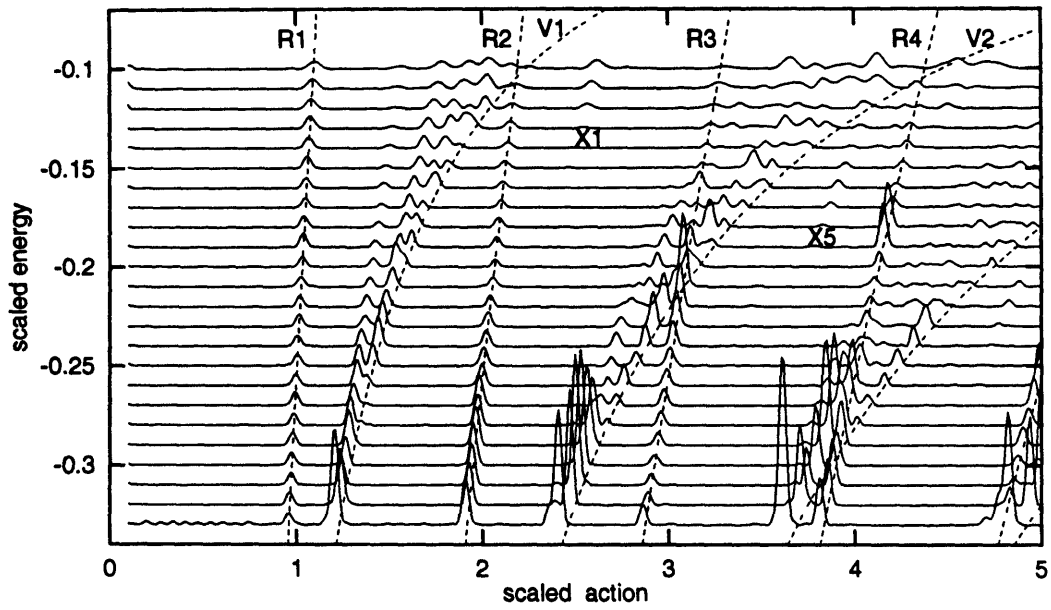

Figure 7-2: Low-action recurrence spectra for even-parity diamagnetic hydrogen, $m = 0$. Dashed lines are the scaled action of R_n and V_n. Some exotic orbits are also labeled according to their designations in [HMW88].

Having listed all of the advantages of computing the recurrence spectrum over Welge's measurements, I should say that the computational approach is only justified because the computations have been found to agree with experiments at fixed field. The scaling is easier to perform numerically than in the laboratory. The computed recurrence spectra presented here provide general confirmation of the many interesting and new discoveries of Welge's experiments. Furthermore, they support the applicability of closed-orbit theory and classical interpretation of recurrence spectra to much higher action than previous work.

The recurrence spectrum of even-parity diamagnetic hydrogen for $0 \leq \tilde{S}_B \leq 5$ is shown in Figure 7-2. The dashed lines are the scaled actions of the repetitions of the main rotator and vibrator orbits. These provide the organizing principles for interpreting the recurrence spectrum. The lowest action closed orbit is the quasi-Landau orbit, R_1. It does not bifurcate, and its recurrence strength slowly decreases as the scaled energy is raised. At low ϵ_B, V_1 has nearly the same scaled action as R_1. As the scaled energy increases toward 0, the scaled action of V_1 goes to ∞. Orbits which bifurcate from V_1 have scaled actions which are lower than V_1. These orbits form a "mountain range" between V_1 and V_1^1 (the first orbit to bifurcate from V_1).

These bifurcations and many of the bifurcations which created the new recurrences seen in Figure 7-2 are discussed in detail by Mao and Delos [MAD92]. The recurrence strength of R_2 shrinks as ϵ_B is raised and becomes very small above $\epsilon_B = -0.127$ because R_1 becomes unstable at that scaled energy, and the recurrence strength of its repetitions decreases exponentially.

The first exotic X_1 lies between R_2 and the sequence of orbits which bifurcate from V_2. The exotic orbits are unique because they are created by "saddle node" bifurcations which do not require an existing orbit to occur. The X_1 bifurcation occurs at $\epsilon_B = -0.115$ [MAD92], but it is visible in the recurrence spectrum as low as $\epsilon_B = -0.12$ in Figure 7-2. In fact, in a blowup of Figure 7-2, X_1 is visible as low as $\epsilon_B = -0.15$. This occurs because the uncertainty principle allows the quantum system to see the new orbits before they are actually created. Quantum mechanics cannot distinguish an orbit which leaves and returns to a volume of phase space of size $\hbar^n$ (where n is the dimension of the physical space) from a periodic orbit. This dependence on the size of $\hbar$ provides a window into how recurrence spectra change as $\hbar$ changes, and we will examine this later in more detail. An alternate view is provided by extending the dynamics of the system to complex coordinates. The new periodic orbits come down onto real coordinates from complex phase space [MAD92, KHD93].

The second mountain range is located on the low-action side of V_2. As random as these peaks appear, they can be reproduced by careful application of closed-orbit theory [MWW94]. R_3 crosses the second mountain range as the scaled energy is increased. Its increase in recurrence strength near $\epsilon_B = -0.22$ is due to a bifurcation. At higher action, the same general pattern is followed, except that the scaled action at which bifurcations begin generally increases as the scaled energy is lowered. Exotic orbits also appear at lower scaled energy for the higher actions. Occasional large recurrences are caused by nearby bifurcations.

Higher action recurrence spectra are shown in Figures 7-3, 7-4, and 7-5. For $5 \leq \tilde{S}_B \leq 10$, repetitions of R_1 and V_1 still provide a way to understand the basic structure. The R_n have visible recurrences. The V_n provide ridges on the high-action side of recurrences which bifurcated from them and moved to lower scaled

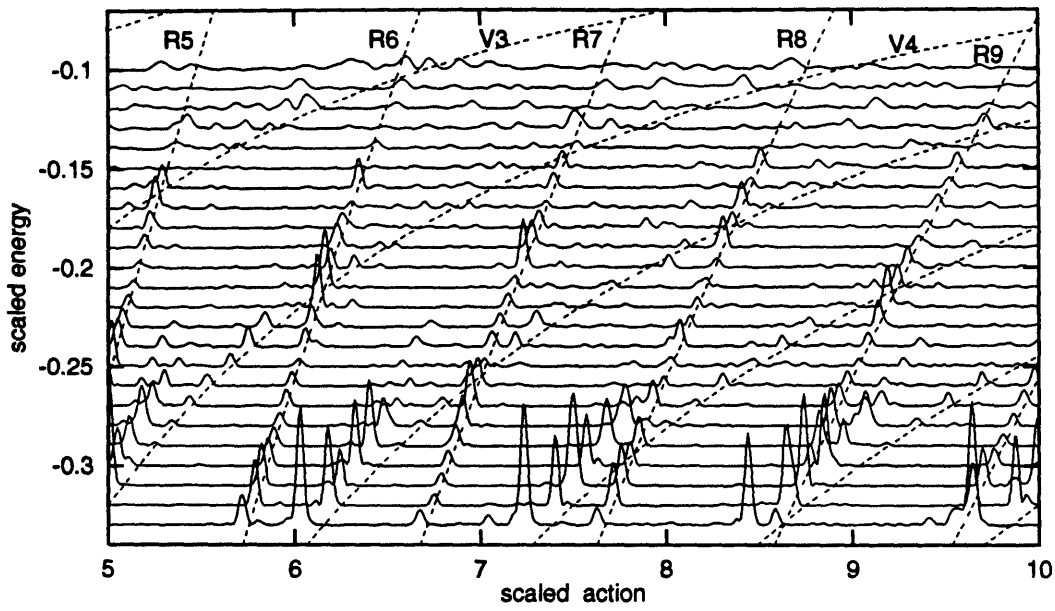

Figure 7-3: Recurrence spectra for $m = 0$ even-parity diamagnetic hydrogen for $5 \leq \tilde{S}_B \leq 10$.

action. Near $\epsilon = -0.32$ there are prominent peaks corresponding to vibrators which bifurcated from the repetitions of V_1.

In principle, closed-orbit theory should be able to reproduce the complex structure of the high-action structure of the chaotic region. In practice, the proliferation of orbits and the difficulty of finding orbits and computing their recurrence strengths will make this challenging. Consequently, for $10 \leq \tilde{S}_B \leq 15$ (Figure 7-4) and $15 \leq \tilde{S}_B \leq 20$ (Figure 7-5), the recurrence spectra do not allow any simple association with repetitions of V_1. In contrast, repetitions of R_1 are the only easily identifiable feature at higher scaled energy. Reproducing the detailed structure of the chaotic regions will prove quite challenging to closed-orbit theory, but the disappearance of the V_n before the R_n can be understood simply. The recurrence strength of an unstable orbit decreases exponentially as a function of the number of repetitions. The vibrators become unstable at lower ϵ_B and are not easily recognized. In contrast, the R_n are stable for $\epsilon_B < -0.127$. Consequently, their spectral signature remains strong to high action.

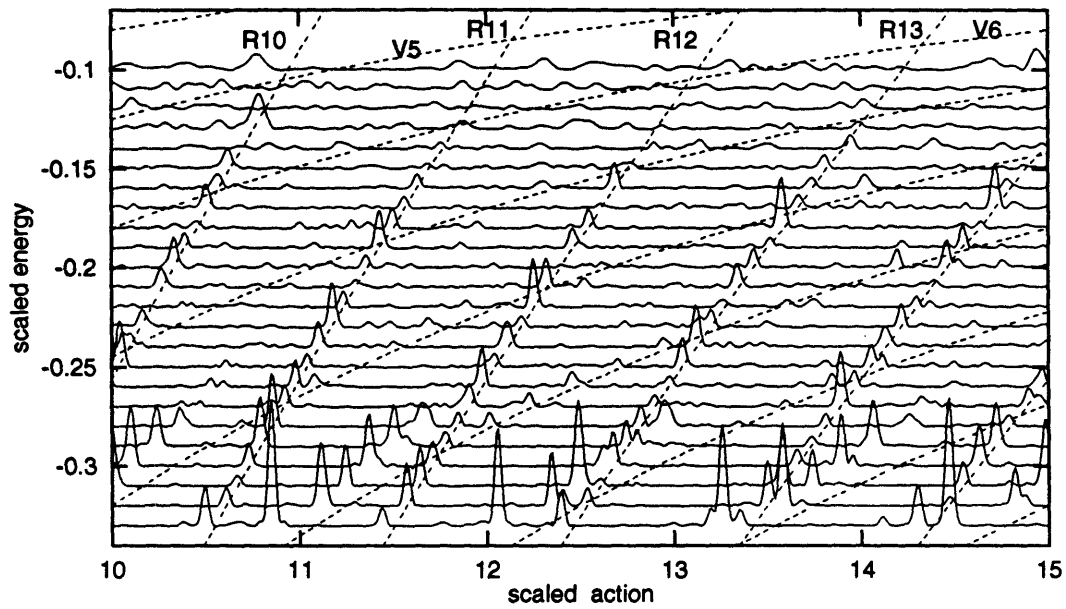

Figure 7-4: Recurrence spectra for $m = 0$ even-parity diamagnetic hydrogen for $10 \leq \tilde{S}_B \leq 15$.

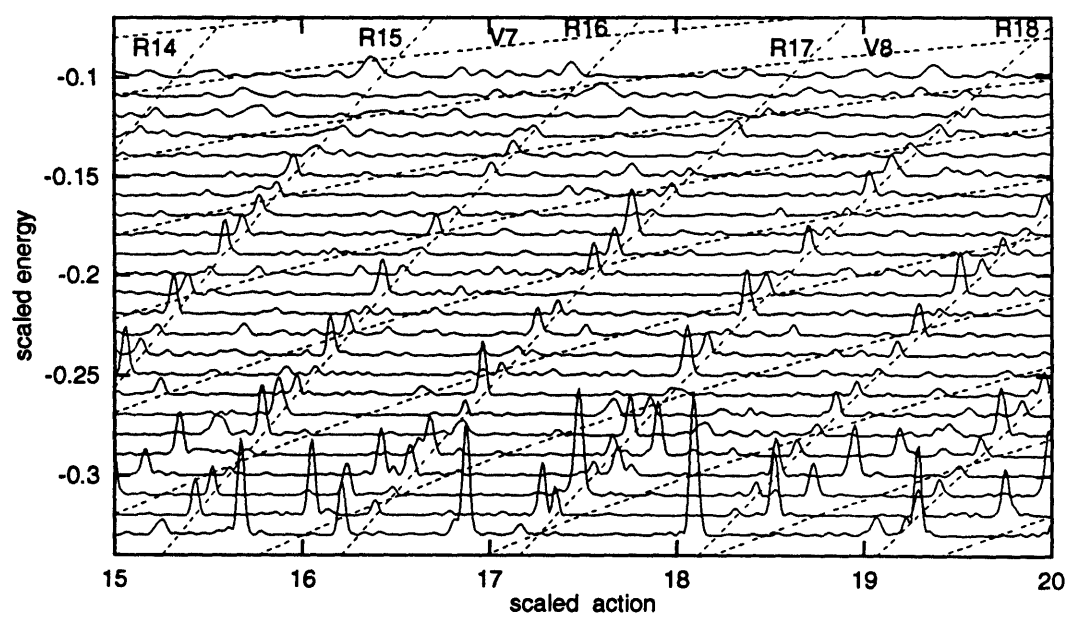

Figure 7-5: Recurrence spectra for $m = 0$ even-parity diamagnetic hydrogen for $15 \leq \tilde{S}_B \leq 20$.

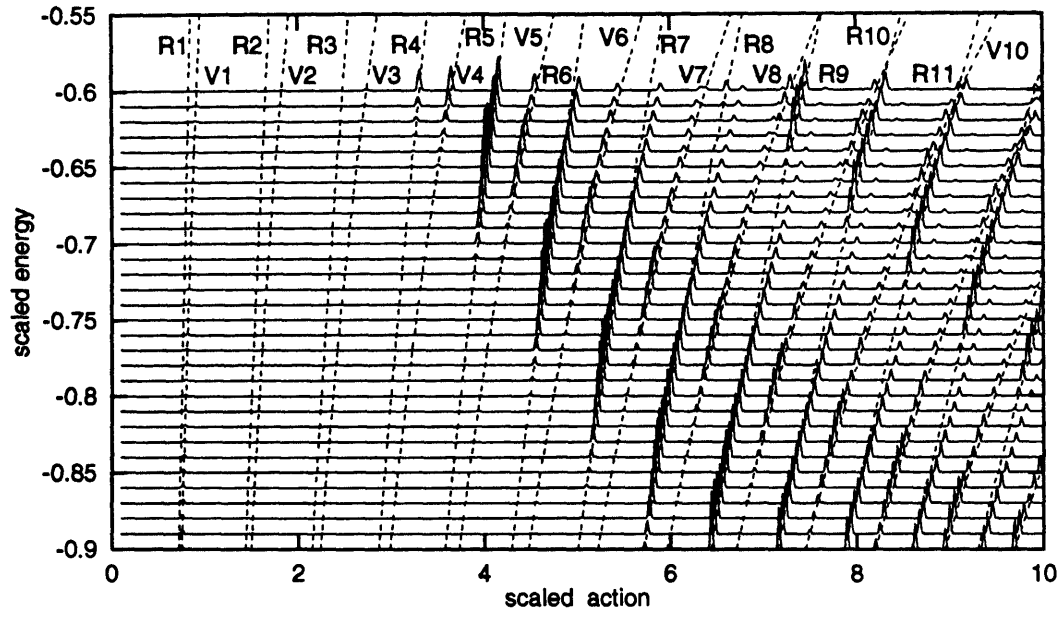

Figure 7-6: Recurrence spectra for $m = 0$ odd-parity diamagnetic hydrogen for $-0.9 \leq \epsilon_B \leq -0.6$.

7.1.2 Perpendicular Orbit in Odd-Parity Spectrum

A panoramic map of the odd-parity recurrence spectrum for $-0.9 \leq \epsilon_B \leq -0.6$ is shown in Figure 7-6. The classical dynamics is regular in this region, and the recurrence spectra can be simply interpreted in terms of R_n, V_n, and the first few orbits which bifurcate from them. At $\epsilon_B = -0.9$ the first large recurrences do not appear until R_8 and V_8. The appearance of large recurrences occurs at lower repetitions as the scaled energy is increased. The large increases in recurrence strength as the scaled energy is raised are due to bifurcations. The repetitions of R_1 and V_1 which have not yet bifurcated have small recurrence strengths. These recurrence strengths become large near a bifurcation and slowly shrink afterward. At the bifurcation, the newly created orbit has the same scaled action as the parent, but the action slowly moves away as the scaled energy increases beyond the bifurcation.

The scaled energy of a newly created rotator moves to a higher action than its parent. For example, R_9 bifurcates at about $\epsilon_B = -0.9$, and the recurrence strength is rather large. At $\epsilon_B = -0.75$ the newly created orbit (R_9^1) can be seen moving to higher action than R_9, and it takes most of the recurrence strength with it. Near $\epsilon_B = -0.6$, R_9 begins to grow again in anticipation of another bifurcation. In contrast,

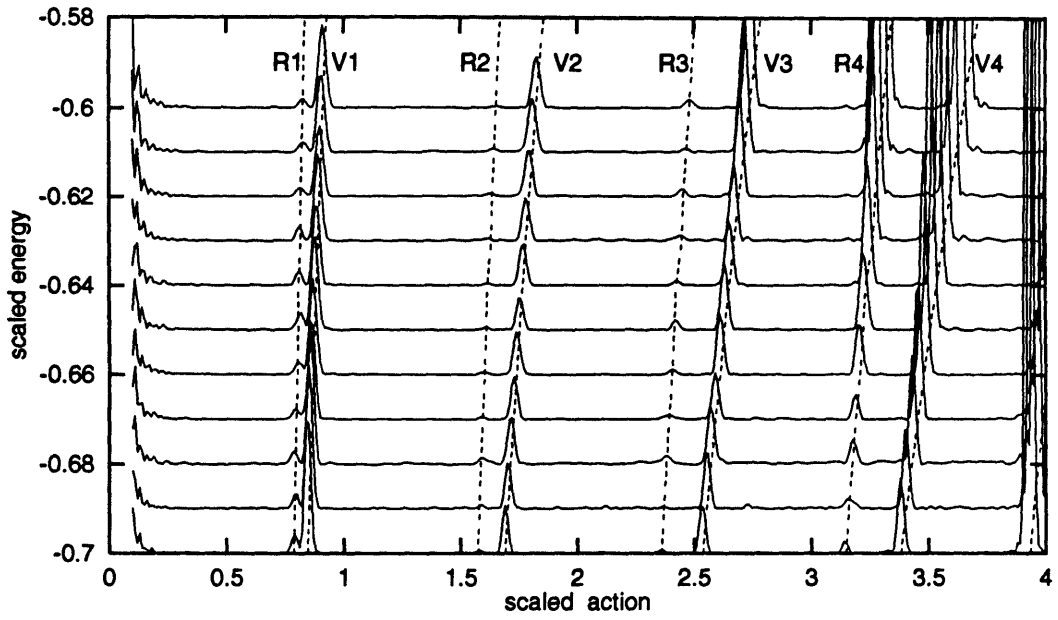

Figure 7-7: Recurrence spectra for $m = 0$ odd-parity diamagnetic hydrogen for $-0.7 \leq \epsilon_B \leq -0.6$, low fields.

the scaled energy of a newly created vibrator moves to slightly lower action than its parent. For example, V_7 bifurcates at about $\epsilon_B = -0.75$, and the recurrence strength is rather large. At $\epsilon_B = -0.6$, the newly created orbit (V_7^1) can just be resolved at lower action than V_7.

Closed-orbit theory asserts that the recurrence strength of any particular classical orbit is related to the angular distribution of the outgoing quantum waves. In particular, it predicts that the recurrence strength is zero if a returning orbit lies on a node of the outgoing quantum wavefunction. Du and Delos [DUD88b] made the approximation that the returning waves are similar to Coulomb scattering waves, and their amplitude is proportional to the amplitude of the outgoing wave at the initial angle of the closed orbit. Of course, if the initial angle of the closed orbit is in the node of an outgoing wave, then its recurrence strength is zero.

The quasi-Landau orbits R_n are in the $z = 0$ plane. Consequently, this orbit is in the node of odd-parity wavefunctions, and its recurrence strength was predicted to be zero. However, the blowup of Figure 7-6 (80X) shown in Figure 7-7 shows that these orbits have a small but finite recurrence strength.[2] These recurrence spectra were

[2] R_4 appears very large as the scaled energy is raised above $\epsilon_B \approx -0.65$ because a bifurcation

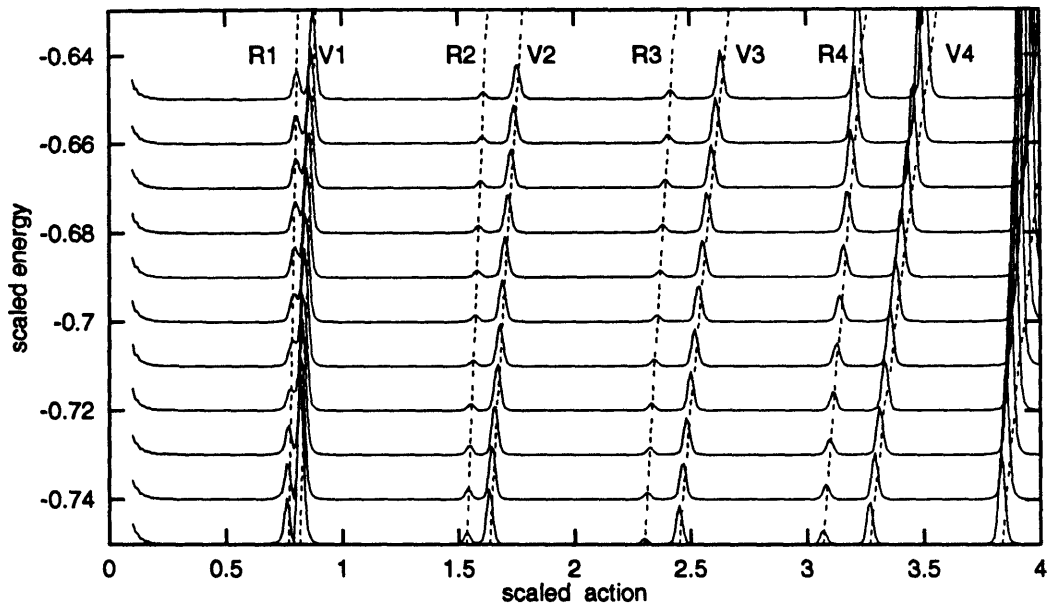

Figure 7-8: Recurrence spectra for $m = 0$ odd-parity diamagnetic hydrogen for $-0.75 \leq \epsilon_B \leq -0.65$, high fields.

computed for $0.15T < B < 0.4T$. The strength of these recurrences increases as a function of field (private communication from John Shaw). Figure 7-8 shows another map of recurrence spectra near the same region, but these recurrence spectra were computed at larger fields, $0.6T < B < 8T$. The recurrence strengths of the R_n are indeed larger.

How can we understand these recurrences which the original formulation of closed-orbit theory said would have zero recurrence strength? The crucial point is that the neighbors of a closed orbit also carry a small amount of recurrence strength. When the recurrence strength of the closed orbit is large, the recurrence strength of the neighbors can be neglected in comparison. But when the recurrence strength of the closed orbit is exactly zero, the recurrence strength of the neighbors makes a visible contribution to the recurrence spectrum. By considering the neighbors, John Shaw and John Delos have developed a semiclassical formula which finds agreement with the quantum mechanical recurrence strengths. Figure 7-9 shows a comparison between some of the quantum computations shown in Figure 7-8 and the closed-orbit computations of Shaw and Delos. Agreement is good, though the theory is not yet

produces another closed orbit with nearly the same action. This new orbit has a large recurrence strength.

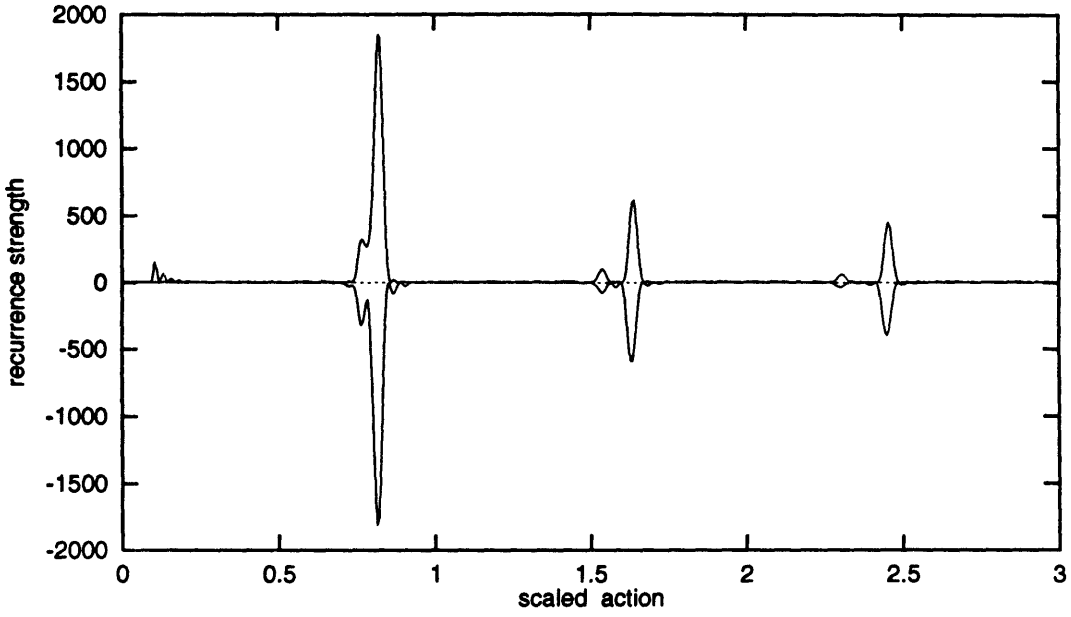

Figure 7-9: Comparison of quasi-Landau recurrences in odd-parity spectrum (top) with closed-orbit theory (bottom) at $\epsilon_B = -0.75$. Closed-orbit theory recurrence spectrum courtesy of John Shaw.

in its final form.

7.1.3 Nearly Circular Orbit

Diamagnetic hydrogen has a periodic orbit which goes around the origin in the ρ, z plane. As $\epsilon_B \to -\infty$ this orbit becomes a perfect circle. At high scaled energies, it is more spread out in ρ. This orbit is unstable for all scaled energies, and it becomes stable asymptotically as $B \to 0$. The near-circular orbit has symmetry properties which need to be considered when interpreting R_{ds}. If its period is T_0, then the position and momentum coordinates at $T_0/2$ are the negative of what they were at $T = 0$. This gives recurrences whose scaled action is half the total scaled action of the periodic orbit.

The recurrence amplitude, $\sqrt{R_{ds}}$, for even-parity hydrogen at $\epsilon_B = -0.6$ is shown in Figure 7-10. ($\sqrt{R_{ds}}$ is plotted here to emphasize the smaller peaks.) The rotators and vibrators make their expected appearances, but the peaks labeled O_n are actually located at the repetitions of $\tilde{S}_B(O)/4$, and not at $\tilde{S}_B(O)/2$ as expected. The scaled action of a full period of the near-circular orbit is roughly $\tilde{S}_B = 1.8$. (This makes

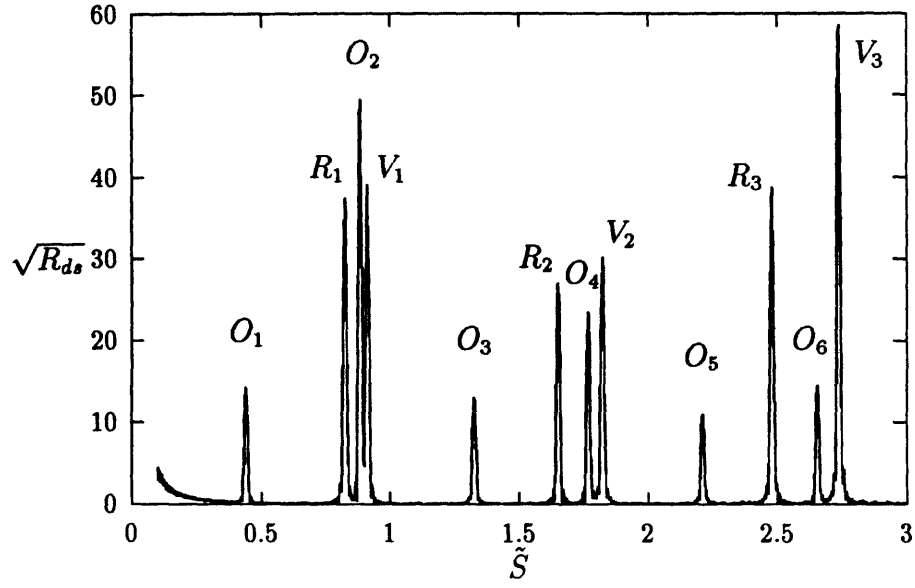

Figure 7-10: Recurrences corresponding to the near-circular orbit are seen in R_{ds}. Rotators and vibrators are also visible.

sense because the orbit travels about twice as far as R_1 which has $\tilde{S}_B \approx 0.85$.) John Shaw has suggested that the recurrences at $\tilde{S}_B(O)/4$ result from further symmetries in the problem (private communication).

The instability exponent of an orbit grows linearly with the number of repetitions. For example, the density of returning neighbors is half the size on the second return compared to the first. Consequently, from Eqn. 6.8 we expect that the recurrence strength of repetitions of an unstable periodic orbit will decrease like $1/\sinh(n\chi/8)$, where χ is the instability of O_1. There is an extra factor of 4 in the denominator because $n = 4$ is a complete period. We see this dependence in the half-period recurrence amplitudes (even n in our notation) but observe a $1/\cosh(n\chi/8)$ dependence in the recurrence amplitudes of the quarter-periods (odd n in our notation). Figure 7-11 shows these dependencies.

There seems to be provision for both of these dependencies in Gutzwiller's formulation [GUT90]. The dependence on sinh and cosh result from hyperbolic and inverse hyperbolic fixed points, respectively. However, our results here are empirical, and they need to be explained fully in terms of the symmetries of the problem and the nature of the near-circular orbit.

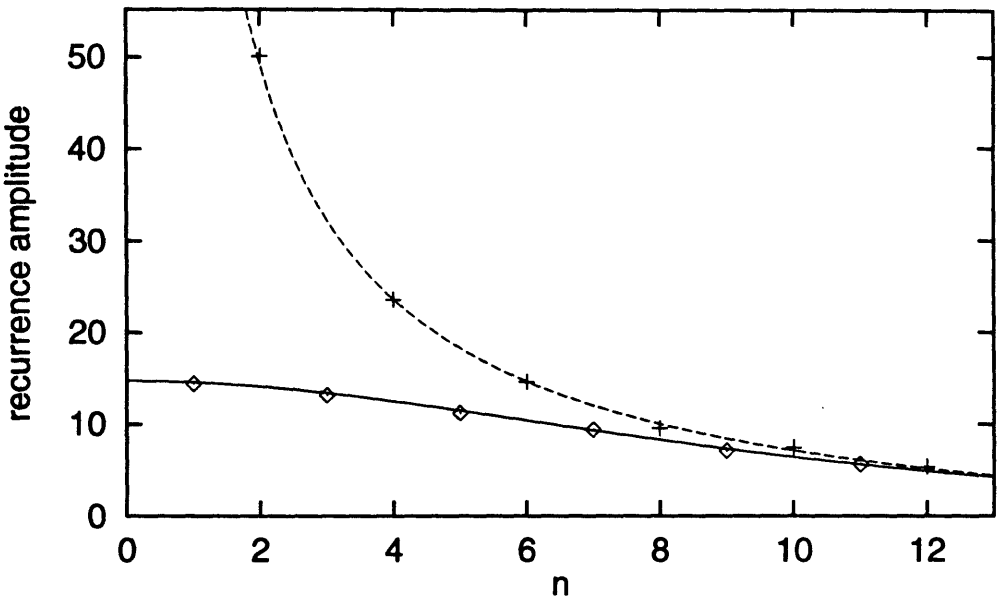

Figure 7-11: Dependence of recurrence amplitudes as a function of the number of quarter periods, n. Diamonds are odd quarter-periods. Plus signs are even quarter periods. Solid line is $A/\cosh(n\chi/8)$. Dashed line is $A/\sinh(n\chi/8)$, where $A = 14.75$ and $\chi = 1.18$.

This example illustrates the potential of periodic-orbit theory for extracting classical information from the quantum spectrum. Not only can the classical action of periodic orbits be seen in the spectrum, the instability of periodic orbits can also be determined.

7.1.4 Pre-Bifurcation Recurrences

The size of $\hbar$ has a profound influence on recurrence spectra near bifurcations. In particular, the finite size of $\hbar$ causes a new recurrence to appear in the quantum system before a new classical orbit is created by bifurcation. Quantum mechanics cannot distinguish an orbit which leaves and returns to a volume of phase space of size $\hbar^n$ (where n is the dimension of the physical space) from a periodic orbit. This dependence on the size of $\hbar$ provides a window into how recurrence spectra change as $\hbar$ changes.

This effect is present for all bifurcations, but it is most prominent in recurrences for exotic orbits created from saddle-node bifurcations because these orbits are not created from existing orbits, and any recurrence strength which is present before the

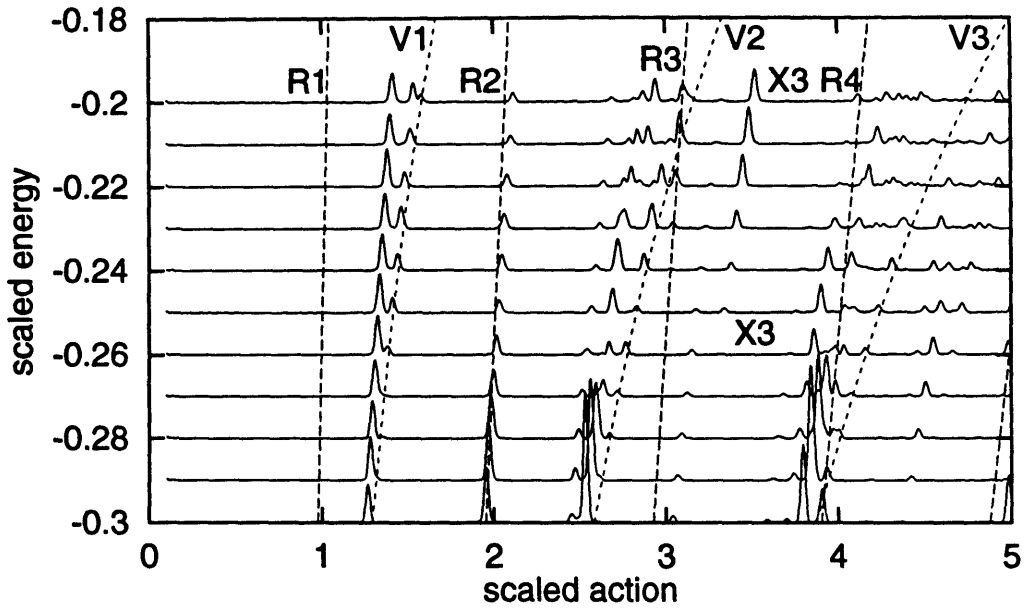

Figure 7-12: R_{os} for odd-parity diamagnetic hydrogen spectrum in low-action region. The X_3 bifurcation is clearly visible.

bifurcation is attributable to this effect. Figure 7-12 shows the low-action recurrence spectrum of odd-parity diamagnetic hydrogen for $-0.3 \leq \epsilon_B \leq -0.2$. The X_3 bifurcation occurs at $\epsilon_B = -0.227$ (private communication from John Shaw), and is visible in the recurrence spectrum.

R_{os} for odd-parity diamagnetic hydrogen is shown in Figure 7-12. The constant scaled energy spectra were computed for $0.6T \leq B \leq 8T$, which is roughly $35 \leq w_B \leq 75$. The scaled actions of R_n and V_n are also shown. The recurrence strengths of the R_n are too small to see on this scale. R_2^1 and R_3^1 are visible at slightly higher action than R_2 and R_3, respectively. The first few V_n and the orbits which bifurcate from them are also visible. The X_3 recurrence becomes visible near $\tilde{S}_B = 3.4$ at $\epsilon_B = -0.26$, which is significantly lower than the bifurcation energy $\epsilon_B = -0.227$. X_3 grows quickly and is among the largest recurrences at $\epsilon_B = -0.2$.

Planck's constant has the same dimensions as action, so it scales in the same way. Recalling that $S = 2\pi w_B \tilde{S}$, we see that the effective size of $\hbar$ scales as $\hbar = 1/w_B = B^{1/3}$. At a given ϵ_B, larger w_B corresponds to higher energies where the semiclassical approximations are more appropriate. Consequently, if we focus on a particular pre-bifurcation recurrence and compute the quantum mechanical recur-

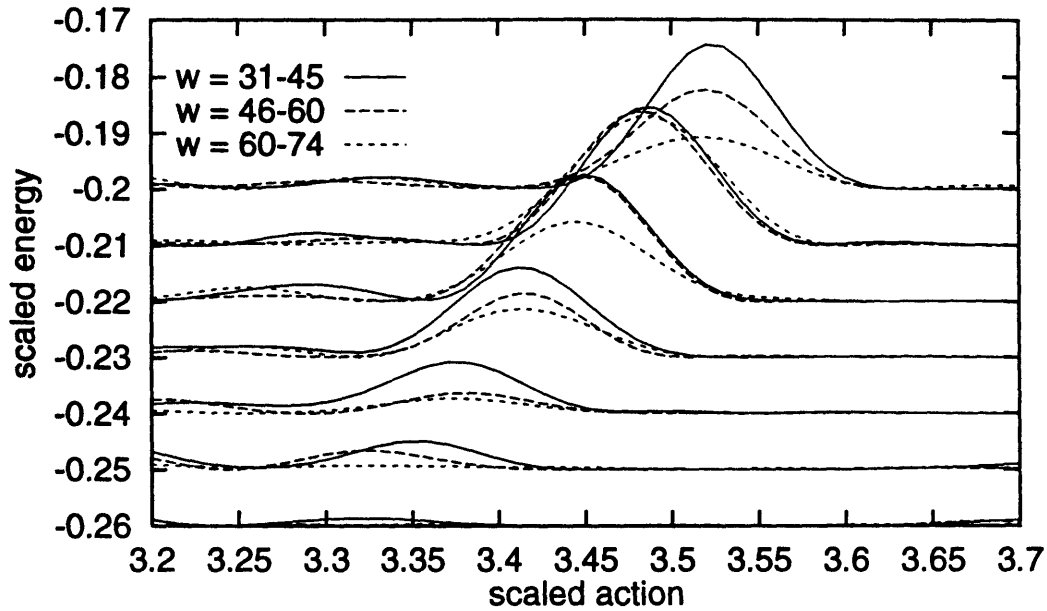

Figure 7-13: Blowup of X_3 in odd-parity diamagnetic R_{os}.

rence strength in various field regions, we should find that the recurrence strength has a strong dependence on the w_B region of our computations. This approach is used on X_3 and the result is shown in Figure 7-13. For the lowest range of w_B, X_3 is clearly visible below the bifurcation energy. In the mid-range of w_B, X_3 is smaller, particularly below the bifurcation. In the highest range of w_B, X_3 is not clearly visible until just before the bifurcation at $\epsilon_B = -0.23$.

7.1.5 Very Long Period Orbits

There is a fundamental interest in whether or not periodic-orbit theory and closed-orbit theory converge for chaotic systems. Long period orbits are of particular interest because they determine the resolution that closed-orbit theory can achieve, and because they play a crucial role in determining how well the theory's predictions converge to the true quantum spectrum. However, long period orbits are difficult to study theoretically because the number of them proliferates exponentially as a function of period (or action) and they can be highly unstable for chaotic systems. Consequently, the limits of periodic-orbit theory and closed-orbit theory are not well understood. While many groups have published low-action diamagnetic recurrence spectra and identified the affect of short-period orbits, the highest-action recurrence

spectra presented [VVH93] only covered $\tilde{S}_B \leq 20$ which corresponds to about 25 repetitions of the quasi-Landau orbit. We will identify recurrences in the spectrum of diamagnetic hydrogen at considerably higher actions.

Some care needs to be used when using the terms "long-period" and "high-action" interchangeably. We will examine recurrences and identify them by their scaled action. We will make contact with the time domain by approximating the period of a nearby repetition of R_n. However, there is not a $1:1$ mapping between scaled action and period, and the actual period of a closed orbit with scaled action near a repetition of R_n can be many times longer than R_n. At $E = 0$, R_1 has a period $2T_c/3$, where T_c is the cyclotron period. The period of R_1 is a bit shorter for $E < 0$.

Long-Period Absorption Recurrence Spectra

At $\epsilon_B = -0.6$, the dynamics of diamagnetic hydrogen is regular, and R_n and V_n dominate at low action. At $\tilde{S}_B \approx 4$ new orbits begin to be born by bifurcations, and the recurrence spectra become more complicated. By $\tilde{S}_B \approx 15$ it becomes difficult to resolve individual recurrences, even with the narrow recurrences obtained by Fourier transforming a spectrum from $31 < w_B < 133$. However, large recurrences are still visible in the recurrence spectrum at high action.

The recurrence spectrum of even-parity diamagnetic hydrogen for $190 \leq \tilde{S}_B \leq 200$ is shown in Figure 7-14. Every repetition of the perpendicular orbit between R_{230} and R_{241} is visible. Repetitions of the parallel orbit between V_{209} and V_{219} are also visible, though they are somewhat smaller. At $\epsilon_B = -0.6$, the quasi-Landau period is roughly $T_c/2$ which gives a period of these orbits in the vicinity of $120T_c$.

The rest of the recurrence spectrum looks like noise, but it probably is not. Presumably, closed-orbit theory should be able to reproduce every peak. Even without identifying every peak, the identification of the R_n and V_n represents confirmation of closed-orbit theory at very high action.

The accuracy of the computed recurrence spectrum has only been validated carefully for $\tilde{S}_B < 500$, but the check on accuracy gives a conservative estimate,[3] and the

[3]The accuracy is checked by performing an additional interpolation using only every other field

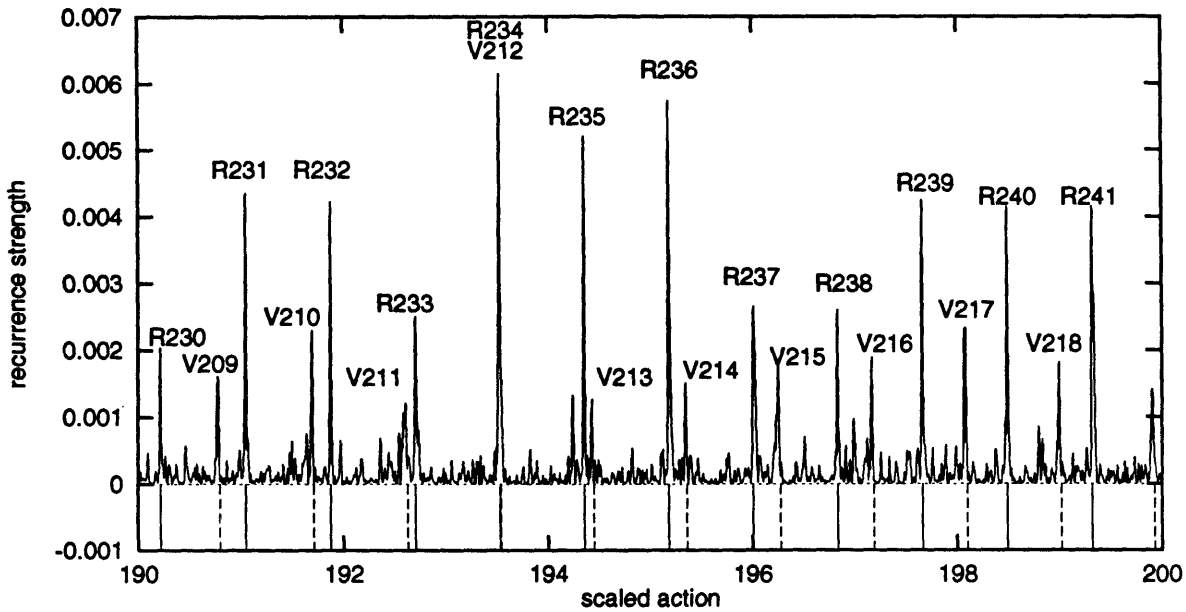

Figure 7-14: Recurrence spectrum near $\tilde{S}_B = 200$ for even-parity diamagnetic hydrogen, $\epsilon_B = -0.6$. Parallel and perpendicular orbits are labeled. Solid and dashed vertical lines are the classical action of repetitions of R_1 and V_1, respectively.

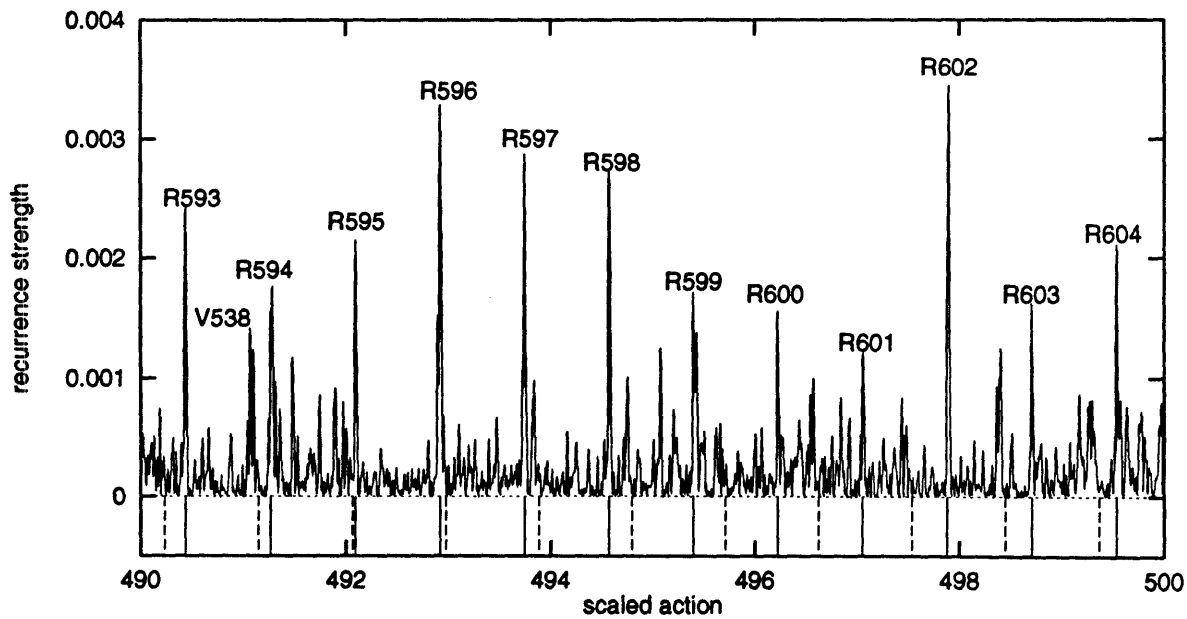

Figure 7-15: Recurrence spectrum near $\tilde{S}_B = 500$ for even-parity diamagnetic hydrogen, $\epsilon_B = -0.6$. Parallel and perpendicular orbits are labeled. Solid and dashed vertical lines are the classical action of repetitions of R_1 and V_1, respectively.

Table 7.1: Scaled action of R_n near $\tilde{S}_B = 500$ for $\epsilon_B = -0.6$. The classical value is $\tilde{S}_B(R_n)/n = 0.827036$.

Orbit	$\tilde{S}_B^{qm}$	$\tilde{S}_B^{qm}/n$
R_{593}	490.4348	0.827040
R_{594}	491.2609	0.827039
R_{595}	492.0866	0.827036
R_{596}	492.9146	0.827038
R_{597}	493.7428	0.827040
R_{598}	494.5667	0.827035
R_{599}	495.3959	0.827038
R_{600}	496.2231	0.827038
R_{601}	497.0524	0.827042
R_{602}	497.8871	0.827038
R_{603}	498.7030	0.827037
R_{604}	499.5308	0.827038
Average		0.827038(2)

recurrence spectrum is probably accurate to even higher actions. Rotators and vibrators can be identified in the recurrence spectrum of even-parity diamagnetic hydrogen for $490 \leq \tilde{S}_B \leq 500$ shown in Figure 7-15. Every repetition of the perpendicular orbit between R_{593} and R_{604} is visible. Repetitions of the parallel orbit between V_{538} and V_{547} are also visible, though they are no longer prominent in the spectrum. The period of these orbits is roughly $300T_c$.

Comparing the scaled action of the R_n with the classical values provides a more critical test than just looking at the figure. The classical scaled action of R_1 at $\epsilon_B = -0.6$ is $\tilde{S}_B^{cl}(R_1) = 0.827036$. Table 7.1 gives the scaled actions of the R_n which are shown in Figure 7.1. Agreement with $\tilde{S}_B^{cl}(R_1) = 0.827036$ is excellent: good to 3 parts in 10^6. The small deviation is probably due to bifurcations of the R_n which produce new closed orbits which slowly move to higher scaled action as the scaled

value and comparing the two recurrence spectra. It can also be checked by using a linear interpolation rather than a cubic spline. Consequently, $\tilde{S}_B < 500$ applies to the less accurate recurrence spectrum.

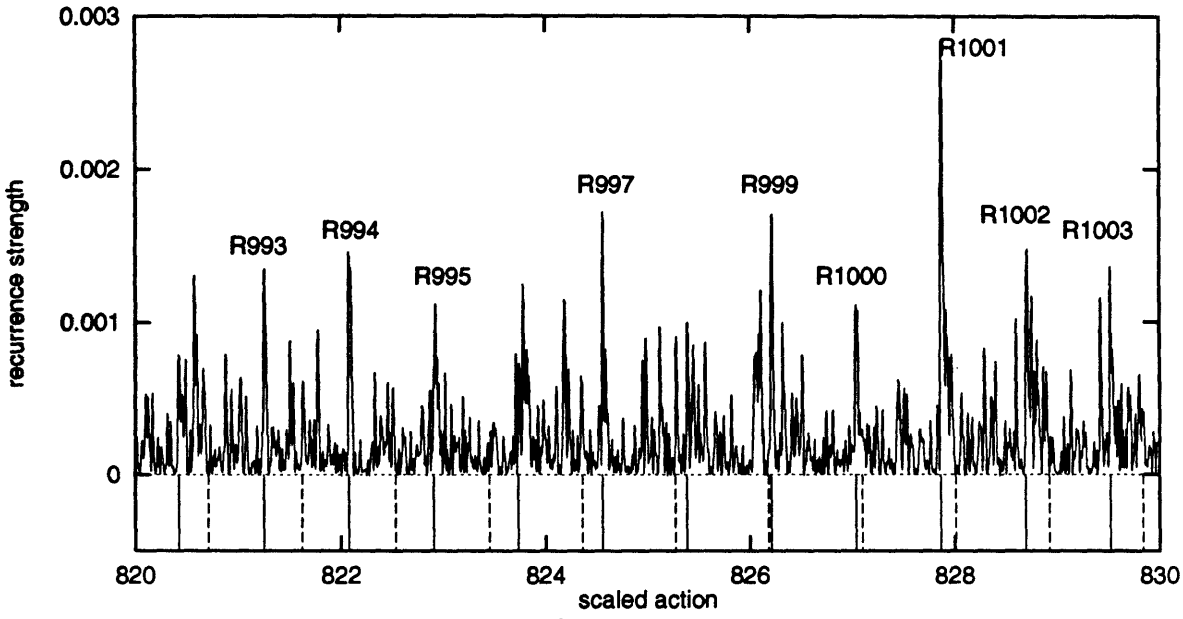

Figure 7-16: Recurrence spectrum near $\tilde{S}_B = 830$ for even-parity diamagnetic hydrogen, $\epsilon_B = -0.6$. Perpendicular orbits are labeled. Solid and dashed vertical lines are the classical action of repetitions of R_1 and V_1, respectively.

energy is raised above the bifurcation energy. Failure to resolve these as separate peaks could lead to a systematic shift to slightly higher $\tilde{S}_B$. These large scaled actions typically agree better with the classical value than small scaled actions because the fractional error in determining the center of a peak decreases linearly with increasing number of repetitions.

Having seen the 600^{th} repetition of the quasi-Landau orbit, the possibility of going to the 1000^{th} was irresistible. Results are shown in Figure 7-16. The repetitions of the parallel orbit have long since disappeared, and some of the repetitions of the perpendicular orbit are small, but the evidence for R_{1000} is clear. The period of these orbits is roughly $500T_c$.

Identifying long-period recurrences at higher scaled energies is inherently more interesting because this provides a test of closed-orbit theory in a chaotic region. Several things effect the identification of high-action recurrences at higher scaled energies. Computing spectra over such a wide range of fields is more difficult because of the large matrices which need to be diagonalized at the low field end of the constant scaled energy curve. This produces a more poorly resolved recurrence spectrum. High-action recurrence spectra in the chaotic region were obtained from the computed

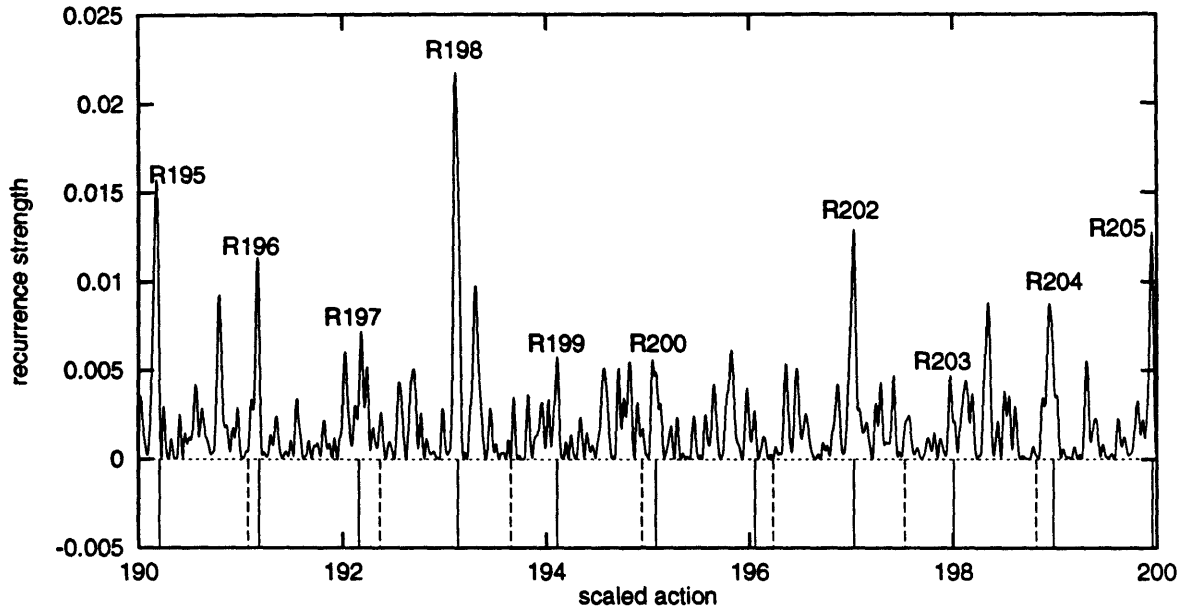

Figure 7-17: Recurrence spectrum near $\tilde{S}_B = 200$ for even-parity diamagnetic hydrogen, $\epsilon_B = -0.3$. Solid and dashed vertical lines are the classical action of repetitions of R_1 and V_1, respectively.

oscillator strength spectra for $1\,T \leq B \leq 8\,T$. The other issues are more fundamental. The parallel orbit can be unstable above $\epsilon_B = -0.54$, and this leads to an exponential decay in the recurrence strength as a function of repetition. The perpendicular orbit is stable up to $\epsilon_B = -0.127$, but there are many more recurrences above $\epsilon_B = -0.54$, and there is only so much recurrence strength to go around.[4]

The recurrence spectrum of even-parity diamagnetic hydrogen at $\epsilon_B = -0.3$ is shown in Figure 7-17 for $190 \leq \tilde{S}_B \leq 200$. Most of the repetitions of R_1 between R_{195} and R_{205} are clearly visible. In contrast, definite assignment of any of the peaks as repetitions of V_n is not possible.

Figure 7-18 shows that the repetitions of R_n are much less prominent for $\epsilon_B = -0.2$. R_{185} and R_{186} are clearly apparent. In addition, probable associations can be made for R_{184}, R_{188}, R_{189}, R_{190}, R_{192}, and R_{193}. A couple of the actions of the V_n line up with peaks, but this may be accidental.

[4]This difficulty has a simple analog in the oscillator strength spectrum. At a given field, the sum of all the oscillator strengths is 1. If the initial state is an S state, then all the oscillator strength is in the nP states for the field-free atom. Applying a magnetic field distributes the oscillator strength over $n/2$ levels in each n manifold. Applying a crossed electric field distributes the oscillator strength over $n^2/2$ levels.

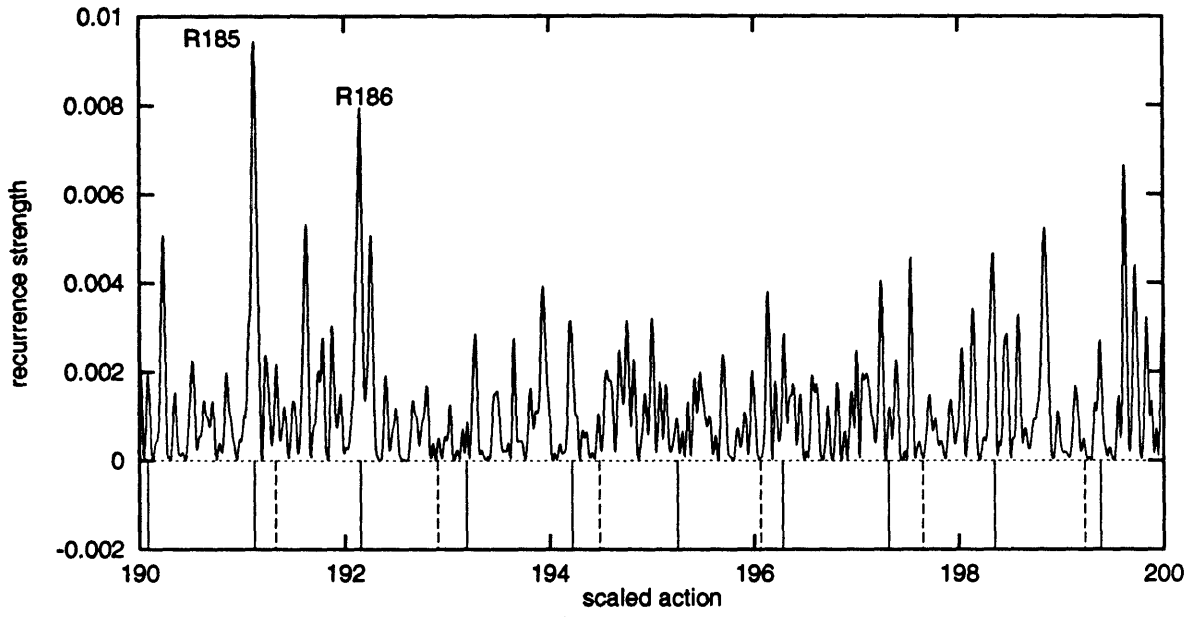

Figure 7-18: Recurrence spectrum near $\tilde{S}_B = 200$ for even-parity diamagnetic hydrogen, $\epsilon_B = -0.2$. Solid and dashed vertical lines are the classical action of repetitions of R_1 and V_1, respectively.

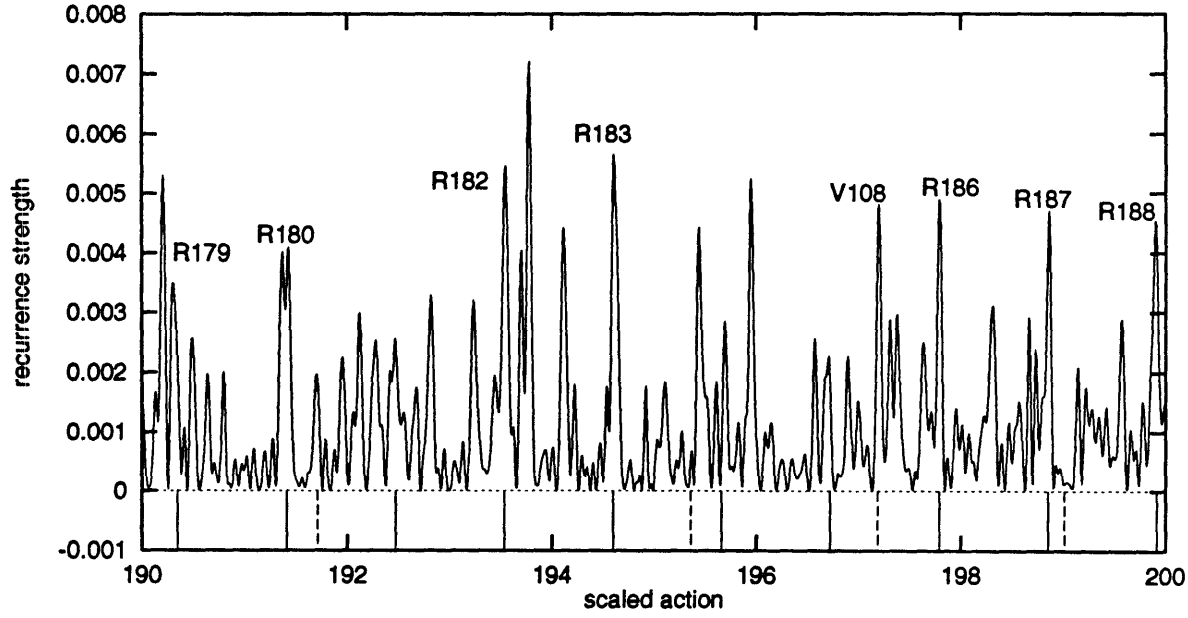

Figure 7-19: Recurrence spectrum near $\tilde{S}_B = 200$ for even-parity diamagnetic hydrogen, $\epsilon_B = -0.15$. Solid and dashed vertical lines are the classical action of repetitions of R_1 and V_1, respectively.

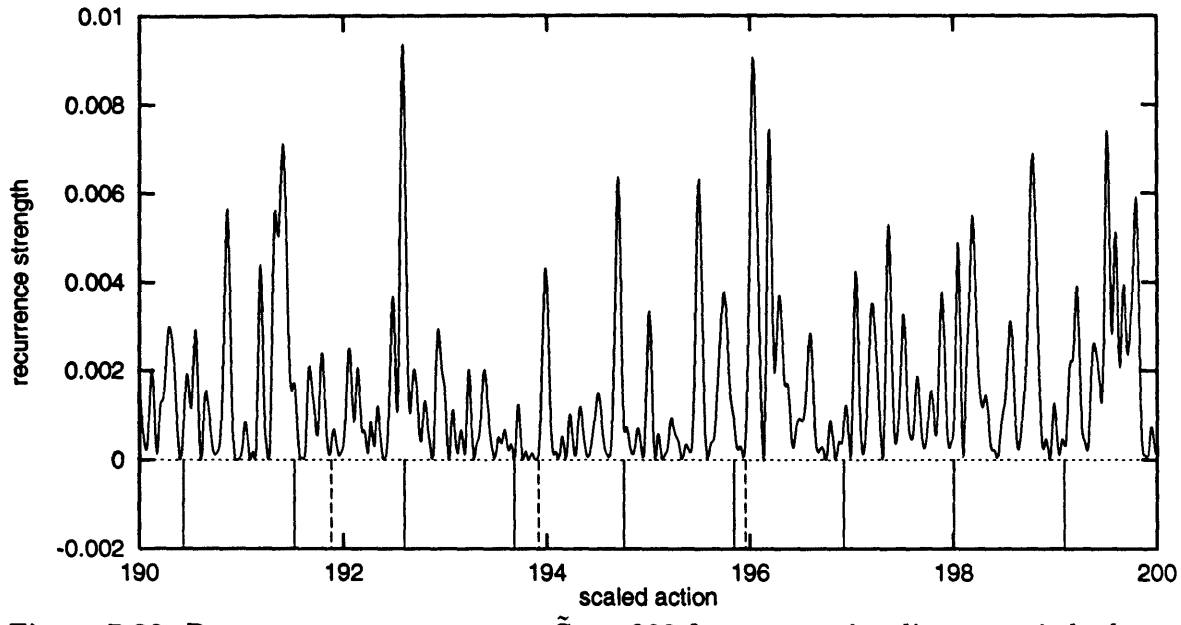

Figure 7-20: Recurrence spectrum near $\tilde{S}_B = 200$ for even-parity diamagnetic hydrogen, $\epsilon_B = -0.12$. Solid and dashed vertical lines are the classical action of repetitions of R_1 and V_1, respectively.

At $\epsilon_B = -0.15$, repetitions of R_1 are prominent again in the recurrence spectrum, as shown in Figure 7-19. One can also make tentative assignments of V_{108} and V_{106}. The stability of V_1 is a rapidly oscillating function of scaled energy in this region, and repetitions of the parallel orbit undergo a large number of bifurcations. This may lead to the increase of recurrence strength observed here.

At $\epsilon_B = -0.12$, repetitions of R_1 can be tentatively identified, but they are small, as shown in Figure 7-20. All the closed orbits of the system are unstable, and the classical system shows hard chaos in this region.

The identification of high-action recurrences at $\epsilon_B = -0.6$ was convincing and impressive. The identification of these high-action recurrences at higher scaled energy was less impressive. One might argue that there are a lot of peaks in the spectrum, and I just happened to hit a few with the scaled action of a few closed orbits. Taking the Fourier transform of these high-action recurrence spectra answers these arguments and introduces a way to untangle the repetitions of basic closed orbits from even more complicated recurrence spectra without having to do a peak by peak identification.

The idea of taking a Fourier transform of recurrence spectra (which is itself the Fourier transform of the oscillator strength or density of states) should be explained.

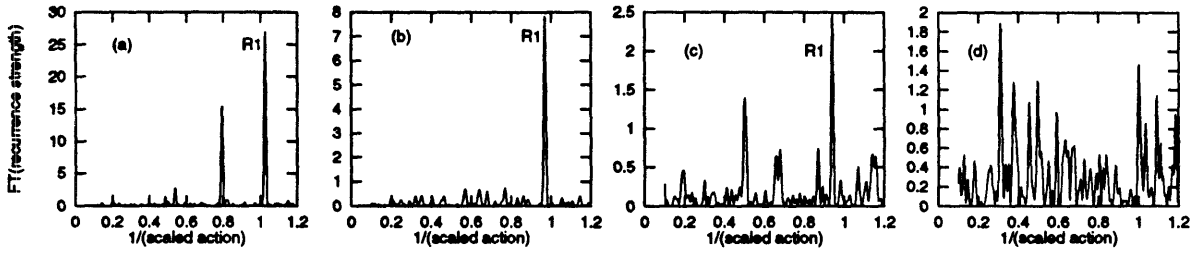

Figure 7-21: Fourier transforms of diamagnetic recurrence spectra. (a) $\epsilon_B = -0.3$; (b) $\epsilon_B = -0.2$; (c) $\epsilon_B = -0.15$; (d) $\epsilon_B = -0.12$.

What we are actually doing is taking a power spectrum of a power spectrum. The first power spectrum (the recurrence spectrum) identifies the periodicities in the spectrum. Since the repetitions of periodic orbits are also periodic, the recurrence spectrum itself has strong periodicities which are the scaled actions of the primitive orbits which have strong repetitions. Consequently, the power spectrum of the recurrence spectrum will reveal these repetitions. Therefore, I refer to it as the *repetition spectrum.*

Figure 7-21 shows the Fourier transforms of diamagnetic recurrence spectra. Only the high-action range ($100 \leq \tilde{S}_B \leq 200$) is included. Figure 7-21(a) is the repetition spectrum at $\epsilon_B = -0.3$. The largest peak corresponds to the scaled action of R_1. The inverse of its position is $\tilde{S}_B^{qm} = 0.9753$. The scaled action of R_1 at $\epsilon_B = -0.3$ is $\tilde{S}_B^{cl}(R_1) = 0.9754$. The prominent peak near $1/\tilde{S}_B = 0.8$ corresponds to V_1^1. The repetition spectrum at $\epsilon_B = -0.2$ is shown in Figure 7-21(b). The largest peak again corresponds to R_1. The inverse of its position is $\tilde{S}_B^{qm} = 1.0331$. The scaled action of R_1 at $\epsilon_B = -0.2$ is $\tilde{S}_B^{cl}(R_1) = 1.0331$. Figure 7-21(c) is the repetition spectrum at $\epsilon_B = -0.15$. The inverse of the position of the peak labeled R_1 is $\tilde{S}_B^{qm} = 1.0645$. The scaled action of R_1 at $\epsilon_B = -0.15$ is $\tilde{S}_B^{cl}(R_1) = 1.0634$.

In contrast, the repetition spectrum at $\epsilon_B = -0.12$ is shown in Figure 7-21(d). None of the peaks correspond to the scaled action of R_1 which is $\tilde{S}_B^{cl}(R_1) = 1.0820$. The reason is as follows. We have seen that the stability of R_1 below $\epsilon_B = -0.127$ results in its repetitions having a strong signature in the recurrence spectrum. At low ϵ_B, the strength of these recurrences compared with other recurrences allows a determination of the classical action of R_1 which is accurate to several parts in 10^6.

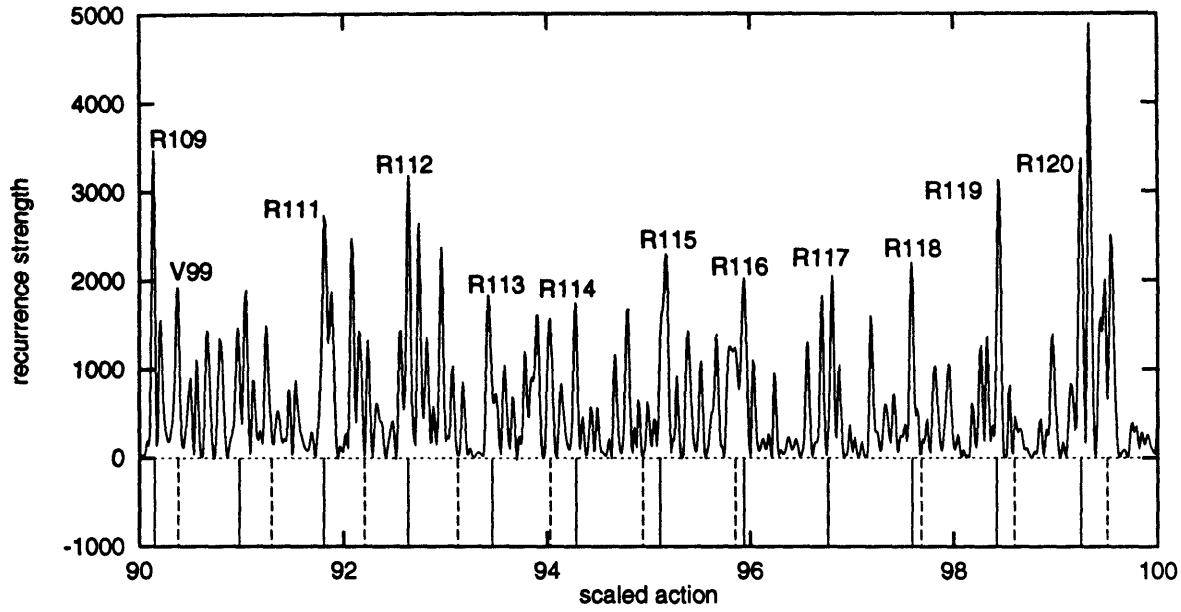

Figure 7-22: State density recurrence spectrum near $\tilde{S}_B = 100$ for even-parity diamagnetic hydrogen, $\epsilon_B = -0.6$. Solid and dashed vertical lines are the classical action of repetitions of R_1 and V_1, respectively.

The very long repetitions of R_1 gradually decrease in strength as the scaled energy is raised. Once it becomes unstable, the recurrences corresponding to many repetitions of R_1 no longer provide a distinctive feature in the spectrum.

Long-Period State Density Recurrence Spectra

The state density recurrence spectra R_{ds} should contain information about every periodic orbit in the system. There are a large number of large peaks, and extracting information about simple orbits is more difficult than just looking at a graph. Yet in spite of the increased complexity, the rotators and vibrators still play a prominent role.

At $\epsilon_B = -0.6$, R_{ds} can be obtained by transforming the density of states for $0.1T \leq B \leq 8T$. The trouble is that the peaks are so narrow and there are so many recurrences, that it just looks like noise at large action. One can identify individual recurrences by blowing up the scaled action axis and finding peaks at the scaled action of repetitions of R_1 and V_1. Peaks can be positively identified in this way, but the density of other large recurrences prevents determination of their positions

to the precision obtained for the absorption recurrence spectrum. Decreasing the resolution enhances the appearance of the R_n and V_n, and R_{ds} is shown in Figure 7-22. Most of the rotators are visible, but the vibrators are difficult to identify with certainty. Detailed identification of all the peaks would require computation of all the periodic orbits with actions in this range. This is a challenging task, and the recurrence spectrum gives some idea how difficult it is to implement the trace formula to compute the level density of a complex system.

7.1.6 Ionizing Orbits of Diamagnetic Hydrogen

Closed-orbit theory predicts that in the semiclassical limit, quantum spectra can be computed by summing over the closed orbits of the classical system. In Rydberg atoms in strong fields, both narrow spectral features and periodic orbits persist for some distance above the ionization limit. Interpreting spectral features in terms of periodic orbits has been successful both above and below the ionization limit.

It is natural to ask whether the ionizing orbits can be related to the quantum features. I have computed many ionization times for ionizing orbits of hydrogen in a magnetic field. If we consider the classical linewidth to be the inverse of the ionization time, then both the average classical linewidth and the distribution of classical linewidths are similar to the quantum result in the region where the quantum ionization times (linewidths) are known.

To compute the ionization time, an orbit is started near the origin and computed for a time which corresponds to a linewidth of less than $30MHz$. The time at which the orbit last passed through the $z = 0$ plane is taken as the ionization time. Orbits which do not return to the origin even once are omitted from consideration, as any contribution they would have to the quantum spectrum is assumed to be in the broad continuum background and not the narrow spectral features.

In the region above the ionization limit and below the first excited Landau level, the quantum mechanical probability distribution has been found to be given by the Porter-Thomas distribution [GDG93]. In the region where there is one Landau channel open ($B/2 < E < 3B/2$, roughly $3\,cm^{-1} < E < 9\,cm^{-1}$ at $B = 6\,T$), the quantum

linewidth distribution is well approximated by

$$P(\Gamma) = \frac{1}{\sqrt{2\pi\Gamma}} e^{-\Gamma/2}, \tag{7.6}$$

where the linewidths Γ are normalized so that the average is one. It is useful to view the probability of having a linewidth less than Γ, which is given by

$$Pl(\Gamma) = \int_0^\Gamma \frac{1}{\sqrt{2\pi\Gamma}} e^{-\Gamma/2}\, d\Gamma. \tag{7.7}$$

The quantum linewidth distribution has not been measured in the region where there is more than one channel available for ionization, but it has been predicted that each time a Landau threshold is crossed, another factor of Γ enters the linewidth distribution. This predicts a dramatic effect when the first Landau threshold is crossed, because the most probable linewidth is no longer zero. In the region where there are two Landau channels open ($3B/2 < E < 5B/2$, roughly $9\,cm^{-1} < E < 15\,cm^{-1}$ at $B = 6\,T$), the quantum linewidth distribution is predicted to be

$$P(\Gamma) = \sqrt{\frac{\Gamma}{2\pi}} e^{-\Gamma/2}. \tag{7.8}$$

So,

$$Pl(\Gamma) = \int_0^\Gamma \sqrt{\frac{\Gamma}{2\pi}} e^{-\Gamma/2}\, d\Gamma. \tag{7.9}$$

In the regions where there is one Landau channel open, the classical linewidth distribution is similar to the Porter-Thomas distribution, as shown in Figure 7-23. When there is more than one Landau channel open, the distribution of classical ionization times is still peaked at zero with the same shape as it had with only a single open Landau channel. All that has happened is that the average classical linewidth has become larger. This is because the classical system knows nothing of Landau levels.

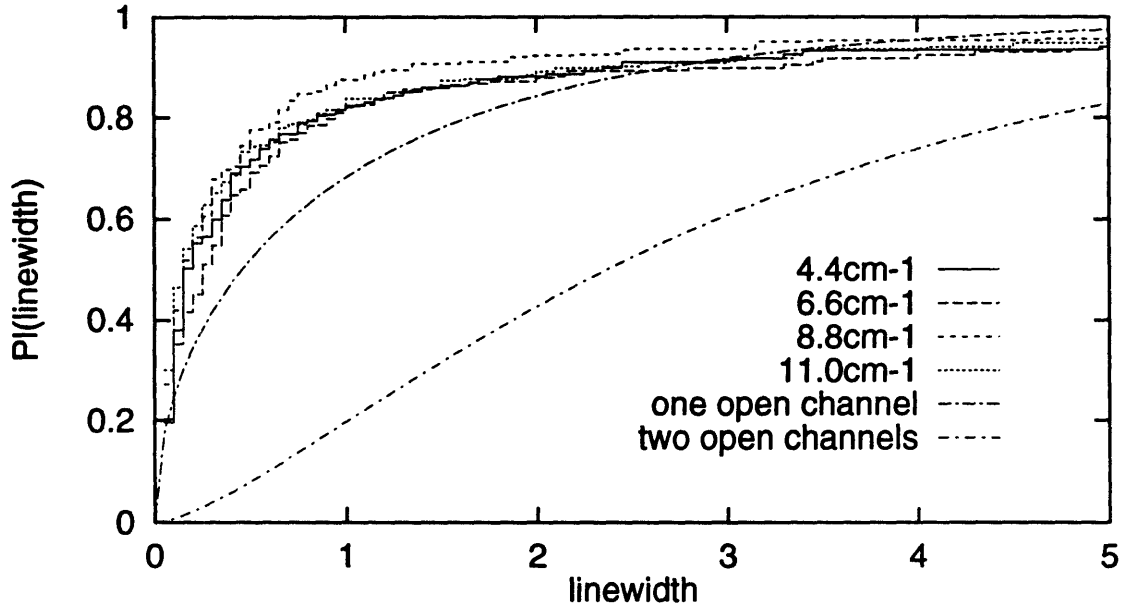

Figure 7-23: Classical linewidth distributions compared with predicted quantum behavior.

7.2 Lithium

The charge distribution of the $1S$ electrons fails to shield the charge of the nucleus at close distances. This gives rise to significant quantum defects for the S and P states. We have seen that the core potential can cause chaos in the classical dynamics of diamagnetic lithium. Furthermore, it can cause large level repulsions and a Wigner distribution of energy levels in even-parity lithium, even in the range where diamagnetic hydrogen is regular. In contrast, in odd-parity diamagnetic lithium, level repulsions are small and the nearest-neighbor distribution is Poisson-like in the region where hydrogen is regular.

Closed-orbit theory accounts for the core by the scattering of recurrences from one orbit into another by the alkali-metal core. This process produces larger core-scattered recurrences in the even-parity recurrence spectrum, but I will show that it gives a chaotic proliferation of recurrences in both the even- and the odd-parity recurrence spectra.

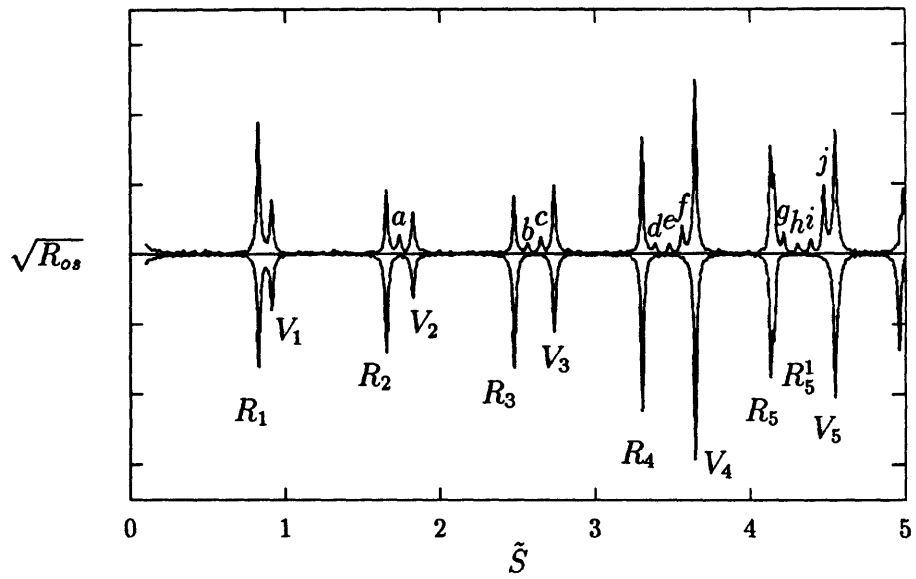

Figure 7-24: Even-parity recurrence spectra for $\epsilon_B = -0.6$, $m = 0$. R_{os} for lithium (top) and hydrogen (bottom). Rotators and vibrators are labeled in the hydrogenic spectrum. The extra recurrences in the lithium spectrum can be understood as scattering from one orbit into another by the alkali-metal core, as shown in Table 7.2.

7.2.1 Core Scattering

Figure 7-24 compares R_{os} for even-parity lithium and hydrogen. Rotators and vibrators are labeled in the hydrogenic spectrum. Only the main rotators and vibrators are present for $\tilde{S}_B < 4$. R_5 and V_5 have bifurcated giving R_5^1 and V_5^1, respectively. At this scale, the two recurrence spectra are similar, except that the recurrence strengths of R_2 and R_3 differ, and several extra recurrences appear in lithium. These extra recurrences can be understood as scattering from one orbit into another by the alkali-metal core. For example, the recurrence labeled a is at an action which is the sum of the actions of R_1 and V_1, indicating that this recurrence arises from a wave which travelled out and back along R_1 and then was scattered into V_1. Recurrences marked b–j can be understood similarly, as shown in Table 7.2. Core-scattered recurrences are also present in R_{os} for odd-parity lithium, but they tend to be smaller than in even-parity lithium, and they only appear at higher action ($\tilde{S}_B > 6$).

The core-scattered recurrences listed in Table 7.2 provide an opportunity to test

Table 7.2: Scaled actions of selected core-scattered recurrences in R_{os} for even-parity lithium for $m = 0$, $\epsilon_B = -0.6$ are compared with the sum of the actions of their components. A^{qm} is the recurrence amplitude in the computed recurrence spectrum. A^{ss} is the singly-scattered recurrence amplitude. A^{ds} is the doubly-scattered recurrence amplitude.

$\tilde{S}_B^{qm}$	Components	Sum	Label	A^{qm}	A^{ss}	A^{ds}
1.7389	$R_1 + V_1$	1.7397	a	9.74	9.74	9.74
2.5674	$R_2 + V_1$	2.5670	b	5.18	4.70	5.18
2.6532	$R_1 + V_2$	2.6533	c	8.57	7.67	8.57
3.3928	$R_3 + V_1$	3.3931	d	4.88	4.33	4.57
3.4828	$R_2 + V_2$	3.4807	e	5.14	3.70	4.45
3.5671	$R_1 + V_3$	3.5666	f	14.9	12.9	13.7
4.2188	$R_4 + V_1$	4.2199	g	8.97	8.84	9.38
4.3084	$R_3 + V_2$	4.3068	h	5.47	3.40	4.24
4.3935	$R_2 + V_3$	4.3938	i	8.22	6.10	7.33
4.4778	$R_1 + V_4$	4.4772	j	37.2	33.1	36.0

the formula for singly-scattered recurrence amplitudes,

$$A_{i+j} = A_i A_j K P_{\theta_i,\theta_j} \tag{7.10}$$

where A_{i+j} is the amplitude of the core-scattered recurrence, A_i is the amplitude of one of the components, A_j is the amplitude of the other, P_{θ_i,θ_j} is the probability of scattering from θ_i into θ_j, and K is a proportionality constant which represents the fact that we do not know the correct overall normalization. Since all the single-scattering events which produce the recurrences in Table 7.2 have the same KP_{θ_i,θ_j}, we should be able to simply compute $KP_{0,\frac{\pi}{2}} = KP_{\frac{\pi}{2},0}$ for $R_1 + V_1$ and use this number to compute the singly-scattered recurrence amplitudes A^{ss} of the other core-scattered recurrences. Table 7.2 shows good agreement between the actual quantum mechanical recurrence amplitudes and those given by the single-scattering model. However, the amplitudes are systematically low because multiple scattering becomes possible for the higher-action core-scattered recurrences.

Accounting for the doubly-scattered components of the higher action recurrences is difficult. Both parallel orbits and the scattering probability between them must be

considered. I obtained K from the amplitude of $R_2 + V_1$ and $P_{0,\pi}$ from $R_1 + V_2$. $P_{0,\pi}$ represents the probability of scattering from the parallel orbit for $z > 0$ (V_n^+) into the parallel orbit for $z < 0$ (V_n^-). A^{ds} is computed by adding the amplitudes of all the combinations of orbits which sum to the right action. For example,

$$A^{ds}_{R1+V2} = K\left(4P_{0,\frac{\pi}{2}}A_{R_1}A_{V_2} + 4P^2_{0,\frac{\pi}{2}}A_{R_1}A^2_{V_2} + 4P_{0,\frac{\pi}{2}}P_{0,\pi}A_{R_1}A^2_{V_2}\right). \tag{7.11}$$

$4P_{0,\frac{\pi}{2}}A_{R_1}A_{V_2}$ accounts for the four possible combinations
$(R_1 + V_2^+)$,
$(R_1 + V_2^-)$,
$(V_2^+ + R_1)$, and
$(V_2^- + R_1)$.
$4P^2_{0,\frac{\pi}{2}}A_{R_1}A^2_{V_2}$ accounts for the four possible combinations
$(V_1^+ + R_1 + V_1^+)$,
$(V_1^+ + R_1 + V_1^-)$,
$(V_1^- + R_1 + V_1^+)$, and
$(V_1^- + R_1 + V_1^-)$.
$4P_{0,\frac{\pi}{2}}P_{0,\pi}A_{R_1}A^2_{V_2}$ accounts for the four possible combinations
$(R_1 + V_1^- + V_1^+)$,
$(R_1 + V_1^+ + V_1^-)$,
$(V_1^- + V_1^+ + R_1)$, and
$(V_1^+ + V_1^- + R_1)$.
Needless to say, enumerating all the possibilities for the core-scattered recurrences at higher action gets rather messy. However, Table 7.2 shows that the doubly-scattered recurrence amplitudes A^{ds} are consistently closer to the quantum mechanical recurrence amplitudes A^{qm} than the singly-scattered recurrence amplitudes A^{ss}. One may think that accounting for higher-order multiple scattering would account for the remaining error, but it does not, and the additional amplitudes due to triple scattering are extremely small. The errors are more likely due to an underestimation of $P_{0,\pi}$.

John Shaw (private communication) has provided some preliminary results using

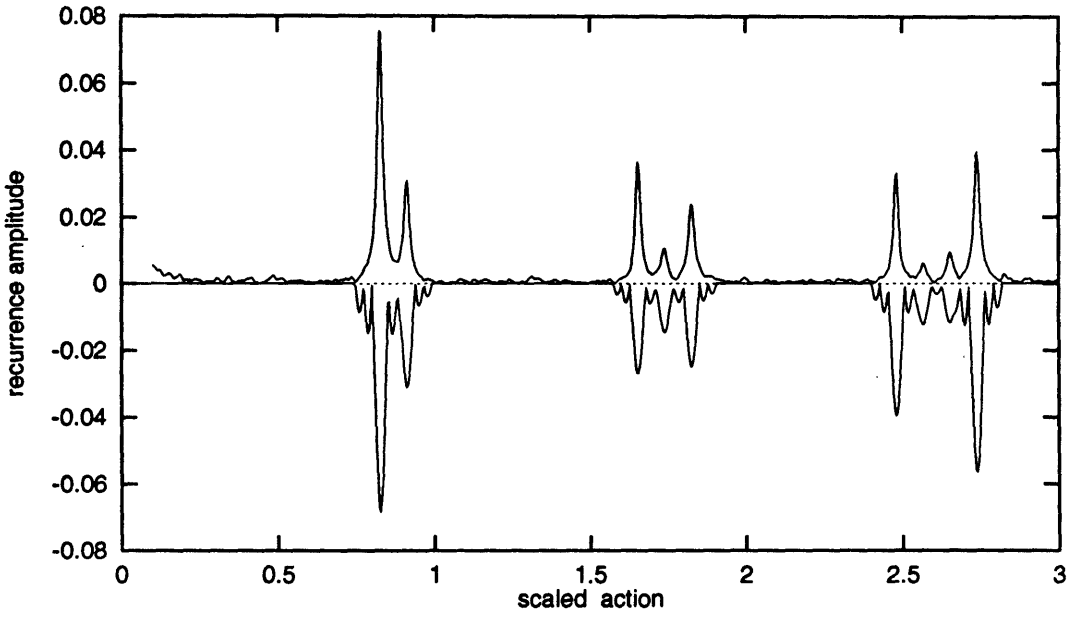

Figure 7-25: Comparison of core-scattered recurrences in quantum recurrence spectrum (top) with closed-orbit theory (bottom) at $\epsilon_B = -0.6$. (Closed-orbit theory recurrence spectrum courtesy of John Shaw.)

closed-orbit theory to compute core-scattered recurrences. These are compared with the quantum recurrence spectra in Figure 7-25. His spectra have a number of spurious oscillations due to his failure to use a windowing function when performing Fourier transforms. Aside from this, the agreement with the quantum results is good.

The state density recurrence spectrum R_{ds} of even-parity lithium also shows recurrence scattering. R_{ds} for even-parity lithium and hydrogen are compared in Figure 7-26(a). As discussed previously, we see the periodic orbit around the nucleus and its repetitions (O_n). The recurrence strength of the rotators and vibrators differs significantly between lithium and hydrogen because these orbits pass through the alkali-metal core. The recurrence strength of the orbit around the nucleus is the same for lithium and hydrogen, because this orbit does not pass through the core. The recurrence strength of the rotators is strongly affected by the core. R_2 is smaller in lithium than in hydrogen, and R_3 is much smaller. Perhaps this is due to the recurrence strength of the first return being scattered into other orbits and consequently not being present in the second and third repetitions.

For $\tilde{S}_B < 4$, the positions of recurrences in R_{ds} are the same for hydrogen and lithium. For $\tilde{S}_B > 4$ there are a number of small peaks in lithium which do not

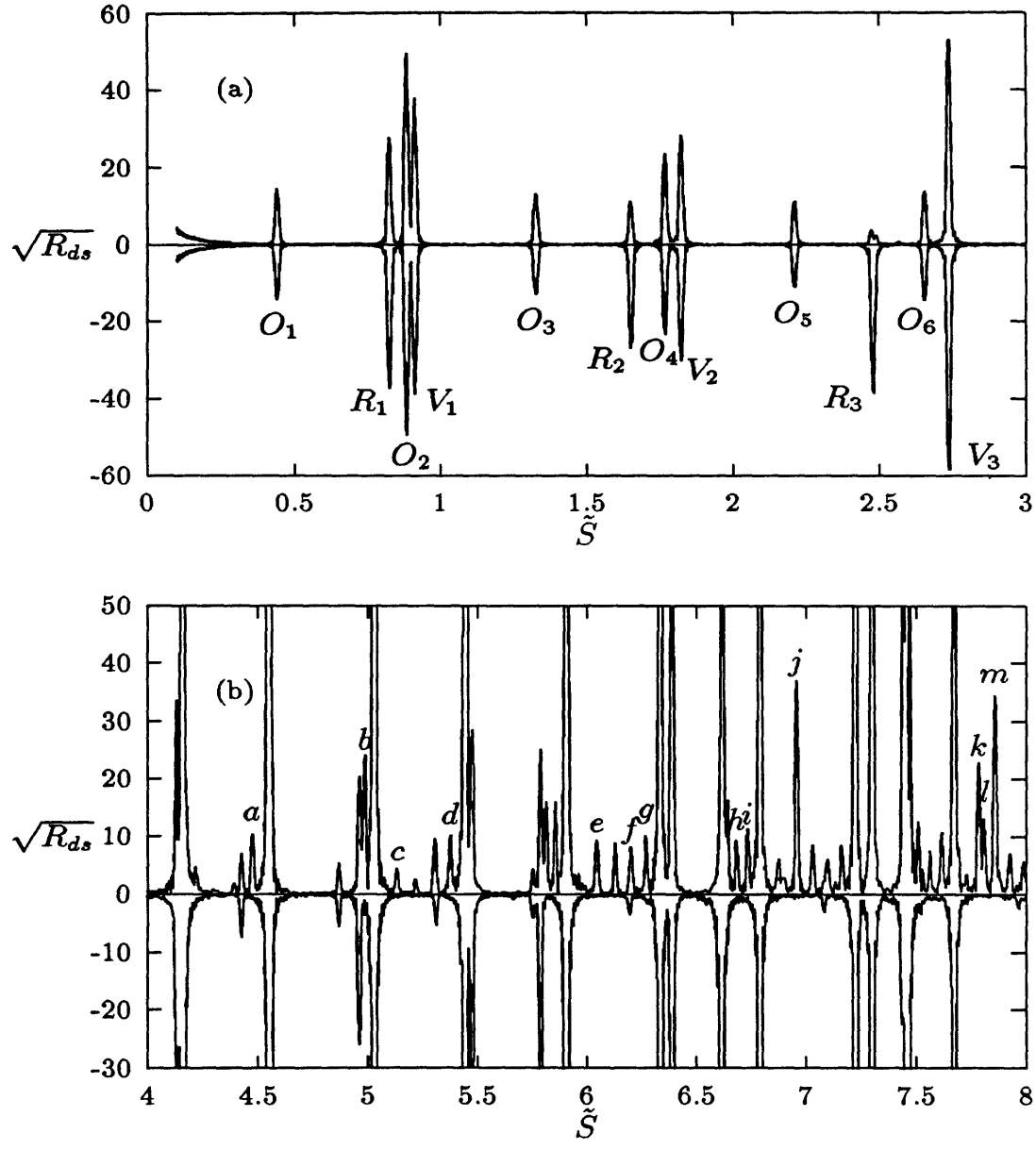

Figure 7-26: Even-parity recurrence spectra for $\epsilon_B = -0.6$, $m = 0$. R_{ds} for lithium and hydrogen. The top of each mirror plot is lithium. The bottom of each mirror plot is hydrogen. Rotators and vibrators are labeled in the low action hydrogenic spectrum. The extra recurrences in the lithium spectra can be understood as scattering from one orbit into another by the alkali-metal core, as shown in Table 7.3.

Table 7.3: Scaled actions of selected core-scattered recurrences in R_{ds} are compared with the sum of the actions of their components.

$\tilde{S}_B^{qm}$	Components	$\tilde{S}_{sum}$	Label
4.4778	$R_1 + V_4$	4.4762	a
4.9886	$R_5^1 + R_1$	4.9866	b
5.1340	$R_4 + V_2$	5.1341	c
5.3781	$R_1 + V_5$	5.3772	d
6.0470	$R_4 + V_3$	6.0471	e
6.2027	$R_2 + V_5$	6.2030	f
6.2719	$R_1 + V_6$	6.2715	g
6.6843	$R_2 + R_6^1$	6.6827	h
6.7351	$R_7^1 + R_1$	6.7348	i
6.9580	$R_4 + V_4$	6.9581	j
7.7854	$R_5 + V_4$	7.7832	k
7.8086	$R_5^1 + V_4$	7.8096	l
7.8588	$R_4 + V_5$	7.8590	m

occur in hydrogen, as shown in Figure 7-26(b). Many of these recurrences can be interpreted in terms of core scattering because they are located at an action which is the sum of the actions of other recurrences. Some of the extra recurrences in lithium are identified in this way in Table 7.3.

For odd-parity lithium and hydrogen, R_{ds} are almost identical for $\tilde{S}_B < 50$. There are some very small features in R_{ds} for odd-parity lithium, but they are at the same level as the noise (about 2000 times smaller than the largest recurrence peaks), and we have not been able to positively identify them as core-scattered recurrences. Some discrepancies begin to appear for $\tilde{S}_B > 50$, but individual recurrences are not resolved at these high actions.

Core scattering is more prominent in R_{os} than R_{ds}, and it presents some simplifications and some difficulties for closed-orbit theory and periodic-orbit theory. It suggests that the core can be accounted for by considering hydrogenic orbits and their permutations and combinations. As a result, using these theories to compute spectra may not require computing the closed orbits of lithium which are not found in hydrogen. The need to modify the theories to include a quantum model of core

scattering is a consequence of the failure of the semiclassical approximation in the core region, because when a trajectory passes through the core region, it has a relatively small angular momentum compared with $\hbar$. As a result, it is more reasonable to approximate an incoming wave with a partial wave expansion than with a classical trajectory.

7.2.2 Recurrence Proliferation as a Measure of Chaos

If we denote the number of periodic orbits with action less than S as $N(S)$, it is a general result [GUT90] that regular systems have

$$N(S) \propto S^n, \tag{7.12}$$

where n is the number of degrees of freedom. Irregular systems have

$$N(S) \propto e^S. \tag{7.13}$$

The number of closed orbits in a system proliferates in the same manner. Being able to see the signature of closed orbits in quantum recurrence spectra suggests that the difference between regular and chaotic systems should be manifest in the recurrence spectra.

If we define $N_{os}(\tilde{S}_B)$ as the number of peaks in $R_{os}(\tilde{S}_B)$ with action less than $\tilde{S}_B$, then we expect that $N_{os}(\tilde{S}_B)$ will be larger for chaotic systems than for regular systems. Figure 7-27(a) shows $N_{os}(\tilde{S}_B)$ for $m = 0$ even-parity lithium and hydrogen at $\epsilon = -0.6$. We find that the number of recurrences is greater in lithium than in hydrogen, a result which is qualitatively consistent with the proliferation of orbits in chaotic systems. However, due to the width of the recurrence peaks, there is a maximum in the number of peaks which can be resolved in an action interval, and $N_{os}(\tilde{S}_B)$ approaches a line at large $\tilde{S}_B$. The slope of this line depends mainly on the width of the recurrence peaks, but there is also a dependence on the distribution of recurrence heights about their mean. The difference in the slopes in Figure 7-27(a) is

Table 7.4: χ^2 for and parameters of best-fit polynomials to $N_{os}(\tilde{S})$ for $N_{os}(\tilde{S}) \approx \sum_1^n a_n \tilde{S}^n$.

Atom	Parity	a_1	a_2	a_3	χ^2
Hydrogen	even	1.39	0.261	0	2.40
Hydrogen	even	1.50	0.247	0.0042	2.31
Lithium	even	−2.20	1.502	0	2.37
Lithium	even	1.16	0.292	0.103	0.81
Lithium	odd	−0.448	0.536	0	1.88
Lithium	odd	1.01	0.192	0.0191	0.94

because recurrence heights are more broadly distributed about their mean in hydrogen than in lithium.

To quantitatively compare $N_{os}(\tilde{S}_B)$ with $N(\tilde{S})$, we must look at $N_{os}(\tilde{S}_B)$ for $\tilde{S}_B$ lower than where the peak density is saturated. Figure 7-27(b) shows that $N_{os}(\tilde{S}_B)$ for even-parity hydrogen finds excellent agreement with a second order polynomial with no constant term. Recurrence peaks proliferate much more quickly in even-parity lithium, and a region of lower action needs to be examined to avoid saturation. For $\tilde{S}_B < 8$, we find that a third order polynomial provides a statistically significant better fit than a second order polynomial (Figure 7-27(c)). We can understand this in terms of core scattering.

Core scattering gives rise to recurrences in even-parity lithium which are permutations and combinations of those in even-parity hydrogen. If only singly scattered recurrences contributed, the proliferation of recurrences would be cubic. If every possible doubly scattered recurrence is present, the proliferation is exponential. However, many of the doubly scattered recurrences have the same action as singly scattered recurrences. For example, $R_2 + V_2$ has the same action as $R_1 + V_2 + R_1$. Furthermore, the permutations of a given combination of closed orbits also have the same action. For example, $R_5^1 + V_1 + R_1$ has the same action as $R_1 + R_5^1 + V_1$. Therefore, we expect the proliferation of observed peaks in the recurrence spectrum to be cubic in even-parity lithium due to the high degeneracies of core-scattered peaks.

Beyond confirming the exponential growth of orbits predicted by Eqn. 7.13, one

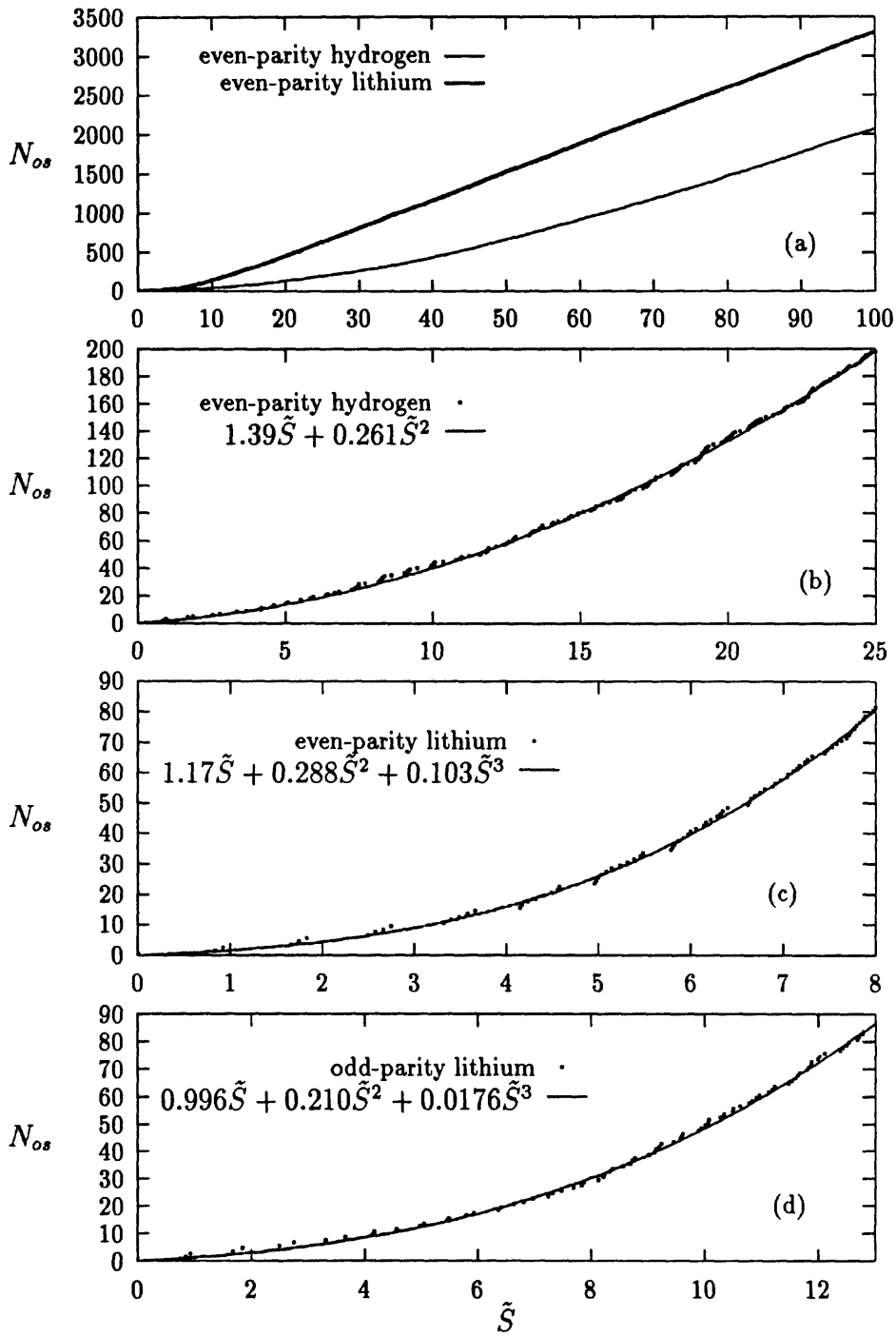

Figure 7-27: Accumulated recurrences less than $\tilde{S}$ (N_{os}).

can use the values of N_{os} computed from the quantum spectrum to reveal the presence of chaotic motion in a system that may appear to be regular. The odd-parity states of lithium provide an example of this approach. N_{os} for odd-parity lithium (Fig. 7-27(d)) clearly displays a cubic proliferation of recurrences much like even-parity lithium. This is also shown in Table 7.4. Not only is χ^2 smaller for a cubic polynomial, but the linear term in the best-fit quadratic polynomial has become negative as in the case of even-parity lithium.

The analysis in this section has enabled us to identify disorderly behavior in lithium in a regime where the nearest-neighbor distribution provided little insight. This procedure, which can be loosely described as recurrence counting, constitutes a potentially valuable general technique for predicting classical behavior from the quantum response.

Chapter 8

Recurrence Spectroscopy in an Electric Field

For it is written, "I will destroy the wisdom of the wise; the intelligence of the intelligent I will frustrate." –1 Corinthians 1:19

Previous to this work, the connections between classical dynamics and Stark spectra had not been as fully elucidated as they have been in the case of diamagnetism. Freeman [FEB78, FRE79] performed the analog of the Garton-Tomkins experiment and connected a single periodic modulation at $E = 0$ with a closed orbit parallel to the field. Eichmann [ERW88] performed scaled-energy spectroscopy in sodium for $\epsilon_F = -2.5$ and connected peaks in the recurrence spectrum with closed orbits of hydrogen at low scaled action.

The Hamiltonian of hydrogen in an electric field F in the z direction (atomic units),

$$H = \frac{p^2}{2} - \frac{1}{r} + Fz. \tag{8.1}$$

As described in Chapter 3, this Hamiltonian can be rescaled using the substitutions $r = F^{-1/2}\tilde{r}$ and $p = F^{1/4}\tilde{p}$. The scaled Hamiltonian, $\tilde{H} = F^{-1/2}H$, has no explicit dependence on the field, and the classical dynamics depends only on the scaled energy

$\epsilon = EF^{-1/2}$, not on E and F separately.

The work presented here represents a much fuller experimental and theoretical examination. The work in the continuum ($\epsilon_F > -2.0$) has been carried out in collaboration with Jing Gao and John Delos, who used closed-orbit theory to make predictions about continuum Stark spectra [GAD94, CJS95]. The primary motivations for the continuum experiments presented here were to test these predictions and also to test the repair closed-orbit theory near bifurcations. Our results in the bound state region ($\epsilon_F < -2.0$) are in anticipation of the application of closed-orbit theory in that regime.

The photoabsorption spectrum of a single-electron atom in an electric field F changes strikingly with decreasing energy [FRE79, LDB81]. In the positive energy regime, the spectrum is smooth and displays a single periodic oscillation. Below the classical ionization threshold ($\epsilon_F = -2$), the spectrum is quasidiscrete. These contrasting patterns reflect complementary aspects of atomic behavior: the former can be simply interpreted in terms of classical dynamics, while the latter is naturally described in terms of the system's eigenstates. As the energy decreases from $\epsilon_F > 0$ to $\epsilon_F = -2$, the broad peaks become narrow and new resonances gradually appear. Quantum calculations are possible in this region [LUB80], but they offer little insight into the connections with classical dynamics. This region is fertile territory for investigating the connections between quantum and classical descriptions.

Below $\epsilon_F = -2$, the spectrum for hydrogen is relatively simple. The energy-level spectrum is well approximated by a perturbation expansion. Each eigenstate can be assigned parabolic quantum numbers, and levels can cross each other due to an additional symmetry which can be expressed as conservation of a generalized Runge-Lenz vector, as described in Chapter 2. In contrast, computing the spectrum of alkali-metals requires a large numerical effort. Once levels from two or more n manifolds have been mixed, assignment of quantum numbers is difficult. Furthermore, strong level repulsions prevent the levels from crossing. Figure 2-2 contrasts the behavior of lithium and hydrogen in the quasidiscrete regime. Lithium displays chaotic classical motion in most of this regime, so studying the connections between quantum and

classical features is of great interest.

Closed-orbit theory provides the foundation for interpreting recurrence spectra in terms of closed classical orbits. The recurrence spectra of single-electron atoms is dominated by the orbits parallel to the electric field and those which bifurcate from them. Consequently, the classical dynamics of hydrogen in an electric field is much more tractable than in the case of diamagnetic hydrogen. A detailed discussion of the closed orbits is presented here to provide the foundation for interpreting the Stark recurrence spectra presented later.

8.1 Hydrogenic Closed Orbits

8.1.1 Hamiltonian and Separation of Variables

The Hamiltonian of hydrogen in an electric field is separable in parabolic and semiparabolic coordinates. In contrast, the valence electron in alkali-metal atoms experiences a potential which deviates from $1/r$ near the origin due to the charge distribution of the inner electrons. This potential is spherically symmetric, but it prevents the separation of variables in the presence of an applied electric field. As a result, the motion can be chaotic for certain energy and field values. However, we begin by discussing the closed orbits of hydrogen in an electric field because recurrence spectra of lithium can be interpreted in terms of these orbits and the process of scattering by the core.

As discussed in Chapter 3, the classical dynamics of hydrogen in an electric field depends only on $\epsilon_F = EF^{-1/2}$ and not on E and F separately. The action scales such that $S = 2\pi w_F \tilde{S}_F$ where $w_F = F^{-1/4}$.[1] Furthermore, separation of variables can be accomplished using semiparabolic coordinates ($u = (r+z)^{1/2}$, $v = (r-z)^{1/2}$). The

[1]The F subscript on the scaled action will be dropped for the remainder of this chapter, because there is no possibility of confusion with $\tilde{S}_B$, and because subscripts on $\tilde{S}$ will be used for other purposes. The subscript F is retained on the scaled energy and the scaled field.

Hamiltonian (for $L_z = 0$) is

$$H = \frac{1}{2(u^2+v^2)}({p_u}^2 + {p_v}^2 - 4) + \frac{1}{2}F(u^2 - v^2). \tag{8.2}$$

For numerical computations a "regularized" Hamiltonian, $h = (u^2+v^2)(H-E)+2$, is introduced to remove the singularity:

$$h = \frac{{p_u}^2}{2} + \frac{{p_v}^2}{2} + \frac{1}{2}F(u^4 - v^4) - E(u^2+v^2) = 2. \tag{8.3}$$

Note that the regularized energy is always equal to two, and the real energy, E, enters the regularized Hamiltonian as a parameter. For $F = 0$ and $E < 0$, the regularized Hamiltonian represents two uncoupled oscillators both having frequency $\omega = (-2E)^{1/2}$. The electric field introduces anharmonic terms but does not couple the oscillators. The separation of variables and the resulting quasiperiodic motion is the consequence of a constant of motion in addition to E and L_z [RED64].

8.1.2 Period Ratios and Their Relation to Closed Orbits

Gao and Delos [GAD94] discussed the behavior of closed orbits and their birth by bifurcations in the continuum regime. Here we discuss the behavior of closed orbits in both the continuum and quasidiscrete regions. The quasiperiodic motion of a given trajectory can be understood in terms of the periods along the two axes. If we define T_u and T_v as the periods of the u and v motion, then the period ratio, T_u/T_v, is not generally a rational number. However, for certain initial conditions, T_u/T_v is a rational number, m/l, and the motion is periodic with total period $T_{total} = lT_u = mT_v$. Within each family of periodic orbits with period ratio, T_u/T_v, there is one orbit which passes through the origin. This orbit is of special interest because closed-orbit theory [DUD88a, GAD94] asserts that orbits which are closed at the nucleus produce modulations in the absorption spectrum. Some of these closed orbits are shown in Figure 8-1.

At any scaled energy, closed orbits have a range of allowed period ratios. Closed

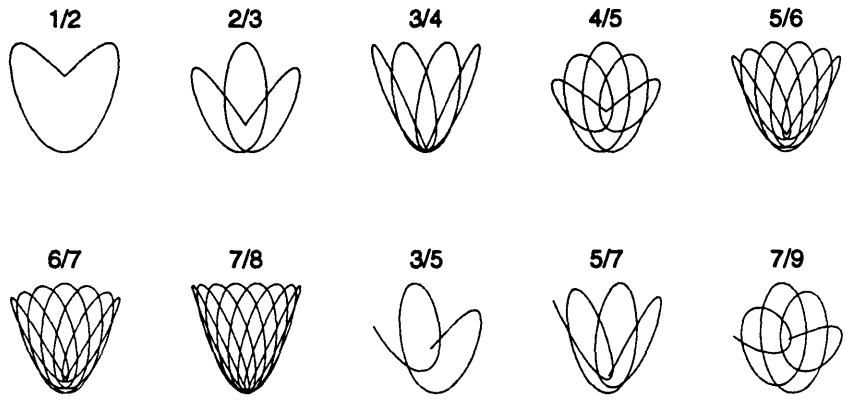

Figure 8-1: Some closed orbits of hydrogen in an electric field. (Courtesy of Jing Gao.)

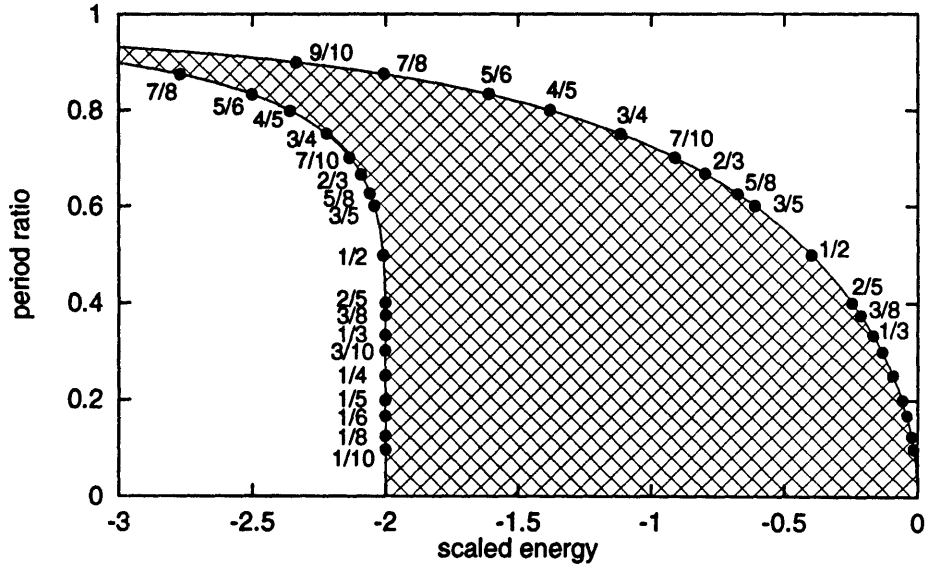

Figure 8-2: The shaded region represents allowed period ratios. Bifurcations occur on the edges of the shaded region.

orbits are created and destroyed on the edges of the allowed range of period ratios. The closed orbit with the maximum period ratio is the orbit on the u axis, which corresponds to the positive z axis.[2] This orbit is called the "uphill" parallel orbit because it goes back and forth between the origin and classical turning point in the direction of infinite potential. This orbit is denoted U_1, and its repetitions are denoted U_n, where n is the number of repetitions. Above $\epsilon_F = -2$, an orbit which begins at the origin ionizes if its initial angle with the u axis is larger than the initial angle of the orbit with $T_u/T_v = 0$. At $\epsilon_F = -2$, the orbit on the v axis has $T_u/T_v = 0$, and ionization is no longer possible. Below $\epsilon_F = -2$, the closed orbit with the minimum period ratio is the orbit on the v axis, which corresponds to the negative z axis. This is the "downhill" parallel orbit. This closed orbit and its repetitions are denoted D_n. Figure 8-2 shows the minimum and maximum period ratios as a function of scaled energy.

For $\epsilon_F > 0$, all trajectories ionize except the U_n. For $\epsilon_F < 0$, closed orbits bifurcate from the U_n as the scaled energy is lowered. For $\epsilon_F > -2$, the minimum period ratio is zero and there is a range of period ratios between 0 and a maximum [GAD94]. All of the rational period ratios within this range represent closed orbits. For $\epsilon_F = 0$, the maximum period ratio is 0, and it increases monotonically to 1 as $\epsilon_F \to -\infty$. Each time the maximum period ratio passes through a rational number, a new closed orbit is born by bifurcation. Each new orbit is labeled with an unreduced fraction which represents its period ratio, m/l.

When a closed orbit is born with a period ratio, m/l, its initial angle with the u axis is infinitesimal, and it is nearly indistinguishable from the parallel orbit from which it bifurcated. As the scaled energy is lowered from the point of bifurcation, the initial angle of a closed orbit with period ratio m/l increases monotonically. As ϵ_F decreases, the minimum period ratio T_u/T_v begins increasing from 0 at $\epsilon_F = -2$. As the scaled energy is lowered, the initial angle a given closed orbit makes with the v axis goes to zero as the minimum period ratio approaches the period ratio of

[2]Of course, the orbits on the u and v axes are one-dimensional and cannot have period ratios. The period ratios really describe their neighbors.

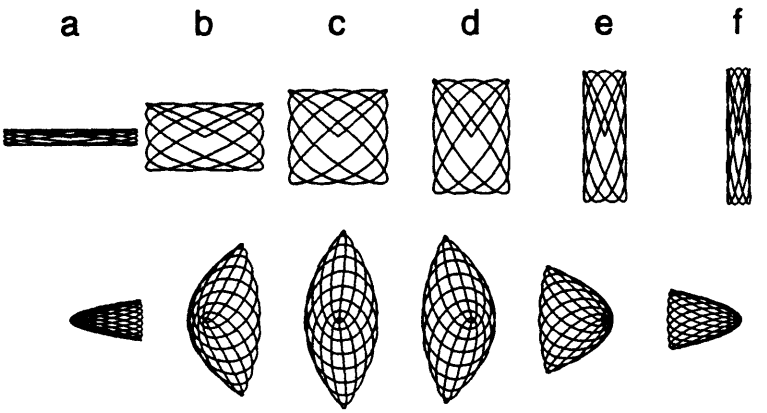

Figure 8-3: Pictures of the 9/10 orbit as the scaled energy changes. Top row: semiparabolic coordinates, u horizontal, v vertical. Bottom row: cylindrical coordinates, z horizontal, ρ vertical. (a) $\epsilon_F = -2.35$; (b) $\epsilon_F = -2.50$; (c) $\epsilon_F = -2.65$; (d) $\epsilon_F = -2.80$; (e) $\epsilon_F = -2.95$; (f) $\epsilon_F = -3.00$.

that closed orbit. Consequently, closed orbits with small period ratios begin to be destroyed at $\epsilon_F = -2$ by colliding with the orbit on the v axis (the downhill parallel orbit).

8.1.3 An Illustration: The Closed Orbit With Period Ratio 9/10

The destruction of a closed orbit as the scaled energy is lowered is the same as the creation of a closed orbit as the scaled energy is raised. Consequently, as ϵ_F is increased, a new closed orbit is created by a bifurcation of the downhill parallel orbit every time the minimum period ratio passes through a rational number. For example, as the scaled energy is raised to $\epsilon_F = -3.025$, the minimum period ratio goes through 9/10 and the orbit shown in Figure 8-3 is born by bifurcation of D_9. This orbit exists until the maximum period ratio goes through 9/10 and the orbit is destroyed by a collision with U_{10} at $\epsilon_F = -2.342$. Figure 8-3 shows pictures of the 9/10 orbit in semiparabolic and cylindrical coordinates. In Figure 8-3(a) $\epsilon_F = -2.35$

and the 9/10 orbit is well localized near the $+z$ axis (u axis). As the scaled energy is lowered it moves away from the $+z$ axis and has a tulip shape for $\epsilon_F = -2.50$, as shown in Figure 8-3(b). At $\epsilon_F = -2.65$ (Figure 8-3(c)), the 9/10 orbit looks like an eye and splits its time almost evenly on either side of the $z = 0$ plane. At $\epsilon_F = -2.80$ (Figure 8-3(d)), the orbit is evolving back into a tulip shape. The tulip shape has reappeared for $\epsilon_F = -2.95$, (Figure 8-3(e)), only now the orbit spends most of its time on the negative side of the $z = 0$ plane. As the scaled energy decreases further to $\epsilon_F = -3.00$, the 9/10 orbit begins to collapse back onto the $-z$ axis (v axis).

Finding these closed orbits at a given scaled energy is a simple matter of computing the period ratio of orbits launched from the origin at various initial angles. The period ratio is a slowly varying function of initial angle, so it is easy to converge upon the desired period ratio with a simple iterative procedure. In practice, an orbit is started at the nucleus with a given initial angle. Its trajectory and period ratio are computed by numerically integrating the equations of motion. The initial angle can then be changed in order to converge upon the desired period ratio. The evolution of these closed orbits and their birth by bifurcations is the key to the semiclassical interpretation of the spectrum.

8.2 Recurrence Spectra in the Continuum Regime

At large positive energies, the photoabsorption spectrum of single-electron atoms in an electric field displays a single sinusoidal oscillation [FEB78, FRE79, LDB81]. For $E > 0$, the only closed orbit is parallel to the field and extends from the nucleus to the classical turning point. The spectrum contains a fundamental Fourier component from this orbit (U_1) plus harmonics from its repetitions (U_n). U_1 is unstable for $\epsilon_F > 0$, and none of its neighbors returns to the nucleus. Consequently, the amplitude of the harmonics decreases roughly exponentially. Just above $E = 0$, many harmonics contribute, and the spectrum resembles a sawtooth. The exponential decay rate increases as ϵ_F is increased [GDB92, GAD94], resulting in a single sinusoid at large positive energy [FRE79, GDB92, LDB81].

As the energy is lowered below $E = 0$, new closed orbits are created by bifurcations of the parallel orbit and its repetitions [GAD94]. As explained by Gao and Delos, the maximum value of the period ratio, T_u/T_v, is zero at $\epsilon_F = 0$ and increases as the scaled energy decreases. For $-2 < \epsilon_F < 0$, closed orbits exist for every rational period ratio between zero and the maximum. As the scaled energy is decreased, a bifurcation produces a new closed orbit every time the maximum ratio is a rational number. Short period closed orbits correspond to ratios of small integers.

8.2.1 Continuum Recurrence Spectra for Small Action

The scaled actions of U_1 and its repetitions are shown in Figure 8-4. The scaled action of this orbit is

$$\tilde{S} = \frac{1}{2\pi}\oint \tilde{\mathbf{p}}\cdot d\tilde{\mathbf{q}} = \frac{1}{2\pi}\oint \tilde{p}_z\, d\tilde{z} = \frac{1}{\pi}\int_0^{\tilde{z}_{max}} \sqrt{2(\epsilon_F + \frac{1}{\tilde{z}} - \tilde{z})}\, dz, \tag{8.4}$$

where $\tilde{z}_{max}$ is the classical turning point. The positions at which new orbits are created by bifurcations are marked and labeled with the period ratio of the newly created closed orbit. Figure 8-5 shows a single recurrence spectrum for $\epsilon_F = -1.6$. This recurrence spectrum is the Fourier transform of the experimental photoabsorption spectrum at $\epsilon_F = -1.6$. The energy was varied from roughly $E = -65\,cm^{-1}$ to $E = -50\,cm^{-1}$ while the field was simultaneously varied to hold the scaled energy constant. The recurrence strength is plotted on the scaled energy axis in arbitrary units. The peaks in the recurrence spectrum correspond to repetitions of the parallel orbit. Furthermore, the recurrence strength is large for U_5, U_6, and U_{11}. This is a consequence of the 4/5, 5/6, and 9/11 bifurcations which occurred at scaled energies slightly higher than $\epsilon_F = -1.6$.

To show the evolution of recurrence spectra from $E = 0$ to the classical ionization threshold, we reduce the vertical scale by a factor of 20 and form a map of experimental recurrence spectra for $-2.1 \leq \epsilon_F \leq -0.37$. Figure 8-6 shows recurrences with scaled actions corresponding to repetitions of the uphill parallel orbit.

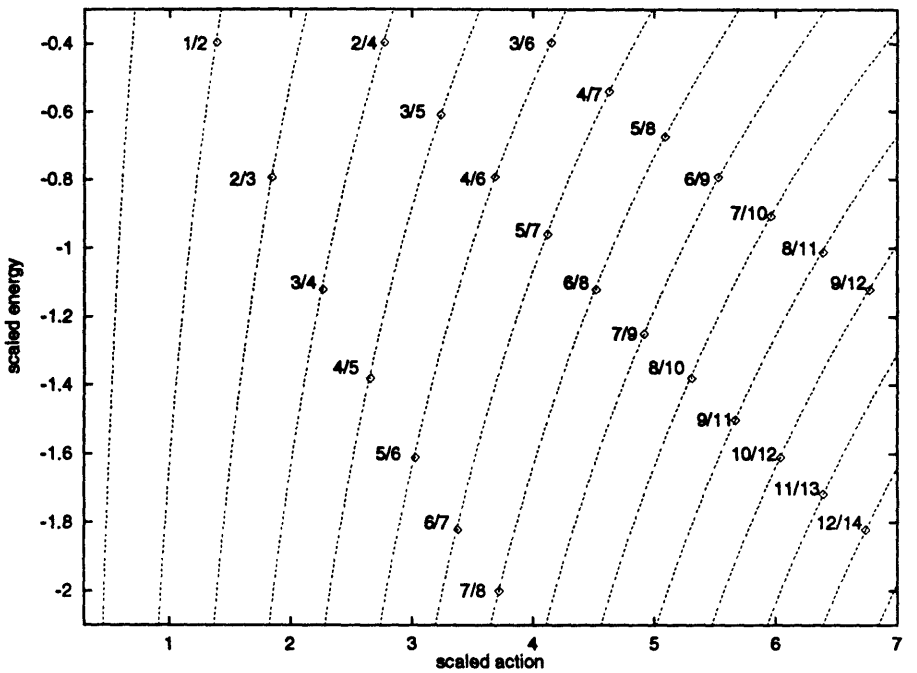

Figure 8-4: The scaled action of repetitions of the uphill parallel orbit U_n as a function of scaled energy. Points where bifurcations occur are labeled with the period ratio of the newly created orbit.

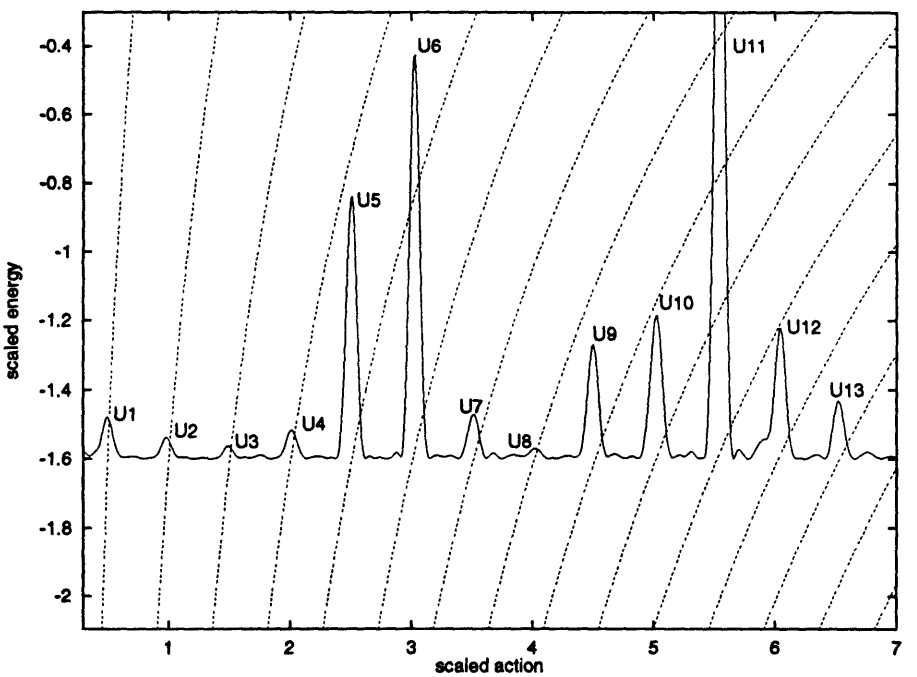

Figure 8-5: Experimental recurrence spectrum for $\epsilon_F = -1.6$. The recurrence strength is plotted on the scaled energy axis in arbitrary units. Each peak corresponds to a repetition of the parallel orbit.

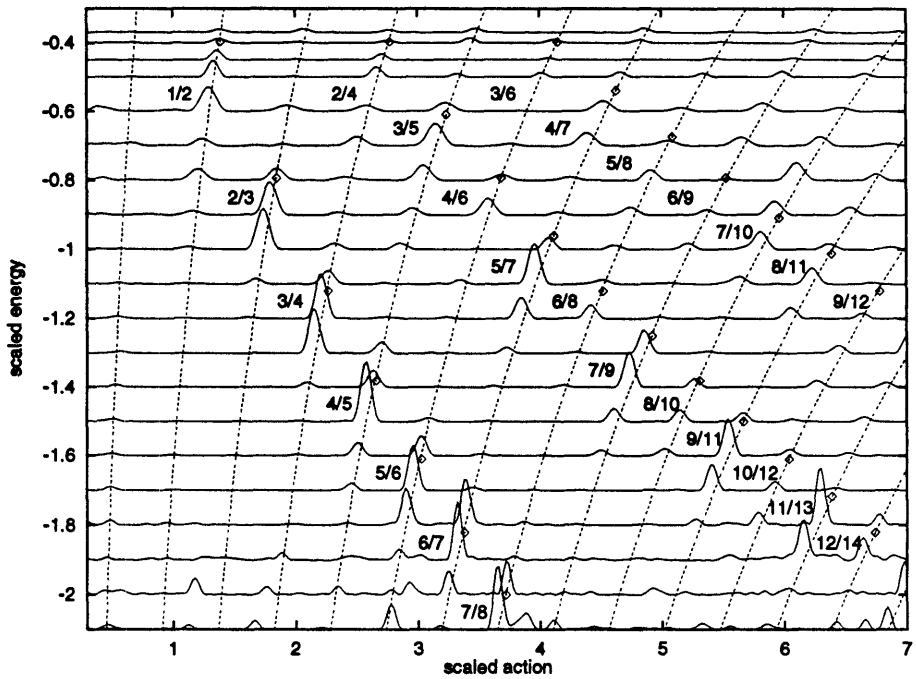

Figure 8-6: Experimental recurrence spectra for $-2.1 \leq \epsilon_F \leq -0.37$. Bifurcations are marked with diamonds.

8.2.2 Behavior at a Bifurcation

The strength of these recurrences near bifurcations follows the general pattern which was discussed in Chapter 6. As the scaled energy approaches the bifurcation from above, the recurrence strength increases significantly. The uncertainty principle allows the quantum system to "see" the bifurcation before it occurs classically [KHD93]. As the scaled energy passes through the bifurcation the recurrence strength increases rapidly, achieving its maximum value slightly after the bifurcation. This large increase in recurrence strength is the result of the focusing of the incoming wave nearly to a point at the bifurcation and can be understood quantitatively by incorporating diffraction effects into closed-orbit theory [CJS95].

At a bifurcation, the parent and the newly created orbit have the same scaled action. At scaled energy slightly below a bifurcation (where the recurrence is large), the newly created orbit carries most of the recurrence strength. Its action is slightly less than that of the repetition of the uphill orbit from which it bifurcated. These

scaled actions are not far enough apart to produce resolved peaks, but the dominance of the newly created orbit shifts the peak position slightly from the scaled action of the repetition.

To illustrate this point, we consider the recurrence spectrum at $\epsilon_F = -1.6$ which is shown in Figure 8-4. Only the large peaks will be considered because experimental noise prevents accurate determination of the position of the smaller peaks. The scaled action of the 5^{th} peak is $\tilde{S}_{exp}(U_5) = 2.506(3)$, where the number in parentheses indicates the experimental error in the last digit.[3] The classical action of U_5 is $\tilde{S}_{cl}(U_5) = 2.520$, which is higher than the experimental value. However, the action of 4/5 (which carries most of the recurrence strength) is $\tilde{S}_{cl}(4/5) = 2.511$, which is almost within the experimental error of the measured value. In contrast, U_6 is not shifted by a newly created orbit. $\tilde{S}_{exp}(U_6) = 3.027(3)$, and $\tilde{S}_{cl}(U_6) = 3.024$, as expected because the 5/6 bifurcation has not yet occurred.

The U_9, U_{10} and U_{11} peaks at $\epsilon_F = -1.6$ also provide good examples of bifurcation shifted recurrences. U_9 is shifted the most from $\tilde{S}_{cl}(U_9) = 4.536$ because it is far from the 7/9 bifurcation. $\tilde{S}_{cl}(7/9) = 4.493$, which agrees with $\tilde{S}_{exp}(U_9) = 4.501(5)$. U_{10} is also shifted from $\tilde{S}_{cl}(U_{10}) = 5.040$. The experimental peak position, $\tilde{S}_{exp}(U_{10}) = 5.024(5)$, agrees well with $\tilde{S}_{cl}(8/10) = 5.022$. In contrast, U_{11} at $\tilde{S}_{exp}(U_{11}) = 5.543(6)$ is not significantly shifted from $\tilde{S}_{cl}(U_{11}) = 5.544$ because the 9/11 bifurcation is sufficiently close that $\tilde{S}_{cl}(9/11) = 5.540$.

Three main sequences of bifurcations are shown in Figure 8-6. The bifurcations at lowest action produce orbits with period ratios of the form $n/(n+1)$. Such bifurcations include 1/2, 2/3, 3/4, etc. All of these bifurcations result in large recurrence strengths. The $n/(n+2)$ sequence of bifurcations occurs at roughly twice the action of the $n/(n+1)$ sequence. Bifurcations which produce closed orbits whose periods are irreducible fractions give stronger recurrence strengths than those associated with reducible fractions. The reason is that orbits with reducible period ratios are repetitions

[3]This error is partly due to the error in the electric field calibration and non-uniformity across the interaction volume, which are discussed in Chapter 4. There is also a contribution from the statistical uncertainty in determining the center of the peak.

of the corresponding reduced fraction. Consequently, in the $n/(n+2)$ sequence the 3/5, 5/7, 7/9, 9/11, and 11/13 bifurcations produce larger recurrences than the 2/4, 4/6, 6/8, 8/10, 10/12, and 12/14 bifurcations. The pattern of the irreducible fractions giving larger recurrences is also apparent in the $n/(n+3)$ sequence of bifurcations which is located roughly at three times the action of the $n/(n+1)$ sequence.

Figure 8-6 reveals a general loss of recurrence strength as ϵ_F is increased. This can be understood simply. For $\epsilon_F = -2.1$ there is a quasidiscrete spectrum, and all of the photoabsorption signal appears in the Fourier transform. As the scaled energy is raised, the continuum background grows and the photoabsorption resonances become small peaks on a large background. Consequently, most of the signal is piled up at zero frequency in the Fourier transform.

8.2.3 Comparison with Closed-Orbit Theory

Periodic-orbit theory and closed-orbit theory diverge at bifurcations, as discussed in Chapter 6. However, Gao and Delos have developed a modification of the theory to deal with this problem. To test the modified closed-orbit theory near bifurcations, recurrence spectra were measured near the 1/2 and 2/4 bifurcations in small steps of ϵ_F. The results are displayed in Figure 8-7. The stick spectra represent recurrence strengths computed from closed-orbit theory, and the solid lines are convolutions of the stick spectra to account for the experimental resolution of the recurrence spectra.[4] The dotted lines are measured recurrence spectra.

The 1/2 and 2/4 bifurcations affect peaks 2 and 4, respectively. Their bifurcation energy is $\epsilon_F = -0.4$. There are actually two orbits underneath peaks 2 and 4, but they are not distinguishable because their actions are nearly equal. In contrast, multiple orbits are visible in the stick spectra under peaks 3 and 5. These orbits were created

[4]The experimental width is simulated in the theory by Fourier transforming the stick spectra to obtain a predicted photoabsorption spectrum in the same region as the experiments, and then inverse Fourier transforming the predicted photoabsorption spectrum. This naturally leads to the question, "Why don't you compare the photoabsorption spectra instead of the recurrence spectra?" The experimental spectra have much higher resolution and many more orbits would need to be included in the theory to reproduce it.

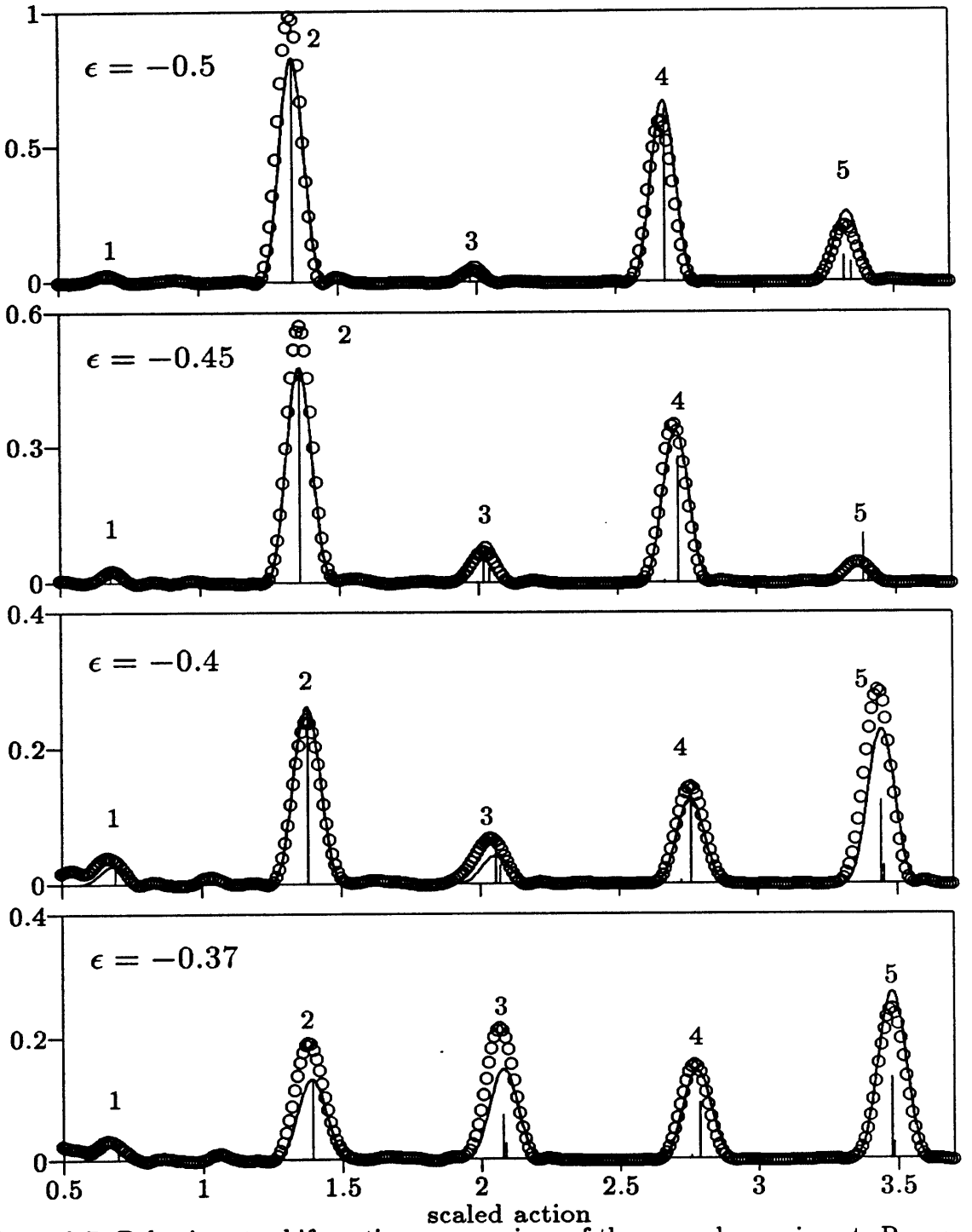

Figure 8-7: Behavior at a bifurcation: comparison of theory and experiment. Recurrence strength near the 1/2 bifurcation. $\epsilon_F = -0.4$ is the bifurcation energy. Stick spectra: theory. Line: theory smoothed for comparison with experiment. Circles: experiment. Vertical axis is recurrence strength in arbitrary units. Theory courtesy of Jing Gao and John Delos.

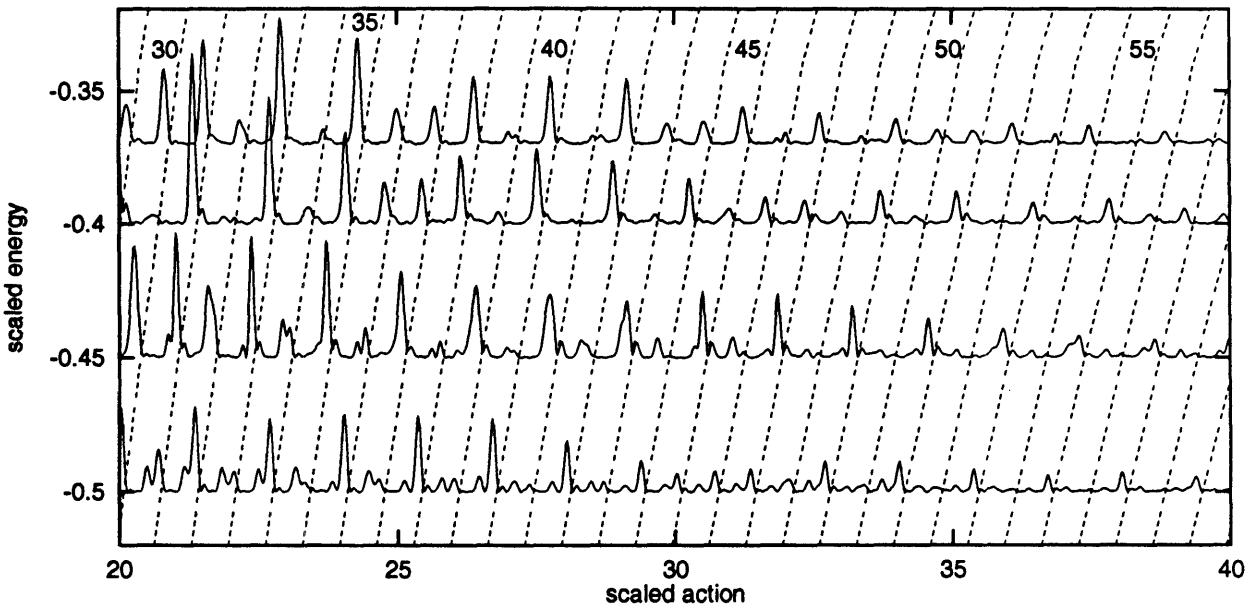

Figure 8-8: Experimental recurrence spectra at large action for $-0.5 \leq \epsilon_F \leq -0.37$. The dashed lines are the action of repetitions of the parallel orbit. The numbers to the left of the dashed line give the number of repetitions.

by the 1/3 and 2/5 bifurcations, respectively. Note that the contributions of two orbits to a single recurrence peak add coherently. For example, peak 5 at $\epsilon_F = -0.45$ is smaller than the stick spectra, indicating a destructive interference. At $\epsilon_F = -0.5$, peak 5 displays constructive interference.

8.2.4 Continuum Recurrence Spectra for Large Action

The pattern of peaks in the recurrence spectrum near repetitions of the parallel orbit continues to high action, and provides the spectral signature of long period orbits. Figure 8-8 shows a blowup (recurrence strengths multiplied by a factor of 25 compared with Figure 8-6) of recurrence spectra for $20 < \tilde{S} < 40$ in the range $-0.5 \leq \epsilon_F \leq -0.37$. The dashed line represents the action of repetitions of the parallel orbit as a function of scaled energy. Most of the prominent peaks are at actions just below repetitions of the parallel orbit. We attribute this to the bifurcation shift that pulls the scaled action of recurrences to slightly lower action than the parents from which they bifurcate.

For $\tilde{S} < 7$ large increases in recurrence strength can be associated with bifurcations

Table 8.1: Scaled actions and bifurcation energies of orbits contributing to the U_{45} recurrence at $\epsilon_F = -0.45$.

Orbit	$\tilde{S}$	ϵ_F^{bif}
23/45	30.560	−0.42
22/45	30.560	−0.38
21/45	30.532	−0.34
20/45	30.519	−0.30
19/45	30.471	−0.28

in a simple way. Things are more complicated at higher action. Because of the larger denominators in the relevant period ratios, the density of bifurcations is much higher than at low action. For example, in Figure 8-8 U_{45} is large for $\epsilon_F = -0.45$. The 23/45, 22/45, 21/45, 20/45, and 19/45 bifurcations have all just occurred, and the recurrence strength of these new orbits will add coherently. The scaled action of U_{45} at $\epsilon_F = -0.45$ is $\tilde{S}_{cl}(U_{45}) = 30.58$. The experimental peak position is $\tilde{S}_{exp}(U_{45}) = 30.50(3)$. The newly created orbits and their actions are shown in Table 8.1. It is reasonable to suggest that these recurrences are combining coherently to shift the experimental peak to an action below that of U_{45}. Even at the small recurrences in Figure 8-8, a number of bifurcations contribute large recurrence strengths, but they interfere destructively. It is interesting to note that the largest recurrences of the parallel orbit are for odd U_n at $\epsilon_F = -0.45$ and for even U_n at $\epsilon_F = -0.5$, but we have no simple explanation.

In addition to the recurrences corresponding to repetitions of the parallel orbit, there are a few additional peaks in the recurrence spectrum for $\epsilon_F = -0.37$, and the number of additional peaks increases as the scaled energy is lowered. These peaks are due to orbits which bifurcated from the parallel orbit and their repetitions. These newly created orbits were not visible as distinct peaks in the low action spectra shown in Figure 8-6 because the action of a newly created orbit is close to that of the repetition of the parallel orbit from which it bifurcated. However, the repetitions of many such orbits are resolved at the higher actions shown here.

We should mention two other possibilities to explain the recurrences whose scaled

action is roughly 0.4% less than the scaled action of simple repetitions of the uphill parallel orbit. Such a regular displacement suggests the possibility of a systematic error in the electric field calibration. However, the discrepancy we see would require our field calibration to be wrong by roughly 16 times what we estimate. Furthermore, the bifurcation shift in Figure 8-8 has been reproduced in separate experiments using separate field calibrations.

Another way to explain the displaced positions of long-action recurrences is to compute the scaled action by beginning and ending the trajectory at the core radius. This approach gives good agreement with the data, but does not seem rigorous. We mention it because (as will be explained) this approach works for the long-action recurrences in the quasidiscrete region, whereas attempting to account for the systematic shift of those recurrences by looking at the action of newly created orbits fails.

This experimental study of recurrence spectra in the continuum regime provides a semiclassical interpretation of continuum Stark spectra. Furthermore, these results provide a clear picture of the role of bifurcations in the observed spectrum and detailed confirmation of the closed-orbit theory. They illustrate the fundamental process by which new orbits are created as the energy is decreased and a simple continuum spectrum becomes complex and discrete. The bifurcation process studied here is generic to single-electron atoms. Similar bifurcations occur in diamagnetic hydrogen and lead to the proliferation of recurrences that characterizes classical chaos. Consequently, this study of bifurcations illuminates a fundamental process that connects classical and quantum descriptions of both regular and chaotic systems.

8.3 Recurrence Spectra in the Quasidiscrete Regime

8.3.1 Recurrence Spectrum at High Action

We have studied the signature of very long-period orbits in the Stark spectrum of lithium for $\epsilon_F = -3$ [CJS94]. This study appears in Appendix A. We identified

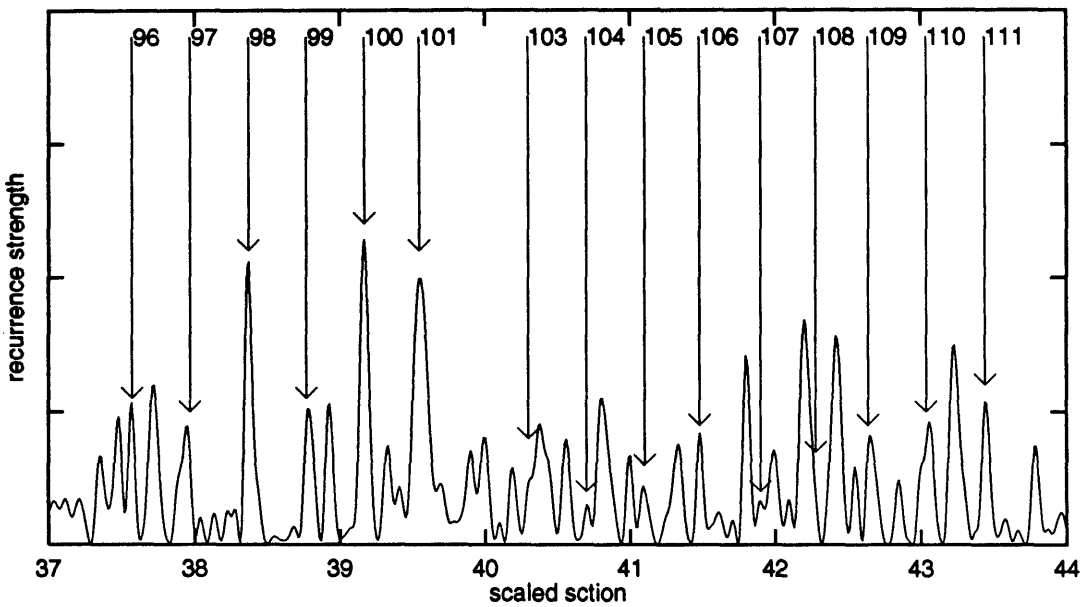

Figure 8-9: Experimental lithium recurrence spectrum at large action for $\epsilon_F = -3$. Peaks at integer multiples of $\tilde{S} = 0.3915$ are marked with arrows.

recurrences associated with repetitions of the uphill parallel orbit, including those beyond U_{100}. To identify those long-period orbits, we computed the scaled action by starting and ending the classical orbits near the core radius instead of using the hydrogenic scaled action for the complete trajectory, as explained later. This led us to use $\tilde{S} = 0.3915$ as the scaled action U_1 instead of the hydrogenic value, $\tilde{S} = 0.3935$, which is slightly higher. The experimental recurrence spectrum is shown in Figure 8-9.

However, unlike the case of long-period orbits in the continuum region, we are unable to interpret the downward shift in scaled action as due to the bifurcation shift. For example, the peak identified as U_{101} has a scaled action $\tilde{S}(U_{101}) = 39.56(4)$ which agrees with $101 \times 0.3915 = 39.54$ but not with $101 \times 0.3935 = 39.74$. Consequently, the right scaled action seems to be given by beginning the orbit at the core radius and not by using the hydrogenic action.

This difficulty will be considered in more detail later in this chapter. It cannot be explained by considering a bifurcation shift, as in the case of the long-period recurrences in the continuum spectra. The 94/101 recurrence at $\tilde{S}(94/101) = 39.73$

has a scaled action which is too high. The 93/101 orbit at $\tilde{S}(93/101) = 39.63$ is also an unlikely candidate. Its scaled action is still too high, and it is likely to have a small recurrence strength at $\epsilon_F = -3$ because it bifurcated at $\epsilon_F = -2.72$.

At high actions there are peaks in addition to those due to repetitions of the uphill orbit. Conclusive identification of all the features in the recurrence spectrum at high actions presents a formidable challenge to closed-orbit theory. However, we anticipate that many of the peaks can be understood in terms of orbits produced by bifurcations and core-scattered recurrences. Consequently, we will focus our attention on understanding these two processes and their effect on the evolution of the spectrum.

8.3.2 Recurrence Spectrum at Low Action

At low action, the bifurcations of repetitions of the uphill parallel orbit (U_n) follow the same pattern as in the continuum regime. Furthermore, recurrences associated with the downhill parallel orbit and its repetitions (D_n) are added to the spectrum. (These orbits immediately ionize above $\epsilon_F = -2$.) These recurrences follow the same pattern as the uphill recurrences near a bifurcation, except that the D_n orbits bifurcate as the scaled energy is increased. The recurrence strength begins to increase just before the bifurcation and reaches its maximum slightly after the bifurcation.

Bifurcations of the D_n and U_n are visible in the experimental recurrence spectra shown in Figure 8-10. The near vertical solid lines are the scaled actions of the D_n. The dashed lines are the scaled actions of the U_n. All of the prominent recurrences shown in Figure 8-10 are located at one of these actions. Bifurcations of the D_n are marked with crosses. Bifurcations of the U_n are marked with diamonds. The two series of prominent peaks at low action correspond to the $n/(n+1)$ sequences of D_n and U_n bifurcations.

In this region, spectra can be computed accurately using standard techniques (as described in Chapter 3), and recurrence spectra can be obtained by taking the Fourier transform. To verify our methods, the experimental recurrence spectrum at $\epsilon_F = -3$ is compared with a recurrence spectrum obtained from quantum computations in

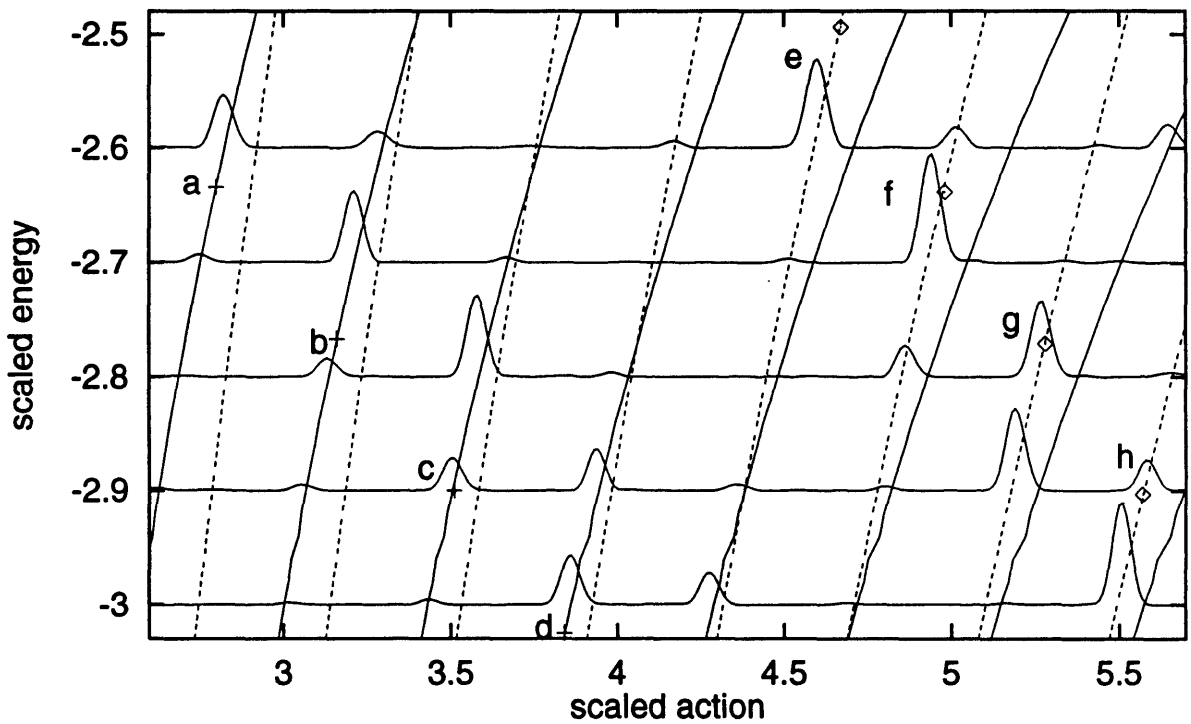

Figure 8-10: Experimental recurrence spectra for $-3 \leq \epsilon_F \leq -2.6$. Near vertical solid lines are the scaled actions of repetitions of the downhill parallel orbit. Dashed lines are the scaled actions of repetitions of the uphill parallel orbit. Bifurcations of the downhill orbit are marked with crosses: (a) 6/7; (b) 7/8; (c) 8/9; (d) 9/10. Bifurcations of the uphill orbit are marked with diamonds: (e) 11/12; (f) 12/13; (g) 13/14; (h) 14/15.

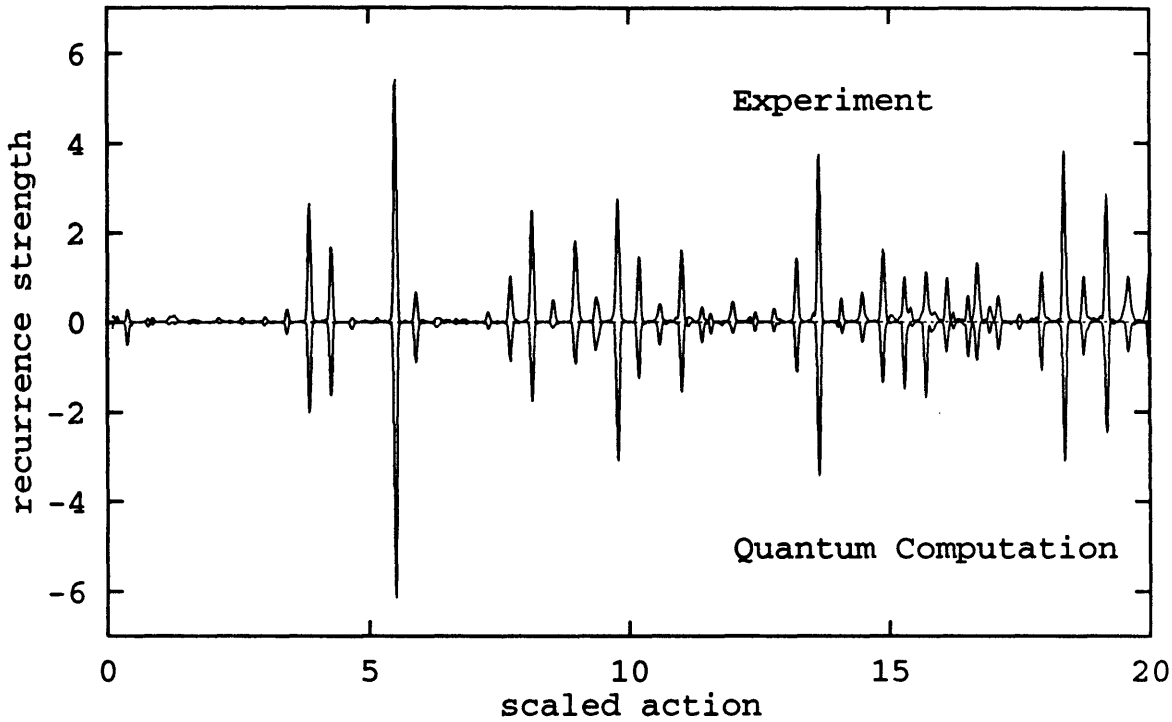

Figure 8-11: Lithium recurrence spectrum for $\epsilon_F = -3$. A mirror plot is used for comparison of the experimental spectrum (top) with the results of a quantum computation (bottom). The computed spectrum has been normalized to provide comparable heights.

Figure 8-11.[5] Agreement is generally good. Computing recurrence spectra allows investigation at scaled energies where experimental data is unavailable and also provides comparison with hydrogen. Furthermore, it permits study of the onset of chaos in the recurrence spectrum as the quantum defect is varied from $\delta_s = 0$ (hydrogen) to $\delta_s = 0.4$ (lithium).

8.3.3 Evidence for Core Scattering

Comparison between the experimental recurrence spectrum of lithium and the computed recurrence spectrum of hydrogen for $\epsilon_F = -3$ reveals that lithium begins to

[5]Note that this recurrence spectrum is from a repeat of the experiment presented in [CJS94] and shown in Figure 8-9. The noise was lower in the repeated scan, but the scaled energy was really $\epsilon_F = -2.996$ because the field to voltage ratio F/V was low by 0.3% due to either a change in the plate spacing, or (more likely) in a change in the stray electric field of about $100\,mV/cm$ from the day before when F/V was measured. Data taken at the same time as the constant scaled energy confirms that F/V had changed by the time of the scan. This can all be accounted for to bring the experimental errors back within the quoted ranges. These questions of parts in a thousand are not relevant to the points made in this discussion.

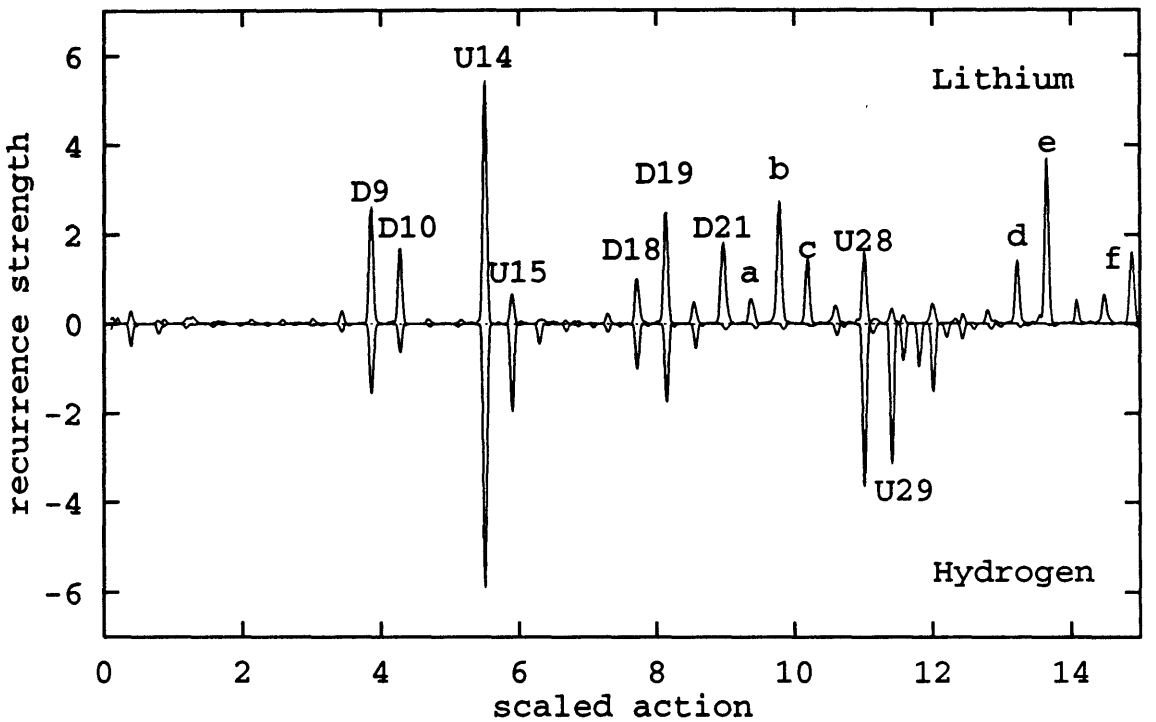

Figure 8-12: Comparison of recurrence spectrum of lithium and hydrogen for $\epsilon_F = -3$. Top: experimental recurrence spectrum of lithium. Bottom: computed recurrence spectrum of hydrogen. The labels a through f denote core scattered recurrences, as explained in the text and Table 8.2.

Table 8.2: Scaled actions of selected core scattered recurrences in the experimental spectrum at $\epsilon_F = -3$ are compared with the sum of the actions of their components.

$\tilde{S}$	Components	Sum	Label
9.357	$U_{14} + D_9$	9.364	a
9.784	$U_{14} + D_{10}$	9.782	b
10.193	$U_{15} + D_{10}$	10.177	c
13.224	$U_{14} + D_{18}$	13.222	d
13.641	$U_{14} + D_{19}$	13.641	e
14.882	$U_{15} + D_{21}$	14.872	f

show large differences from hydrogen for $\tilde{S} > 8$ (Figure 8-12). All of the peaks in the recurrence spectrum of hydrogen correspond either to repetitions of the parallel orbits or to orbits which bifurcated from them. Furthermore, each of the prominent peaks in the hydrogenic spectrum is large because of a nearby bifurcation. At low action, D_9 and D_{10} are large because of the nearby 9/10 and 10/11 bifurcations, respectively. U_{14} and U_{15} are large because they are close to the 13/14 and 14/15 bifurcations. These same recurrences are large in lithium and these bifurcations were shown in Figure 8-10. D_{18} and D_{19} are also large because they are near the 18/20 and 19/21 bifurcations. Similarly, U_{28} and U_{29} are large in hydrogen, but only U_{28} is large in lithium.

Some of the recurrences in the lithium spectrum are not at the scaled action of a closed orbit, but they can be understood in terms of the core scattering process because they occur at scaled actions which are the sum of closed orbits. We see core-scattered recurrences at actions which are the sum of large recurrences because the amplitude of a core-scattered recurrence is proportional to the amplitude of each of its components. Table 8.2 shows that the recurrences labeled a through f in Figure 8-12 may be interpreted as effects of core scattering.

Computing recurrence spectra for $\epsilon_F = -3$ as the quantum defect is varied in small steps from $\delta_s = 0$ (hydrogen) to $\delta_s = 0.4$ (lithium) illustrates the growth of the core-scattered recurrences as the quantum defect is increased (Figure 8-13). The recurrence spectrum shows little change for $\tilde{S} < 8$ as the quantum defect is varied. For higher action, the recurrence spectrum changes in several ways. The core-scattered recurrences labeled a through f appear and grow as the quantum defect is increased to $\delta_s = 0.36$. They shrink a bit over the last increment of the quantum defect to $\delta_s = 0.4$. D_{21} also grows larger as δ_s is increased. The cluster of hydrogenic recurrences between $\tilde{S} = 11$ and $\tilde{S} = 12$ (U_{28}, U_{29}, D_{27}, U_{30}, and D_{28}) decreases as the quantum defect increases.

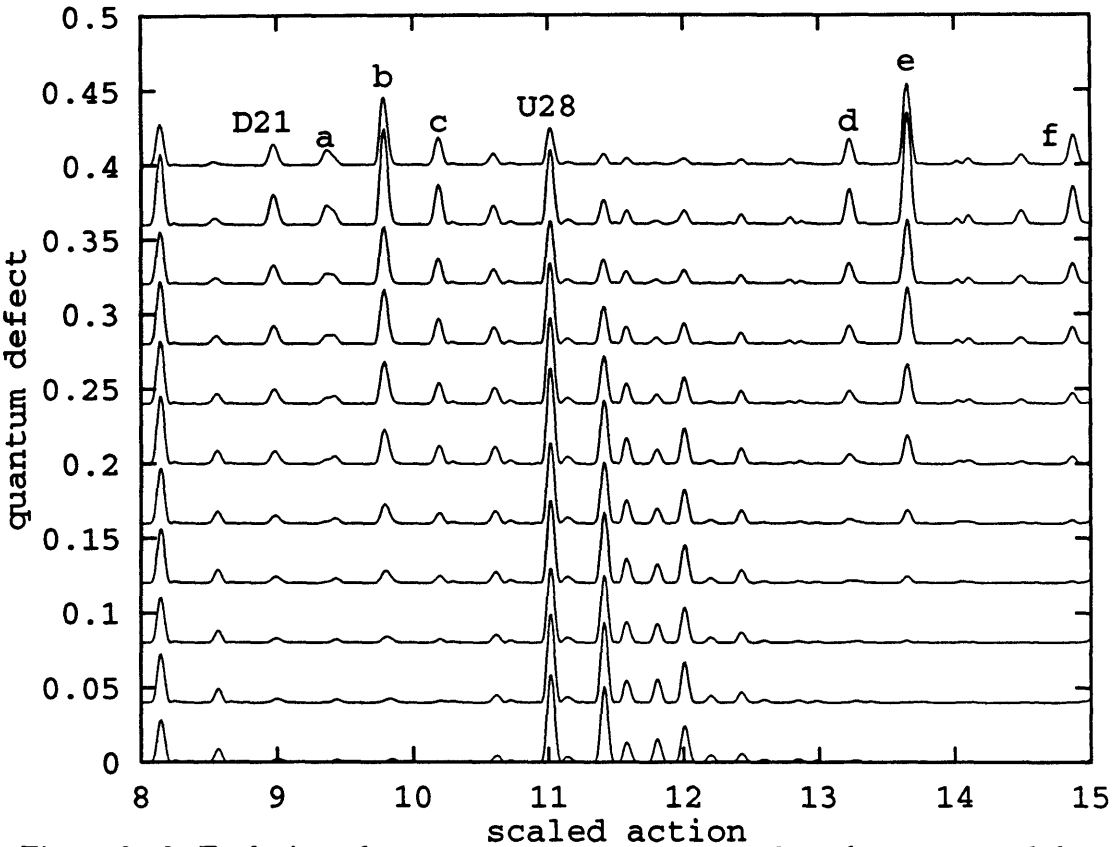

Figure 8-13: Evolution of recurrence spectra at $\epsilon_F = -3$ as the quantum defect δ_s is increased. core-scattered recurrences a through f appear as δ_s is increased.

8.3.4 Core Scattering and Spectral Evolution

Core scattering strongly affects the evolution of recurrence spectra as the scaled energy is lowered. In hydrogen, the recurrence spectra is simply dominated by orderly sequences of bifurcations, as shown in Figure 8-14. In region A, there are no bifurcations, and most recurrences are small. There is a variation in the strength of the first peak which is probably due to interference between D_1 and U_1. The lowest action sequence of bifurcations is the downhill $n/(n+1)$ and occurs in region B. The uphill $n/(n+1)$ sequence of bifurcations is adjacent to it at slightly higher actions in region C. These regions begin to overlap at the lower scaled energies, and the bifurcation energies of uphill and downhill orbits converge as $\epsilon_F \to -\infty$. Region D is a wasteland with no large recurrences. The increase in recurrence strength associated with the downhill $n/(n+2)$ bifurcations occurs in region E. Region F lies between the downhill and uphill $n/(n+2)$ bifurcation sequences and has no large recurrences. Region G encloses the large recurrences associated with the uphill sequence of $n/(n+2)$ bifur-

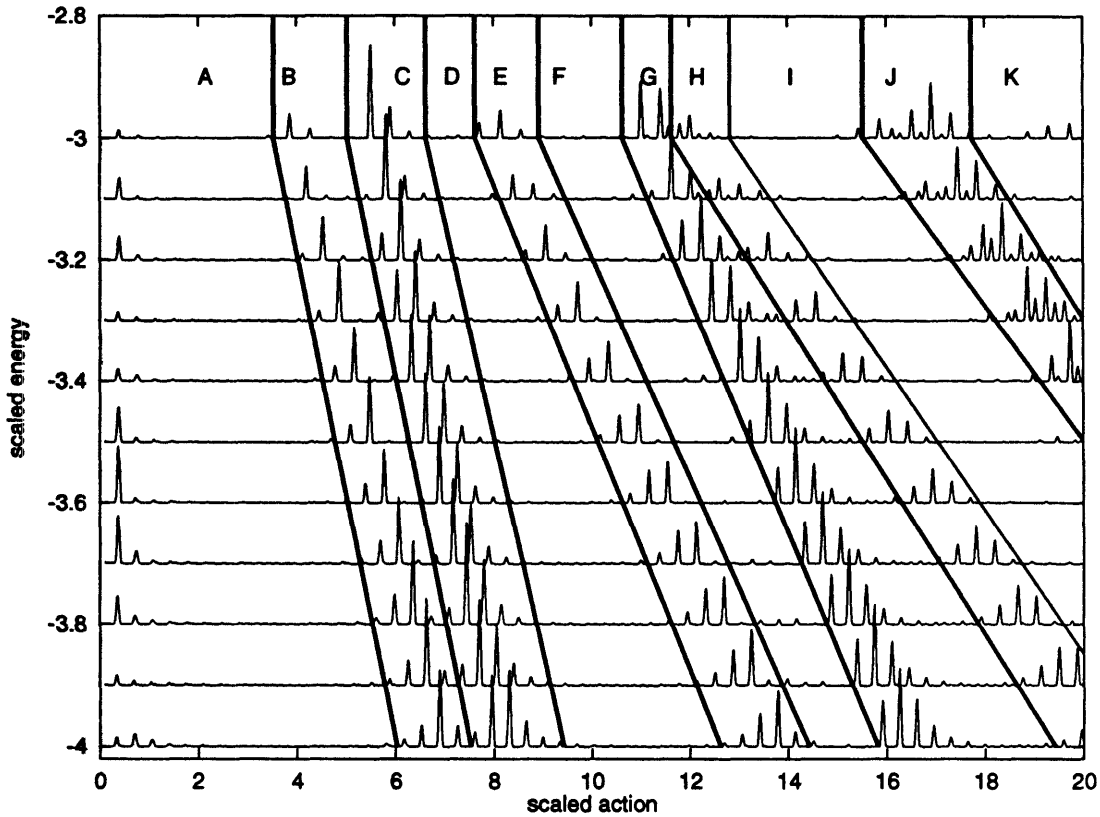

Figure 8-14: Computed recurrence spectra for hydrogen $-4 \leq \epsilon_F \leq -3$. Regions where different bifurcation sequences occur are marked.

cations. The increase in recurrence strength associated with the downhill $n/(n+3)$ bifurcations occurs in region H. Region I is another wasteland between bifurcation sequences, and region J encompasses both the uphill $n/(n+3)$ and downhill $n/(n+4)$ bifurcations. Region K is another wasteland.

Figure 8-15 is a map of computed lithium recurrence spectra for $-4 \leq \epsilon_F \leq -3$. Regions A, B, C, and D are at low action and are similar to hydrogen. However, in region E the downhill $n/(n+2)$ sequence is generally weaker in lithium, and region F has many large recurrences in lithium, while region F had none in hydrogen. Region G has few large recurrences in lithium, whereas in hydrogen it is filled with large recurrences from the uphill $n/(n+2)$ bifurcation sequence. The explanation is that in hydrogen the large recurrences from the $n/(n+1)$ bifurcation sequences are backscattered and on their next return, they form the $n/(n+2)$ bifurcation sequences. In lithium, the large recurrences from the uphill $n/(n+1)$ bifurcation sequence are scattered into the downhill $n/(n+1)$ bifurcation sequence so that on returning, they

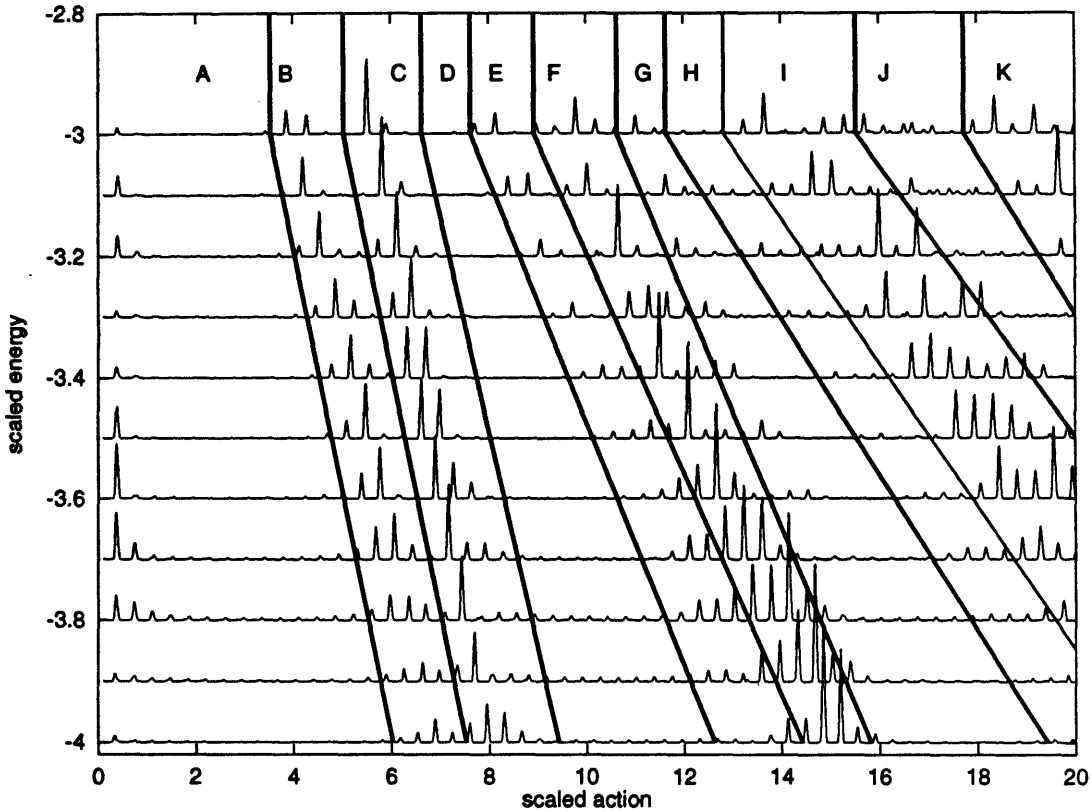

Figure 8-15: Computed recurrence spectra for lithium $-4 \leq \epsilon_F \leq -3$. Regions where different bifurcation sequences occur are marked.

have actions between the uphill and downhill $n/(n+2)$ sequences. Detailed analysis of the recurrences in region F shows that most of these recurrences are at the action of a large downhill recurrence added to the action of a large uphill recurrence. The dearth of large recurrences in regions G, H, J and the plethora of them in region I can be understood in a similar manner. Consequently, the evolution of the recurrence spectrum in lithium is dominated by bifurcations and core scattering.

8.3.5 Recurrence Spectrum at Low Scaled Energy

To understand the recurrence spectra at low scaled energy, we measured a recurrence spectrum at $\epsilon_F = -6$. The constant scaled energy scan covered from roughly $E = -27.9\,cm^{-1}$ to $E = -37.2\,cm^{-1}$ while the field was varied from $2.3\,V/cm$ to $4.1\,V/cm$. This energy range covers the $n = 54$ to $n = 62$ manifolds, and there is no n-mixing in this region.

The experimental recurrence spectrum of lithium is compared with the computed

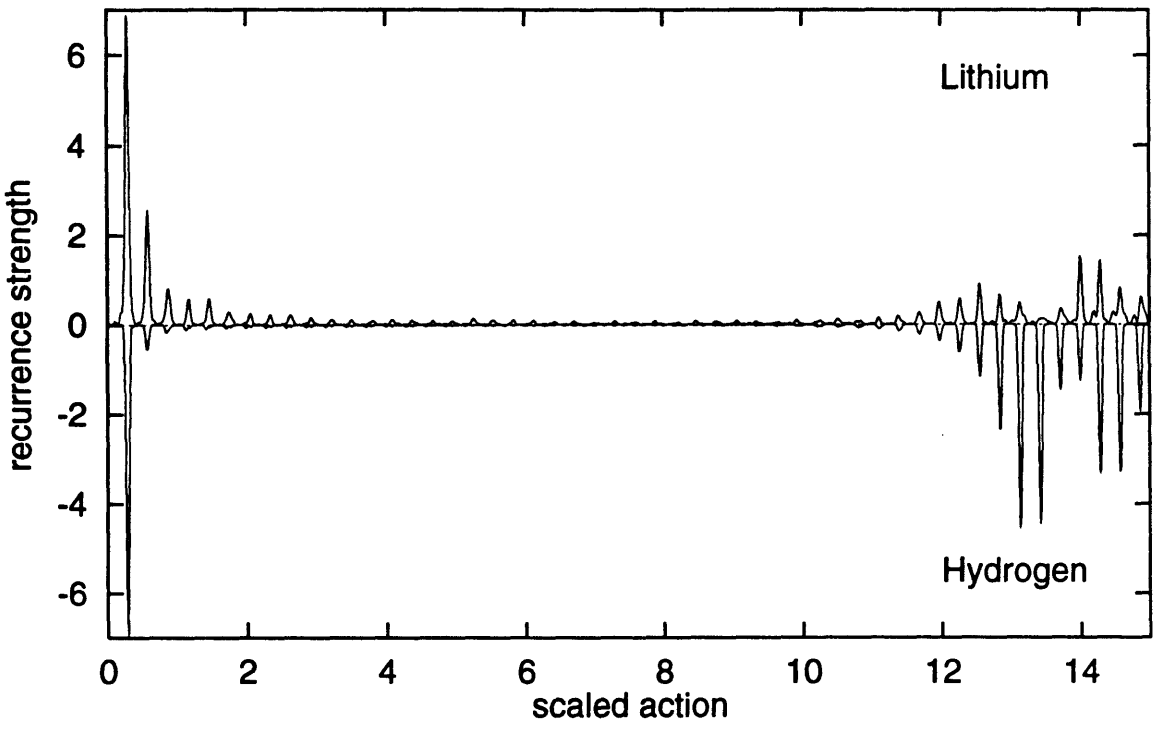

Figure 8-16: Recurrence spectra for $\epsilon_F = -6$. Top: Lithium experiment. Bottom: Hydrogen computation.

hydrogenic recurrence spectrum in Figure 8-16. $\tilde{S}_{cl}(U_1) = 0.286$ and $\tilde{S}_{cl}(D_1) = 0.292$. The periods of these orbits converge to the inverse of the zero-field Rydberg separation as $F \to 0$. The lowest action recurrence corresponds to D_1 and U_1. It is large because, without n-mixing, the Rydberg separation is the strongest frequency in the spectrum. The flurry of peaks at $12 < \tilde{S} < 15$ in the hydrogenic recurrence spectrum is a result of the uphill and downhill $n/(n+1)$ bifurcation sequences which are also converging. This means that these orbits are destroyed at scaled energies close to where they are created. The period of the short-lived newly bifurcated orbits is essentially the inverse of the energy spacing between adjacent levels of a Stark manifold.

The recurrence spectrum is similar in lithium, because before n-mixing, the energy levels of lithium and hydrogen follow the same pattern. However, the oscillator strengths are distributed differently, with lithium having most of the oscillator strength in the lowest state in the manifold. Consequently, the recurrences at small multiples of the inverse Rydberg spacing have a stronger presence in lithium. Furthermore, the distribution of oscillator strengths among the upper part of the n manifold differs from hydrogen, so the recurrence strengths of the bifurcation peaks

at $12 < \tilde{S} < 15$ are also distributed differently.

8.4 Recurrence Spectra for $m = 1$

Recurrence spectra for $m = 0$ are dominated by the orbits which lie on the z axis and those which bifurcate from them. In contrast, parallel orbits do not exist for $m \neq 0$ because there is a singular potential barrier at the z axis. Consequently, we do not expect the parallel orbits to have a signature in the spectrum for $m \neq 0$. This is consistent with the lack of modulations for $E > 0$ in $m = 1$ spectra [FEB78, FRE79].

However, the singularity at $z = 0$ has little effect on the classical dynamics of hydrogen in an electric field except very close to the z axis. When an orbit approaches the z axis for small but non-zero m, it experiences a reflection off the centrifugal barrier which is nearly identical to a reflection off of a wall. Consequently, P_ρ changes sign, P_z is unaffected, and the dynamics for non-parallel orbits are nearly identical to those in the $m = 0$ case. These considerations are central to our examination of Stark recurrence spectra for $m = 1$.

As we have seen, core scattering is strong for $m = 0$ states of lithium. However, the largest quantum defect mixed into $m = 1$ states ($\delta_p = 0.05$) of lithium is much smaller than that mixed into $m = 0$ states ($\delta_p = 0.4$). Thus, it is also of interest to investigate the core scattering process for $m = 1$ states of lithium.

A map of recurrence spectra of lithium for $m = 1$ is shown in Figure 8-17. Notice that there are no recurrences present for $\tilde{S} < 2$.[6] Repetitions of the parallel orbits are not present. Recurrences exist for only the short range of scaled energies, which corresponds to the allowed range of their period ratios.

Figure 8-18 shows a blowup of Figure 8-17. The large recurrences are localized between the bifurcation energies where orbits are allowed. In the case of $m = 0$, there was a local maximum in the recurrence strength near each bifurcation. Here,

[6] Careful examination of a blowup of the recurrence spectra at low action reveals the presence of a very small peak near the scaled action of U_1 and D_1. This is somewhat surprising , since it suggests that the nearly parallel neighboring orbits of the parallel orbits carry enough recurrence strength to be visible.

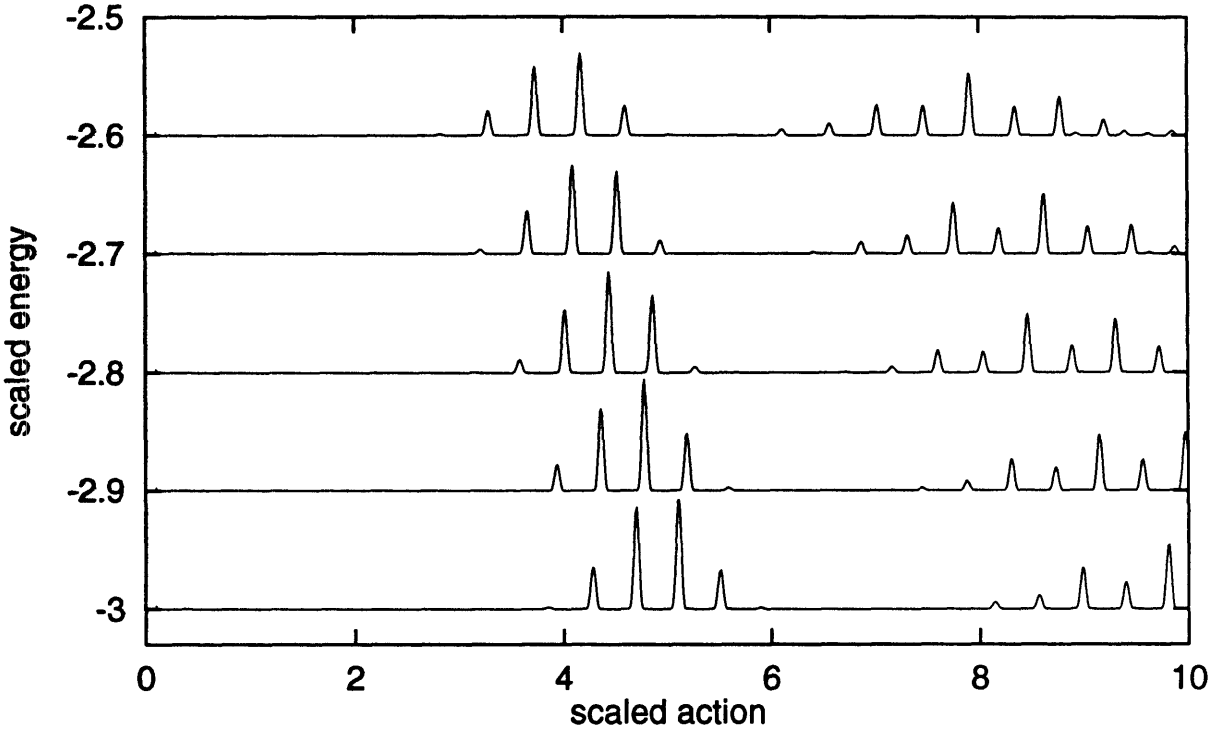

Figure 8-17: Computed recurrence spectra for $-3 \leq \epsilon_F \leq -2.6$.

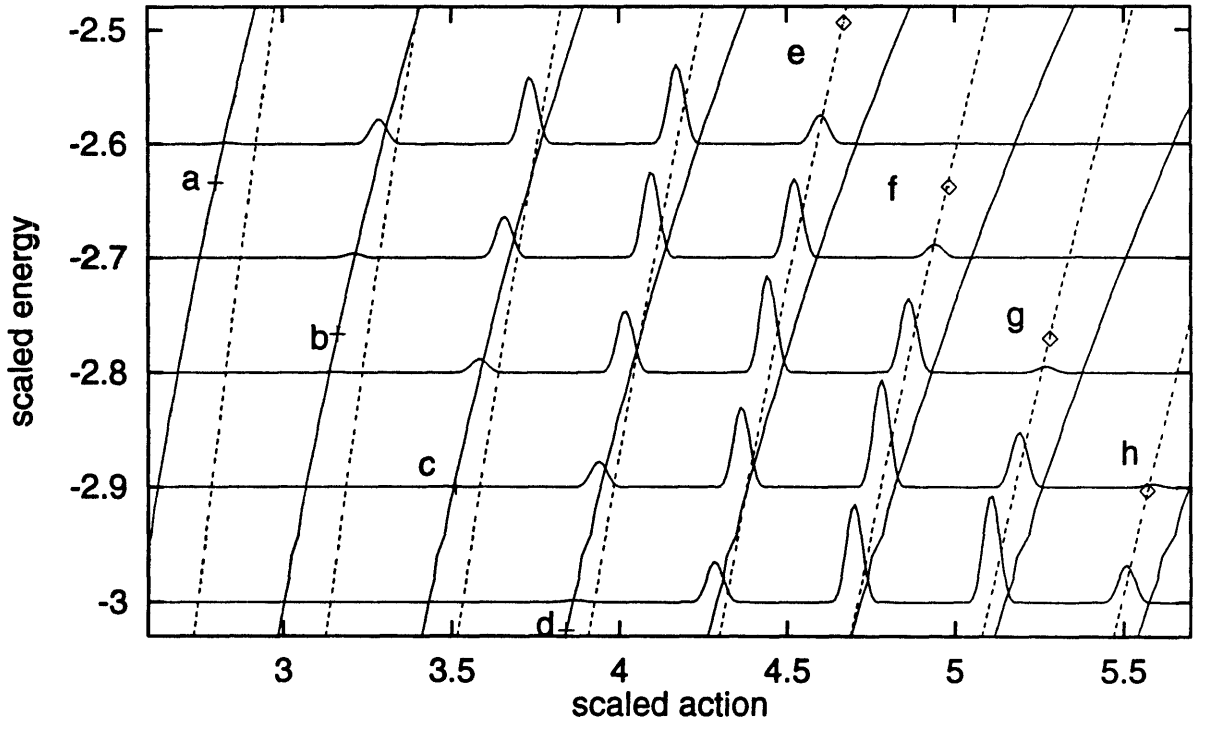

Figure 8-18: Blowup of Figure 8-17. Near vertical solid lines are the scaled actions of D_n. Dashed lines are the scaled actions of U_n. Bifurcations of the downhill orbit are marked with crosses: (a) 6/7; (b) 7/8; (c) 8/9; (d) 9/10. Bifurcations of the uphill orbit are marked with diamonds: (e) 11/12; (f) 12/13; (g) 13/14; (h) 14/15.

there is a single maximum about halfway between the bifurcations. This is due to the excitation process. Exciting $m = 0$ states from the $3S$ initial state requires light polarized along the z axis, which results in orbits with small initial angles with the z axis having large recurrence strengths. In contrast, exciting $m = 1$ states from the $3S$ initial state requires light polarized perpendicular to the z axis, which results in orbits with small initial angles with the z axis and having small recurrence strengths. Near a bifurcation an orbit has a small initial angle with the z axis and has a large recurrence strength for $m = 0$, but a small recurrence strength for $m = 1$. Midway between bifurcations an orbit is nearly perpendicular to the z axis and has a large recurrence strength for $m = 1$, but a small recurrence strength for $m = 0$. Closer examination of the recurrence spectrum reveals that there are actually very small peaks slightly outside of the allowed period ratios, but they become undetectable quickly enough to conclude that they are the usual pre-bifurcation recurrences.

There is a rigorous explanation of this behavior. The recurrence strength of each orbit is proportional to the spherical harmonic evaluated at the initial angle of the orbit. This gives a $\cos\theta_i$ dependence for the $3S \rightarrow nP_{m=0}$ transition and a $\sin\theta_i$ dependence for the $3S \rightarrow nP_{m=1}$ transition, which is what is observed. Perhaps a more physical interpretation is that the probability of the oscillating laser field "kicking" the electron out onto a given orbit is proportional to the dot product of the laser polarization and the initial momentum of the orbit. This is an appealing classical picture of the excitation process, but it breaks down when applied to excitation processes involving higher spherical harmonics.

A comparison of recurrence spectra of lithium and hydrogen at $\epsilon_F = -3.0$ is shown in Figure 8-19. The lithium recurrences show some height differences, but the extra peaks which provide the signature of core scattering are not easily visible. There are a few very small extra peaks at large action ($\tilde{S} > 30$). We conclude that core scattering is a weak process in the $m = 1$ lithium Stark spectrum.

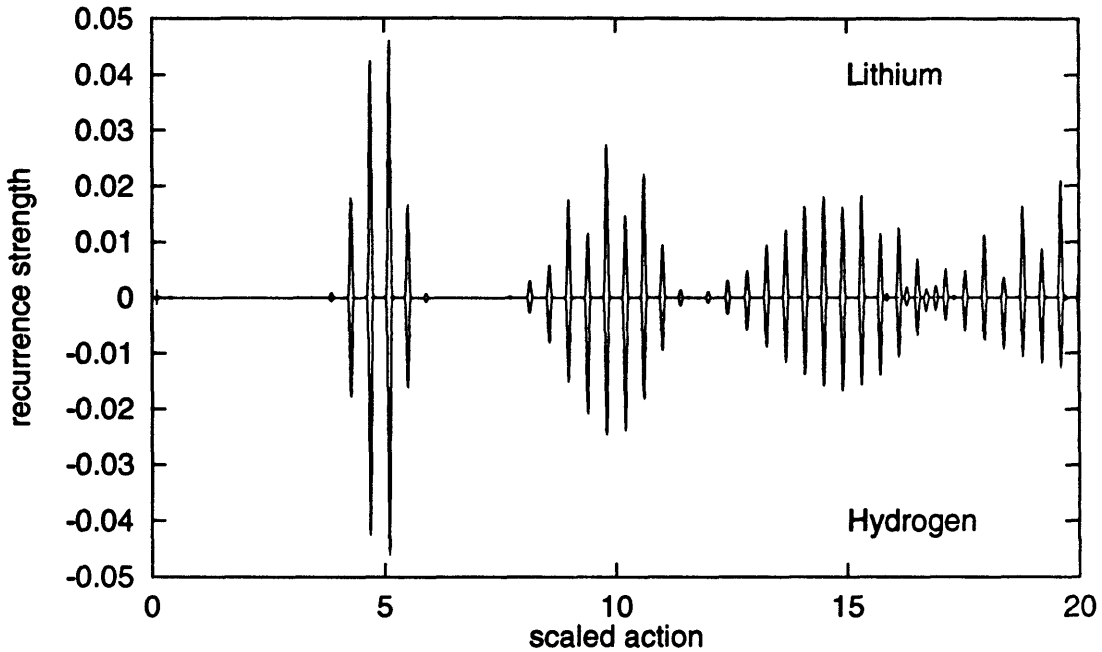

Figure 8-19: Stark recurrence spectra of lithium and hydrogen for $\epsilon_F = -3.0$, $m = 1$.

8.5 Which Scaled Action?

The position of each peak in a fully resolved recurrence spectrum should be located at the scaled action of a closed orbit. To interpret recurrence spectra of alkali-metal atoms, we need to account for the breakdown of the scaling rule inside the core region. There are two possible methods of doing this. The first is to use the scaled action of the hydrogenic orbit, and the arguments presented in Chapter 6 for doing so seem rigorous. The second possibility is to compute the action of an orbit beginning and ending at the core radius, so the orbit only accumulates action in the region of space where the scaling rule holds. The arguments for this approach seem less rigorous, but find some support in the experimental evidence presented earlier in this chapter. In the spectra considered here, the difference between the two methods is about 0.5% for the scaled action of the first repetition of short-period orbits in lithium. The difference is hard to detect in the first repetition of a closed orbit, but the difference in the peak position grows linearly with the number of repetitions and has played a role in our interpretation of long-action recurrences.

However, before we determined that the scaled action of the hydrogenic orbits

should be used, we found good agreement with long-period orbits in the lithium Stark spectrum by using the scaled action of a closed orbit beginning and ending at some core radius [CJS94]. The scaled action of the uphill parallel orbit was taken to be $\tilde{S}_{Li}^{cl}(r_0) = 0.3915$. The recurrence spectrum and peaks corresponding to multiples of this scaled action are shown in Figure 8-9.

Some comments should be made concerning the computation of $\tilde{S}_{Li}^{cl}(r_0) = 0.3915$. This number is likely to be dependent on the model core potential. Furthermore, some thought should be given to which core radius r_0 is used. Should the root mean square radius of the model or of the actual charge distribution of the core be used? Or should the average radius be used? Whichever radius is used for r_0, there is still some of the charge distribution outside of that radius which prevents the scaling rule from being exact. In practice, we obtained $\tilde{S}_{Li}^{cl}(r_0) = 0.3915$ by treating r_0 as an adjustable parameter and finding agreement with long-period experimental recurrences. $r_0 = 0.26$ gives $\tilde{S}_{Li}^{cl}(r_0) = 0.3915$. This radius is smaller than the root mean square of $f(r)$ ($r_{rms} = 0.54$), but it is a bit larger than the average radius of $f(r)$ ($r_{avg} = 0.21$).

One might think that treating the core radius as an adjustable parameter is fudging it because this effectively makes $\tilde{S}_{Li}^{cl}(r_0)$ an adjustable parameter also. Agreement with some high-action peaks would be easy to find if we were allowed to vary $\tilde{S}_{Li}^{cl}(r_0)$. However, by looking at the Fourier transform of the recurrence spectrum, we can show that the dominant frequencies in the recurrence spectrum correspond to $\tilde{S}_{Li}^{cl}(r_0)$ of both the uphill and downhill parallel orbits.

Figure 8-20 shows the Fourier transform of the computed lithium recurrence spectrum at $\epsilon_F = -3$. The peak corresponding to the spacing between repetitions of the uphill orbit corresponds to $\tilde{S}_{Li}^{qm} = 0.3918$. The same peak in the Fourier transform of the experimental lithium recurrence spectrum at $\epsilon_F = -3$ corresponds to a spacing of $\tilde{S}_{Li}^{exp} = 0.3920(4)$. These values compare favorably with $\tilde{S}_{Li}^{cl}(r_0) = 0.3915$ for the uphill parallel orbit. The corresponding spacing for hydrogen is $\tilde{S}_{H}^{qm} = 0.3935$ which is in good agreement with $\tilde{S}_{H}^{cl} = 0.3935$ for U_1.

The peak corresponding to the spacing between repetitions of the downhill orbit

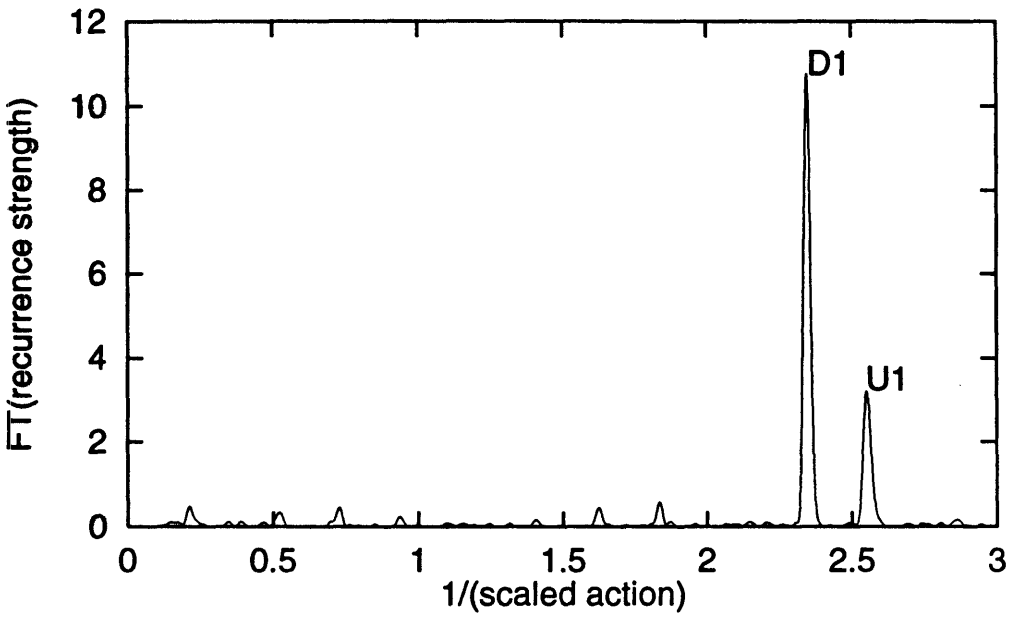

Figure 8-20: The Fourier transform of the lithium recurrence spectrum at $\epsilon_F = -3$ has two prominent peaks whose frequencies correspond to the scaled action of U_1 and D_1.

in the computed lithium recurrence spectrum corresponds to $\tilde{S}_{Li}^{qm} = 0.4262$. The same peak in the Fourier transform of the experimental lithium recurrence spectrum at $\epsilon_F = -3$ corresponds to a spacing of $\tilde{S}_{Li}^{exp} = 0.4260(4)$. These compare favorably with $\tilde{S}_{Li}^{cl}(r_0) = 0.4268$ for D_1. The corresponding spacing for hydrogen is $\tilde{S}_H^{qm} = 0.4288$ which is in good agreement with $\tilde{S}_H^{cl} = 0.4289$ for D_1. Consequently, we conclude that the recurrence spectrum really does have strong underlying periodicities corresponding to $\tilde{S}_{Li}^{cl}(r_0)$ of U_1 and D_1.

There seems to be two possible approaches to computing the scaled action of recurrences in spectra of alkali-metal atoms in strong fields. For low action, there appears to be no doubt that the scaled action of recurrences is given by the hydrogenic scaled action. However, for high action it appears that the position of recurrences is given by a scaled action computed by excluding the core region.

I do not know how to reconcile these seemingly contradictory results, but I mention the possibility of some interference effect causing a frequency pulling. We have tried to account for the shift in the high action recurrences by some interference effect due to the quantum defect. The closed orbit sum in Eqn. 6.9 is actually a sum over Fourier series, with each primitive orbit contributing a Fourier series. Replacing S

with its value in alkali metals gives

$$Df(E) = \sum_k \sum_{n=1}^{\infty} A_{nk} \sin\left[2\pi n(w\tilde{S}_H + \delta_s) - \Phi_{nk}\right]. \tag{8.5}$$

If the quantum defect were a constant phase in every term, it could not cause a shift in the peak positions. However, the phase due to the quantum defect is multiplied by n, and I am unsure what strange effects this could introduce.

8.6 Summary and Discussion

Lithium in an electric field provides an experimentally accessible system for studying the connections between classical and quantum features of a chaotic system. The alkali-metal core prevents the separation of variables which can be employed to solve the hydrogenic Stark problem. The core induces chaos in the classical system by scattering the valence electron from one hydrogenic trajectory into another each time it passes through the core. For all but the smallest of electric field strengths, this leads to the destruction of tori and ergodic or nearly ergodic motion which characterizes classical chaos.

By employing principles of closed-orbit theory, spectral evolution can be interpreted in terms of classical orbits. Above the classical ionization limit, bifurcations play a dominant role by increasing an orbit's contribution to the spectrum and adding frequency components so that a continuous spectrum can evolve into a quasidiscrete spectrum. Below the classical ionization limit, core-scattered recurrences also have a strong spectral signature. From the point of view of closed-orbit theory, this process accounts for the only difference between lithium and hydrogen. Therefore it must be the origin of chaos in the quantum system.

Adding the core scattering mechanism to closed-orbit theory may allow computation of the chaotic lithium spectrum using only the hydrogenic orbits. This would circumvent some of the difficulties usually present in the application of closed-orbit theory to chaotic problems. In particular, all of the orbits are stable, and they are

easy to compute. However, a detailed quantitative model for including core scattering into closed-orbit theory is lacking. Furthermore, multiple core scattering requires many more terms in the closed-orbit sum and causes an exponential proliferation of recurrences as a function of action, in contrast to the quadratic proliferation of a two-dimensional integrable systems such as hydrogen in an electric field.

The possibility of using closed-orbit theory to quantize a chaotic system using the classical mechanics of a related regular system makes us wonder whether lithium in an electric field might provide an example of a chaotic system which is approachable by Einstein-Brillouin-Keller tori quantization. Core effects might be included by considering scattering from one hydrogenic torus to another and would cause level repulsions similar to the manner in which tunnelling between tori can break energy-level degeneracies.

Chapter 9

Parallel Field Recurrence Spectra

For the foolishness of God is wiser than man's wisdom, and the weakness of God is stronger than man's strength. –1 Corinthians 1:25

Recurrence spectra of Rydberg atoms in parallel fields have been studied experimentally in the continuum regime (in fact, above $E = 0$) [MRB93], but the quasidiscrete region ($\epsilon_F < -2$) is largely unexplored. In many ways we expect the recurrence spectrum in the discrete region for parallel fields simply to combine features which are well known for the separate electric and magnetic field systems. In the regime where the magnetic field dominates, we expect rotators and vibrators. When the electric field dominates, we expect uphill and downhill orbits. We do not know what happens in intermediate fields which cause effects of comparable magnitude, but we expect that there will be bifurcations which give new orbits and large recurrences. For alkali-metals, there will be core scattering.

The parallel field system gives us another knob to turn. Where do we look in this multi-parameter space? The approach we will take is to begin with diamagnetic recurrence spectra and turn up the electric field. The two relevant parameters are ϵ_B and ϵ_F. We will show the evolution of the recurrence spectra as the electric field is increased by defining a scaled field as the ratio of electric and magnetic scaled

energies. The scaled field parameter is

$$G(F,B) = \frac{\epsilon_B}{\epsilon_F} = \frac{EB^{-2/3}}{EF^{-1/2}} = \frac{F^{1/2}}{B^{2/3}}. \tag{9.1}$$

This scaled field parameter is a measure of the relevant strength of the electric to magnetic fields in the classical system. Note the difference from $\beta = 12F/5B^2n^2$ which played the role of a measure of the relative strength of electric to magnetic fields in the quantum system, as discussed in Chapter 2.

9.1 Hydrogen in Parallel Fields

Unlike the simpler cases of diamagnetism and the Stark effect, no one has hunted out closed orbits in the quasidiscrete region of the parallel field problem. Viewing the spectral evolution of the recurrence spectrum at constant ϵ_B while the electric field is raised and knowing about the diamagnetic and Stark orbits provides some simple clues. The degeneracy in action of the parallel orbits is lifted for $F \neq 0$, and these orbits have the scaled action of the uphill and downhill orbits in the electric field problem, although the $\tilde{S}_F$ of these orbits must be transformed into the appropriate $\tilde{S}_B = w_F\tilde{S}_F/w_B$. Furthermore, we expect that the perpendicular orbit will see the electric field and not remain confined to the $z = 0$ plane. It will bend toward the uphill direction as the electric field is increased, and its action should decrease slightly.

Figure 9-1 shows a map of computed recurrence spectra at low action for $\epsilon_B = -0.6$ as the scaled field is raised. The $3S$ initial state was used for all parallel field recurrence spectra shown in this chapter. The long and short dashed lines are scaled actions of uphill and downhill parallel orbits, respectively. The spectrum is clearly not dominated by these orbits as in the Stark effect. The rotators provide the largest peaks in the recurrence spectrum, and some of them persist as the scaled field is raised to the ionization threshold, although their strength varies and they move to slightly lower action. However, the overall impression of Figure 9-1 is that the recurrence spectrum changes little as the scaled field is raised, except that the purely diamagnetic

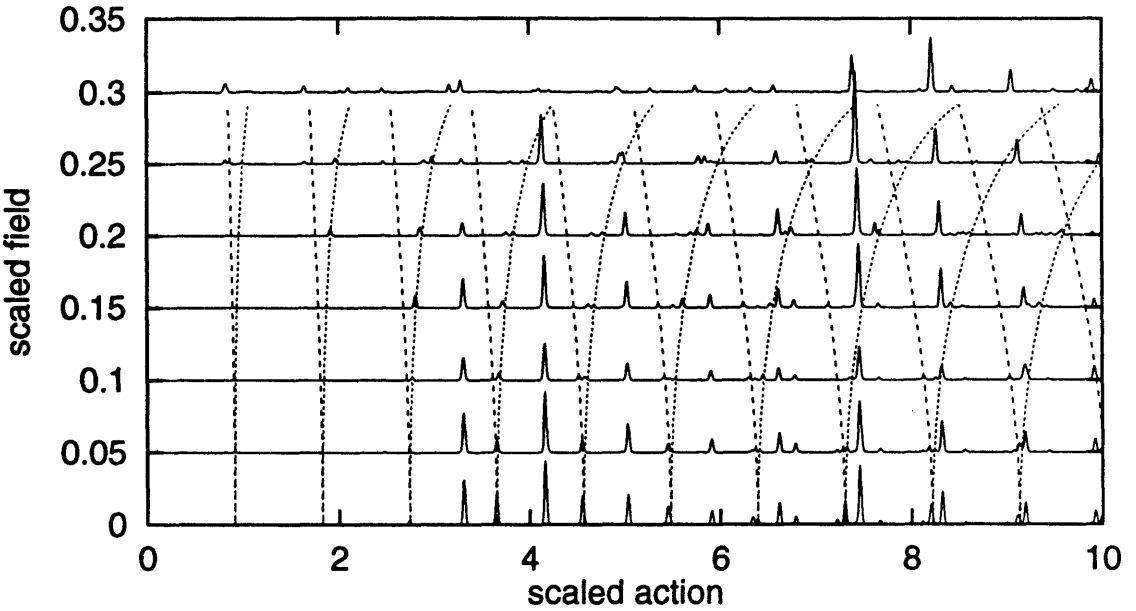

Figure 9-1: Hydrogen recurrence spectra in parallel fields for $\epsilon_B = -0.6$. Long and short dashed lines are scaled actions of uphill and downhill parallel orbits, respectively.

spectrum has recurrences which are generally larger than the recurrences at a scaled field of 0.3.

A blowup of Figure 9-1 is shown in Figure 9-2. We can clearly see the splitting of the parallel orbits into an upfield and downfield components. In addition, new peaks seem to be splitting off of these uphill and downhill orbits.

More detailed interpretation of the parallel field recurrence spectra requires computing the closed-orbits for each set of ϵ_B and scaled field parameter $G = \epsilon_B/\epsilon_F$. This will not be done for all the parallel field recurrence spectra shown in this chapter. However, I have found some low-action closed orbits for $\epsilon_B = -0.6$ and $G = \epsilon_B/\epsilon_F = 0.2$. This corresponds to $\epsilon_F = -3$. These orbits are shown in Figure 9-3. As shown in Table 9.1, these closed orbits are labeled as a function of increasing initial angle with the $+z$ axis. (Note that the apparent angles in Figure 9-3 are deceptive because the z and ρ axes have different scales.)

The "uphill" and "downhill" parallel orbits are not shown because they are trivially located on the $+z$ and $-z$ axes, respectively. They will be denoted by U_n and D_n, just as in the electric field case. The orbits labeled a,b, and c have small initial angles and similar shapes. They are distinguishable because of the number of passes

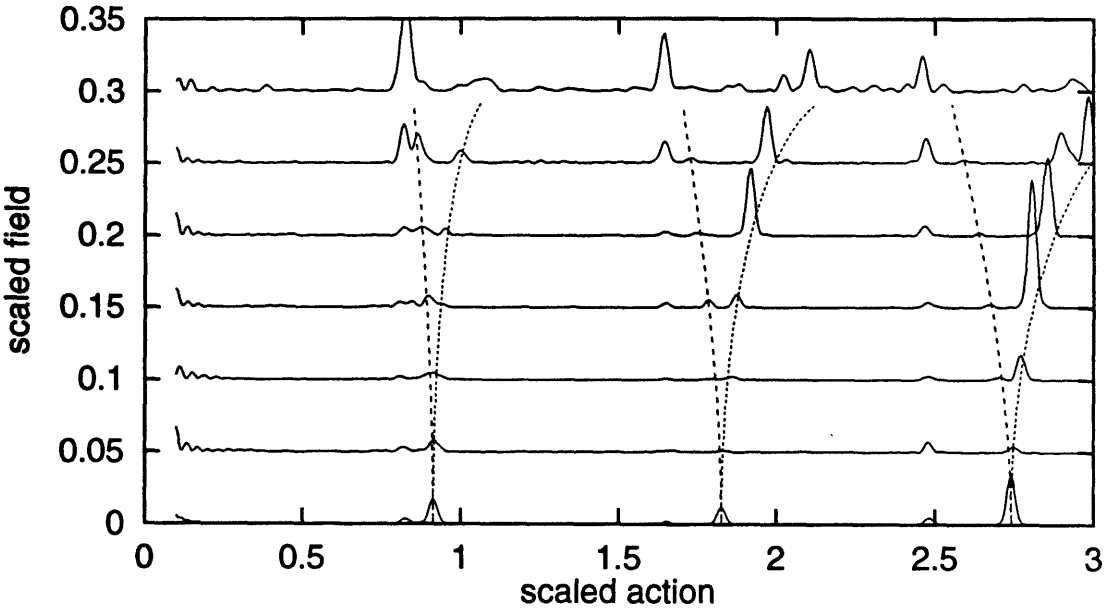

Figure 9-2: Hydrogen recurrence spectra in parallel fields for $\epsilon_B = -0.6$. Long and short dashed lines are scaled actions of uphill and downhill parallel orbits, respectively.

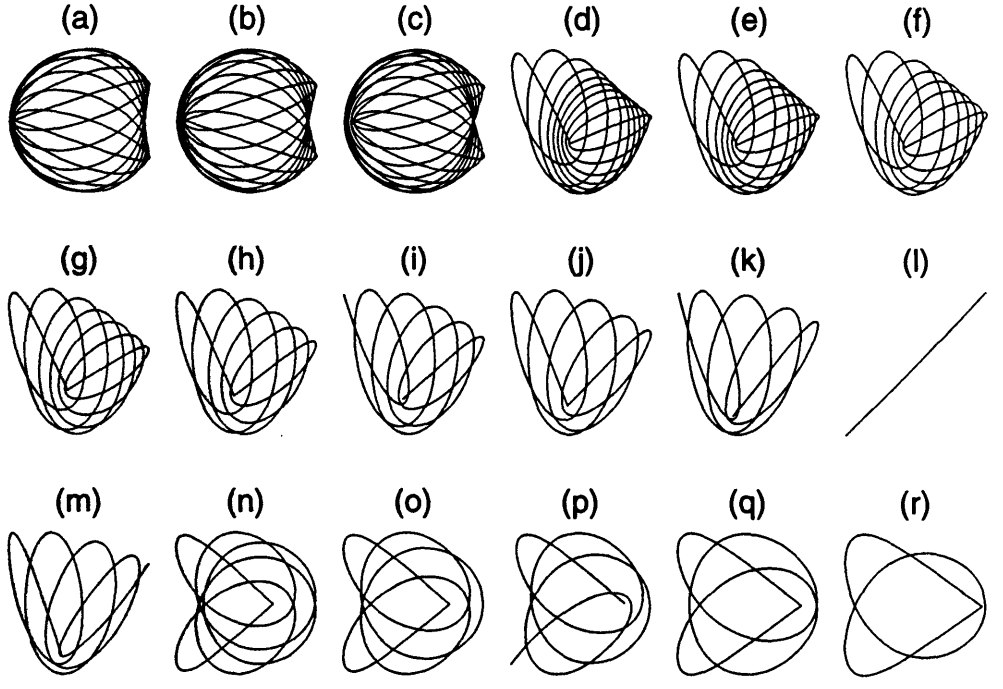

Figure 9-3: Hydrogenic closed orbits $\epsilon_B = -0.6$ and $\epsilon_F = -3$. The z axis is horizontal and the ρ axis is vertical. The action and initial angle of these orbits are given in Table 9.1. The corresponding recurrences are shown in Figure 9-4.

they make close to the nucleus before returning to it exactly. a travels out and back 9 times, has an action close to U_9, and is analogous to the 8/9 orbit in the electric field problem. b and c travel out and back 10 and 11 times, have an action close to U_{10} and U_11, and are analogous to the 9/10 and 10/11 orbits, respectively.

For $B = 0$, the system is separable and all of the closed orbits can be described by their period ratio. For $\epsilon_B = -0.6$ and $\epsilon_F = -3$, the system is non-separable, and there is a separatrix in phase space. As in the case of diamagnetism, for small initial angles with the z axis, the orbits have a vibrational nature. For small initial angles with the ρ axis, the orbits have a vibrational nature. There is a range of angles between the initial angles of the vibrators and rotators which is near the separatrix in phase space. The orbits d-m are on the other side of the separatrix and have rotational character: they are the parallel field generalizations of the rotators of diamagnetism. In particular, the orbit labeled l can be continuously traced to the perpendicular orbit R_n as $F \to 0$. At $\epsilon_F = -3$ it makes an 80.87° angle with the z axis. The orbits d-m are skewed rotators.

The orbits labeled n-r represent vibrators on the downhill side. n makes 5 round trips and has an action close to D_5. o, q, and r make 4, 3, and 2 round trips and have actions close to D_4, D_3 and D_2, respectively. p makes 7 round trips and has an action close to D_7. (Note that p retraces itself after 3.5 round trips.) These orbits also have diamagnetic analogs which are listed in Table 9.1.

Figure 9-4 shows the parallel field recurrence spectra for $\epsilon_B = -0.6$ and $\epsilon_F = -3$. (The recurrence amplitude is plotted to make the smaller peaks more visible.) Most of the recurrences are labeled as corresponding to closed orbits. Many of the recurrences have more than one orbit contributing, and are labeled appropriately. There are some recurrences for which no corresponding orbit has been found. The method used to find orbits does not guarantee finding all of the orbits[1] and it is easier to find the more stable orbits. Because the more stable orbits tend to have larger recurrence strengths, it is not surprising that orbits corresponding to the larger recurrences in the spectrum have been found.

[1]Finding all of the closed orbits of a non-integrable system is not generally possible.

Table 9.1: Closed orbits in parallel fields for $\epsilon_B = -0.6$ and $\epsilon_F = -3$. The labels a-o are used in Figures 9-3 and 9-4.

Orbit	θ_i	$\tilde{S}_B$	Diamagnetic Analog
U_1	0	0.8799	V_1^+
a	6.9930	7.9211	V_8^1
b	9.1476	8.8030	V_9^1
c	10.2744	9.6776	V_{10}^1
d	14.5777	8.5011	R_{10}^1
e	15.8760	7.6266	R_9^1
f	17.8423	6.7536	R_8^1
g	20.9077	5.8799	R_7^1
h	25.9884	5.0129	R_6^1
i	29.9340	9.1595	R_4^2
j	35.7372	4.1513	R_5^1
k	45.6696	7.4462	R_9^2
l	80.8700	0.8313	R_1
m	111.875	7.4446	R_9^2
n	136.314	4.6563	V_5^1
o	140.632	3.7641	V_4^1
p	143.816	6.6182	V_7^2
q	148.161	2.8549	V_3^1
r	165.616	1.9208	V_2^1
D_1	180	0.9591	V_1^-

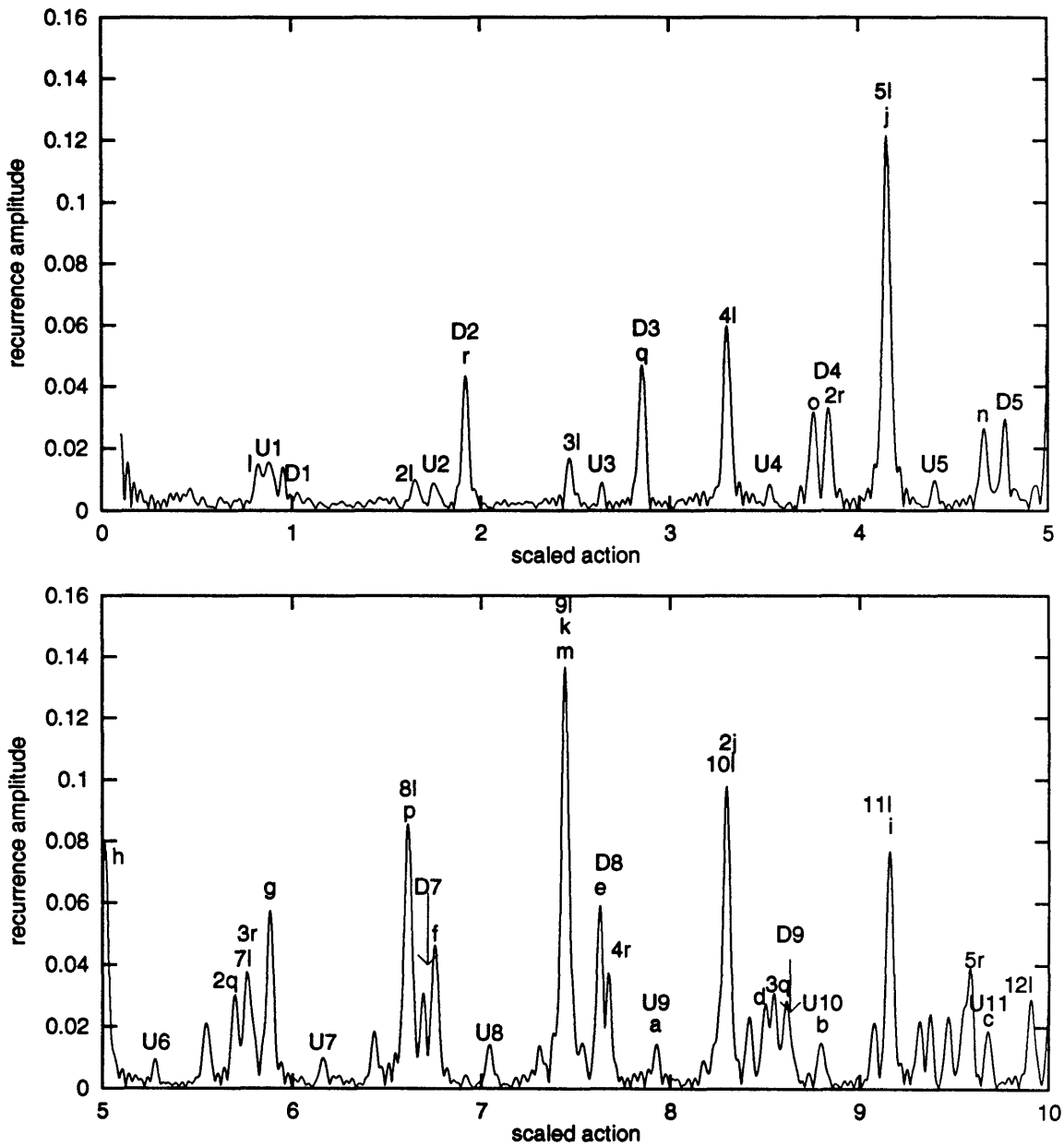

Figure 9-4: Parallel field recurrence spectra for $\epsilon_B = -0.6$ and $\epsilon_F = -3$. Most recurrences are labeled with the corresponding closed orbit.

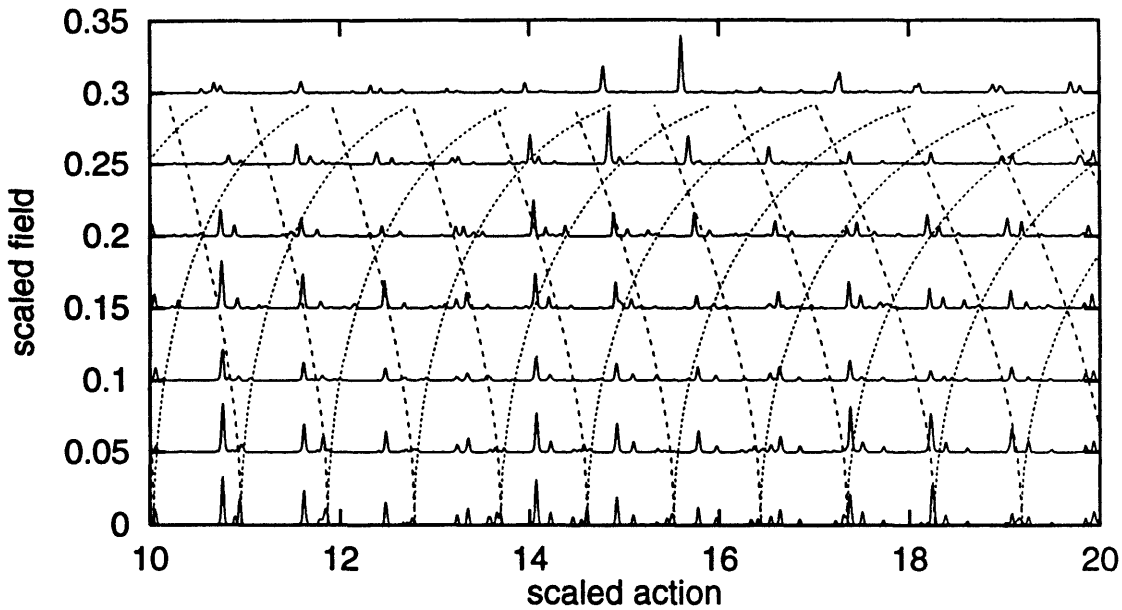

Figure 9-5: Hydrogen recurrence spectra in parallel fields for $\epsilon_B = -0.6$ at high action. Long and short dashed lines are scaled actions of uphill and downhill parallel orbits, respectively.

Figure 9-5 shows a map of recurrence spectra at high action for $\epsilon_B = -0.6$ as the scaled field is raised. The parallel orbits are not prominent. The large peaks which move to slightly lower action as the scaled field is raised are repetitions of the orbit which is perpendicular to the magnetic field for $F = 0$. Most large recurrences for $F = 0$ lose their recurrence strength as the scaled field is raised, and the recurrence spectrum actually looks simpler at $\epsilon_B/\epsilon_F = 0.3$. However, I suspect that the classical system at $\epsilon_B/\epsilon_F = 0.3$ actually has more closed orbits than at $\epsilon_B/\epsilon_F = 0$, and the appearance of the recurrence spectrum is due to most of them having small recurrence strengths.

Figures 9-6 and 9-7 show parallel field recurrence spectra for $\epsilon_B = -0.4$ as ϵ_F is increased. Once again, the spectrum does not lend itself to easy interpretation, except to say that the uphill and downhill parallel orbits seem to be present but not dominant and that the orbit which begins perpendicular to the field appears to remain strong as F is increased. There are many other features which can presumably be identified by finding closed orbits and computing their recurrence strengths.

Parallel field recurrence spectra for $\epsilon_B = -0.3$ are shown in Figures 9-6 and 9-7. Again, the parallel orbits are weak. However, as the scaled field is raised, even the

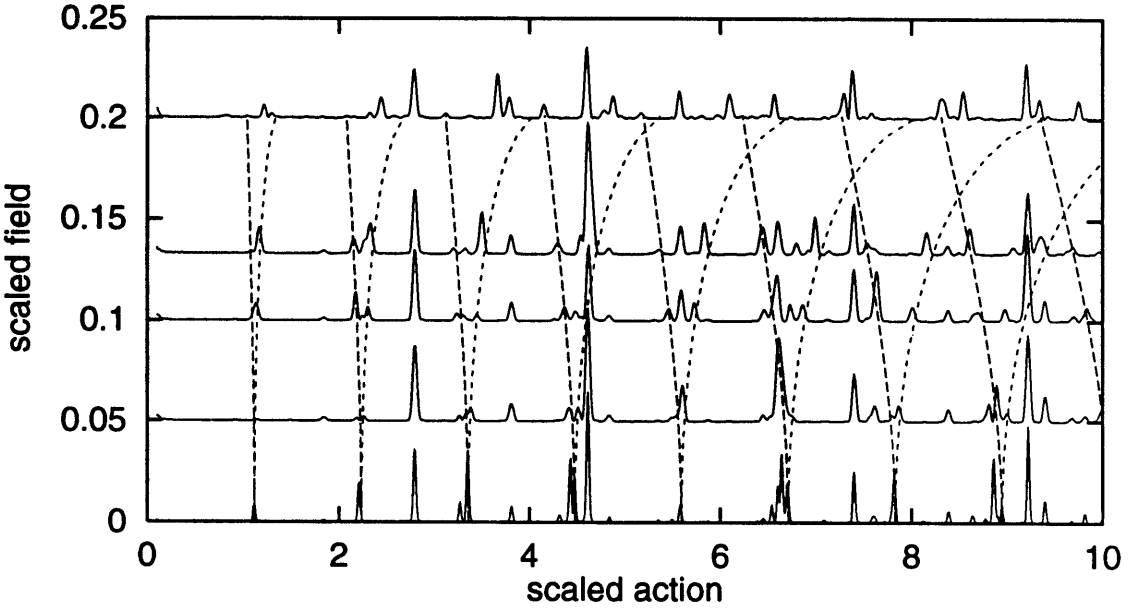

Figure 9-6: Hydrogen recurrence spectra in parallel fields for $\epsilon_B = -0.4$. Long and short dashed lines are scaled actions of uphill and downhill parallel orbits, respectively.

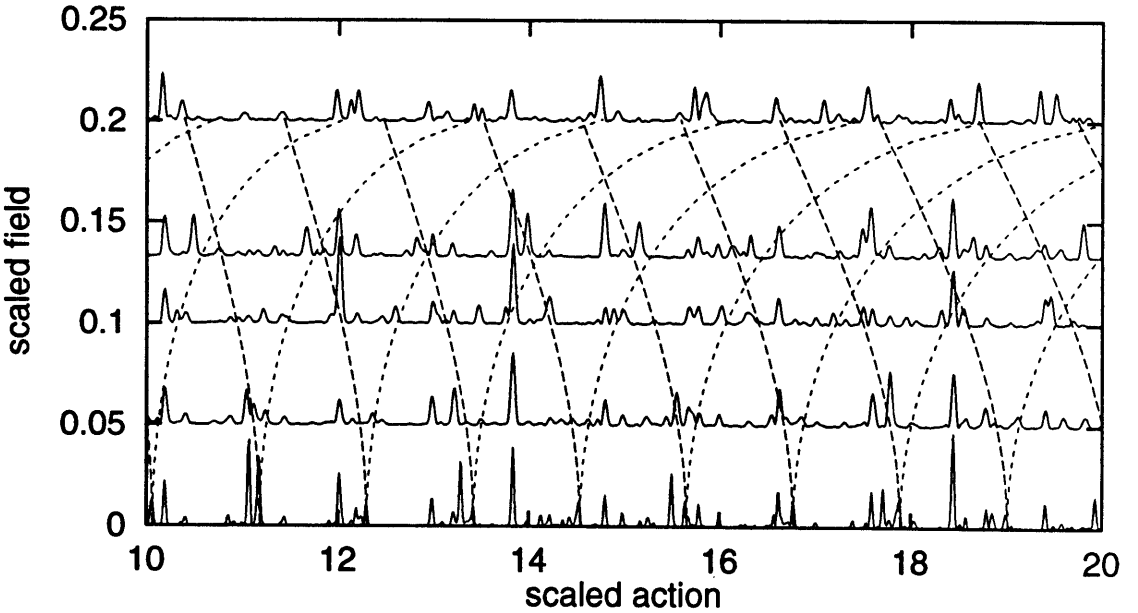

Figure 9-7: Hydrogen recurrence spectra in parallel fields for $\epsilon_B = -0.4$ at high action. Long and short dashed lines are scaled actions of uphill and downhill parallel orbits, respectively.

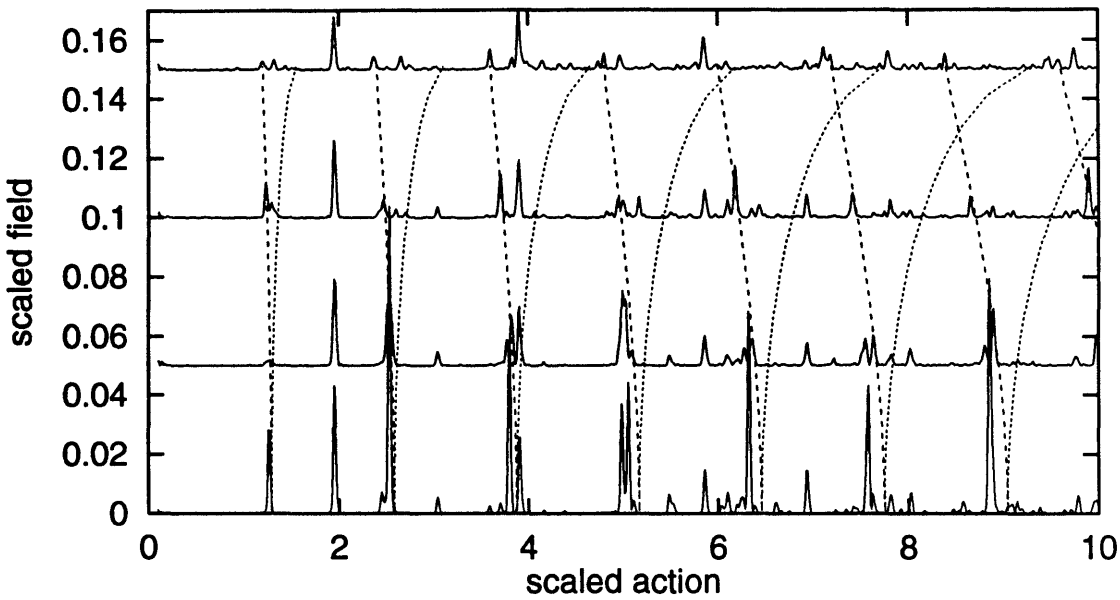

Figure 9-8: Hydrogen recurrence spectra in parallel fields for $\epsilon_B = -0.3$. Long and short dashed lines are scaled actions of uphill and downhill parallel orbits, respectively.

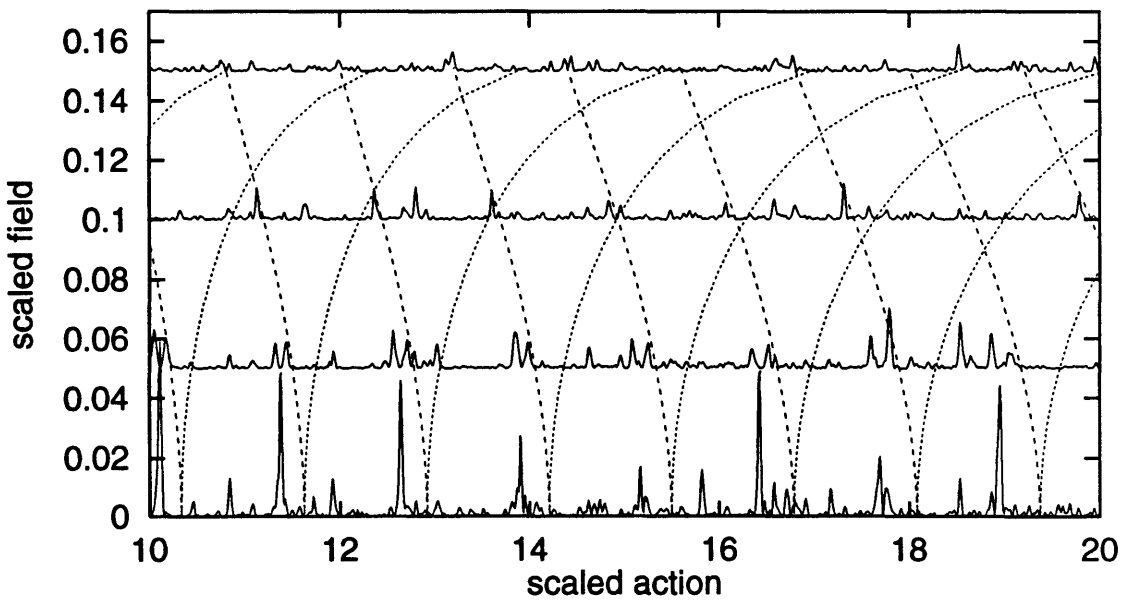

Figure 9-9: Hydrogen recurrence spectra in parallel fields for $\epsilon_B = -0.3$ at high action. Long and short dashed lines are scaled actions of uphill and downhill parallel orbits, respectively.

perpendicular orbits seem to lose most of their recurrence strength. At $G = \epsilon_B/\epsilon_F = 0.15$, the spectrum looks like noise, particularly at high action. Accounting for this recurrence spectrum should prove to be quite a challenge for closed-orbit theory.

Even though detailed interpretation of parallel field recurrence spectra requires searching for the closed orbits and computing semiclassical recurrence strengths, the dominance of the perpendicular orbit can be understood simply by examining surfaces of section. For $F = 0$, the rotator orbits wind around tori which have two intersections with the $u = 0$ plane. The perpendicular orbit is the elliptic fixed point at the center of these curves. In contrast, the vibrators wind around tori with a single intersection with the $u = 0$ plane and form the outer curves for the surfaces of section at low scaled energy. The parallel orbits lie on the u and v axes which are the $+z$ and $-z$ axes, respectively. The parallel orbit on the u axis merely passes through the origin of the p_v vs. v surface of section. The parallel orbit on the v axis lies on the outer boundary of the energetically accessible part of the surface of section, and the neighboring tori are also vibrators.

Figure 9-10 shows that the rotators are very robust as ϵ_F is raised at constant ϵ_B. A few outer rotator tori may be destroyed by the electric field, but the perpendicular orbit itself remains surrounded by a large region of regular phase space. In contrast, the magnetic field alone is sufficient to destroy vibrators above $\epsilon_B = -0.54$. Stable vibrators only appear briefly near bifurcations. Furthermore, they are isolated and become unstable quickly as ϵ_F or ϵ_B is changed further.

9.2 Lithium in Parallel Fields

This section presents recurrence spectra for lithium in parallel fields. Their interpretation has not yet been worked out, so the results are presented without comment.

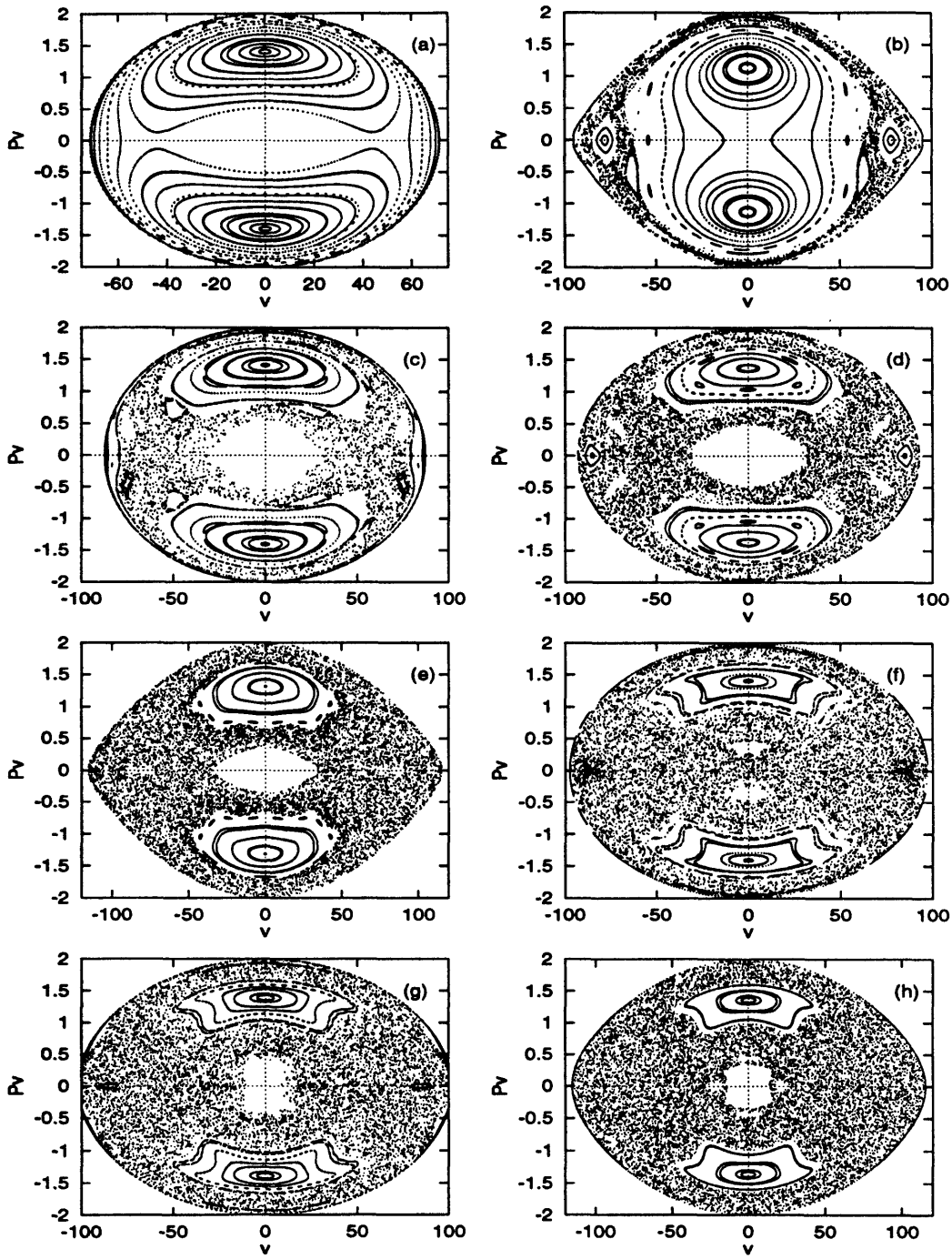

Figure 9-10: Poincaré surfaces of section for hydrogen in parallel fields. (a) $\epsilon_B = -0.6$, $\epsilon_F = -6$; (b) $\epsilon_B = -0.6$, $\epsilon_F = -2$; (c) $\epsilon_B = -0.4$, $\epsilon_F = -8$; (d) $\epsilon_B = -0.4$, $\epsilon_F = -3$; (e) $\epsilon_B = -0.4$, $\epsilon_F = -2$; (f) $\epsilon_B = -0.3$, $\epsilon_F = -6$; (g) $\epsilon_B = -0.3$, $\epsilon_F = -3$; (h) $\epsilon_B = -0.3$, $\epsilon_F = -2$.

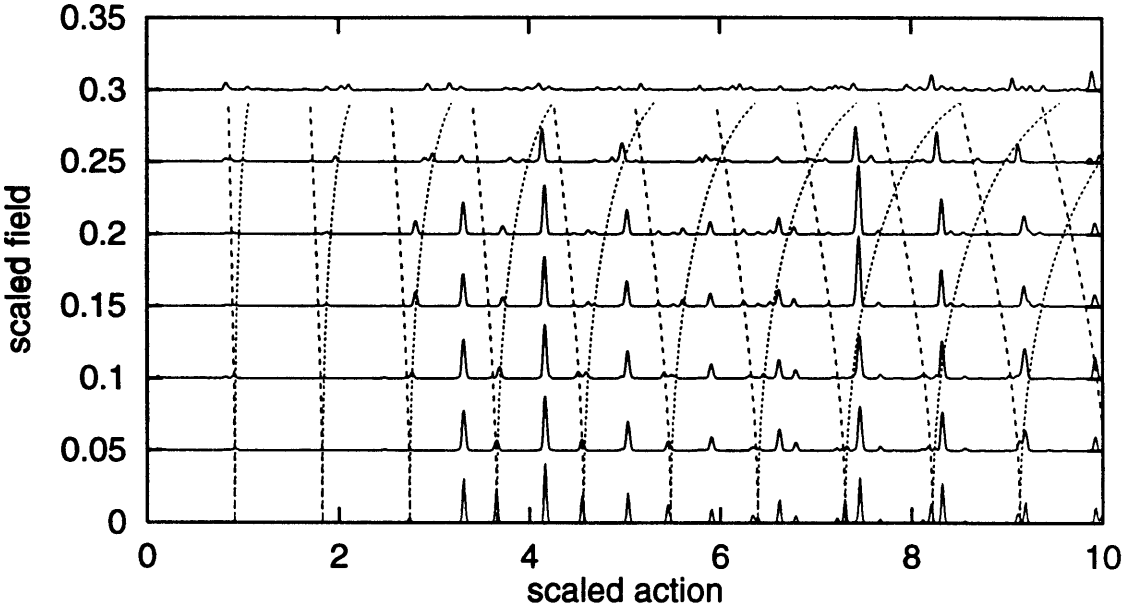

Figure 9-11: Lithium recurrence spectra in parallel fields for $\epsilon_B = -0.6$. Long and short dashed lines are scaled actions of uphill and downhill parallel orbits, respectively.

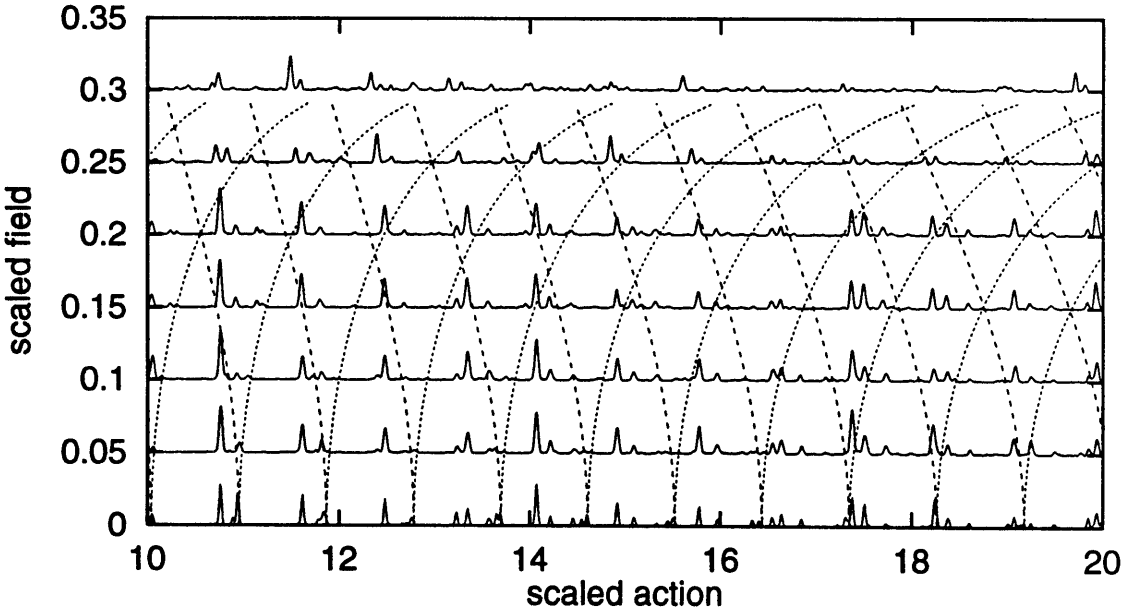

Figure 9-12: Lithium recurrence spectra in parallel fields for $\epsilon_B = -0.6$ at high action. Long and short dashed lines are scaled actions of uphill and downhill parallel orbits, respectively.

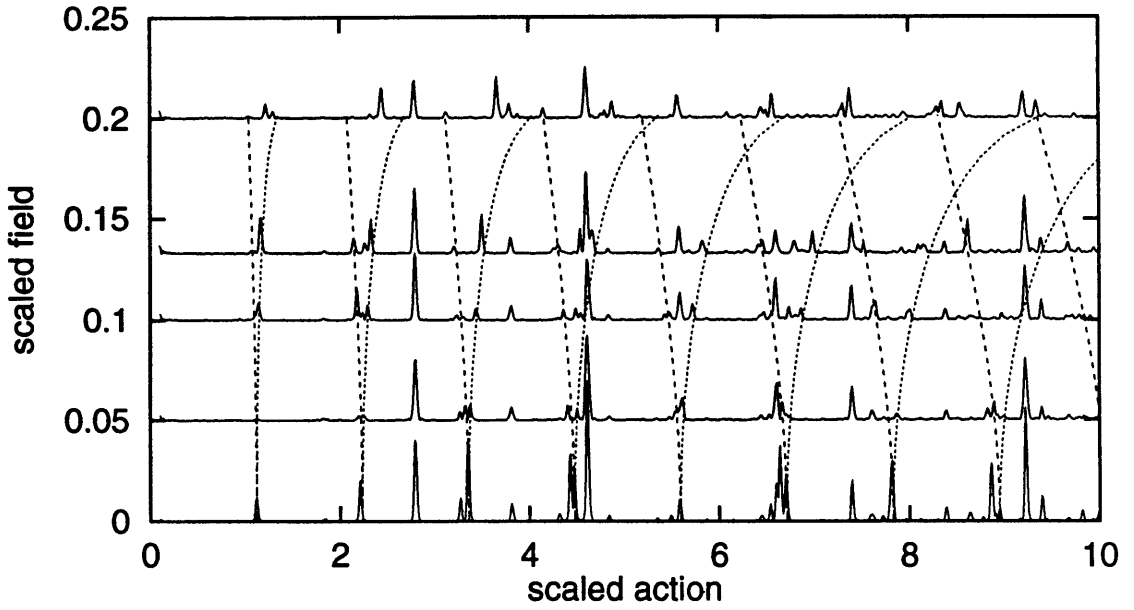

Figure 9-13: Lithium recurrence spectra in parallel fields for $\epsilon_B = -0.4$. Long and short dashed lines are scaled actions of uphill and downhill parallel orbits, respectively.

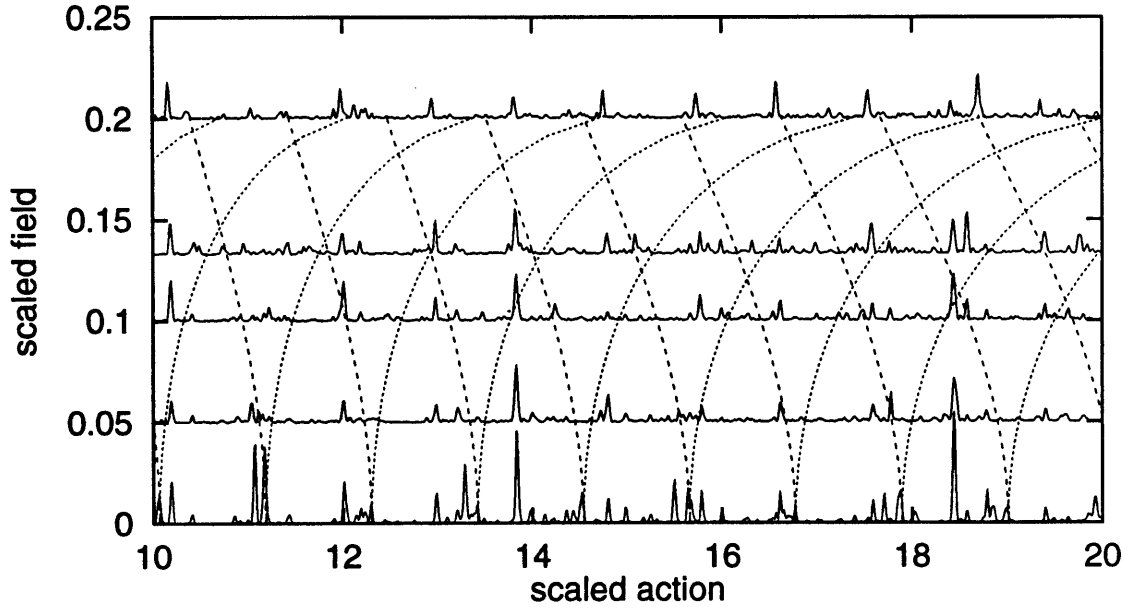

Figure 9-14: Lithium recurrence spectra in parallel fields for $\epsilon_B = -0.4$ at high action. Long and short dashed lines are scaled actions of uphill and downhill parallel orbits, respectively.

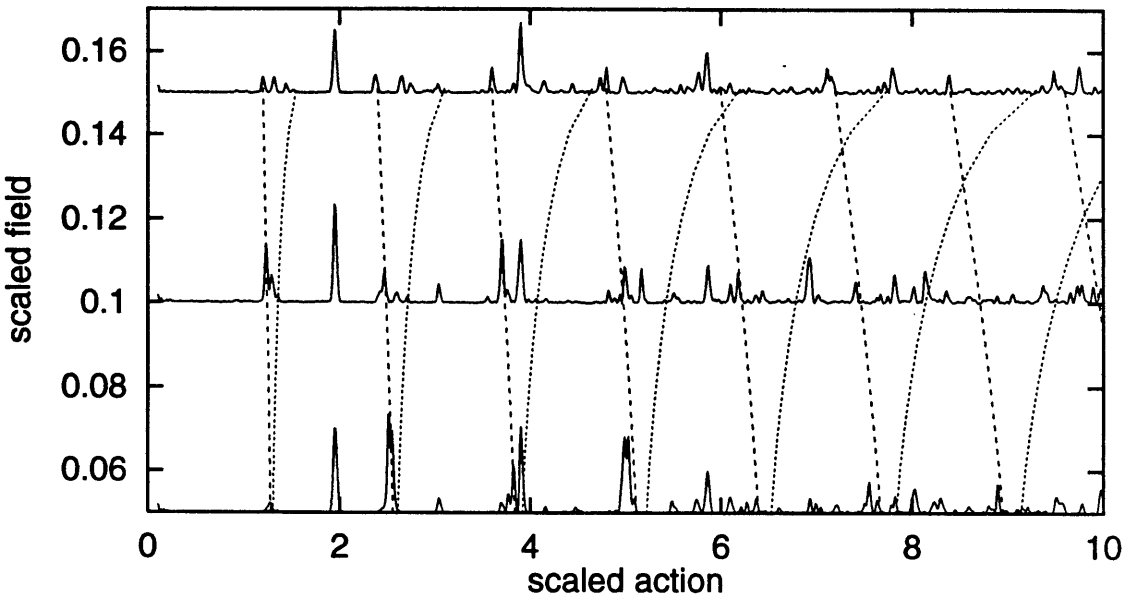

Figure 9-15: Lithium recurrence spectra in parallel fields for $\epsilon_B = -0.3$. Long and short dashed lines are scaled actions of uphill and downhill parallel orbits, respectively.

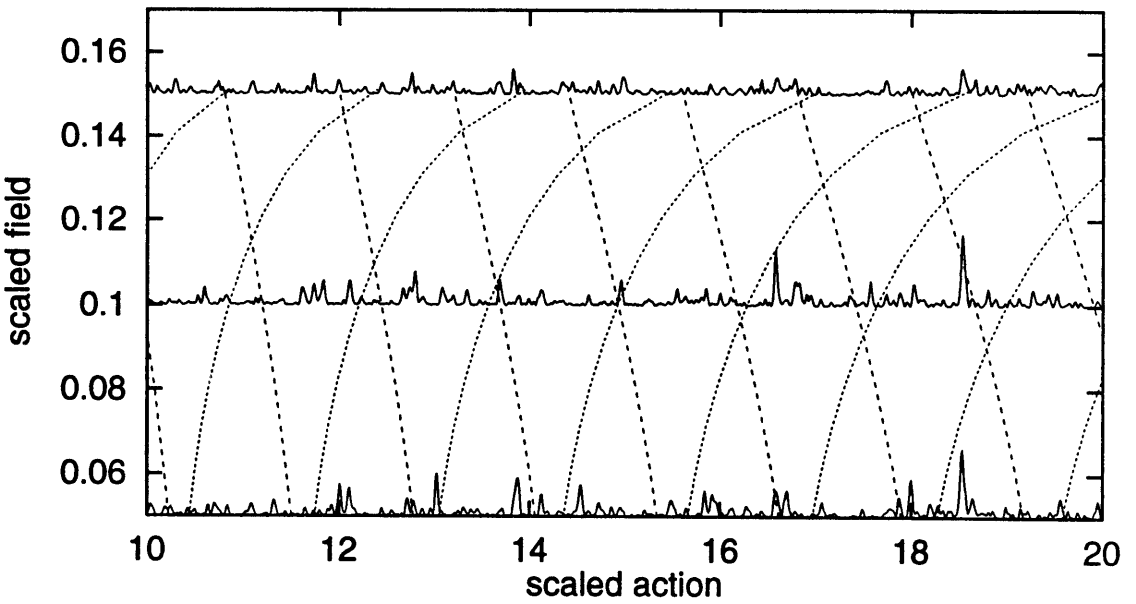

Figure 9-16: Lithium recurrence spectra in parallel fields for $\epsilon_B = -0.3$ at high action. Long and short dashed lines are scaled actions of uphill and downhill parallel orbits, respectively.

Chapter 10

Recurrence Statistics

"Come now, let us reason together," says the LORD. *"Though your sins are like scarlet, they shall be as white as snow; though they are red as crimson, they shall be like wool."*
–Isaiah 1:18

I demonstrated in Chapter 7 that recurrence counting can be a useful tool for characterizing recurrence spectra. In particular, studying the proliferation of recurrences revealed the chaotic nature of odd-parity diamagnetic lithium in a region where energy-level statistics failed. The difficulty in applying this technique lies in the need to have fully resolved recurrence spectra at high enough action to discern the nature of the proliferation of recurrences. Another difficulty is the highly degenerate nature of recurrence spectra.

The direct link between recurrence spectra and classical orbits motivates continued work in this area. Perhaps there is a way to learn more from recurrence spectra about the nature of a system's classical dynamics. Here I will present several ways of looking at global properties of recurrence spectra. Part of the interpretation will come from the idea of recurrence proliferation. Part will come from the dependence of recurrence strengths on the stability of an orbit. Detailed predictions may be possible from first principles, but this would require more understanding of closed-orbit theory than is currently available. I expect that the ingredients in a rigorous statistical description

of recurrence spectra will require quantitative descriptions of core scattering and bifurcations. The problem undoubtedly requires considerable statistical ability.

In contrast, I have taken an empirical approach by computing some simple global properties which seem relevant. Recurrence counting is motivated by the exponential proliferation of closed (and periodic) orbits in a chaotic system. Looking at the area under the recurrence spectrum is similarly motivated. The motivation for studying the distribution of recurrence heights came from noticing that regular recurrence spectra tend to have many more large recurrences than chaotic recurrence spectra.

10.1 Onset of Chaos in Diamagnetic Hydrogen

We have already shown a successful application of recurrence counting in the case of diamagnetic lithium and hydrogen. We defined $N_{os}(\tilde{S})$ as the number of peaks in the oscillator strength recurrence spectrum with an action less than $\tilde{S}$. By analogy $N_{ds}(\tilde{S})$ is the number of peaks in the state density recurrence spectrum. This technique is only applicable if individual recurrences can be resolved to high enough action to distinguish a particular type of proliferation. This is not the case for the available recurrence spectra showing the onset of chaos in diamagnetic hydrogen.

If every orbit had roughly the same recurrence strength, and if recurrence amplitudes did not add coherently, then there would be a global shift of recurrence strength to higher action. However, recurrence strengths can vary widely and amplitudes must be added coherently. Nonetheless, we can at least look at the accumulated area under recurrence spectra and see if the proliferation of closed orbits leads to a global shift of recurrence strength to higher action.

The area under the recurrence spectrum for an action less than $\tilde{S}$ is

$$A(\tilde{S}) = \int_0^{\tilde{S}} R(\tilde{S})\, d\tilde{S}, \tag{10.1}$$

where $R(\tilde{S})$ can be either the state density recurrence spectrum R_{ds} or the oscillator

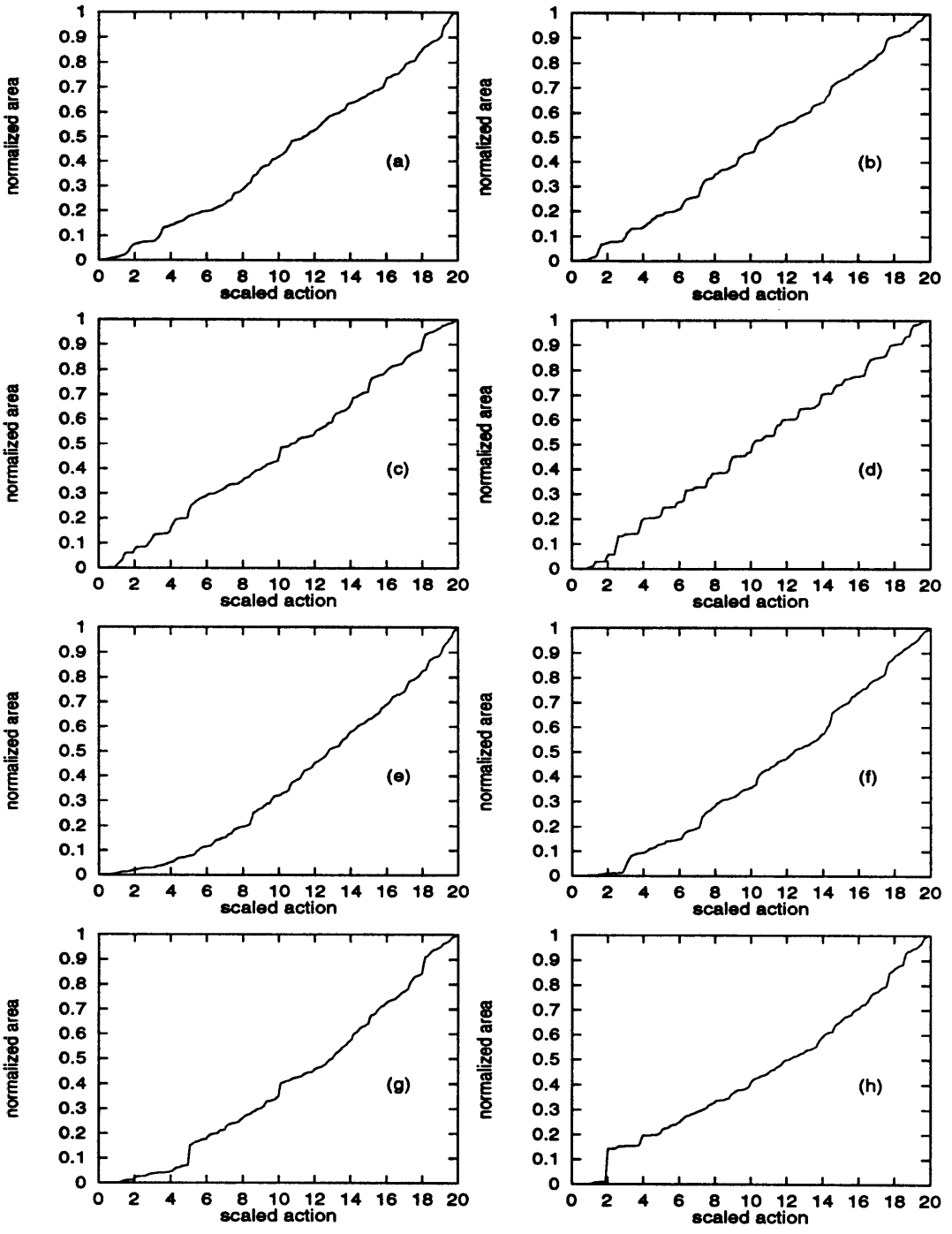

Figure 10-1: Normalized area under recurrence spectra of even-parity diamagnetic hydrogen for $m = 0$. (a) $\epsilon_B = -0.15$, R_{os}; (b) $\epsilon_B = -0.20$, R_{os}; (c) $\epsilon_B = -0.25$, R_{os}; (d) $\epsilon_B = -0.30$, R_{os}; (e) $\epsilon_B = -0.15$, R_{ds}; (f) $\epsilon_B = -0.20$, R_{ds}; (g) $\epsilon_B = -0.25$, R_{ds}; (h) $\epsilon_B = -0.30$, R_{ds}.

strength recurrence spectrum R_{os}. We define the *normalized area* as

$$A_n(\tilde{S}) = \frac{A(\tilde{S})}{A(\tilde{S}^{max})}, \tag{10.2}$$

where $\tilde{S}^{max}$ is the maximum scaled action in the region under consideration.

The normalized area as a function of scaled action is shown in Figure 10-1 for even-parity diamagnetic hydrogen in the region where the onset of chaos occurs. The graphs are not very illuminating because all the curves are nearly diagonal: they show a roughly uniform accumulation of area under the recurrence spectrum. The features are much clearer if we plot the deviation of the normalized area from the diagonal,

$$\Delta A_n(\tilde{S}) = \frac{\tilde{S}}{\tilde{S}^{max}} - A_n(\tilde{S}). \tag{10.3}$$

This function represents the deviation of the actual accumulation of area under the recurrence spectrum from the average. It is shown in Figure 10-2.

There is some degree of chaos present for all of the scaled energies shown in Figure 10-2. Figure 10-2(a) shows the area under R_{os} for $\epsilon_B = -0.15$. The dynamics is nearly completely chaotic here, and we see that the area under the oscillator strength recurrence spectra show the largest deviation from the diagonal. ΔA_n becomes smaller as the scaled energy is lowered toward the regular region. The sharp "triangle" like features are caused by sudden jumps in the recurrence strength near a bifurcation or sequence of bifurcations. In particular, the regular "saw" pattern in Figure 10-2(d) for $\epsilon_B = -0.3$ is due to a regular pattern of bifurcations.

Figures 10-2 (e-h) show ΔA_n for the density of states for the same energies as Figure 10-1. These areas generally show a larger deviation from the diagonal than the corresponding areas for R_{os}. In particular, Figure 10-2 (e) has a "bow" shape which will turn out to be a common feature of chaotic recurrence spectra. As the scaled energy is lowered toward the regular region, $\Delta A_n(\tilde{S})$ becomes smaller.

The saw-like features which are particularly prominent in Figure 10-2(d) arise from a number of localized recurrences which are much larger than average. To investigate

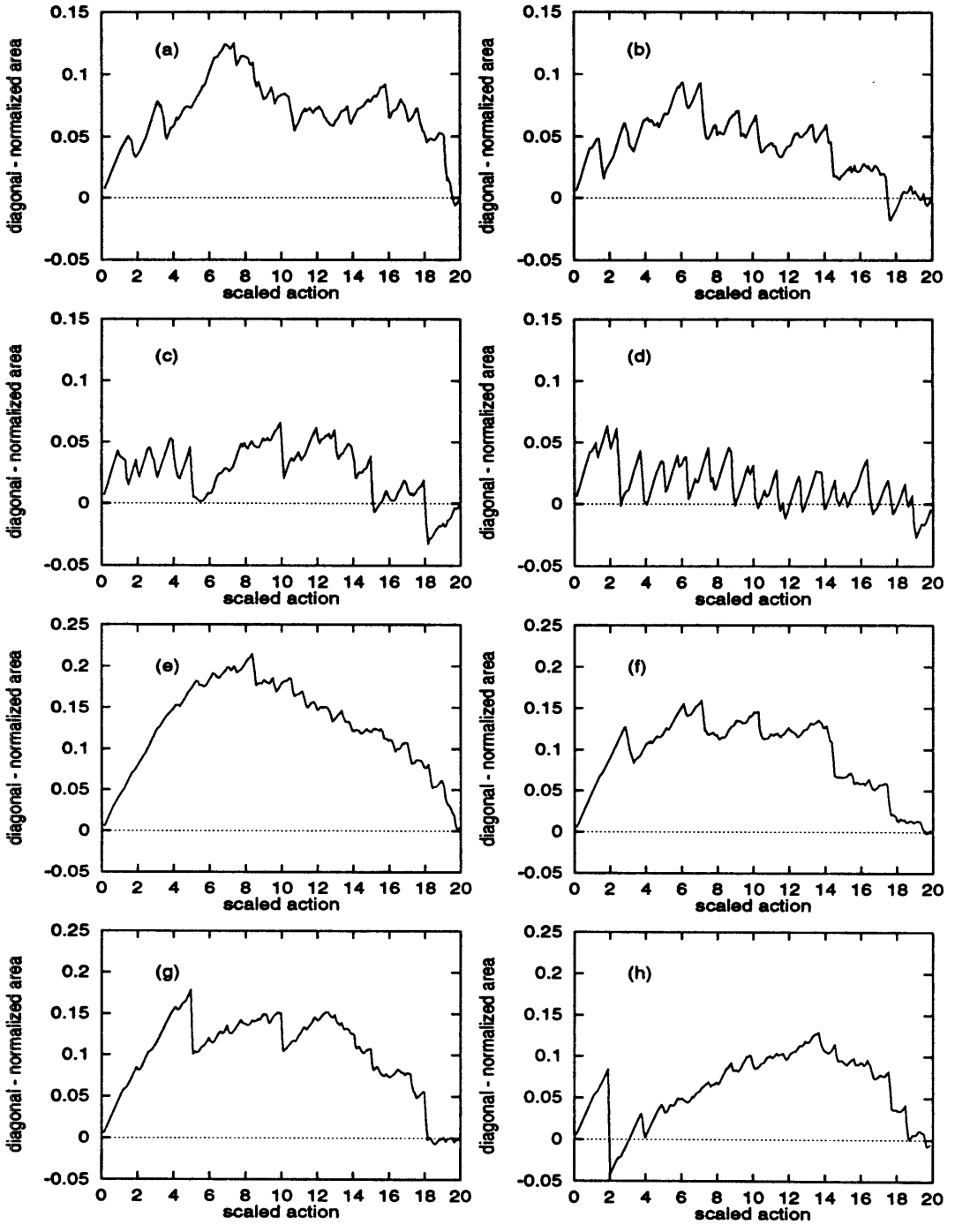

Figure 10-2: ΔA_n for recurrence spectra of even-parity diamagnetic hydrogen for $m = 0$. (a) $\epsilon_B = -0.15$, R_{os}; (b) $\epsilon_B = -0.20$, R_{os}; (c) $\epsilon_B = -0.25$, R_{os}; (d) $\epsilon_B = -0.30$, R_{os}; (e) $\epsilon_B = -0.15$, R_{ds}; (f) $\epsilon_B = -0.20$, R_{ds}; (g) $\epsilon_B = -0.25$, R_{ds}; (h) $\epsilon_B = -0.30$, R_{ds}.

the distribution of recurrence heights about their mean, we define the probability $P(h)$ as the probability of a local maximum in the recurrence spectrum having height h, where h is the normalized recurrence height. The average h is 1 by definition, and the area under $P(h)$ is also unity. There is a general trend for chaotic systems to show a Poisson-like distribution of recurrence heights and for more regular systems to have a much broader distribution of peak heights about the mean.

This behavior is shown in Figure 10-3 for even-parity diamagnetic hydrogen. At $\epsilon_B = -0.15$, $P(h)$ is strongly peaked in the first few bins and has a width of about 1.0 (Figure 10-3(a)). As the system becomes more regular, the height distributions of both R_{os} and R_{ds} become more strongly peaked at low action, and they have a width of about 0.2 at $\epsilon_B = -0.3$. This behavior makes it difficult to believe that $h_{avg} = 1$, but this constraint is responsible for the narrowly peaked maximum in $P(h)$ at low h. $P(h)$ acquires a long tail as the system becomes regular and a few large recurrences (about $15h$) can sharply raise h_{avg}, which has the effect of pushing all the other recurrences to lower h in the $P(h)$ distribution.

10.2 Diamagnetic Lithium

Considering global properties of recurrence spectra of diamagnetic lithium is of special interest because the behavior of the nearest-neighbor distribution (NND) of energy levels in odd-parity diamagnetic lithium fails to identify the chaos in the classical system. In contrast, the even-parity NND is in good agreement with the Wigner distribution which characterizes the energy spectrum of many classically chaotic systems. We have seen that the proliferation of recurrences in both odd- and even-parity oscillator strength recurrence spectra is an accurate indicator of chaos in the classical system, and we return to diamagnetic lithium to look at other global properties of recurrence spectra.

Comparing diamagnetic lithium and hydrogen at $\epsilon_B = -0.6$ allows us to compare a chaotic system with a closely related regular system. Figure 10-4(a) compares the proliferation of peaks in R_{os} in lithium and hydrogen at $\epsilon_B = -0.6$. The short-dashed

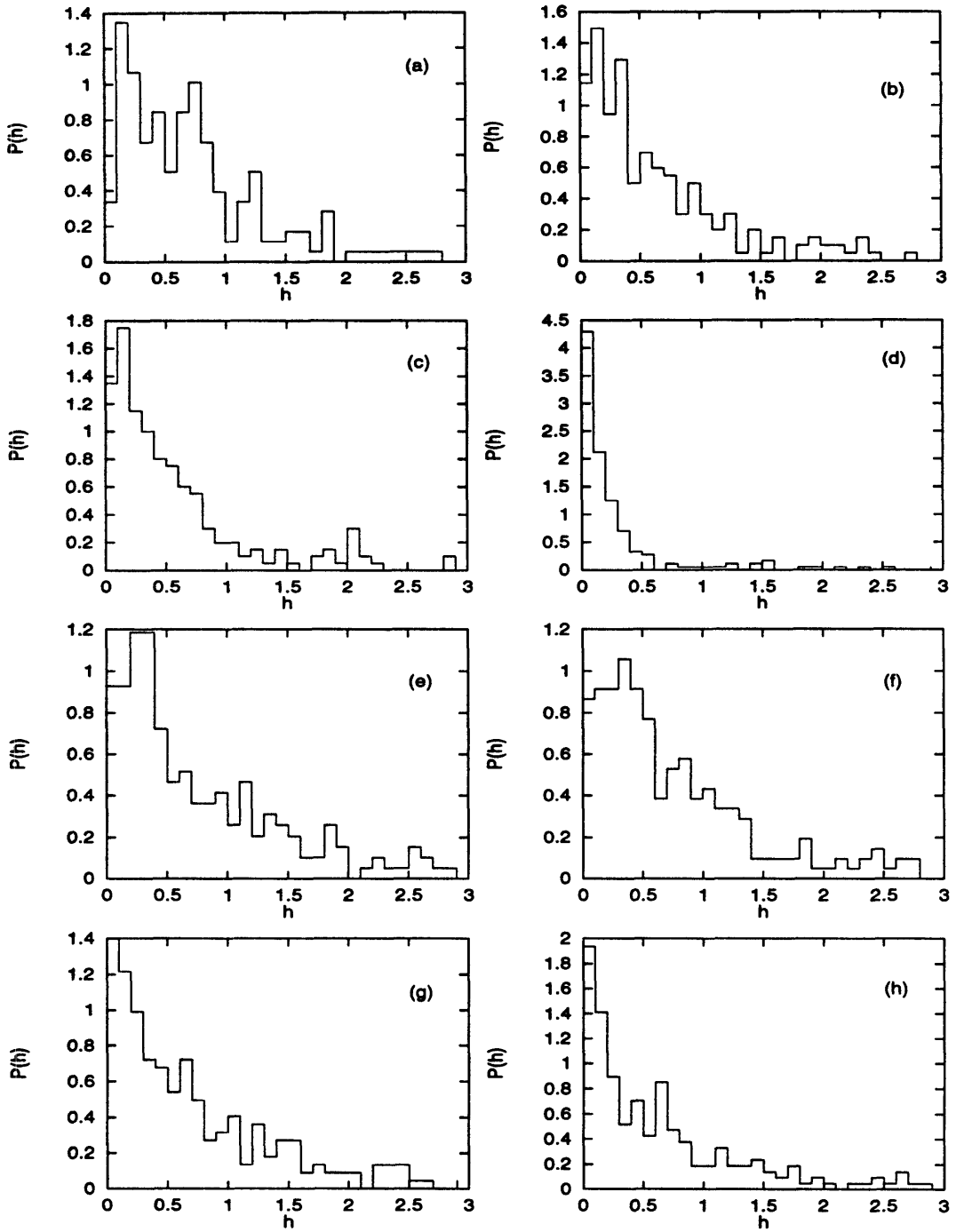

Figure 10-3: Recurrence height distributions for even-parity diamagnetic hydrogen for $m = 0$. (a) $\epsilon_B = -0.15$, R_{os}; (b) $\epsilon_B = -0.20$, R_{os}; (c) $\epsilon_B = -0.25$, R_{os}; (d) $\epsilon_B = -0.30$, R_{os}; (e) $\epsilon_B = -0.15$, R_{ds}; (f) $\epsilon_B = -0.20$, R_{ds}; (g) $\epsilon_B = -0.25$, R_{ds}; (h) $\epsilon_B = -0.30$, R_{ds}.

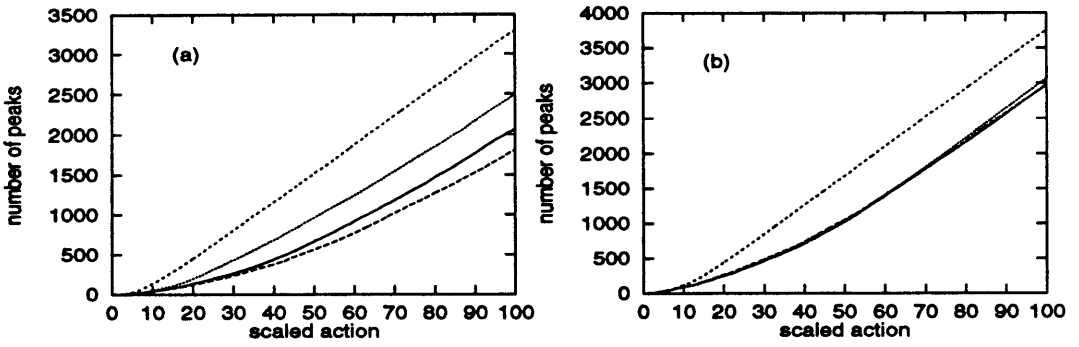

Figure 10-4: Recurrence proliferation in diamagnetic lithium at $\epsilon_B = -0.6$. Short-dashed line: even-parity lithium. Dotted line: odd-parity lithium. Solid line: even-parity hydrogen. Long-dashed line: odd-parity hydrogen. (a) R_{os}; (b) R_{ds}.

line on top shows that even-parity lithium has the fastest proliferation of recurrences. The dotted-line beneath it shows that odd-parity lithium has a lower rate of recurrence proliferation, but still has more recurrences than even-parity and odd-parity hydrogen, which are represented by the solid and long-dashed lines, respectively. Odd-parity hydrogen has fewer recurrences in R_{os} than even-parity hydrogen because orbits with an initial angle nearly perpendicular to the field have small recurrence strengths and are easily masked by other peaks. In contrast, the outgoing wave for an even-parity final state has a large S-wave component which gives all of the recurrences substantial strength. This effect of the node on the odd-parity recurrence spectrum of lithium is more pronounced because not only are recurrences near the node small, but the probability of core-scattering into these recurrences is also small.

Figure 10-4(b) shows the proliferation of peaks in R_{ds} for lithium and hydrogen at $\epsilon_B = -0.6$. Recurrences clearly proliferate faster in even-parity lithium, but even- and odd-parity hydrogen and odd-parity lithium are bunched together. The absorption process is not included in R_{ds} and there is nothing to distinguish between parity in the Gutzwiller trace formula. (Although we have seen the need to include core scattering which would distinguish odd and even-parity diamagnetic lithium.) Furthermore the absorption spectrum of odd-parity lithium is much more strongly affected by the core than the odd-parity energy-level spectrum. Consequently, R_{os} shows evidence of core scattering, but R_{ds} is nearly identical to odd-parity hydrogen.

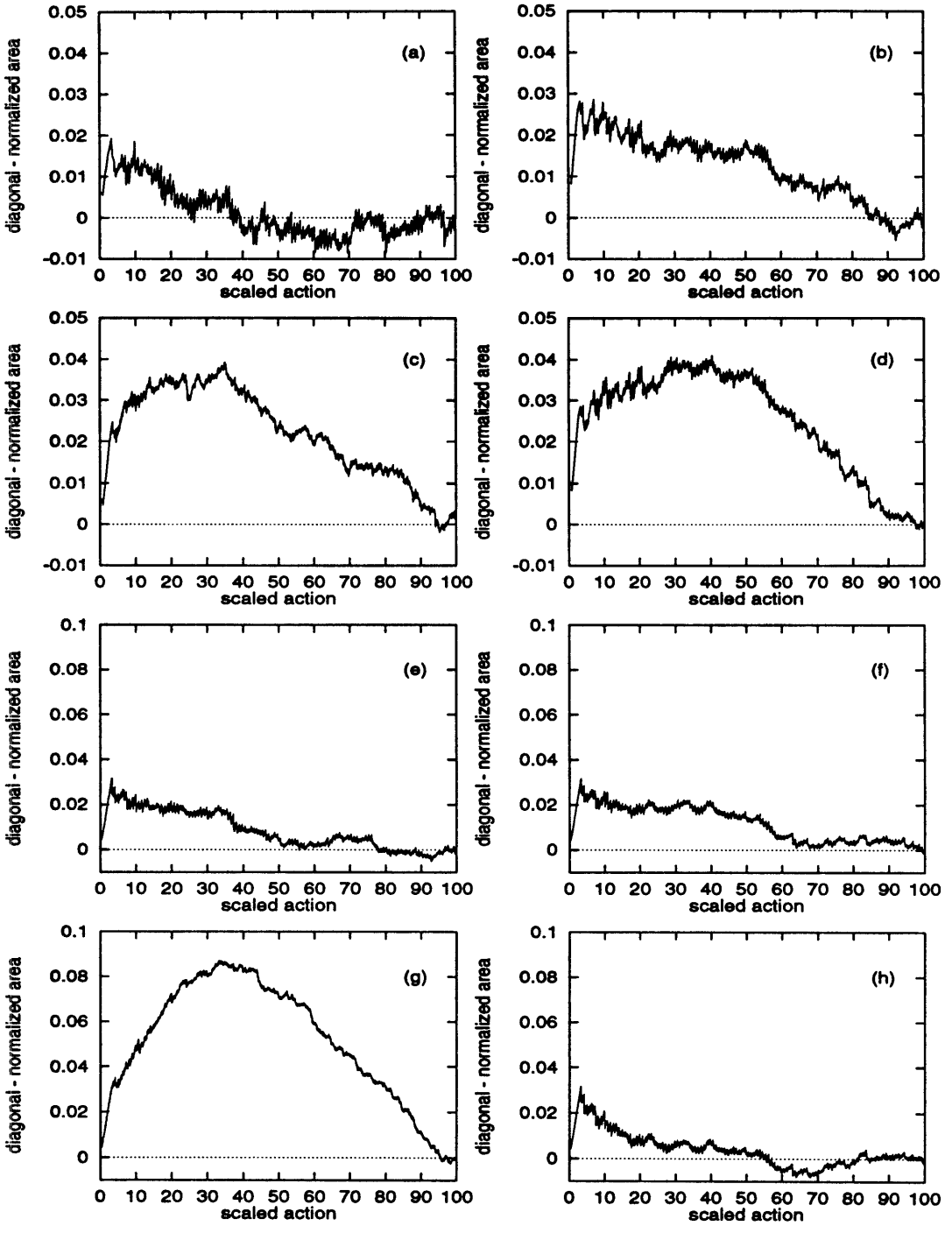

Figure 10-5: ΔA_n for recurrence spectra of diamagnetic lithium and hydrogen $m = 0$, $\epsilon_B = -0.6$. (a) Even-parity hydrogen, R_{os}; (b) Odd-parity hydrogen, R_{os}; (c) Even-parity lithium, R_{os}; (d) Odd-parity lithium, R_{os}; (e) Even-parity hydrogen, R_{ds}; (f) Odd-parity hydrogen, R_{ds}; (g) Even-parity lithium, R_{ds}; (h) Odd-parity lithium, R_{ds}.

ΔA_n for diamagnetic lithium and hydrogen recurrence spectra at $\epsilon_B = -0.6$ are shown in Figure 10-5. The top four graphs, (a-d), show ΔA_n for R_{os}. For even-parity hydrogen, R_{os} accumulates area nearly linearly. For odd-parity hydrogen, R_{os} accumulates area more slowly at low action, and the area function deviates from the diagonal. The area accumulation of R_{os} shows large deviations from the diagonal for both even and odd-parity diamagnetic lithium. This indicates that there is more area under R_{os} at higher action. The bottom four graphs, (e-h), of 10-5 show the deviations from the diagonal of R_{ds}. Even-parity lithium shows the largest deviation from the diagonal in 10-5(h). Even and odd-parity hydrogen and odd-parity lithium are all similar and show small deviations from the diagonal compared with even-parity lithium.

Figure 10-6 shows the recurrence height distributions for diamagnetic lithium and hydrogen for $\epsilon_B = -0.6$. Figures 10-6(a) and (e) show that the recurrence height distributions of R_{os} and R_{ds} for even-parity hydrogen are narrowly peaked at small h, indicating a few large recurrences making the average recurrence height larger and compressing the distribution at small h. In contrast, the recurrence height distributions of R_{os} and R_{ds} of even-parity lithium have a Poisson-like distribution, as shown in Figures 10-6(c) and (g). The differences between odd-parity hydrogen and lithium do not manifest strongly in the distribution of recurrence heights. Recurrence height distributions of the odd-parity R_{os} and R_{ds} show strong similarities between lithium and hydrogen, as shown in 10-6(b),(d),(f) and (h).

10.3 Lithium Stark Spectra

Having made some progress in identifying chaos in a system from looking at the global properties of recurrence spectra in diamagnetic lithium, we turn now to applying these ideas to lithium in an electric field. Figure 10-7 (a) compares the number of peaks in R_{os} for lithium and hydrogen at $\epsilon_F = -3$. The dashed line is the number of peaks in lithium, and the solid line is the number of peaks in hydrogen. Lithium clearly has many more peaks, but unlike the case of diamagnetic hydrogen, large recurrence

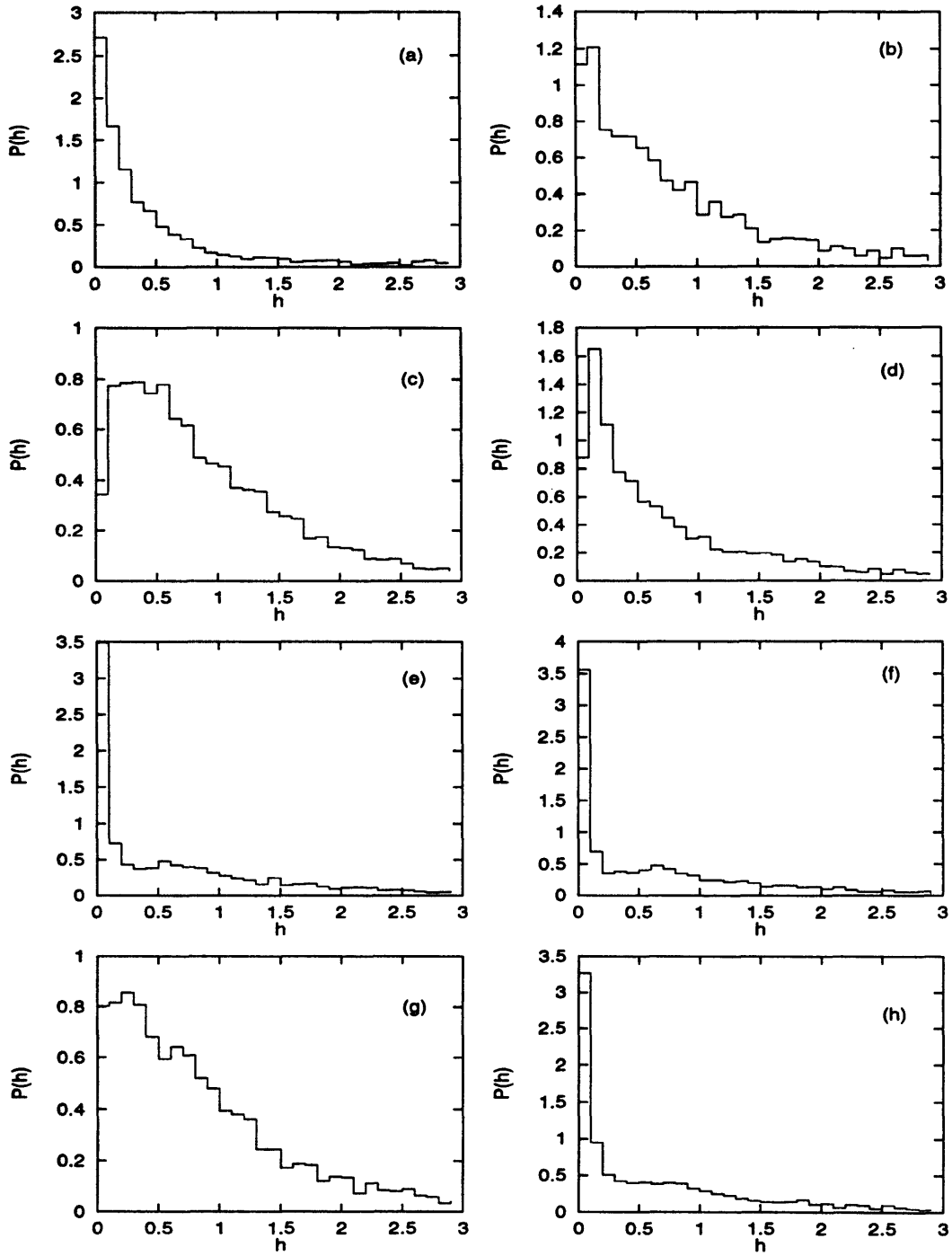

Figure 10-6: Recurrence height distributions for diamagnetic lithium (left) and hydrogen (right) for $\epsilon_B = -0.6$, $m = 0$. (a) Even-parity hydrogen, R_{os}; (b) Odd-parity hydrogen, R_{os}; (c) Even-parity lithium, R_{os}; (d) Odd-parity lithium, R_{os}; (e) Even-parity hydrogen, R_{ds}; (f) Odd-parity hydrogen, R_{ds}; (g) Even-parity lithium, R_{ds}; (h) Odd-parity lithium, R_{ds}.

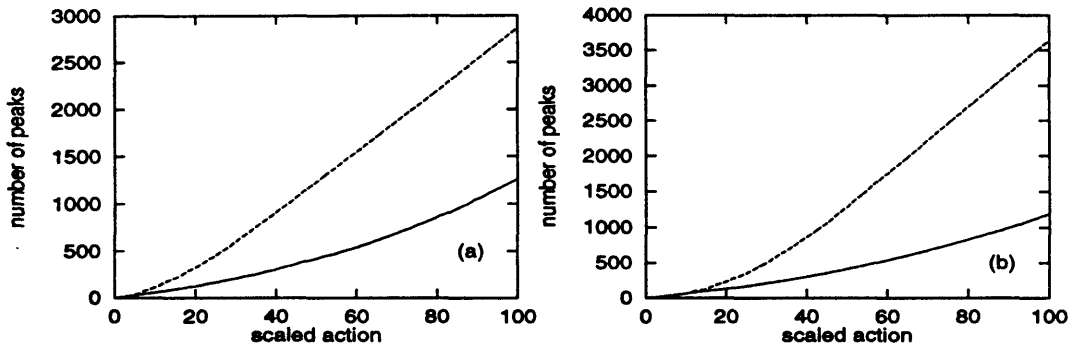

Figure 10-7: Recurrence proliferation in Stark spectra at $\epsilon_F = -3$, $m = 0$. Short-dashed line: lithium. Solid line: hydrogen. (a) R_{os}; (b) R_{ds}.

degeneracies prevent finding agreement with quantitative models of recurrence proliferation. In hydrogen, peaks which are born by bifurcations are located at nearly the same scaled action as their parents. Consequently, they are not resolved until their third or fourth repetition, and hydrogen does not begin to show a quadratic component to its recurrence proliferation until high scaled action. In lithium, this effect couples with large degeneracies of core-scattered recurrences to prevent an exponential or even an identifiably cubic proliferation of peaks in the recurrence spectra. Consequently, viewing the recurrence proliferation only gives qualitative agreement with the idea that recurrences proliferate at a much faster rate in chaotic systems. Figure 10-7 (b) shows the proliferation of recurrences in R_{ds}. The number of recurrences in lithium again greatly exceeds the number in hydrogen, but we are again limited to qualitative comments.

Figure 10-8 shows ΔA_n for Stark recurrence spectra of lithium and hydrogen at $\epsilon_F = -3$. Hydrogen has a saw-like appearance for R_{os} (Figure 10-8(a)) because area is accumulated quickly at scaled actions near a series of bifurcations and slowly between series of bifurcations. In lithium, only the first series of bifurcations is strong in R_{os}, and the spectrum is dominated by core scattering at high action. Figure 10-8(b) shows that R_{os} for lithium accumulates more recurrence strength at higher action. The saw-like appearence is not as strong in R_{ds} of hydrogen, as shown in Figure 10-8(c). This is probably because large recurrences due to bifurcations are emphasized more strongly in the absorption spectrum than in the density of states. Figure 10-8(d)

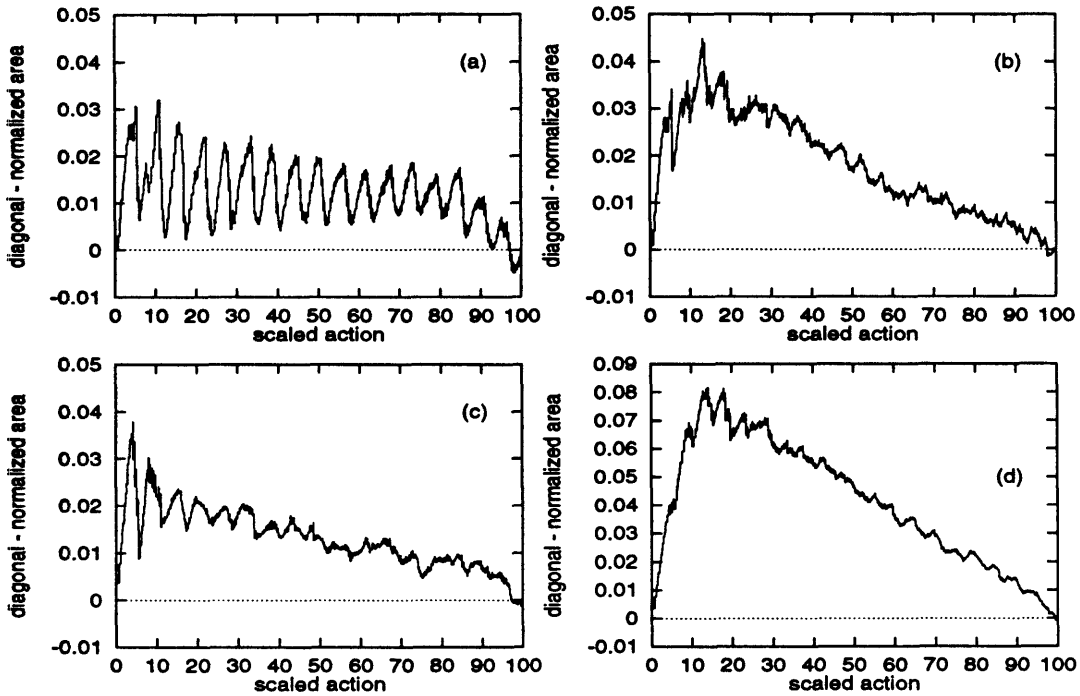

Figure 10-8: ΔA_n for Stark recurrence spectra at $\epsilon_F = -3$, $m = 0$. (a) hydrogen, R_{os}; (b) lithium, R_{os}; (c) hydrogen, R_{ds}; (d) lithium, R_{ds}.

shows that R_{ds} for lithium accumulates more recurrence strength at higher action, as demonstrated by its large deviation from the diagonal.

Turning to the peak height distributions in the Stark recurrence spectra, Figure 10-9 shows that $P(h)$ displays the common behavior for R_{os}: a narrow peak at low h for the regular hydrogenic system (Figure 10-9(a)) and a Poisson-like distribution for the chaotic lithium recurrence spectrum (Figure 10-9(b)). The recurrence height distributions for R_{ds} are harder to interpret. The peak height distribution of hydrogen has two local maxima. One is at low heights, and the other is close to the average. The peak height distribution of lithium is not far from being Poisson, but the first bin is depleted and the second bin is enhanced.

10.4 Summary of Recurrence Statistics

We have applied three statistical measures in an attempt to find a correlation between classical chaos and recurrence spectra. If the recurrence spectra are sufficiently resolved, simply counting recurrences can give quantitative agreement with a quadratic

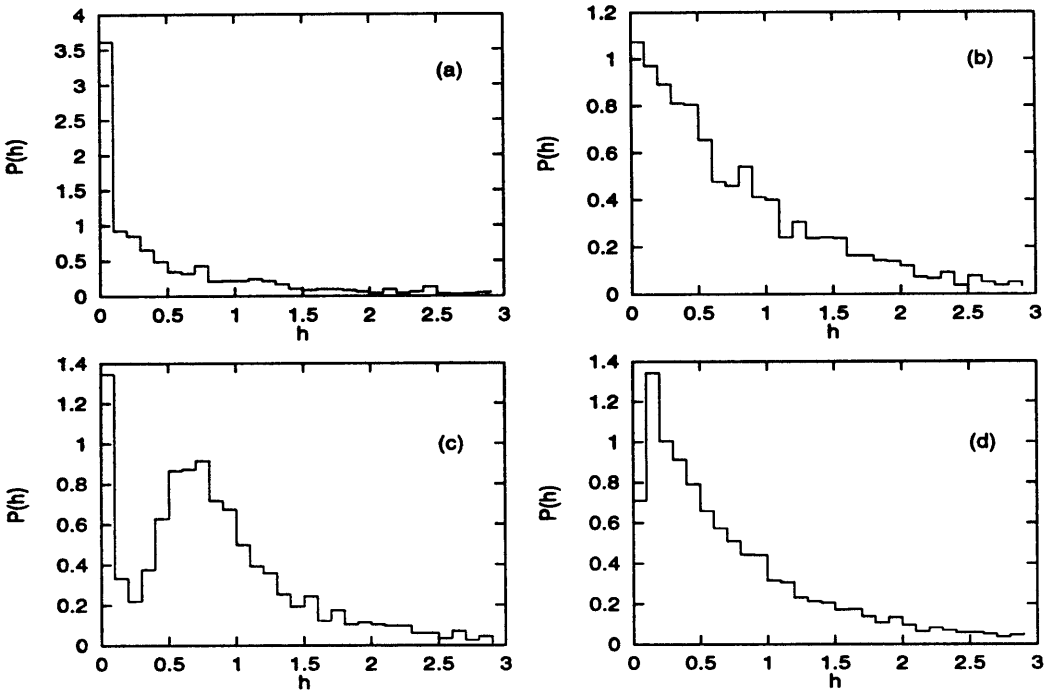

Figure 10-9: Peak height distributions in Stark recurrence spectra for $\epsilon_F = -3$, $m = 0$. (a) hydrogen, R_{os}; (b) lithium, R_{os}; (c) hydrogen, R_{ds}; (d) lithium, R_{ds}.

proliferation of orbits in an integrable system and a faster than quadratic proliferation in a chaotic system. Recurrences also tend to proliferate faster even when every recurrence is not resolved. In fact, this behavior persists into the range of actions where the recurrence spectrum is saturated and $N(\tilde{S})$ is linear in $\tilde{S}$ because the distribution of recurrence heights about their mean is much greater in regular systems.

I have demonstrated the possible usefulness of the integrated area under the recurrence spectrum and the distribution of recurrence heights about their mean as indicators of chaos in cases where the recurrence spectrum is not sufficiently resolved to allow recurrence counting. Regular recurrence spectra accumulate area while tending to stay closer to a constant rate of increase, although they may make relatively rapid oscillations around it. Chaotic recurrence spectra tend to be smoother and are usually bowed beneath the average rate of increase. This indicates a trend toward having more recurrence strength at higher action. The recurrence height distribution seems to be a consistent indicator of chaos. For R_{os} it shows a Poisson-like distribution in chaotic systems and a distribution which is strongly peaked at low action for regular systems. The peak height distributions for R_{ds} are similar, but do not follow

these tendencies as strongly.

Although the results presented in this chapter are far from compelling, they suggest a few ways of viewing global properties of recurrence spectra. I believe this is an important step toward determining whether the classical motion is chaotic from the quantum system. My hope is that an approach can be developed and rigorously proved which allows one to make definite statements about the degree of chaos in a classical Hamiltonian by looking at the quantum recurrence spectrum.

Chapter 11

Summary and Discussion

For we must all appear before the judgment seat of Christ, that each one may receive what is due him for the things done while in the body, whether good or bad. –2 Corinthians 5:10

11.1 Summary of Contributions

This thesis represents the following contributions to the study of Rydberg atoms (in particular) and quantum chaos (in general):

- Pointed out that Rydberg atoms in strong static fields provide a number of experimentally accessible chaotic systems. Previous to this work, the diamagnetic hydrogen atom was the only case which had been extensively studied.

- Showed that the evolution of Stark spectra with energy has a natural and intuitive interpretation in terms of classical orbits.

- Demonstrated the failure of the nearest-neighbor distribution to predict classical chaos in certain cases.

- Provided data to test several key advances in closed-orbit theory.

  - Scattering of recurrences from one closed orbit into another by the alkali-metal core.
  - Contribution of an orbit's neighbors to the recurrence strength.
  - Repair of semiclassical amplitudes at a bifurcation by including diffraction.

- Demonstrated semiclassical effects which depend on the size of $\hbar$.
- Confirmed closed-orbit theory and periodic-orbit theory with much higher precision than previously obtained.
- Suggested the use of recurrence counting as a possibly rigorous approach to recognizing classical chaos from the quantum spectrum.

The diamagnetic hydrogen atom is widely recognized as a paradigm system for the study of quantum chaos. This work represents a substantial expansion of the playground. As the tools of quantum chaos mature, they can be used to give new insights into old problems. The work presented here on the Stark effect is a good example. The problem of an atom in an electric field has been widely studied from the earliest days of quantum mechanics. Yet the transition from a discrete to a continuous spectrum had eluded simple descriptions. The study of quantum chaos gave us new tools for a semiclassical interpretation of the spectral evolution.

In addition to the successful demonstration of one new tool (closed-orbit theory), we have showed that another (energy-level statistics) can give deceptive results. This is hardly a disaster, but it does point out the need for caution.

The closed-orbit theory of Du and Delos [DUD88a, DUD88b] was a major achievement in its original formulation. It permitted application of periodic-orbit theory to absorption spectra and yielded good agreement with diamagnetic hydrogen. However, in its original form, it broke down near bifurcations, could not describe all the recurrences of alkali-metal atoms, and predicted zero recurrence strength for some orbits whose recurrence strength is not zero. The breakdown near bifurcations was realized from the beginning, but the details of the repair were only recently completed, following our experimental results on the continuum Stark spectrum of lithium.

The core scattering process was predicted in 1992 [GAD92]. Our electric field work provides a clear experimental signature and the most quantitative identification to date.[1] Furthermore, the computational work in diamagnetic lithium shows that all combinations of recurrences are present at low action and the physical picture of core scattering is verified by examination of the amplitudes of the recurrences and not only the positions.

The error in closed-orbit theory's prediction of zero recurrence strength for the perpendicular orbit in odd-parity diamagnetic hydrogen was not realized until I discovered finite recurrence strength in the quantum spectrum. This is a rather esoteric point which may never be confirmed experimentally due to the smallness of the peaks. Nonetheless, it is important because it points out the contribution of an orbit's neighbors to its recurrence strength. In order to converge to the true quantum spectrum, closed-orbit theory must give more accurate recurrence amplitudes than it does currently. The repair of the theory to account for the contributions of the neighbors is key in this regard. Having a quantum mechanical recurrence spectrum in which the contribution of the neighbors was not masked by the contribution of a closed orbit allowed John Delos and John Shaw to account for the neighbors.

The demonstration of the dependence of pre-bifurcation recurrences on the size of $\hbar$ provides hints about what future corrections to closed-orbit theory and periodic-orbit theory may look like. The basic point is that quantum mechanics cannot distinguish a closed orbit from its neighbors which are within $\hbar$ of being closed. The hand-waving explanation is easy. The rigorous mathematics should be formidable.

The position of recurrences can be found from the spectrum to several parts in 10^6. The major challenge to closed-orbit theory is to compute recurrence amplitudes. If the positions of recurrences differ at all from the classical action, the difference is certainly very small. Michael Berry has commented (private communication) that it can be shown rigorously that the Fourier transform of a spectrum of $1/\hbar$ eigenvalues

[1] Some small recurrences in diamagnetic helium were identified with the core scattering process [DTH94], but these recurrences are not much larger than the noise and there is no quantitative analysis of the peak positions, only the statement that the positions are the sum of other recurrences.

gives peaks whose classical actions correspond exactly to the periodic orbits of a system. This needs to be explained. Usually one solves the Schrödinger equation for the values of E which give stationary states. One can also find the values of $\hbar$ which give stationary states for a fixed E. It is the Fourier transform of the $1/\hbar$ spectrum obtained in this way which yields peaks at the actions of periodic orbits.[2]

Once the issue of the position of recurrences is nailed down, we have a rigorous method for determining whether a system is classically chaotic from the quantum spectrum. We simply compute the recurrence spectrum and see how the recurrences proliferate as a function of action. Practical implementation requires computing the spectrum over a large enough range of $1/\hbar$ to resolve recurrences to sufficiently high action to distinguish an algebraic proliferation of orbits from an exponential proliferation. It may be possible to make the implementation of this method simpler by providing a theoretical foundation for recurrence statistics.

11.2 Thoughts on Quantum Chaos

My intuition tells me that the fundamental question, "How does quantum mechanics give rise to chaotic classical dynamics?" will probably have to be answered by studying the time evolution of wave packets directly. If the time evolution of expectation values of position and momentum are given accurately by Newton's laws, then everything is fine. Certainly, this is a sufficient condition, but is it necessary?

One could argue that there is no difference between the time and energy domain descriptions of quantum mechanics because the eigenvalues describe the time evolution of the eigenvectors. A Fourier series gives the time evolution of a conservative Hamiltonian, and a Fourier transform can be used to obtain a spectrum from the time evolution of a wavefunction. If one believes Fourier analysis, then a quantum description in terms of eigenvectors and energy levels should be sufficient.

This essential point has been at the heart of the approach of Chapters 5-8, in

[2]Recall that in our systems, the scaling rules resulted in w_F and w_B functioning as $1/\hbar$. In non-scaling systems, the size of $1/\hbar$ must be varied artificially.

which semiclassical methods were tested by using the Fourier transform to compare time-domain classical information with quantum spectra. Does a wavefunction really stay localized near a classical trajectory for hundreds of repetitions of an orbit, as a naive interpretation of high-action recurrence spectra might suggest? The answer is no. A recurrence represents a constructive interference between waves, and does not always have a correspondence with a localized wave packet propagated in time. Consequently, semiclassical methods can yield accurate results for times much longer than the time it takes for a wavepacket to spread due to diffraction and other quantum effects. This has been pointed out [TOH91], but is still largely unappreciated.

In practice, closed-orbit theory (much like periodic-orbit theory) has limited utility in computing discrete spectra of bound systems. There are too many orbits, and the approximations which go into computing the recurrence strengths are too coarse. In all of the test cases so far, it is easier to compute the spectra using brute-force quantum mechanics. In principle, however, these tools provide analogs to simple Bohr quantization of chaotic systems. Furthermore, they provide ways to interpret complex spectra semiclassically.

In contrast, periodic-orbit theory should be useful for understanding and accurately computing resonances in unbound systems. In fact, it makes one bold assertion: *an unbound system has resonances if and only if it has periodic orbits.* For certain systems, using periodic-orbit theory and/or closed-orbit theory to compute continuous spectra may actually be easier than a quantum treatment. Furthermore, when one realizes that disassociation (which is analogous to ionization) is half of a chemical reaction, it is clear that these ideas are relevant to application of these semiclassical principles to the control of chemical reactions by laser excitation.

11.3 Unanswered Questions

The following questions remain unanswered:

- Can closed-orbit theory and periodic-orbit theory be written as expansions in $\hbar$?

- Why do the high-action recurrences in the lithium Stark spectrum appear to be shifted to lower action?

- Is it possible to describe chaotic systems by the WKB approximation plus a mechanism for crossing between tori?

- The ionization of diamagnetic hydrogen has different classical and quantal scalings. How can semiclassical theory account for this?

The first question was discussed above, and the second in Chapter 7. The third was mentioned briefly, but deserves a few more comments. In the regular regime, eigenvalues of diamagnetic hydrogen are well approximated by tori quantization, as are those of hydrogen in an electric field. The possibility of tunneling between tori can break degeneracies and generally causes level repulsions. In lithium, core scattering induces chaos by making it possible for trajectories to jump between tori. Closed-orbit theory can account for this by core scattering and, in principle, it can be used to compute the spectrum from the hydrogenic orbits and a model for scattering between orbits. The analogous quantization might be accomplished using the WKB method and accounting for jumping between tori. This would represent the successful application of the WKB method to a nonintegrable system, a feat which is widely believed to be impossible.

The scaling of the ionization process in diamagnetic hydrogen raises another unanswered question. A quantum picture suggests that the system scales as EB^{-1}, which represents the number of open Landau channels. The semiclassical view suggests scaling as $EB^{-2/3}$, which represents the classical dynamics of the system. The more closed orbits there are, the narrower the linewidths. How is the semiclassical picture breaking down here?

11.4 Suggestions for Further Work

11.4.1 Further Experiments on Rydberg Atoms

As far as the systems studied in this thesis, I cannot really see milking much more out of the Stark effect. (Others have probably said this before.) There is not much left in diamagnetism either, except in the continuum regime. It would be nice to observe the change in linewidth statistics as Landau channels are opened. It would also be nice to perform scaled energy spectroscopy at a single scaled energy in regions where different numbers of Landau channels are open and study the breakdown of the semiclassical scaling. But these are both formidable experiments. The stray electric field must be under strict control, and strong signal will be needed. I suggest moving on to parallel fields which will reveal more interesting physics for less effort.

The most interesting regime of the parallel field spectrum should be near $\epsilon_F = -2$. Since the Hamiltonian of an electron in parallel fields separates, ionized electrons should still have $(n + m + 1/2)B$ energy in the x, y plane. By turning on the electric field, we can effectively pull the Landau channels down into an energy region where there are fewer levels and stronger oscillator strengths. This makes studying linewidths and ionization processes much easier, yet the ionization process in parallel fields should be a bit more challenging for theorists who seem to have a handle on the diamagnetic and Stark problems separately. The conflict between quantum and semiclassical scalings persists for parallel fields, but should be easier to study because the electric field can be adjusted to give any desired ionization limit. $m = 1$ states of lithium are essentially hydrogenic, so the core can be turned on and off by changing the polarization of the excitation laser. In addition, methods for computing the spectra in parallel fields need to be motivated and tested in the region above $\epsilon_F = -2.0$. The problem of crossed fields is tempting, but presents serious experimental difficulties in the short term. The oscillator strength is reduced by a factor of n, a slight misalignment of the fields strongly mixes parities, one cannot dial up hydrogen by changing the polarization, and the problem is still intractable above the saddle point ($\epsilon_F = -2$).

11.4.2 Experimental Quantum Chaos

The list of systems for studying quantum chaos is nearly as large as the quantum world. Most quantum systems exhibit strong interactions between many bodies which make them difficult to approach theoretically. I believe that the study of quantum chaos will bear more fruit by considering systems which are complex enough to demonstrate chaos yet simple enough to be tractable without resorting to statistical approaches. Here I list those which represent what seems to be the next level of difficulty above the systems studied in this thesis. These systems have been the subject of vigorous research programs for many years, but their connections with quantum chaos has just recently been recognized.

- Microwave ionization of Rydberg atoms.
- Hydrogen in crossed electric and magnetic fields.
- Helium and planetary atoms.
- The H_2^+ molecular ion.
- Vibrational structure of tri-atomic molecules.

Several groups have been working on microwave ionization of Rydberg atoms. Some simple features can be described by a one-dimensional model of hydrogen in an oscillatory field, but detailed interpretation of experimental results is lacking. In addition, cleaner and more sophisticated experiments are desirable. This problem is attractive because it represents one of the simplest time-dependent chaotic experimentally accessible quantum systems. Furthermore, it scales and can be investigated in many regimes in as much as multiphoton ionization of low-lying states can be viewed as an analogous process to microwave ionization of Rydberg atoms.

Hydrogen in crossed electric and magnetic fields has long been a problem with great interest and few tangible results. The quantum chaos toolbox should help a bit, but accurate experiments and rigorous theoretical approaches are still needed. In the infinite mass limit, finding eigenvalues by brute force matrix diagonalization is

becoming possible. The large mass approximation applies well below $\epsilon_F = -2$, and in this regime hydrogen in crossed fields provides a chaotic experimental system with three degrees of freedom. This provides new challenges for the classical side of the problem. For example, the surfaces of section are four-dimensional, and new ways are needed for viewing the dynamics in a simple way. Finding a few closed orbits is not difficult, but knowing that all of them have been found is not generally possible. In the region where the motion of the nucleus becomes important, the system is fully six-dimensional in configuration space. Some appealing physical arguments can be given in this regime, but concrete connections between the classical dynamics and quantum spectrum are not currently available.

Chaos has long prevented semiclassical quantization of the helium atom. Some recent progress has been made [ERT91], but only a few eigenvalues were obtained from a small subset of the orbits. A full exploration and characterization of the classical phase space has not been carried out. Consequently, there is still work to do on a full semiclassical quantization of helium. Planetary atoms are atoms with two valence electrons in Rydberg states. Most of these states are auto-ionizing, and the systems are analogous to adding a core to helium.

The H_2^+ molecular ion is another three body problem, except instead of two light particles and one heavy particle, there is one light particle and two heavy particles. The system is separable in the approximation that the protons are fixed, and some insights can be gained by quantizing this system. The system is chaotic if the protons are allowed to move, and the full quantization presents another formidable challenge.

There are a lot of tri-atomic molecules whose vibrational spectra are readily available and/or easily measured. These systems provide opportunities for studying chaotic systems with greater than two dimensions. However, the dimensionality of these systems becomes much greater if the Born-Oppenheimer approximation breaks down, and the systems become intractable.

The future of experimental quantum chaos seems to be in time-dependent systems and systems with more than two degrees of freedom. Before we're done we will probably have to develop new techniques for our toolbox and make many exciting

new discoveries. Who knows, we might even find something useful.

Appendix A

Long-Period Orbits in the Stark Spectrum of Lithium, M. Courtney et al., Phys. Rev. Lett. 73, 1340 (1994)

The next few pages are a short paper which was published in *Physical Review Letters*.

Long-Period Orbits in the Stark Spectrum of Lithium

Michael Courtney, Hong Jiao, Neal Spellmeyer, and Daniel Kleppner
Department of Physics and Research Laboratory of Electronics, Massachusetts Institute of Technology, 77 Massachusetts Avenue, Cambridge, Massachusetts 02139
(Received 27 May 1994)

We report observation of the signature of very-long-period orbits in the Stark spectrum of lithium in a regime of classical chaos. We identify recurrences associated with the orbits parallel to the electric field, including those beyond the 100th return of the primitive orbit. We also identify recurrences due to scattering of an incoming wave from one orbit into another by the alkali-metal core.

PACS numbers: 32.60.+i, 03.65.Sq, 05.45.+b

Periodic-orbit theory provides an important link between quantum theory and classical dynamics in regimes of disorderly (chaotic) motion [1]. The closely related closed-orbit theory [2,3] predicts the photoabsorption spectrum of a system from knowledge of its closed classical orbits. Long-period orbits are of particular interest because they determine the resolution the theory can achieve, and because they play a crucial role in determining how well the theory's predictions converge to the true quantum spectrum. However, long-period orbits are difficult to study experimentally and theoretically. Consequently, the limits of periodic-orbit theory are not well understood. We report here an experimental study of the spectrum of lithium in an electric field that reveals the signature of very-long-period closed orbits in a regime of disorderly motion.

An important result of periodic-orbit theory is the Gutzwiller trace formula, an expression for the level density that is obtained from the trace of the semiclassical Green's function [1]:

$$g_c(E) = \sum_k T_k \sum_{n=1}^{\infty} \frac{1}{2\sinh(\chi_{nk}/2)} e^{i(nS_k - \alpha_{nk}\pi/2)} \quad (1)$$

(atomic units). The index k distinguishes the primitive periodic orbits: the shortest period orbits for a given set of initial conditions. T_k is the period and S_k is the action of a periodic orbit. Each primitive orbit retraces itself, leading to new orbits with periods nT_k and actions nS_k, where n is an integer. Hence, every repetition of a periodic orbit is another periodic orbit. The quantity χ_{nk} is related to the stability of an orbit, and α_{nk} is the orbit's Maslov index.

Spectroscopic experiments measure transition probabilities, not level densities. Delos and co-workers have made contact between periodic-orbit theory and experiment in a formulation known as closed-orbit theory [2,3]. This theory, which is similar to the trace formula in derivation, yields the oscillator strength as a function of energy. Only orbits that begin and end at the nucleus are important in closed-orbit theory. Physically, these are associated with the outgoing waves that are generated when a tightly bound electron is excited to a high-lying state.

According to closed-orbit theory, the average oscillator strength density is given by a smooth background plus an oscillatory sum of the form [3]

$$Df(E,F) = \sum_k \sum_{n=1}^{\infty} A_{nk} \sin(nS_k - \alpha_{nk}\pi/2 - \phi_{nk}), \quad (2)$$

where E is the energy and F is the electric field. A_{nk}—the recurrence amplitude of a closed orbit—contains information about the stability of the orbit, its initial and final directions, and the matrix element of the dipole operator between the initial state and a zero-energy Coulomb wave. α_{nk} is the Maslov index, and ϕ_{nk} is an additional phase that depends on details of the orbit.

Computing a spectrum with resolution ΔE requires summing over all closed orbits of the system with periods up to $2\pi\hbar/\Delta E$. For low resolution, where only short-period orbits need to be considered, the theory has enjoyed considerable success [2,4,5]. However, extending the theory to high resolution presents a formidable challenge. Not only does the number of periodic orbits proliferate exponentially with period or action for chaotic systems, long-period orbits are difficult to compute because they become increasingly unstable and sensitive to numerical details [1].

We have studied the Stark spectrum of lithium, a system that is similar to hydrogen except for one crucial difference: the classical motion of lithium displays a transition to chaos, whereas the motion of hydrogen is always orderly. The classical dynamics of hydrogen in an electric field follows a simple scaling law. Its Hamiltonian ($H = p^2/2 - 1/r + Fz$, atomic units) can be rescaled using the substitutions $r = F^{-1/2}\tilde{r}$ and $p = F^{1/4}\tilde{p}$, so that $\tilde{H} = F^{-1/2}H$ has no explicit dependence on the field. As a result, the classical dynamics depends only on the scaled energy $\epsilon = EF^{-1/2}$, not on E and F separately. This classical scaling is a good approximation for lithium.

The scaled action of a given closed orbit, $\tilde{S}_k = F^{-1/4}S_k$, depends only on ϵ. If the spectrum is recorded while the field and energy are varied simultaneously so as to keep ϵ constant, the classical dynamics remains constant [6]. This approach has been used on several

systems [6–8]. An orbit's scaled action and recurrence strength can be obtained directly from the Fourier transform of the spectrum. This Fourier transform is called the recurrence spectrum because, in principle, each peak is located at the scaled action of a periodic orbit, and the height of each peak is proportional to that orbit's recurrence strength. We have applied this approach to the lithium Stark spectrum with higher accuracy than previously achieved in such studies, making it possible to search for high-action closed orbits.

In applying these ideas to lithium, an essential point is that the potential of lithium differs significantly from $1/r$ only near the nucleus where the electron penetrates the core charge of the lithium ion. We have modeled this classically by adding a short range potential to the hydrogenic Hamiltonian, chosen to give the proper quantum defects. Within these constraints, a variety of model potentials yields essentially the same classical behavior. In particular, as the scaled energy is increased, lithium shows a transition from regular to chaotic motion at about $\epsilon = -16$.

This behavior is shown in Fig. 1, which displays two Poincaré surfaces of section. Below $\epsilon = -16$ the trajectories form well-defined curves, each curve being a slice through a two-dimensional torus in four-dimensional phase space. Regular trajectories are confined to these tori. At $\epsilon = -16$, some of the tori have been destroyed, indicating the onset of chaos. At $\epsilon = -3$, the motion is chaotic throughout most of phase space, though small regular regions remain.

We have carried out laser spectroscopy on an atomic beam of lithium in an applied electric field. One laser excites the $2S \rightarrow 3S$ two-photon transition. A second laser excites the atoms to $m = 0$ Rydberg states in the vicinity of $n = 45$. The excited atoms are detected by electric field ionization. A spectrum at $\epsilon = -3.000(2)$ (the number in parentheses is the estimated error in the last digit) was obtained by scanning the laser from -65 to $-50\ \mathrm{cm}^{-1}$ relative to the zero field ionization limit, while the scaled field, $w = F^{-1/4}$, was scanned between 100 and 120 (atomic units). The absolute error in w is estimated to be $\delta w \approx 0.025$. The recurrence spectrum (Fig. 2) was obtained by Fourier transforming the scaled-energy spectrum plotted with respect to w. The recurrence spectrum is expected to be accurate for $\tilde{S}_{\max} \leq \pi/\delta w \approx 100$ [9].

To verify our methods, the experimental recurrence spectrum at $\epsilon = -3.000$ is compared with a recurrence spectrum obtained from quantum computations [10] in Fig. 2. Agreement is generally good, although there are some discrepancies which we believe arise from experimental noise and neglect of the continuum in the computations.

Closed orbits parallel to the field play an important role in the spectrum. These form two classes: "uphill" orbits, directed toward the cathode, and "downhill" orbits, directed toward the anode. For $\epsilon = -3.000(2)$, the first return of the uphill orbit has a scaled action $\tilde{S}_1^u = 0.3915$, and the first return of the downhill orbit has $\tilde{S}_1^d = 0.4285$. As a result, the recurrence spectrum is expected to have peaks at $\tilde{S}_n^u = 0.3915n$ and $\tilde{S}_n^d = 0.4285n$. In Fig. 3 most of the prominent peaks for $\tilde{S} \leq 10$ are identified as corresponding to repetitions of the parallel orbits.

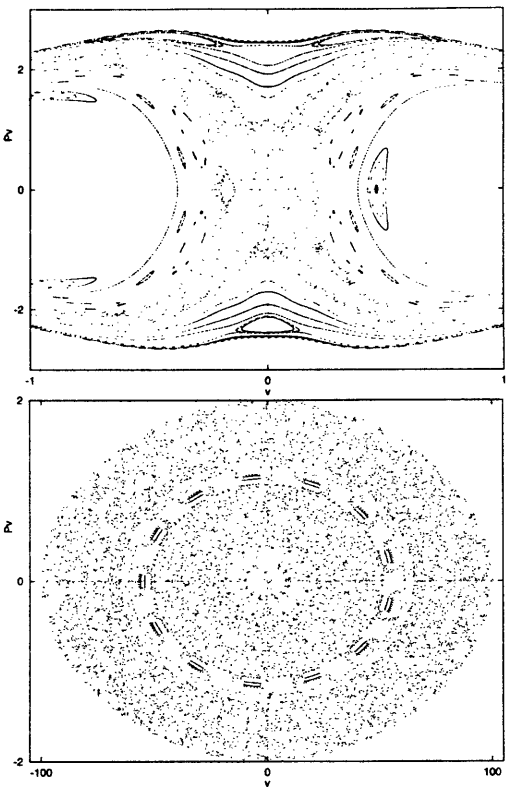

FIG. 1. Poincaré surfaces of section in semiparabolic coordinates ($u = (r + z)^{1/2}$, $v = (r - z)^{1/2}$) for lithium $m = 0$. Top: Early stages of the breakup of tori are visible in the region near the core at $\epsilon = -16$. Bottom: Most of the phase space is chaotic for $\epsilon = -3$, and the near-ergodic orbits are excluded from small regions by remaining tori.

Gao and Delos [3] have studied the Stark problem for hydrogen and have found that every repetition of the parallel orbits gives rise to new orbits by a series of bifurcations of these main orbits. The scaled action of a newly created orbit is close to the scaled action of the parent orbit. With respect to the behavior of alkali-metal atoms, Eichmann *et al.* [8] showed that the recurrence spectra of hydrogen and sodium are similar for $\tilde{S} < 6$. We have found that lithium is similar to hydrogen

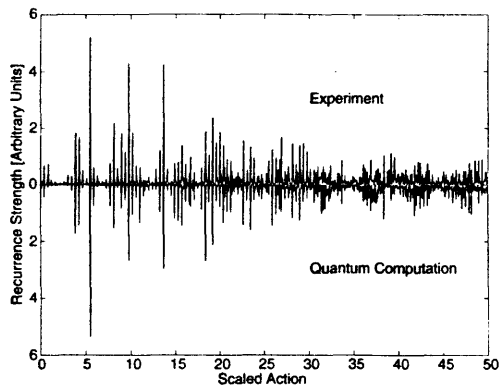

FIG. 2. Lithium recurrence spectrum for $\epsilon = -3.000(2)$. A mirror plot is used for comparison of the experimental spectrum (top) with the results of a quantum computation (bottom). The computed spectrum has been normalized to provide comparable heights.

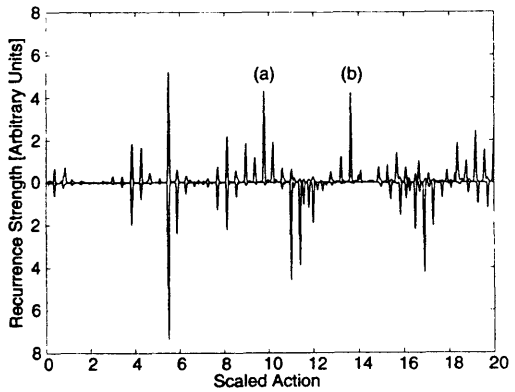

FIG. 4. Comparison of experimental recurrence spectrum for lithium (top) with computed recurrence spectrum for hydrogen (bottom). Peaks a at $\tilde{S} = 9.792(3)$ and b at $\tilde{S} = 13.658(4)$ are due to core scattering, as described in the text.

for $\tilde{S} < 8$ [11]. However, as shown in Fig. 4, we find significant differences for $\tilde{S} > 8$. The existence of extra peaks in the lithium spectrum as the action is increased is consistent with the proliferation of closed orbits in chaotic systems.

For high action, the parallel orbits continue to display a strong signature in the spectrum. We have identified recurrences near the 100th return of the uphill parallel orbit (Fig. 5). This illustrates the power of closed-orbit theory to associate spectral features with long-period orbits. Not all repetitions are visible in the recurrence spectrum because their recurrence strengths may be weak or the repetitions may be masked by other peaks. (In Fig. 5, the $n = 102$ and $n = 108$ repetitions of the uphill orbit are missing.) Furthermore, numerous additional peaks are visible in the spectrum. We believe that some of these extra peaks are repetitions of the downhill orbit, but their recurrence strengths in the range of Fig. 5 are generally too weak to permit a definite association.

A number of processes could generate the unidentified peaks in Fig. 5. In hydrogen, one expects peaks at repetitions of the orbits which bifurcate from the parallel orbits. These orbits have scaled actions slightly different from the repetitions of the parallel orbit and may be

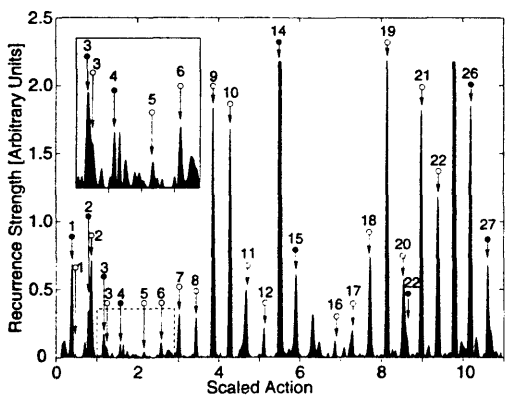

FIG. 3. Blowup of experimental data in Fig. 2. Recurrences corresponding to the parallel orbits are marked with arrows. Filled circles: uphill orbits. Open circles: downhill orbits. The number specifies the number of repetitions of the primitive orbit. The truncated peak at $\tilde{S} = 5.5$ has strength 5.2. The truncated peak at $\tilde{S} = 9.8$ has strength 4.3. The inset shows detail near $\tilde{S} = 2$.

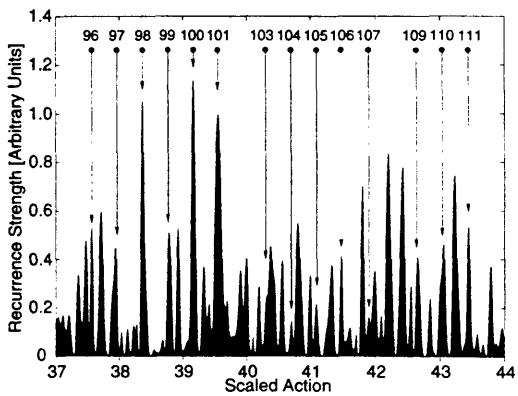

FIG. 5. Blowup of Fig. 2 at large action. Peaks identified with uphill parallel orbits are marked with arrows, as in Fig. 3.

resolved at high action. However, the recurrences due to these orbits have not yet been calculated.

As pointed out by Gao and Delos [12], core effects can be understood by considering scattering from one hydrogenic orbit into another by the alkali-metal core. This effect gives additional recurrences at the sum of actions of combinations of closed orbits [13]. Core-scattered recurrences can be large whenever the amplitudes of their components are large. For example, in Fig. 4, the recurrence at peak a, $\tilde{S} = 9.792(3)$, is located at $\tilde{S}^d_{10} + \tilde{S}^u_{14} = 9.792(3)$ [14], indicating that it can be understood as the core scattered sum of these two recurrences. Similarly, the recurrence at peak b, $\tilde{S} = 13.658(4)$, is located near $\tilde{S}^d_9 + \tilde{S}^d_{10} + \tilde{S}^u_{14} = 13.654(4)$ and $\tilde{S}^d_{19} + \tilde{S}^u_{14} = 13.652(4)$ [15]. However, other recurrences that are found in lithium but not in hydrogen cannot be reliably identified using this scheme. Thus, it is uncertain how far this approach can be applied to compute the high-action recurrences we observe. Nonetheless, the possibility of describing a chaotic system in terms of a related separable system by closed-orbit theory is compelling: It would allow one to compute the closed orbits of an orderly classical system—eliminating the problem of the proliferation of orbits and the difficulties locating long-period orbits—and introduce the core-induced chaos quantum mechanically.

In summary, the high resolution of our experiment demonstrates the validity of closed-orbit theory at much higher actions than in previous work and provides experimental evidence for core scattering. The lithium Stark problem in the regime studied here seems well suited to probing the limits of periodic-orbit theory.

We thank Robert Lutwak for valuable assistance. This work is supported by NSF Grant No. 9221489-PHY and ONR Grant No. N00014-90-J-1322.

[1] M. C. Gutzwiller, *Chaos in Classical and Quantum Mechanics* (Springer-Verlag, Berlin, 1990).

[2] M. L. Du and J. B. Delos, Phys. Rev. A **38**, 1896 (1988).

[3] J. Gao and J. B. Delos, Phys. Rev. A **49**, 869 (1994).

[4] J. Main, G. Wiebusch, K. Welge, J. Shaw, and J. B. Delos, Phys. Rev. A **49**, 847 (1994).

[5] J. Gao, J. B. Delos, and M. Baruch, Phys. Rev. A **46**, 1449 (1992).

[6] A. Holle, J. Main, G. Wiebusch, H. Rottke, and K. H. Welge, Phys. Rev. Lett. **61**, 161 (1988).

[7] T. van der Veldt, W. Vassen, and W. Hogervorst, Euorphys. Lett. **21**, 9 (1993).

[8] U. Eichmann, K. Richter, D. Wintgen, and W. Sander, Phys. Rev. Lett. **61**, 2438 (1988).

[9] The unit of action here is the same as used in [8], but differs by a factor of 2π from that used in [3,5,12].

[10] The method used to compute the spectrum was derived from M. L. Zimmerman, M. G. Littman, M. M. Kash, and D. Kleppner, Phys. Rev. A **20**, 2251 (1979).

[11] We have labeled the recurrences according to the repetition of the parallel orbit. Eichmann *et al.* [8] associated low-action recurrences with the first return of orbits with various initial angles. Inspection of their Table I reveals that most of the classical orbits they report have scaled actions that are integer multiples of parallel orbits. The two approaches are similar because most of the recurrences at small action include contributions from a given repetition of a parallel orbit and an orbit which bifurcated from that repetition.

[12] J. Gao and J. B. Delos, Phys. Rev. A **46**, 1455 (1992).

[13] See also D. Delande, K. T. Taylor, M. H. Halley, T. van der Veldt, W. Vassen, and W. Hogervorst, J. Phys. B (to be published).

[14] The experimental values of S^d_{10} and S^u_{14} are used here. They differ slightly from $10S^d_1$ and $14S^u_1$ because of other orbits with slightly different actions which lie within the peaks. These differences are small compared with the linewidths.

[15] The observed recurrence amplitude is the coherent sum over all orbits with action within the experimental linewidth. Other orbits have actions within these core scattered peaks, but their amplitude in hydrogen is small. Consequently, they are not expected to be important in lithium.

Appendix B

Closed-Orbit Bifurcations in Continuum Stark Spectra, M. Courtney et al., Phys. Rev. Lett. (To be published.)

The next few pages are a short paper which has been submitted to *Physical Review Letters*.

Closed Orbit Bifurcations in Continuum Stark Spectra

Michael Courtney, Hong Jiao, Neal Spellmeyer, and Daniel Kleppner

Department of Physics and Research Laboratory of Electronics, Massachusetts Institute of Technology,

77 Massachusetts Avenue, Cambridge, Massachusetts 02139

J. Gao and J. B. Delos

Department of Physics, College of William and Mary, Williamsburg, VA. 23187

We report an experimental and theoretical study of the effect of bifurcations of closed classical orbits in continuum Stark spectra. Our findings provide a natural way to understand how the spectrum evolves from a simple sinusoidal modulation at positive energy to a quasi-discrete spectrum below the classical ionization limit. The experiment employs scaled-energy spectroscopy of lithium. The results provide the first experimental confirmation of a formulation of closed-orbit theory that provides a quantitative description of the behavior of the spectrum at a bifurcation.

Typeset Using *REVTEX*

The photoionization spectrum of a single-electron atom in an electric field F changes strikingly as the energy decreases [1]. In the positive energy regime (above the zero field ionization limit), the spectrum is smooth and displays a single periodic oscillation. Below the classical ionization threshold ($E_i = -2F^{1/2}$, atomic units), the spectrum is quasi-discrete. These contrasting patterns reflect complementary aspects of atomic behavior: the former can be simply interpreted in terms of classical dynamics, while the latter is naturally described in terms of the system's eigenstates. As the energy decreases in the intermediate region from $E > 0$ to E_i, the broad peaks become narrow and new resonances gradually appear. Quantum calculations are possible in this region [2], but they offer little insight into the connections with classical dynamics. However, the region is fertile territory for investigating the connections between quantum and classical descriptions. We report here the results of theoretical and experimental investigations that provide a detailed physical picture of how the system evolves from one extreme to the other. The results are helpful in understanding the connections between quantum and classical behavior in both regular and chaotic systems. They demonstrate the successful repair of formulas which previously diverged at a bifurcation.

Closed-orbit theory [3,4] is a variant of periodic-orbit theory [5] that is well suited to spectroscopy. It provides both an intuitive picture and a quantitative description of how the spectrum evolves based on the behavior of classical orbits that are closed at the nucleus. In the time domain, a quantum wave packet is emitted from the atom and later returns, a process known as a recurrence [6]. Each recurrence gives rise to a sinusoidal modulation of the absorption spectrum. Gao and Delos [4] recently examined closed orbits and recurrences for single-electron atoms in electric fields. At high energy only one orbit exists, accounting for the sinusoidal modulation in the spectrum. As the energy is decreased, new orbits are predicted to spring into

existence by an orderly sequence of bifurcations. At each bifurcation, a new frequency component is added to the spectrum.

We have studied this bifurcation process experimentally for lithium in an electric field using scaled-energy spectroscopy [7]. Similar studies have been performed in diamagnetic hydrogen [8]. The electric field problem for hydrogen is separable, facilitating a detailed quantitative study of the bifurcation process and the evolution of the spectrum. Alkali-metal atoms in an electric field are fundamentally different from hydrogen because they have non-separable Hamiltonians and display irregular motion. However, the recurrence spectra are nearly identical for the short-period orbits studied here [7]. Consequently, the lithium spectra can be interpreted in terms of the classical dynamics of hydrogen. At longer periods, the recurrence spectra of alkali-metal atoms can differ significantly from hydrogen [9].

The Hamiltonian for hydrogen in an electric field can be rescaled using the substitutions $r = F^{-1/2}\tilde{r}$ and $p = F^{1/4}\tilde{p}$. The scaled Hamiltonian, $\tilde{H} = F^{-1/2}H$, does not explicitly depend on the field, and the classical dynamics depends only on the scaled energy $\epsilon = EF^{-1/2}$, not on E and F separately.

According to closed-orbit theory, the photoabsorption cross section is given by a smooth slowly varying background plus an oscillatory sum of the form [4]

$$Df' = \sum_k \sum_{n=1}^{\infty} D_{nk} \sin(n\tilde{S}_k F^{-1/4} - \Phi_{nk}), \tag{1}$$

where k runs over all of the primitive closed orbits (orbits which are not repetitions), and n runs over repetitions of the primitive orbits. $\tilde{S}_k = S_k F^{1/4}$ is the scaled action of the first repetition of a closed orbit. D_{nk} is the recurrence amplitude of each closed orbit. It contains information about the stability of the orbit, the initial and final angles of the orbit, and the matrix element of the dipole operator between the initial state and zero-energy Coulomb wave. Φ_{nk} is an additional phase which is computed

from the Maslov index and related geometrical considerations. The square of the recurrence amplitude D_{nk} is the recurrence strength. Each closed orbit contributes an oscillatory component to the absorption spectrum. The signature of each closed orbit is a peak in the Fourier transform of spectra taken at constant scaled energy and recorded as a function of $F^{-1/4}$.

For $E > 0$, the only closed orbit is parallel to the field and extends from the nucleus to the classical turning point. The spectrum contains a fundamental Fourier component from this orbit plus harmonics from its repetitions. The parallel orbit is unstable and none of its neighbors return to the nucleus. Consequently, the amplitude of the harmonics decreases roughly exponentially. Just above $E = 0$, many harmonics contribute, and the spectrum resembles a sawtooth. The exponential decay rate increases as ϵ is increased [4] resulting in a single sinusoid at large positive energy [1, 10].

As the energy is lowered below $E = 0$, new closed orbits are created by bifurcations of the parallel orbit and its repetitions [4]. Because the system is separable in semiparabolic coordinates ($u = (r + z)^{1/2}$, $v = (r - z)^{1/2}$), the bound trajectories are quasiperiodic. Periodic orbits occur whenever the ratio of periods of u and v motion, T_u/T_v, is a rational fraction, m/l. Many of these periodic orbits do not touch the nucleus. However, within each family of periodic orbits with period ratio, m/l, there is one closed orbit.

As explained in Ref. [4], the maximum value of the period ratio, T_u/T_v, is zero at $\epsilon = 0$ and increases as the scaled energy decreases. A graph of the maximum period ratio as a function of scaled energy is shown in Fig. 1. At a given scaled energy, closed orbits exist for every rational period ratio between zero and the maximum. As the scaled energy is decreased, a bifurcation produces a new closed orbit every time the maximum ratio is a rational number. Short period orbits correspond to ratios of

small integers. Some bifurcations are labeled in Fig. 1.

To illustrate the bifurcation process, pictures of orbits near a bifurcation are shown in Fig. 2. Orbits which are neighbors of a closed orbit (i.e., having the same scaled energy and beginning at the nucleus, but having slightly different initial directions) form a cusp structure upon returning near the nucleus. As the energy is varied, this cusp moves along the z axis: at the bifurcation, the tip of the cusp touches the nucleus. Therefore, near a bifurcation, there is a family of neighbors which also returns to the nucleus. This focusing effect causes a large increase in the recurrence strength as the scaled energy passes through a bifurcation.

In its original formulation, closed-orbit theory diverges at a bifurcation [4, 11]. Such divergences are familiar in geometrical optics which predicts infinite intensity if a plane wave is focused to a point. These theories are corrected by accounting for diffraction. Two of the authors (J.G. and J.D.) have modified the closed-orbit theory to include such diffraction effects.

We summarize the features of the theory here. A detailed description will be presented elsewhere. For waves in one dimension the semiclassical formula diverges at an ordinary classical turning point where the behavior of the wavefunction changes from oscillatory to exponential. This divergence is corrected using Airy's diffraction integral. The same also holds at a simple boundary between classically allowed and forbidden regions in more than one dimension. In two dimensions, it is common for such regions to come together and form a cusp, as in Fig. 2. The associated diffraction integral is known as a Pearcey function [12]. However, the cusp in our problem has a special symmetry: the axis of the cusp coincides with the direction of the electric field, so the cusp is actually three dimensional and cylindrically symmetric about the vertical axis in Fig. 2. Such cusps are produced by an optical lens, and they cause spherical aberration of a point image; the diffraction function that describes them is

a Fresnel integral [13].

The cusp in our problem has yet another symmetry. The cusp in Fig. 2 is cylindrically symmetric not only about the vertical axis through the nucleus, but also about the horizontal axis through the nucleus. The formulas that describe this cusp make use of the close connection between a hydrogen atom and a four-dimensional harmonic oscillator. The cusp shown in Fig. 2 is a slice through a structure that exists in a four-dimensional extension of the (u, v) space [14].

In spite of the complexity of the cusp, the formulas for the wave function and recurrence strengths are simple. We find that: (i) the recurrence strength is small but non-zero before the classical bifurcation because of wave diffraction effects or tunnelling into the classically forbidden region; (ii) as expected, the recurrence strength is finite at the bifurcation; (iii) the recurrence strength has its maximum after the bifurcation, just as waves are largest slightly inside of a classically-allowed boundary.

The structure of bifurcations can be studied experimentally using scaled-energy spectroscopy. The lasers and field are scanned simultaneously so as to keep the scaled energy—and hence the classical dynamics—constant [7,8]. Our experiment employs a lithium atomic beam which passes through holes in the centers of a pair of electric field plates. Between the field plates, one laser excites the $2S \rightarrow 3S$ two-photon transition, and a second laser, polarized parallel to the applied field, excites continuum states which rapidly ionize. After passing through the second field plate, ions are detected by a channel electron multiplier. The error in scanning the laser to maintain constant scaled energy is $0.002\,cm^{-1}$, the fractional error in the electric field is 0.3%, and the fractional error in the scaled energy is 0.15%.

We have performed scaled-energy spectroscopy on $m = 0$ states of lithium for scaled energies between $\epsilon = -2.1$ and $\epsilon = -0.37$. Recurrence spectra were obtained by Fourier transforming the photoabsorption cross section. A panoramic map of the

recurrence spectra is shown in Fig. 3. We observe small recurrences corresponding to repetitions of the parallel orbit, and large recurrences near bifurcations. The large bifurcation peaks are labeled with the fractions, m/l, used to designate the newly created orbits. These orbits are displayed in Fig. 3.

Our experiments and theory are consistent. As the scaled energy approaches the bifurcation from above, the recurrence strength increases significantly. The uncertainty principle allows the quantum system to "see" the bifurcation before it occurs classically [15]. As the scaled energy passes through the bifurcation the recurrence strength increases rapidly, achieving its maximum value noticeably after the bifurcation.

To test the modified closed-orbit theory near bifurcations, we measured scaled-energy spectra near the 1/2 and 2/4 bifurcations in small steps of ϵ. The results are displayed in Fig. 4. The stick spectra represent the computed recurrence strengths, and the solid lines are convolutions of the stick spectra to account for the experimental resolution of the recurrence spectra. The dotted lines are measured recurrence spectra. The 1/2 and 2/4 bifurcations affect peaks 2 and 4, respectively. Their bifurcation energy is $\epsilon = -0.4$. There are two orbits underneath peaks 2 and 4, but they are not distinguishable because their actions are nearly equal. Multiple orbits are visible in the stick spectra under peaks 3 and 5. These orbits were created by the 1/3 and 2/5 bifurcations, respectively. Note that the contributions of two orbits to a single recurrence peak add coherently. For example, peak 5 at $\epsilon = -0.45$ is smaller than the stick spectra, indicating a destructive interference. At $\epsilon = -0.5$, peak 5 displays constructive interference.

These results provide a clear picture of the role of bifurcations in the observed spectrum and detailed confirmation of the closed-orbit theory. They illustrate the fundamental process by which new orbits are created as the energy is decreased and

a simple continuum spectrum becomes complex and discrete. The bifurcation process studied here is generic to single-electron atoms. Similar bifurcations occur in diamagnetic hydrogen and lead to the proliferation of recurrences that characterizes classical chaos. Consequently, this study of bifurcations illuminates a fundamental process that connects classical and quantum descriptions of both regular and chaotic systems.

The work at M.I.T. is supported by NSF grant 9221489-PHY and ONR grant N00014-90-J-1322. The work at William and Mary is supported by the Jeffress Foundation, ONR, and NSF.

REFERENCES

[1] R. R. Freeman, N. P. Economu, G. C. Bjorkland, and K. T. Lu, Phys. Rev. Lett., **41** 1463 (1978). T. S. Luk, L. DiMauro, T. Bergeman, and H. Metcalf, Phys. Rev. Lett., **47**, 83 (1981).

[2] E. Luc-Koenig and A. Bachelier, J. Phys. B., **13**, 1769 (1980). D. Harmin, Phys. Rev. A, **26** 2656 (1982).

[3] M. L. Du and J. B. Delos, Phys. Rev. A **38**, 1896 (1988).

[4] J. Gao and J. B. Delos, Phys. Rev. A **49**, 869 (1994).

[5] *Chaos in Classical and Quantum Mechanics*, M. C. Gutzwiller, Springer-Verlag (1990).

[6] J. Parker and C. R. Stroud, Jr., Phys. Rev. Lett. **56**, 716 (1986).

[7] U. Eichmann, K. Richter, D. Wintgen, and W. Sandner, Phys. Rev. Lett. **61**, 2438 (1988).

[8] A. Holle, J. Main, G. Wiebusch, H. Rottke, and K. H. Welge, Phys. Rev. Lett. **61**, 161 (1988).

[9] M. Courtney, H. Jiao, N. Spellmeyer, and D. Kleppner, Phys. Rev. Lett. **73**, 1340 (1994).

[10] J. Gao, J. B. Delos, and M. Baruch, Phys. Rev. A **46**, 1449 (1992).

[11] J. Main, G. Wiebusch, K. Welge, J. Shaw, and J.B. Delos, Phys. Rev. A **49**, 847 (1994).

[12] J.N.L. Conner, Mol. Phys. **31**, 33 (1976); J.N.L. Conner and D. Farrelly, J. Chem. Phys. **75**, 2831 (1981).

[13] S.P. Parker, Optics Source Book, McGraw Hill, 1988, p. 17; M. Born and E. Wolf, Principles of Optics, 6th edition, Pergamon 1989.

[14] This results from the fact that the positive and negative z axes are perpendicular in semiparabolic coordinates. A four dimensional space is needed to describe the symmetry in semiparabolic coordinates.

[15] M. Kus, F. Haake, and D. Delande, Phys. Rev. Lett., **71**, 2167 (1993).

FIGURES

FIG. 1. The maximum period ratio, T_u/T_v, as a function of scaled energy. At each scaled energy, all orbits with period ratio in the shaded region are present. Bifurcations occur when this maximum ratio passes through a rational fraction. The short period bifurcations studied here are indicated.

FIG. 2. Cusp structure associated with a family of (a) outgoing and (b) returning orbits near a bifurcation (semiparabolic coordinates).

FIG. 3. The curves in the horizontal plane represent the scaled action of the parallel orbit and its repetitions as a function of scaled energy. Locations of bifurcations are marked with small open circles. New orbits created in bifurcations have almost the same action as the corresponding return of the parallel orbit. Measured recurrence strengths are shown in the z direction. Recurrences are especially strong at scaled energies slightly lower than bifurcations. Orbits created by bifurcation of the parallel orbit are shown along the bottom. The 2/4, 4/6 and 6/8 orbits are repetitions of the 1/2, 2/3, 3/4 orbits respectively, so their shapes are identical.

FIG. 4. Recurrence strength near the 1/2 bifurcation. $\epsilon = -0.4$ is the bifurcation energy. Stick spectra: theory. Solid line: theory smoothed for comparison with experiment. Dotted line: experiment.

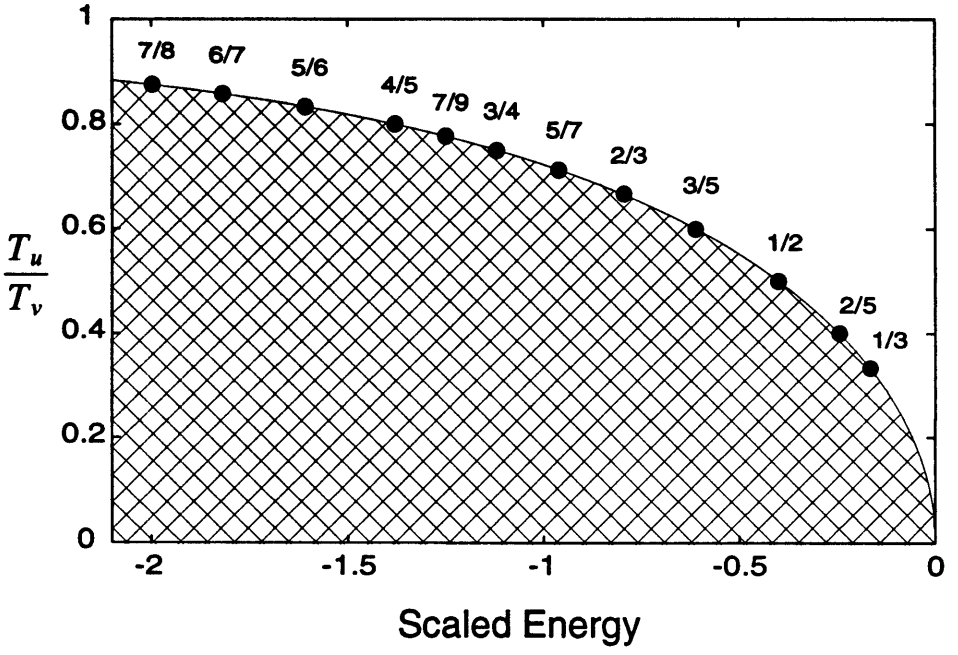
1
0.8
0.6
0.4
0.2
0
$\frac{T_u}{T_v}$
7/8
6/7
5/6
4/5
7/9
3/4
5/7
2/3
3/5
1/2
2/5
1/3
-2
-1.5
-1
-0.5
0
Scaled Energy

(a) outgoing orbits

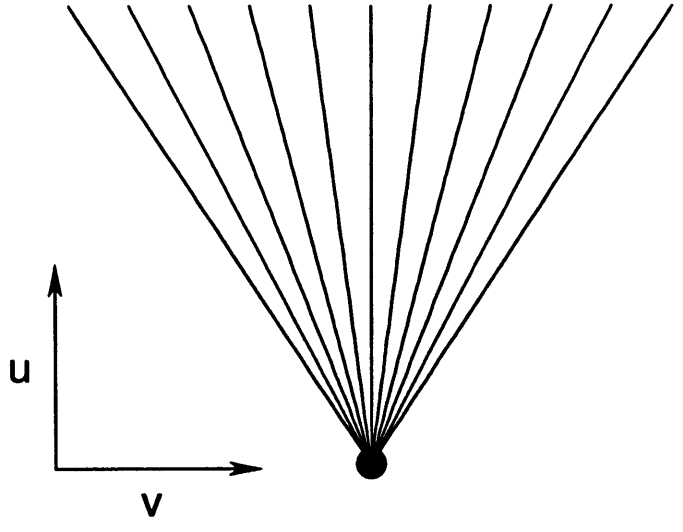

(b) returning orbits

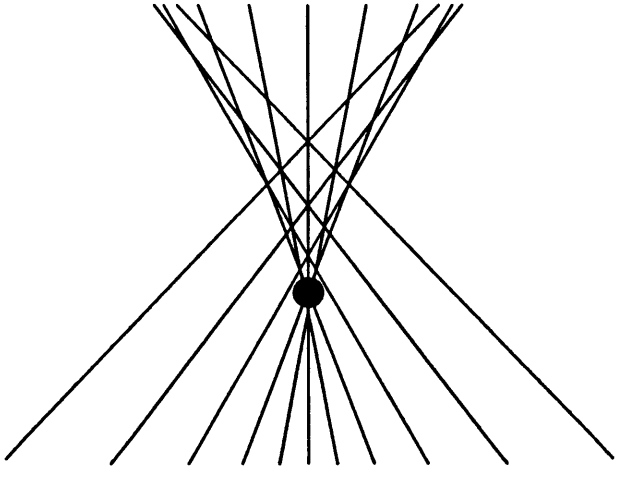

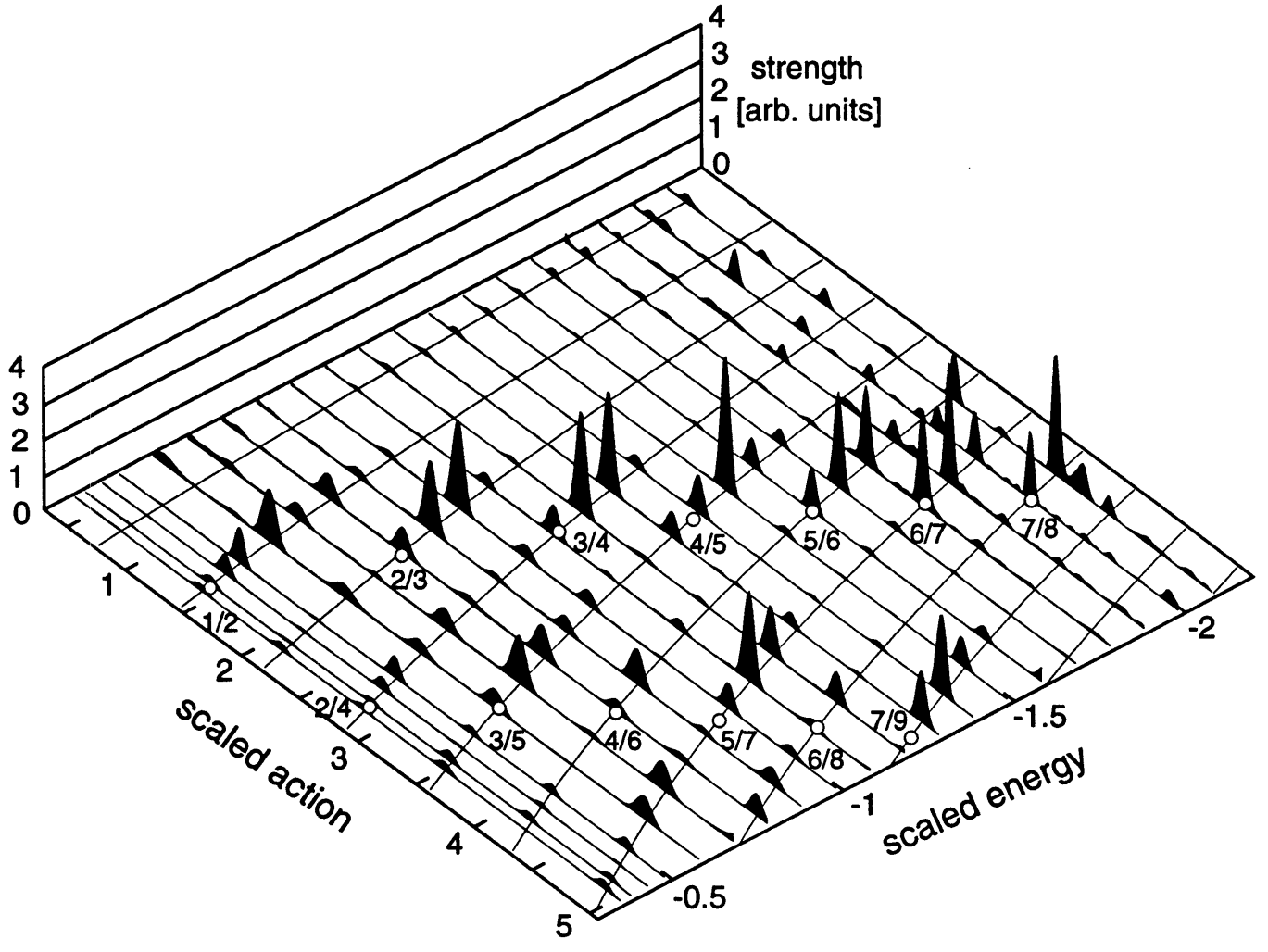
4
3
2
1
0
strength
[arb. units]
4
3
2
1
0
1
1/2
2
2/3
3
3/4
4
4/5
5
5/6
6/7
7/8
scaled action
-0.5
-1
-1.5
-2
scaled energy
2/4
3/5
4/6
5/7
6/8
7/9

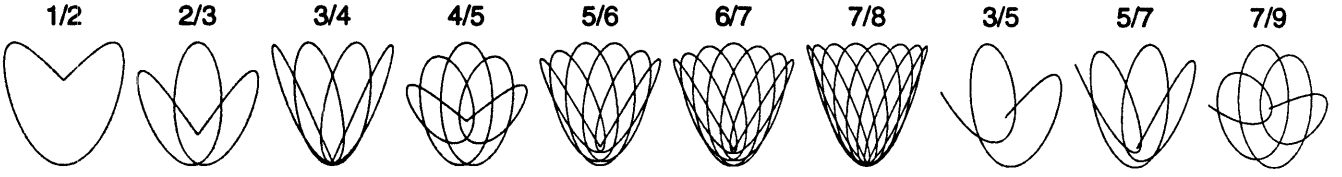
1/2
2/3
3/4
4/5
5/6
6/7
7/8
3/5
5/7
7/9

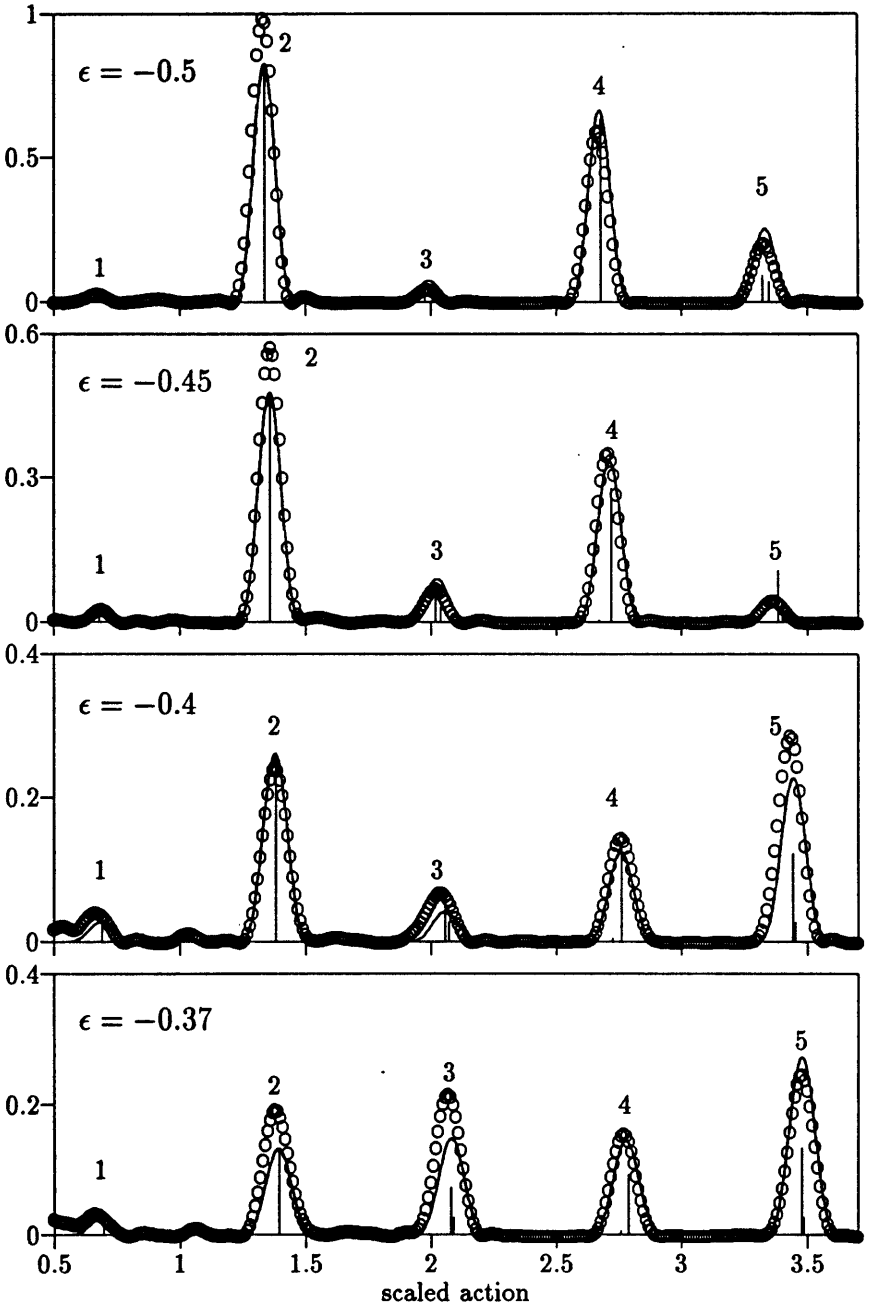
$\epsilon = -0.5$
$\epsilon = -0.45$
$\epsilon = -0.4$
$\epsilon = -0.37$
1
2
3
4
5
0.5
1
1.5
2
2.5
3
3.5
scaled action

Appendix C

Acknowledgments

I am grateful to many for the help they have provided which made this thesis possible. Detailed acknowledgments of all the help I have received would require another 250 pages, so the following brief account will have to suffice.

My wife, Amy Corinne Courtney, has made manifold contributions. She has been a loving, obedient, and faithful wife for over five years. Not once has she quarrelled or done anything to make my life difficult, but rather has been a constant blessing. Not only has she been a partner in this undertaking, but she has done my laundry, cooked my meals, and cleaned my home, and all while earning a Ph. D. from Harvard in Biomedical Engineering.

I am also indebted to Amy's parents, Pastor Gordon Powlison and his wife Linda. In addition to raising Amy to be a wonderful wife, they have been a constant source of support and encouragement to me as well. Without nagging or offering unsolicited advice, they have provided a model for how a marriage should work. Pastor Gordon's book series, **School of the Prophets**, has been especially helpful in all areas of life.

I also thank Pastor Norm Althausen for being another example of a godly man who loves his family and is willing to be spent for them. In addition to this, he has taken up the challenge of being a spiritual counselor to me and has worked hard on my behalf. He has also shown me a thing or two about teaching physics, and I hope to learn more.

My natural father, William B. Courtney, provided the necessary discipline when

I was a boy. Left to my own devices, I might have quit school at a young age, and I certainly would not have pursued excellence. My dad was never satisfied with B's because he knew I was smart enough to get A's. He also gave me my first physics lesson by proving (much to my amazement) that a ball of paper falls as fast as a shoe. In addition, he bore a large part of the financial burden of my undergraduate education, and he worked hard to do so. Perhaps more importantly, on the day before I left for college, he admitted that he had also been afraid in the same situation.

My mother, Jerlyn Courtney, gave immensely of herself to her children and is to be commended for finding fulfillment in the raising of her children. She taught me to read, and she used flash cards to teach me the beginnings of arithmetic. It seems that every time we came to a new subject in school, I was already ahead of the game because my mom had taught me about it. And even though my college years were a difficult time in her life, she worked hard and also made a substantial financial contribution to my college education. She even made good on my father's promise to buy me a new car if I graduated from college with a certain GPA.

In my first few years at MIT, Chris Bang was my best friend. Chris is a man of extraordinary character and faithfulness. For the last few years, David Fuentes has also been an extraordinary friend. David became my friend because God told him to at a time when being my friend was an unpopular choice.

I am also grateful to many Christian pastors in the Boston area who are working hard in overseeing God's people. Eric Schenkle, Mark Fee, Greg Clark, and Larry Showalter have been particular blessings to me. Being a Christian pastor in Boston in the 1990's seems to me one of the most difficult careers possible. These men are working hard for low pay because they love God.

Lee-Peng Ng, Troy Hammond and Dale Fried are three Christians who God sent to MIT. They have been an encouragement to me by being firm in their faith in spite of much opposition. In addition, they are respectable scientists in their own right.

Several professors at Louisiana State University played a key role in my choice to pursue physics at the graduate level. Dr. Greg Hussey taught my freshman physics class with love, grace, and style. As a Dean in the College of Basic Sciences, he

always made sure that the doors were open for me to pursue opportunities. Dr. Ed Zganjar opened my eyes to the wonders of quantum mechanics and the beauty of the hydrogen atom. He also invited me to work in his lab where I discovered the challenges of vacuum equipment, cabling which looked like spaghetti, and LaTeX. It was Dr. Louis DiMauro who introduced me to laser spectroscopy and experimental atomic physics. He invited me to work in his lab and made me an integral part of what was going on. He never showed any sense that I would fail, and never showed any anger when I broke things. When he moved to Brookhaven National Laboratory, he made it possible for me to join him for three separate internships, and it was at his insistence that I applied to MIT and visited the Kleppner and Pritchard groups.

I am thankful to a number of colleagues for helping me through graduate school. Hong Jaio served as my right hand in the laboratory. Hong is a man of considerable prowess as a physicist, both in theory and experiment. He solved a number of experimental difficulties which would have prevented this work. In addition, he provided critical insights into the physics being investigated.

Neal Spellmeyer was the other graduate student on the experiment during the time I was collecting the data for this thesis. One could not imagine a better contributor than Neal. He did nearly everything we asked of him well. He seldom airs his opinion, but when he does, it is worth listening.

Chun-Ho Iu was the graduate student on our experiment immediately before me. He taught me how to use most of our laboratory equipment, and showed great patience in the face of a number of my stupid mistakes. His technical contributions to our experiment were enormous. His theoretical genuis also made for substantial contributions to the diamagnetic Rydberg problem.

I am also grateful to a long line of Kleppner students, most of whom I have not met. Myron Zimmerman developed the basic method of computing spectra of Rydberg atoms in strong fields which was used for most of this thesis. George Welch, Chun-Ho Iu and myself made incremental improvements, but the basic method has been applied successfully in regimes requiring much larger basis sets than Zimmerman originally intended. The original code was developed on a machine with 64 kilobytes

of memory, which allows about 50 basis states. In this thesis, computations were performed using 7200 basis states.

Michael Littman performed the seminal experimental work on the Stark effect in alkali-metal Rydberg atoms. Jarbas Castro performed early work on Rydberg atom diamagnetism. Mike Kash and George Welch set up the laboratory for performing high-resolution spectroscopy of diamagnetic lithium, and the fact that the experimental design was hardly altered for this work is a testimony to their excellence.

Robert Lutwak has been a constant blessing to me from the day I arrived at MIT. He is the current captain of the crew attempting to measure the Rydberg constant. He is a scientist of unmatched laboratory skills and considerable physical insight. In the first few years, he helped me through my classes and general exams by always being willing to discuss problems. He was the person to whom I most often turned to show me how to get something done, and he often took considerable time out from his own work to help me. When it came time to make the experiment work, Robert provided crucial help by explaining the use of channeltrons and high-voltage supplies. Not only did he lend us the necessary equipment, he spent several days making a custom voltage supply for providing the voltage across our electric field plates.

Jeff Holley is another man of considerable skill who always seemed willing to lend advice or equipment. Scott Paine and Peter Chang were the sages of the Rydberg constant measurement team for a number of years. They helped me solve a number of technical and physics problems.

A number of David Pritchard's graduate students have also helped me. Ken Davis, Michael Chapman, Troy Hammond, Chris Ekstrom, Michael Ioffee, Michael Bradley and others provided an atomic physics community at MIT which made it easy to solve technical problems and testing ideas. The addition of Wolfgang Ketterle to the atomic physics faculty provided an even more exciting and friendly environment for doing atomic physics.

A number of other scientists have made important contributions in the area of quantum chaos. I mention only those who have helped me personally. Martin Gutzwiller provided the trace formula as a foundation. He showed great patience

with me in explaining an important detail which had confounded me for some time. John Delos turned Gutzwiller's non-convergent recipe for energy-levels into a workable approach to finding absorption spectra of Rydberg atoms. Yet, the original work of Du and Delos left an unpolished diamond. John Shaw took up the task of turning closed-orbit theory into a true gem by working out the difficult details of core scattering and the contribution of neighboring orbits. Both John Shaw and John Delos were always willing to help me understand their work. Jing Gao also made an important contribution by providing inspiration for the continuum experiments in this thesis, and by providing the detailed theoretical analysis after they were completed.

Michael Berry provided key help by separating the interesting from the trivial. Michel Baranger provided a different perspective and enabled me to see several issues in a new light. Karl Welge provided the experimental method and much of the motivation for this work. Dominique Delande provided reality checks and allowed the use of his implementation of the Lanczos algorithm and code for using the Sturmian basis. They are all world-class scientists.

This thesis is just another rung on the ladder of understanding the physics of Rydberg atoms. Dan Kleppner was one of the first scientists to realize the rich physics of Rydberg atoms, and over the last twenty years he has overseen the work which provided the foundation for this thesis. I may have added a rung, but Dan built the ladder and held it for me as I gazed upon a few new things. Dan loves atomic physics and is very good at it. Just as importantly, he loves teaching young scientists how to pursue excellence in the field.

While Dan made the ladder on which I have stood, we must remember that the Lord God made Dan Kleppner and all the other contributors to this work. Jesus Christ is the creator of all things and the author of all life. Through him, God adopted me as his son and became my heavenly Father. My Father has forgiven my sins and set me free from slavery to sin and from the fear of death. He has given me a new heart and mind. I went to MIT because he sent me. I graduated because he spoke it into being. I am moving to Cleveland because he told me to. God has promised that I will be a professor, and I have taken him at his word. I can testify

that he has been faithful in all of his promises so far.

In the years to come we will see the destruction of the United States and retribution for abortion come onto this land. This will be a testimony to a holy God who hates sin. Yet the resurrection of Jesus Christ serves as a testimony of God's love for man and offer of salvation. We will all die and stand before a holy God in judgement. Those who have trusted in Christ and died to their sin will reap eternal life. Those who have trusted in their own strength will burn forever in hell for their sins.

Bibliography

[BET77] M. V. Berry and M. Tabor, Proc. Roy. Soc. London A **356**, 375 (1977).

[BOG84] O. Bohigas and M. J. Giannoni, in **Mathematical and Computational Methods in Nuclear Physics**, edited by J. S. DeHessa, J. M. G. Gomez, and A. Polls, Lecture Notes In Physics Vol. 209 (Springer-Verlag, New York, 1984).

[BGS84] O. Bohigas, M. J. Giannoni, and C. Schmit, Phys. Rev. Lett. **52**, 1 (1984).

[BRO73] T. A. Brody, Lett. Nuovo Cim. **7**, 482 (1973).

[CJS94] M. Courtney, H. Jiao, N. Spellmeyer, and D. Kleppner, Phys. Rev. Lett. **73**, 1340 (1994). "Long Period Orbits in the Spectrum of Lithium in an Electric Field."

[CJS95] M. Courtney, H. Jiao, N. Spellmeyer, D. Kleppner, J. Gao, and J.B. Delos Phys. Rev. Lett. (To be published.) "Closed Orbit Bifurcations in Continuum Stark Spectra."

[CLP86a] P. Cacciani, E. Luc-Koenig, J. Pinard, C. Thomas, and S. Liberman, J. Phys. B **19**, L519 (1986). "Anticrossing Effect in Odd Rydberg States of Li in the Presence of a Magnetic Field."

[CLP86b] P. Cacciani, E. Luc-Koenig, J. Pinard, C. Thomas, and S. Liberman, Phys. Rev. Lett. **56**, 1124 (1986). "Experimental Studies of a Diamagnetic Multiplet in Odd Rydberg States of Lithium."

[CLL88a] P. Cacciani, S. Liberman, E. Luc-Koenig, J. Pinard, and C. Thomas, J. Phys. B **21**, 3473 (1988). "Rydberg atoms in parallel magnetic and electric

fields: I. Experimental studies of the odd diamagnetic multiplet of lithium; n mixing and core effects."

[CLL88b] P. Cacciani, S. Liberman, E. Luc-Koenig, J. Pinard, and C. Thomas, J. Phys. B **21**, 3499 (1988). "Rydberg atoms in parallel magnetic and electric fields: II. Theoretical analysis of the Stark structure of the diamagnetic manifold of hydrogen."

[CLL88c] P. Cacciani, S. Liberman, E. Luc-Koenig, J. Pinard, and C. Thomas, J. Phys. B **21**, 3523 (1988). "Rydberg atoms in parallel magnetic and electric fields: III. Experimental investigations of the Stark structure of the diamagnetic manifold of lithium."

[CLL89] P. Cacciani, S. Liberman, E. Luc-Koenig, J. Pinard, and C. Thomas, Phys. Rev. A **40**, 3026 (1989). "Anticrossing effects in Rydberg states of lithium in the presence of parallel magnetic and electric fields."

[CLT82] C.W. Clark and K.T. Taylor, J. Phys. B **15**, 1175 (1982). "The Quadratic Zeeman Effect in Hydrogen Rydberg Series: Application of Sturmian Functions."

[COK95] M. Courtney and D. Kleppner, Phys. Rev. A (To be published.) "Core Induced Chaos in Diamagnetic Lithium."

[COO61] J.W. Cooley, Math. Comput. **15**, 363 (1961). "An Improved Eigenvalue Corrector Formula for Solving the Schrödinger Equation for Central Fields."

[COU94a] M. Courtney **TD.EXE User's Guide** (unpublished).

[COU94b] M. Courtney **TD.EXE Programmer's Guide** (unpublished).

[CSJ95] M. Courtney, N. Spellmeyer, H. Jiao, and D. Kleppner, Phys. Rev. A (To be published.) "Classical and Quantum Dynamics of Lithium in an Electric Field."

[CVE89] P. Cvitanović and B. Eckhardt, Phys. Rev. Lett. **63**, 823 (1989). "Periodic-Orbit Quantization of Quantum Systems."

[CZH80] J.C. Castro, M.L. Zimmerman, R.G. Hulet, D. Kleppner, and R. Freeman, Phys. Rev. Lett. **45**, 1780 (1980). "Origin and Structure of the Quasi-Landau Resonances."

[DAM94] P. A. Dando and T. S. Monteiro, J. Phys. A **27**, 2681, (1994). "Quantum surfaces of section for the diamagnetic hydrogen atom: Husimi functions versus Wigner functions."

[DBG91] D. Delande, A. Bommier, and J.C. Gay, Phys. Rev. Lett. **66**,141 (1991). "Positive Energy Spectrum of the Hydrogen Atom in a Magnetic Field."

[DEG84] D. Delande and J.C. Gay, J. Phys. B **17**, L335 (1984). "Group Theory Applied to the Hydrogen Atom in a Strong Magnetic Field. Derivation of the Effective Diamagnetic Hamiltonian."

[DEG86a] D. Delande and J.C. Gay, Comments At. Mol. Phys. **19**, 35 (1986). "The Quantum Analog of Chaos in the Diamagnetic Kepler Problem."

[DEG86b] D. Delande and J.C. Gay, J. Phys. B **19**, L173 (1986). "The Hydrogen Atom in a Magnetic Field. Spectrum from the Coulomb Dynamical Group Approach."

[DEG86c] D. Delande and J.C. Gay, Phys. Rev. Lett. **57**, 2006 (1986). "Quantum Chaos and Statistical Properties of Energy Levels: Numerical Study of the Hydrogen Atom in a Magnetic Field."

[DEG91] D. Delande and J.C. Gay, (Submitted to Phys. Rev. Lett. but not published.) "Supersymmetry of Rydberg Atoms in Parallel Electric and Magnetic Fields."

[DKN84] J.B. Delos, S.K. Knudson, and D.W. Noid, Phys. Rev. A **30**, 1208 (1984). "Trajectories of an Atomic Electron in a Magnetic Field."

[DMJ94] P. Dando, W. Jans, T. S. Monteiro, and W. Schweitzer, Progress in Theoretical Physics, **116**, (1994). "Non-hydrogenic Rydberg atoms in magnetic fields."

[DTH94] D. Delande, K. T. Taylor, M. H. Halley, T. van der Veldt, W. Vassen, and W. Hogervorst, J. Phys. B. **27**, 2771 (1994). "Scaled-energy spectra of non-hydrogenic Rydberg atoms in a magnetic field."

[DUD87] M.L. Du, and J.B. Delos, Phys. Rev. Lett. **58**, 1731 (1987). "Effect of Closed Classical Orbits on Quantum Spectra: Ionization of Atoms in a Magnetic Field."

[DUD88a] M.L. Du, and J.B. Delos, Phys. Rev. A **38**, 1896 (1988). "Effect of Closed Classical Orbits on Quantum Spectra: Ionization of Atoms in a Magnetic Field. I. Physical Picture and Calculation."

[DUD88b] M.L. Du, and J.B. Delos, Phys. Rev. A **38**, 1913 (1988). "Effect of Closed Classical Orbits on Quantum Spectra: Ionization of Atoms in a Magnetic Field. II. Derivation of Formulas."

[EDM70] A. Edmonds, J. Phys. (Paris) Colloq. **31**, C4-71 (1970). "The Theory of the Quadratic Zeeman Effect."

[EDM73] A. Edmonds, J. Phys. B **6**, 1603 (1973). "Studies of the Quadratic Zeeman Effect. I. Application of the Sturmian Functions."

[EIS48] L.P. Eisenhart, Phys. Rev. **74**, 87 (1948). "Enumeration of Potentials for Which One-Particle Schrödinger Equations are Separable."

[ERT91] G.S Ezra, K. Richter, G. Tanner, and D. Wintgen, J. Phys. B **24**, L413 (1991). "Semiclassical cycle expansion for the helium atom."

[ERW88] U. Eichmann, K. Richter, D. Wintgen, and W. Sander, Phys. Rev. Lett. **61**, 2438 (1988). "Scaled-Energy Spectroscopy and Its Relation with Periodic Orbits."

[FEB78] R. R. Freeman, N. P. Economu, G. C. Bjorkland, and K. T. Lu, Phys. Rev. Lett. **41**, 1463 (1978). "Observation of Electric-Field–Induced Resonances above the Ionization Limit in a One-Electron Atom."

[FRE79] R. R. Freeman and N. P. Economu, Phys. Rev. A **20** 2356 (1979). "Electric Field Dependence of the Photo-Ionization Cross Section of Rb."

[FRI82] H. Friedrich, Phys. Rev. A **26**, 1827 (1982). "Bound-state Spectrum of the Hydrogen Atom in Strong Magnetic Fields."

[FRW89] H. Friedrich, and D. Wintgen, Physics Reports *Review Section of Physics Letters*, **183**, 37 (1989). "The Hydrogen Atom in a Uniform Magnetic Field—an Example of Chaos."

[GAD92] J. Gao , J. B. Delos, Phys. Rev. A **46**, 1455 (1992). "Closed-Orbit Theory of Oscillations in Atomic Photoabsorption Cross Sections in a Strong Electric Field. II. Derivation of Formulas."

[GAD94] J. Gao and J. B. Delos, Phys. Rev. A **49**, 869 (1994). "Resonances and Recurrences in the Absorption Spectrum of an Atom in an Electric Field."

[GAT69] W.S. Garton and F.S. Tomkins, The Astrophysical J. **158**, 839 (1969). "Diamagnetic Zeeman Effect and Magnetic Configuration Mixing in Long Spectral Series of Ba I."

[GAY92] J.-C. Gay, ed., **Irregular Atomic Systems and Quantum Chaos**, Gordon and Breach (1992).

[GDB92] J. Gao , J. B. Delos, and M. Baruch, Phys. Rev. A **46**, 1449 (1992). "Closed-Orbit Theory of Oscillations in Atomic Photoabsorption Cross Sections in a Strong Electric Field. I. Comparison Between Theory and Experiments on Hydrogen and Sodium Above Threshold."

[GDG93] G. Greémaud, D. Delande and J.C. Gay, Phys. Rev. Lett. **70**, 1615, (1993). "Origin of Narrow Resonances in the Diamagnetic Rydberg Spectrum."

[GEL78] S. Gerstenkorn and P. Luc, **Atlas of the Absorption Spectra of Molecular Iodine for 14,800 to 20,000 cm^{-1},** (C.N.S., Paris, 1978). We subtract $0.005 cm^{-1}$ from all entries, as per instructions in [GVC82].

[GUT70] M. C. Gutzwiller, J. Math Phys. **12**, 343 (1970). "Periodic Orbits and Classical Quantization Conditions"

[GUT90] M. C. Gutzwiller, **Chaos in Classical and Quantum Mechanics**, (Springer-Verlag. New York, 1990).

[GVC82] S. Gerstenkorn, J. Verges, and J. Chevillard, **Atlas of the Absorption Spectra of Molecules Iodine for 11,000 to 14,000 cm^{-1}.** (C.N.S. II, Aime Cotton, 1982).

[HAA91] F. Haake, **Quantum Signatures of Chaos**, Springer-Verlag (1991).

[HAH83] A. Harada, and Hasegawa, J. Phys. A. **16**, L259 (1983). "Correspondence between Classical and Quantum Chaos for Hydrogen in a Uniform Magnetic Field."

[HER82] D. Herrick, Phys. Rev. A **26**, 323 (1982). "Symmetry of the Quadratic Zeeman Effect of Hydrogen."

[HMW88] A. Holle, J. Main, G. Wiebusch, H. Rottke, and K.H. Welge, Phys. Rev. Lett. **61**, 161 (1988). "Quasi-Landau Spectrum of the Chaotic Diamagnetic Hydrogen Atom."

[HRW81] H. Herold, H. Ruder, and G.Wunner, J. Phys. B **14**, 751 (1981). "The Two-body Problem in the Presence of a Homogeneous Magnetic Field."

[HRW89] H. Hasegawa, M. Robnik, and G.Wunner, No. 98, **New Trends in Chaotic Dynamics of Hamiltonian Systems**, Progress of Theoretical Physics, Supplement, p. 198 (1989). "Classical and Quantum Chaos in the Diamagnetic Kepler Problem."

[HWM86] A. Holle, G. Wiebusch, J. Main, B. Hager, H. Rottke, and K.H. Welge, Phys. Rev. Lett. **56**, 2594 (1986). "Diamagnetism of the Hydrogen Atom in the Quasi-Landau Regime."

[HWM87] A. Holle, G. Wiebusch, J. Main, K.H. Welge, G. Zeller, G. Wunner, T. Ertl, and H. Ruder, Z. Phys. D **5**, 279 (1987). "Hydrogenic Rydberg Atoms in Strong Magnetic Fields: Theoretical and Experimental Spectra in the Transition Region from Regularity to Irregularity."

[IWK89] C. Iu, G. Welch, M.M. Kash, L. Hsu, and D. Kleppner, Phys. Rev. Lett. **63**, 1133 (1989). "Orderly Structure in the Positive Energy Spectrum of a Diamagnetic Rydberg Atom."

[IUC91] C. Iu, Ph.D. Thesis, M.I.T. (1991), "Energy Level Structure of Atoms in Magnetic Fields."

[IWK91] C. Iu, G.R. Welch, M.M. Kash, D. Kleppner, D. Delande, and J.C. Gay, Phys. Rev. Lett. **66**, 145 (1991). "Diamagnetic Rydberg Atom: Confrontation of Calculated and Observed Spectra."

[JES39] F.A. Jenkins, and E. Segré, Phys. Rev. **55**, 52 (1939). "The Quadratic Zeeman Effect."

[JMS93] W. Jans, T. S. Monteiro, W. Schweitzer, and P. Dando, J. Phys. A **26**, 3187, (1993). "Phase-space distributions and spectral properties for non-hydrogenic atoms in magnetic fields."

[KAS88] M.M. Kash, Ph.D. Thesis, M.I.T. (1988), "Rydberg Atom Diamagnetism."

[KGJ80] I.V. Komarov, T.P. Grozdanov, and R.K. Janev, J. Phys. B **13**, L573 (1980). "Influence of the Atomic Core on the Stark Structure of Alkali Atom Rydberg States."

[KHD93] M. Kus, F. Haake, and D. Delande, Phys. Rev. Lett. **71**, 2167 (1993). "Prebifurcation Periodic Ghost Orbits in Semiclassical Quantization."

[LAN50] C. Lanczos, J. Res. Nat. Bur. Stand. **45**, 255 (1950).

[LDB81] T. S. Luk, L. DiMauro, T. Bergeman, and H. Metcalf, Phys. Rev. Lett. **47**, 83 (1981). "Continuum Stark Spectroscopy."

[LKK78] M. G. Littman, M. M. Kash, and D. Kleppner, Phys. Rev. Lett. **41**, 103 (1978). "Field Ionization Processes in Excited Atoms."

[LOU59] R. Loudon, Am. J. Phys. **27**, 649 (1959). "One-Dimensional Hydrogen Atom."

[LTG78] K.T. Lu, F.S. Tomkins, and W.S. Garton, Proc. Phys. Soc. Lond. A **362**, 421 (1978). "Configuration Interaction Effect on Diamagnetic Phenomena in Atoms: Strong Mixing and Landau Regions."

[LUB80] E. Luc-Koenig and A. Bachelier, J. Phys. B **13**, 1769 (1980). "Systematic Theoretical Study of the Stark Spectrum of Atomic Hydrogen II: Density of Oscillator Strengths. Comparison with Experimental Absorption Spectra in Solid-State and Atomic Physics."

[LZD76] M. G. Littman, M. L. Zimmerman, T. W. Ducas, R. R. Freeman, and D. Kleppner, Phys. Rev. Lett. **36**, 14 (1976). "Structure of Sodium Rydberg States in Weak to Strong Electric Fields".

[MAD92] J.-M. Mao and J. B. Delos, Phys. Rev. A. **45**, 1746 (1992) "Hamiltonian Bifurcation Theory of Closed Orbits in the Diamagnetic Kepler Problem"

[MEH67] M.L. Mehta, **Random Matrices and the Statistical Theory of Energy Levels,** (Academic Press, New York 1967).

[MON92] T. S. Monteiro, J. Phys. B **25**, L621 (1992). "Quantum phase-space behavior for the H_2 molecule in a magnetic field."

[MON94] T. S. Monteiro, J. Phys. A **27**, 787 (1994). "Wigner functions for the diamagnetic hydrogen atom: quantum fringes."

[MOW90] T. S. Monteiro and G. Wunner, Phys. Rev. Lett. **65**, 1100 (1990). "Analysis of Quantum Manifestations of Chaos in General Rydberg Atoms in Strong Magnetic Fields."

[MWW94] J. Main, G. Wiebusch, K. Welge, J. Shaw, and J. B. Delos, Phys. Rev. A **49**, 847 (1994). "Recurrence Spectroscopy: Observation and Interpretation of Large-Scale Structure in the Absorption Spectra of Atoms in Magnetic Fields."

[MRB93] J.-M. Mao, K. A. Rapelje, S. J. Blodgett-Ford, J.B. Delos, A. König and H. Rinneberg, Phys. Rev. A **48**, 2117 (1993). "Photoabsorption Spectra of Atoms in Parallel Electric and Magnetic Fields."

[NGL93] L. Ng, B.S. Thesis, M.I.T. (1993), "A Semiclassical Study of the Energy Level Structure in the Diamagnetic Kepler Problem."

[NRV87] J. Neukammer, H. Rinneberg, K. Vietzke, A. König, H. Hieronymus, M. Kohl, H.-J. Grabka, and G. Wunner, Phys. Rev. Lett. **59**, 2947 (1987). "Spectroscopy of Rydberg Atoms at $n \simeq 500$: Observation of Quasi-Landau Resonances in Low Magnetic Fields."

[NUM33] B. V. Numerov, Publ. de l'Observ. Astrophysique Central de Russie **2**, 188 (1933).

[OMA89] P.F. O'Mahony, Phys. Rev. Lett. **63**, 2653 (1989). "Quasi-Landau Modulations in Nonhydrogenic Systems in a Magnetic Field."

[ORT67] J. Ortega in **Mathematical Methods for Digital Computers,** edited by A. Ralston and H.S. Wilf (Wiley, New York, 1967), Vol. II, pp. 94-115. "The Givens-Householder method for symmetric matrices."

[PAR89] S.P. Parker, **Optics Source Book,** McGraw Hill, 1988, p. 17.

[PFT88] W. H. Press, B. P. Flannery, S. A. Teuolsky and W. T. Vetterling, **Numerical Recipes in C**, (Cambridge University Press, New York, 1988).

[POR65] C.E. Porter, ed., **Statistical Theories of Spectra: Fluctuations,** (Academic Press, New York 1965).

[RAL80] A. R. P. Rau and K. T. Lu, Phys. Rev. A **21**, 1057 (1980). "Comments on Near-Zero-Energy Resonance in Atoms in External Fields"

[RED64] Peter J. Redmond, Phys. Rev. B **133**, 1352 (1964). "Generalization of the Runge-Lenz Vector in the Presence of an Electric Field."

[REI83] W.P. Reinhardt, J. Phys. B **16**, L635 (1983). "A Time-dependent Approach to the Magnetic-field-induced Redistribution of Oscillator Strength in Atomic Photoabsorption."

[ROB81] M. Robnik, J. Phys. A **14**, 3195 (1981). "Hydrogen Atom in a Strong Magnetic Field: on the Existence of the Third Integral of Motion."

[SEN87] T. Seligman and H. Nishioka, ed. **Quantum Chaos and Statistical Nuclear Physics,** (Springer Verlag 1987).

[SHC93] B.D. Simons, A. Hashimoto, M. Courtney, D. Kleppner, and B.L. Altshuler, Phys. Rev. Lett. **71**, 2899, (1993). "New Class of Universal Correlations in the Spectra of Hydrogen in a Magnetic Field."

[SOL81] E.A. Solov'ev, JETP Lett. **34**, 265 (1981). "Approximate Motion Integral for a Hydrogen Atom in a Magnetic Field."

[TAB89] M. Tabor, **Chaos and Integrability in Nonlinear Dynamics**, (John Wiley and Sons, New York, 1989).

[TOH91] S. Tomsovic and E. Heller, Phys. Rev. Lett. **67**, 664 (1991). "Semiclassical Dynamics of Chaotic Motion: Unexpected Long-Time Accuracy."

[VVH93] T. van der Veldt, W. Vassen, and W. Hogervorst, Europhys. Lett. **21**, 9 (1993).

[WAK91] S. Watanabe and H. Komine, Phys. Rev. Lett. **67**, 3227 (1991). "Adiabatic-Expansion Method Applied to Diamagnetic Rydberg Atoms."

[WAG89] Q. Wang and C.H. Greene, Phys. Rev. A **40**, 742 (1989). "Quantal Description of Diamagnetic Quasi-Landau Resonances."

[WEL89] G. Welch, Ph.D. Thesis, M.I.T. (1989). "High Resolution Spectroscopy of Rydberg Atoms in a Magnetic Field."

[WHW86] D. Wintgen, A. Holle, G. Wiebusch, J. Main, H. Friedrich, and K.H. Welge, J. Phys. B **19**, L557 (1986). "Precision Measurements and Exact Quantum Mechanical Calculations for Diamagnetic Rydberg States in Hydrogen."

[WIF86a] D. Wintgen, and H. Friedrich, J. Phys. B **19**, 991 (1986). "Matching the Low-field Region and the High-field Region for the Hydrogen Atom in a Uniform Magnetic Field."

[WIF86b] D. Wintgen, and H. Friedrich, Phys. Rev. Lett. **57**, 571 (1986). "Regularity and Irregularity in Spectra of the Magnetized Hydrogen Atom."

[WIG56] E.P. Wigner, Contribution to **Conference on neutron physics by time-of-flight,** Gatlinburg, Tennessee, 1956, reprinted in [POR65]. "Results and Theory of Resonance Absorption."

[WKI89a] G. Welch, M.M. Kash, C. Iu, L. Hsu, and D. Kleppner, Phys. Rev. Lett. **62**, 893 (1989). "Experimental Study of Energy-Level Statistics in a Regime of Regular Classical Motion."

[WKI89b] G. Welch, M.M. Kash, C. Iu, L. Hsu, and D. Kleppner, Phys. Rev. Lett. **62**, 1975 (1989). "Positive-Energy Structure of the Diamagnetic Rydberg Spectrum."

[WRT92] D. Wintgen, K. Richter, G. Tanner, Chaos **2**, 19 (1992). "The semiclassical helium atom."

[WWZ86] G. Wunner, U. Woelk, I. Zech, G. Zeller, T. Ertl, F. Geyer, W. Schweizer, and H. Ruder, Phys. Rev. Lett. **57**, 3261 (1986). "Rydberg Atoms in Uniform Magnetic Fields: Uncovering the Transition from Regularity and Irregularity in a Quantum System."

[ZAD93] J. Zakrzewski and D. Delande, Phys. Rev. E **47**, 1650 (1993). "Parametric motion of energy levels in quantum chaotic systems. I. Curvature Distributions."

[ZCK78] M.L. Zimmerman, J.C. Castro, and D. Kleppner, Phys. Rev. Lett. **40**, 1083 (1978). "Diamagnetic Structure of Na Rydberg States."

[ZDK93] J. Zakrzewski, D. Delande, and M. Kuś, Phys. Rev. E **47**, 1665 (1993). "Parametric motion of energy levels in quantum chaotic systems. II. Avoided-crossing Distributions."

[ZKK80] M.L. Zimmerman, M.M. Kash, and D. Kleppner, Phys. Rev. Lett. **45**, 1092 (1980). "Evidence of an Approximate Symmetry for Hydrogen in a Uniform Magnetic Field."

[ZKW82] M.L. Zimmerman, M.M. Kash, and G.W. Welch, J. de Phys. C2, **43**, 113 (1982). "Avoided Crossings and Autoionization Widths of Hydrogen and Alkali Metals in a Magnetic Field."

[ZLK79] M.L. Zimmerman, M.G. Littman, M.M. Kash, and D. Kleppner, Phys. Rev. A **20**, 2251 (1979). "Stark Structure of the Rydberg States of Alkali-metal Atoms."